



**UNIVERSITÀ DEGLI STUDI DI TRIESTE**

**XXIX CICLO DEL DOTTORATO DI RICERCA IN  
INGEGNERIA E ARCHITETTURA**

---

**ENHANCEMENT OF THE  
SEISMIC PERFORMANCES OF  
HISTORIC MASONRY BUILDINGS THROUGH  
GLASS FIBER-REINFORCED MORTAR**

Settore scientifico-disciplinare: ICAR/09 TECNICA DELLE COSTRUZIONI

**DOTTORANDA  
INGRID BOEM**

**COORDINATORE  
PROF. ING. DIEGO MICHELI**

**SUPERVISORE DI TESI  
PROF. ING. NATALINO GATTESCO**

**ANNO ACCADEMICO 2015/2016**

# INDEX

1	Outlook.....	3
2	Introduction .....	5
2.1	Seismic performances of unreinforced masonry.....	5
2.1.1	Structural behavior and mechanical characteristics .....	6
2.1.2	Testing, design and modeling unreinforced masonry.....	9
2.2	Modern techniques for reinforcing masonry buildings .....	16
2.2.1	Characteristics and classification.....	17
2.2.2	Testing, design and modeling reinforced masonry .....	21
3	GFRM technique and characterisation .....	25
3.1	Reinforcement technique.....	25
3.2	Characteristics of GFRP elements .....	26
3.3	Characterization tests on GFRM .....	31
3.3.1	Pull-out tests .....	32
3.3.2	Lap-splice tests .....	38
3.3.3	Tensile tests.....	41
3.3.4	Shear bond tests .....	47
3.4	Summary.....	54
4	In-plane behaviour.....	57
4.1	Experimental diagonal compression tests.....	57
4.1.1	Specimens characteristics.....	57
4.1.2	Tests apparatus .....	69
4.1.3	Loading procedure and measurements .....	70
4.1.4	Results and discussion.....	72
4.1.5	Interpretation of the results.....	95
4.2	Analytical estimations.....	102
4.3	Numerical simulation of diagonal compression tests .....	115
4.4	Numerical investigations on reinforced masonry buildings.....	124
4.4.1	Modeling .....	124
4.4.2	Method .....	131
4.4.3	Results and discussion.....	133
4.5	Summary.....	138
5	Out-of-plane behaviour.....	141
5.1	Experimental four-point bending tests .....	141
5.1.1	Specimens characteristics.....	142
5.1.2	Tests apparatus .....	145

5.1.3	Loading procedure and measurements .....	148
5.1.4	Results and discussion.....	149
5.1.5	Interpretation of the results.....	154
5.2	Analytical estimations.....	157
5.2.1	Unreinforced specimens.....	157
5.2.2	Reinforced specimens.....	159
5.3	Numerical simulation of out-of-plane bending.....	163
5.3.1	Model characteristics.....	163
5.3.2	Numerical results and discussion .....	167
5.3.3	Parametric study .....	170
5.3.4	Actual out-of-plane performances of reinforced masonry walls.....	172
5.4	Numerical investigation on the behaviour of reinforced masonry vaults.....	177
5.4.1	Model characteristics.....	177
5.4.2	Actual behavior of vaults .....	178
5.4.3	Incidence of load pattern on the vault behavior .....	186
5.5	Summary.....	190
6	Conclusions.....	193
7	References.....	197
8	Figure index .....	209
9	Table index.....	215
10	Acknowledgments .....	219

# 1 OUTLOOK

Seismic events evidence with frequent recurrence that the research and the development of effective intervention techniques for the reduction of the seismic vulnerability of historic masonry buildings is an extremely timely topic.

This study investigates on the behavior of a strengthening technique for unreinforced masonry based on the application, on both the sides of the wall, of a 30 mm thick mortar coating with Glass Fiber-Reinforced Polymer (GFRP) meshes embedded. The effectiveness of this technique, called Glass Fiber Reinforced Mortar (GFRM), for the enhancement of both the in-plane and out-of-plane performances of masonry walls is proved through experimental tests and numerical simulations, which are here described and discussed in detail.

In particular, a contextualization of the study is presented in the introduction section (2), describing briefly the behavior of historic unreinforced masonry buildings subjected to seismic actions and evidencing the main critical aspects to be considered so to ensure an adequate safety against horizontal loads. Some well-known basic notions, testing and analysis methods and interpretations for the evaluation of the performances of masonry resisting elements are summarised. Furthermore, an overview on the state-of-art in the field of reinforcement techniques for masonry structures is reported, focusing, in particular to modern strategies employing composite materials.

In section 3, the considered reinforcement method is described and the experimental results of different characterization tests are shown. The tests, which concern both single GFRP elements (wires and corner elements) and investigations of the behavior of GFRM layers (pull-out, lap-splice, tensile and bond tests), provide useful information for both the interpretation of the actual behavior of reinforced masonry and numerical modeling purposes.

Section 4 concerns the in-plane behavior of GFRM reinforced masonry. The characteristic and the results of a wide number of diagonal compression tests carried out in laboratory field are presented and discussed, evidencing the effectiveness of the technique, on the basis of a comparison with the performances of unreinforced masonry samples. Some considerations on the influence of different parameters (such as the masonry type, thickness, characteristics of both masonry and mortar layers and GFRP reinforcement amount) on the technique effectiveness, based on experimental evidences, are also reported. The tests permit to investigate on the reinforced masonry equivalent diagonal tensile strength, shear modulus and deformation capacity. Analytical formulation, based on the experimental findings, are then proposed to predict the stiffness and the resistance of reinforced masonry specimens; a simple numerical Finite Element

model is elaborated so to check the influence of some masonry and mortar parameters. At last, a preliminary study aimed to the evaluation, at the whole building scale, of the seismic performance improvement due to the application of the reinforcement is performed by applying a simplified modeling method (Equivalent Frame Method). Different building configurations and masonry types are considered. The application of the modified Capacity Spectrum Method permitted to compare the performances of reinforced and unreinforced structures also in terms of maximum resisting ground acceleration.

In section 5, the out-of-plane behavior of GFRM reinforced masonry is investigated. In analogy with the approach adopted for in-plane behavior, the results of some experimental tests (four-point bending) on unreinforced and reinforced full-scale masonry samples of different types are presented and compared, allowing an evaluation of the technique effectiveness in terms of both resistance and displacement capacity. The interpretation of the results permits also to propose simple formulations for the evaluation of the cracking and ultimate bending resistance of reinforced masonry walls. A numerical Finite Element model is then presented to simulate the experimental tests and perform a parametric analysis, varying the main masonry and reinforcement parameters (such as thickness, stiffness and resistance). Some typical configurations of masonry walls of historic buildings subjected to out-of-plane bending are also analysed numerically to evaluate the actual performance improvements. Moreover, the numerical model is applied for the simulation of the behavior of unreinforced and GFRM reinforced masonry vaults subjected to horizontal loads acting in the transversal direction.

Each section ends resuming the respective contents and results. Moreover, the main findings of the study, the final remarks and the future developments of the research are summarised in the conclusion section (6).

## 2 INTRODUCTION

Masonry is a traditional construction material extensively employed all over the world, since ancient times, for the erection of buildings and infrastructures (Singer & al. 1954; Portoghesi, 2011). It is commonly defined as a biphasic material, composed of natural or artificial solid units arranged in different ways and mainly jointed by mortar. The huge number of different masonry types can be classified in different ways (Giuffrè, 1990; Carbonara, 1996; Mannoni, 2005; Borri & al., 2015a), considering the elements nature (sandstone, limestone, tuff, adobe, clay, concrete...), their size and shape (blocks, ashlar, rubble, cobbles...), their arrangements in surface and in thickness (course, erratic, with rows of solid bricks interposed, single/multiple leaf, infilled...) and the presence/quality of the mortar.

Nowadays, most of the historic buildings in the ancient part of European cities are made with solid bricks or stone unreinforced masonry; this architectural heritage is very variegated and ranges from Ancient Roman until Twentieth century structures. Traditionally, masonry buildings were provided by wooden floors and the presence of masonry arches and vaults was also rather frequent; however, in the most recent examples, steel joist with brick or reinforced concrete vaults ceilings, reinforced concrete joist with hollow brick interposed and reinforced concrete plates were also employed for the floors.

The most of these structures were built according to the common practice of the period and of the place, mostly founded on empiric rules of proportion based on experience. Although they usually performed a good behavior under normal operating conditions (Mastrodicasa, 2012), very often, in consequence of a seismic event, showed an high vulnerability, suffering serious damage and attaining, sometimes, even to collapse, as evidenced also recent earthquakes such as East Slovenia 1998-2004, Western Greece 2003, Southern Greece 2006-2008, Central Italy 2009-2016 and Northern Italy 2012 (Gostic & Dolinsek, 2008; Augenti & Parisi, 2010; Parisi & al., 2012a; Penna & al., 2014). Thus, it is a crucial, key topical issue to assure an adequate seismic behavior for such buildings, so to avoid losses in human lives, in economical goods and in assets of the social, cultural and architectural heritage.

### 2.1 Seismic performances of unreinforced masonry

Although it is not a subject of this study to discuss in deep on the methods developed for the analysis of unreinforced masonry buildings, it is necessary a mention to the main aspects that have to be taken into account when approaching to the evaluation of their seismic performances,

referring to investigations reported in the literature for a more detailed discussion on this topic (Lourenco P.B, 1996; Cattari S, 2007; Parisi F., 2010).

In fact, to ensure the seismic safety of historic masonry buildings, it is of fundamental importance to assess, through reliable procedures, their actual structural performances and, if inadequate, to design effective intervention strategies to improve their behavior.

### *2.1.1 Structural behavior and mechanical characteristics*

The ground motions provoked by an earthquake cause a tri-dimensional vibration in masonry buildings that induces vertical and horizontal inertial forces. These inertial forces have to be transmitted from the intermediate floors and the roof to the vertical masonry walls and, then, to the foundation system. Typically, the seismic action is schematized as superposition of three load components: two acting horizontally, in the two in-plan main directions, and one vertically.

Usually, the effects of the vertical component in ordinary historic masonry buildings are negligible, due to the presence of gravitational load and to the quite good resistance reserves against vertical actions.

The repartition of the horizontal seismic loads among the vertical resisting elements depends, in general, from their distribution in the structure, their reciprocal connection and with the floors and the floors in-plane stiffness. In particular, it has been widely experienced and demonstrated (Paulay & Priestley, 1992; Tubi, 1993; Drysdale & al. 1994; Toulaitos, 1996; Magenes & Calvi, 1997; Tomazevic, 1999) that, assuring structural regularity, effective connections between orthogonal walls and between walls and adequately rigid floor diaphragms (attaining, thus, to the so called “box behavior” - Figure 2.1.a), the distribution of the seismic action among the resisting elements depends on their stiffness. Thus, it is possible to exploit the in-plane resistance of the masonry walls oriented in the seismic direction (Figure 2.1.b), limiting out-of-plane actions on the other walls (Figure 2.1.c). Differently, in case of inadequate structural integrity, the walls tend to behave independently, both in-plane and out-of-plane, causing partial collapses due to the activation of several local mechanisms related to rigid motion of parts or whole masonry walls (wall overturning, vertical and/or horizontal bending, overturning of the building corner, collapse of the gable...). Moreover, dangerous torsional vibrations may occur when an unbalanced in-plan or in-height distribution of masonry resisting elements is present.

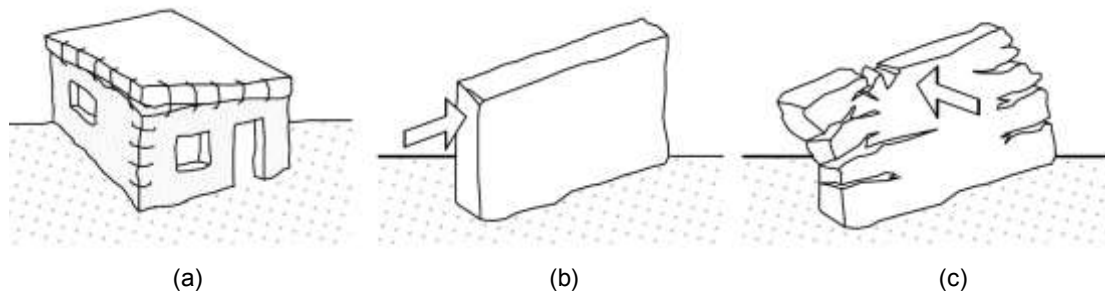


Figure 2.1 – Structural behavior of masonry buildings: (a) schematization of “box behavior”, which leads to the desirable activation of (b) in-plane response of masonry walls, avoiding the activation of (c) out-of-plane, poor resistance reserves

Besides structural integrity and distribution of resisting elements, the seismic behavior of masonry buildings is strictly related to the mechanical characteristics of masonry itself. In fact, despite of its appreciable resistance when subjected to compression, masonry has a very low tensile resistance (Samarasinghe, 1980; Hendry, 1981; Dhanasekar & al., 1985). This mechanical characteristic, usually related to the scarce consistency of mortar joints and of the mortar-units interface, induces the main failure mechanisms in masonry resisting elements, both in-plane and out-of-plane. Moreover, the presence of multiple-leaf masonry walls without effective connections among leaves is also rather frequent; this aspect further weakens the resistance and stiffness characteristics of masonry walls. A proper knowledge of the masonry consistency is thus necessary, as these material deficiencies may lead to the global collapse of the building.

In the study of perforated masonry walls subjected to in-plane horizontal actions (Tomazevic, 1999; Magenes & al., 2000), distinct macro-elements are usually identified, on the basis of experimental evidences: piers and spandrels (Figure 2.2). A masonry portion between two horizontally adjacent openings, or between an opening and a building corner, defines a pier; a masonry portion between two vertically adjacent openings, or between an opening and the roof, a spandrel.

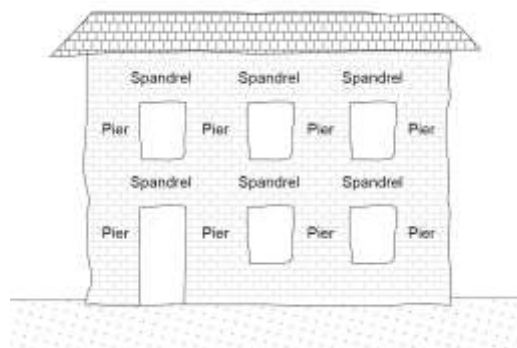


Figure 2.2 – Subdivision of a masonry façade in piers and spandrels

Extensive analyses of the earthquake damages on historic masonry buildings evidenced for both piers and spandrels different failure mechanisms depending on geometry, boundary conditions, amount of gravitational loads, masonry type, texture and quality.

In masonry piers, subjected to the combined action of vertical and horizontal loads, typical failure mechanisms concerned:

- diagonal cracking (Figure 2.3.a): linear or stair-stepped cracks along the compressed diagonal of the panel;
- sliding shear (Figure 2.3.b): horizontal cracks along the mortar bed joints, related to friction;
- bending/rocking (Figure 2.3.c): damage localized at the base and top cross sections, with horizontal cracks in tensed areas and possible masonry crushing at the compressed toes.

Typically, in case of low-rise buildings with low vertical stress, sliding is the main mode of failure. Wall piers subjected to higher vertical loads may fail in diagonal shear, resulting from the combination of the vertical and lateral loads; X-shaped cracks due to cyclic actions are commonly observed in squat piers. Differently, rocking mainly affects slender piers. Compared to rocking and sliding collapses, the diagonal cracking is a brittle mode of failure.

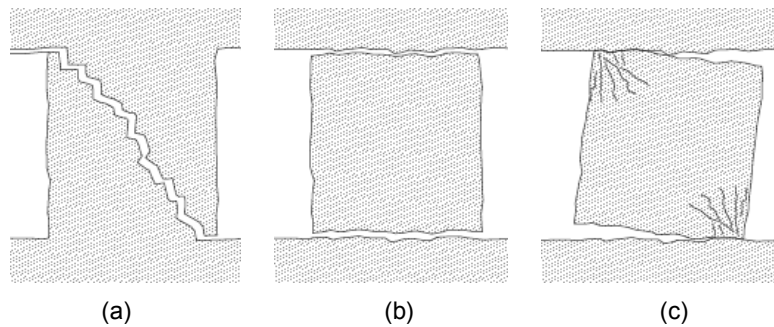


Figure 2.3 – Typical failure mechanisms of masonry piers: (a) shear, (b) sliding and (c) bending/rocking

Masonry spandrels (Figure 2.4), coupling vertical resistant elements, are subject to shear forces and bending moments but, differently from masonry piers, to only very limited compression forces. Thus, they perform a very limited resistance against the rocking failure mechanism (sub-vertical cracks at the spandrel's ends). The presence of effective tie beams at floor levels opposes to this mechanism, leading to a diagonal crack failure pattern. Sliding failure at spandrel lateral ends is unlikely in periodic masonry, as the mortar joints are not continuous along the vertical direction.

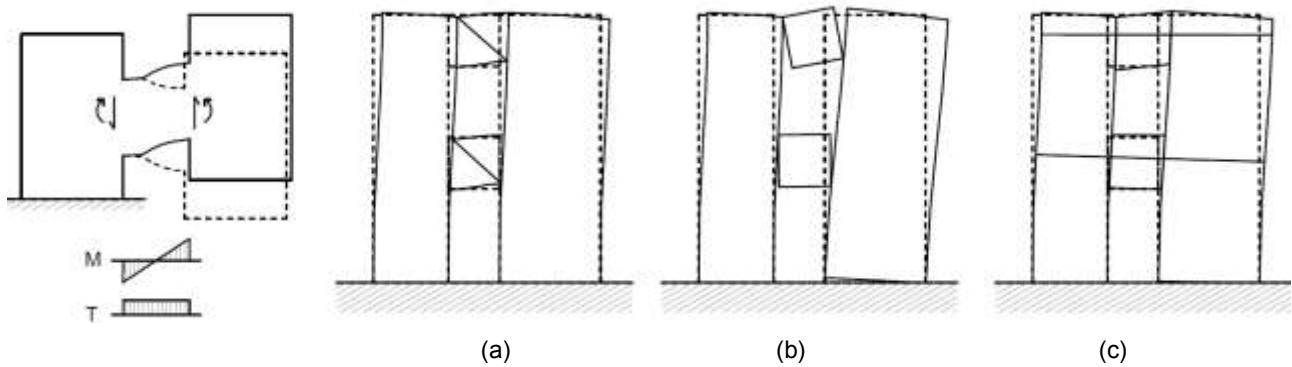


Figure 2.4 – Typical failure mechanisms of masonry spandrels: (a) shear and (b) rocking. Rocking can be effectively prevented through lintels or tie beams (c)

### 2.1.2 Testing, design and modeling unreinforced masonry

The preservation of existing masonry buildings against earthquakes requires reliable tools for the seismic safety assessment, based on the actual behavior of the resisting elements. A proper knowledge of the material and structural characteristics, as well as adequate design and modeling strategies, are thus of fundamental importance (Binda & Saisi, 2002).

A broad number of in-situ and laboratory experimental campaigns, aimed to assess the performances of unreinforced masonry elements when subjected to seismic loads, have been systematically performed since the Seventies till nowadays. Several types of tests were designed and executed, with diverse load pattern (concerning both in-plane and out-of-plane actions), loading rate (monotonic / cyclic, static / dynamic) and specimen dimensions (full-scale / reduced size).

Actually, in-situ destructive tests on in-plane masonry resisting elements refer to two types (Figure 2.5.a-b): direct shear tests and diagonal compression tests (Chiostrini & Vignoli, 1994; Corradi & al., 2003). In the first asset, the specimen is subjected to the equivalent axial load transmitted by overlying masonry and storeys and to a horizontal force at the middle height; in the second one, a diagonal compression load is applied. Even shear test better simulates the actual masonry stress state under horizontal loads, the preparation and execution of the test is more complex than diagonal compression test.

Besides testing whole masonry resisting elements, semi-destructive test on small masonry portions, such as shove tests (ASTM C1531-03; RILEM TC127-MS), are also available. However, these procedures are not able to provide exhaustive information on the global behaviour of the masonry and are aimed only at determining the shear strength of mortar joints in periodic textures.

Furthermore, other possible in-situ investigations concern non-destructive tests, such as georadar, thermograph, vibrational (McCann & Forde, 2001), which can provide useful information on the masonry structural consistency.

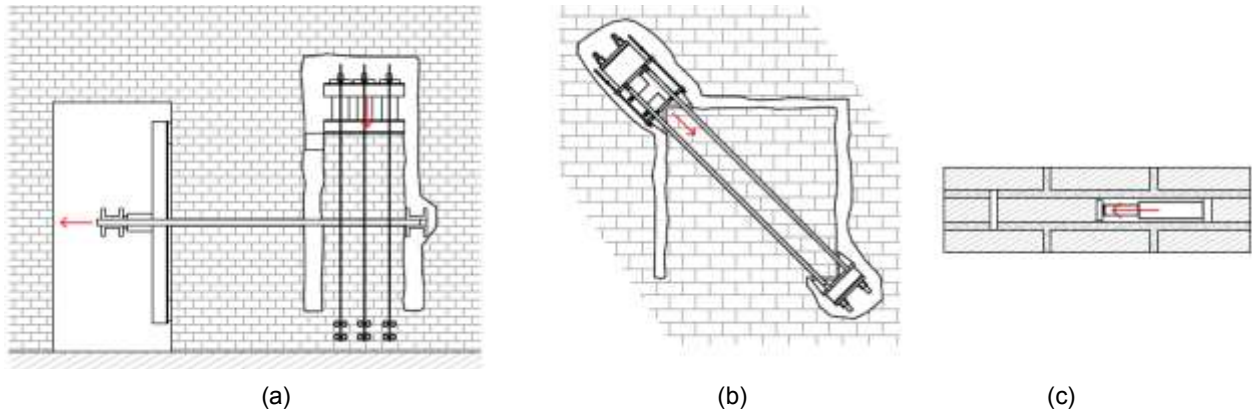


Figure 2.5 – In-situ characterization tests: (a) direct shear test and (b) diagonal compression destructive test on masonry panels and (c) semi-destructive shove test

Because in-situ tests on resisting elements are destructive by nature and sometimes difficult to perform, tests on specimens built and tested in laboratory conditions are also performed. In analogy to in-situ investigations, two type of laboratory tests are commonly considered for masonry resisting elements (Figure 2.6.a-b): shear-compression tests and diagonal compression tests (Chiostrini & al., 2000; Alecci & al., 2013).

In the former, the sample (typically 1500 mm height and 1000 mm length) is fixed both at the base and at the top and a uniform vertical action (representing gravitational loads transmitted by upper storeys) is applied and maintained constant; the horizontal, in-plane load is then applied at the top and varied cyclically, with complete inversion, increasing gradually the load rate till the wall collapse. Strength parameters, displacement capacity and hysteretic energy dissipation properties can be derived.

In the latter, the squared sample (typically 1200x1200 mm<sup>2</sup>) is rotated 45° and loaded along the vertical diagonal (ASTM E519-2010; RILEM TC76-LUM). Loading-unloading cycles are usually performed, so to check the masonry dissipative performances.

Sometimes, variations in the specimens arrangement, boundary restraint and testing setup where adopted by some authors, trying to reproduce as close as possible, the actual stress state in masonry (Gams & Tomazevic, 2012; Petry & Beyer, 2014).

Shear tests on triplets (Figure 2.6.c) are also used for the determination of initial shear strength (RILEM TC 127-MS; EN1052-3:2002/A1:2007), although show the same limits of shove tests.

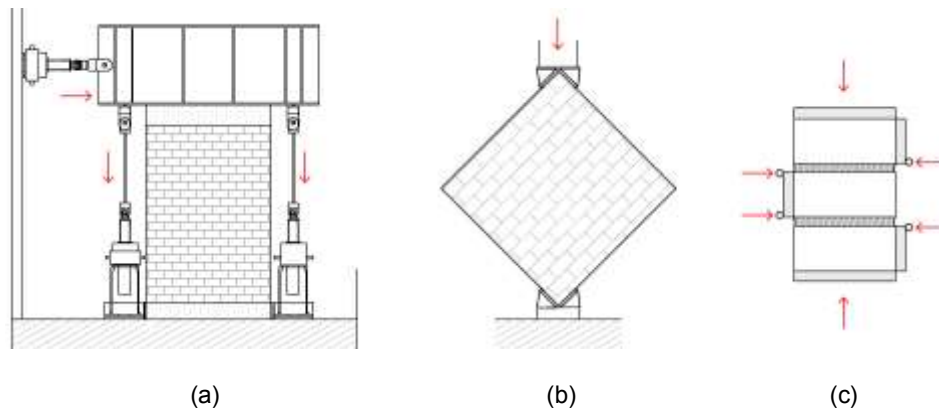


Figure 2.6 – Laboratory characterization tests: (a) shear-compression test and (b) diagonal compression test on masonry panels and (c) shear tests on masonry triplet

In addition, specific laboratory tests were recently designed to evaluate the behavior of masonry spandrels (Amadio & al., 2012; Beyer & Dazio, 2012; Graziotti & al., 2012; Parisi & al., 2012; Gattesco & al., 2016a; Calderoni & al., 2016). These tests concern, for the most, full-scale H-shaped masonry specimens composed of a masonry beam and portions of two masonry piers subjected to compressive stresses. One pier is fixed and the other one is vertically displaced according to determined, increasing cyclic steps (Figure 2.7). Experimental results regarding masonry spandrels are more limited, due to complexity in testing.

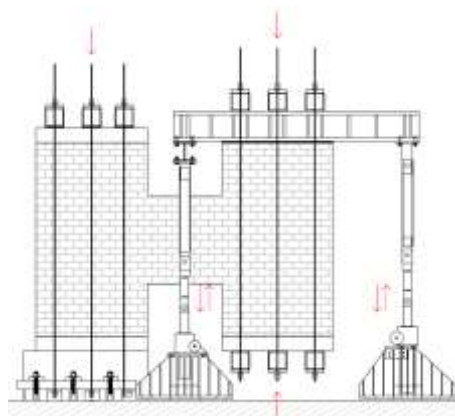


Figure 2.7 – Typical setup for laboratory characterization test on masonry spandrels

Actually, different interpretations of the results provided by in-plane tests on masonry samples are available in the literature, at the varying of the assumed stress state and of the considered limit strength domain (Chiostrini & al., 2000; Corradi & al., 2003; Calderini & al., 2010; Capozucca, 2011; Alecci & al., 2013). In particular, in regard to diagonal compression tests, both ASTM E519-2010 and RILEM TC76-LUM suggest to deduce the masonry diagonal tensile strength from the peak load derived assuming a pure shear state in the panel (Figure 2.8). However, experimental study based on photoelasticity methods (Frocht M.M., 1931) and finite element numerical investigations on elastic materials (Yokel & Fattal, 1975) demonstrated that the stress state at the

center of the panel is not of pure shear and the diagonal tensile strength associate to diagonal cracking is lower. Moreover, specimen dimensions and masonry ortotrophy may influence the results (Ghanem & al., 1994). Brignola & al. (2009) evidenced numerically that the stress redistribution which occurs in the masonry panels when the nonlinear range is attained may further reduce this value when irregular masonry is considered.

Furthermore, experimental in-situ investigations evidenced in some cases significant differences in the results obtained from diagonal compression tests and direct shear tests (Corradi & al., 2003; Borri & al. 2015b).

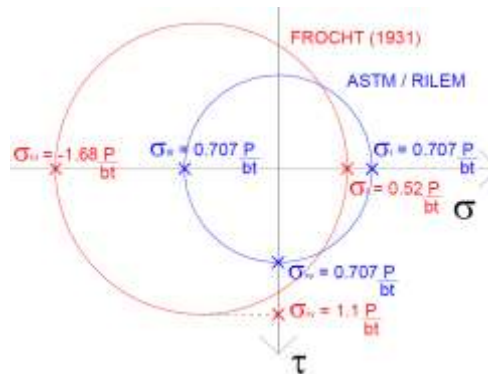


Figure 2.8 – Mohr's circle representation of different interpretations on the stress state in the centre of a panel subjected to diagonal compression

In-situ and laboratory experimental investigations on the out-of-plane performances of masonry walls (Baker, 1979) consist mainly in quasi-static cyclic tests on four-point bending (ASTM E518/E518M-15; Van Der Pluijm, 1999) or air-bag setups (ASTM E72-02, Derakhshan & al., 2013), so to reproduce the effects of the wall inertial load. In laboratory, the presence of gravitational loads transmitted by upper storeys is considered by applying on the top a uniform vertical action. The results interpretation is based on the study of the combined effect of the axial force and of the bending action induced by the horizontal load.

Static and dynamic laboratory tests on entire, full-scale or scaled masonry buildings were also performed (Magenes & al., 2012; Spyrakos & Francioso, 2012; Betti & al., 2014). These tests, even in a limited number, due to difficulties in performing and monitoring, result particularly useful to assess the reliability of simplified predictive models based on the performances deduced from testing single masonry panels (Tomazevic & Lutman, 1996; Rinaldin & Amadio, 2016).

Experimental tests on masonry resisting elements permitted to define and validate reliable mathematical models to estimate the mechanical characteristics of piers and spandrels, (e.g. EN1996-1-1; D.M.14.01.2008; FEMA 306; ACI 530-05; DIN 1053-100). A comparison among the main methods adopted by some building codes is reported in Calderini & al., 2009.

Two main interpretations of the diagonal shear failure of masonry piers are available: the former is based on a discrete schematization of the masonry (blocks and mortar joints) and on the application of the Mohr-Coulomb criteria (e.g. Mann & Muller, 1973) which involves the contributions of cohesion and of friction in mortar joints; the latter, attributable to Turnsek & Cacovic (1971), is based on the schematization of the masonry as a continuum and refers to the equivalent tensile strength of masonry. The Mohr-Coulomb criteria is also adopted for the prediction of the piers resistance against sliding shear failure mechanism. Differently, the pier lateral resistance associated to bending failure is evaluated considering the combined effect of compressive axial load and bending on cracked sections. The pier failure criteria at the varying of the axial load can be evaluated through the minimum envelope of the limit strength domains corresponding to the different failure modes. Typically, slender piers collapse by flexural mechanism while diagonal cracking mechanism tends to prevail in squat piers for increasing levels of vertical compression; bed joint sliding usually affect very squat, low compressed piers.

Similar approaches are dedicated to masonry spandrels with the possibility to consider also, in analogy to the compressive axial force on piers, the beneficial contribution of tie beams (Rinaldin & al., 2017).

Commonly, an elastic-plastic schematization is assumed for the different mechanisms for simplified nonlinear analysis purposes, with linear elastic behavior dependent from both the flexural and shear deformations. The provided values of ultimate displacement (drift) are based on a wide background of experimental results (e.g. Anthoine & al., 1995; Magenes & Calvi, 1997).

Different modeling strategies are available in the literature for the evaluation of the seismic response of masonry walls and buildings, based on different theoretical assumptions and level of detail (Magenes & al., 2000; Roca & al., 2010; Barbieri & al., 2013; Lourenco, 2013; Theodossopoulos & Sinha, 2013). In the framework of the finite-element methods, different approaches may be distinguished: micro-modeling, based on discrete elements or continuum, and macro-modeling.

In the micro-modeling discrete approach - Figure 2.9.a (Gambartta & Lagomarsino, 1997a; Lourenco & Rots, 1997) the masonry units and the mortar joints are modelled separately by means of distinct tri-dimensional or bi-dimensional elements connected through interfaces. Simplified micro-element discrete methods - Figure 2.9.b (Chaimoon & Attard, 2007; Spada & al., 2009) were also developed, assuming the masonry units bounded with interfaces which accounted for both the mortar and the unit-mortar interface behavior. The input data for micro-elements discrete models concern experimental laboratory tests on individual components of the masonry (e.g. compression and flexural tests on units and on mortar samples) and small brickwork samples (e.g. triplets shear tests) so to assess the units, mortar and interfaces specific constitutive laws and failure criteria.

This method requires a high computational effort, thus is typically adopted for simple masonry elements, for investigating, both to the static and dynamic fields, on the masonry non-linearity, micromechanics, local response and details.

In micro-modeling based on continuum (Figure 2.9.c), masonry is treated as a homogeneous material, with equivalent relationship between average stresses and average strains (e.g. Gambarotta & Lagomarsino, 1997b, Lourenco & al., 1998; Brasile & al., 2007; Calderini & Lagomarsino, 2008; Akhaveissy & Milani, 2013). Thus, the input data needed to describe the continuum are deduced from tests on large size masonry specimens (such as masonry wallets, piers and spandrels) or from the results of micro-element discrete numerical models. The reduction of the degrees of freedom and a simple mesh generation (independent from the particular masonry texture) diminish the computational request, making micro-modeling methods based on continuum suitable for the evaluation of the performances of entire masonry walls or buildings. This approach is frequently used for the analysis of the response of masonry elements or walls subjected to static or dynamic loads. Moreover, it represent a useful tool to reproduce the actual behavior of non periodic masonry (such as irregular stone ones).

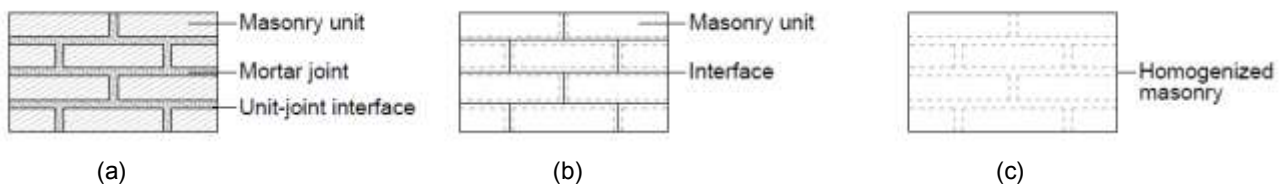


Figure 2.9 – Modeling strategies for masonry: (a) discrete micro-modeling, (b) simplified discrete micro-modeling and (c) based on continuum

With the aim of a further reduction of the computation time, modeling methods based on macro-elements were introduced for the global analysis of masonry buildings (Marques & Lourenco, 2011), based on the subdivision of the masonry walls in a limited number of macro-elements. Macro-elements models represent an evolution of the well-known POR approach (Tomazevic, 1978), based on the hypothesis of storey mechanism and diagonal cracking failure of the piers. Significant improvements (such as the introduction of the possibility of rocking and slip failure of piers and also of spandrels failure) were introduced, so to overcome its main limitations and extend its applicability to a wider range of structures. In simplified macro-elements models, the resisting elements, typically the piers and the spandrels, are usually schematised by means mono-dimensional beam elements, connected by rigid nodes (Magenes, 2000; Pasticier & al., 2008; Roca & al., 2005; Calliari & al., 2010; Lagomarsino & al., 2013; Petrovcic & Kilar, 2013), defining the “Equivalent Frame” model of the structure (Figure 2.10.a). Simplified analytical relationships, based on the possible macro-elements failure mechanisms, are applied to evaluate their resistance. Usually, the nonlinear response is lumped in localised hinges and ultimate

displacement are evaluated on the basis of the experimental results on piers and spandrels. However, different simplified schematizations, based on monodimensional struts (Calderoni & al., 1987) or bi-dimensional elements (D'Asdia & Viskovic, 1994; Caliò & al., 2005; Milani & Bruggi, 2016) are also available (Figure 2.10.b).

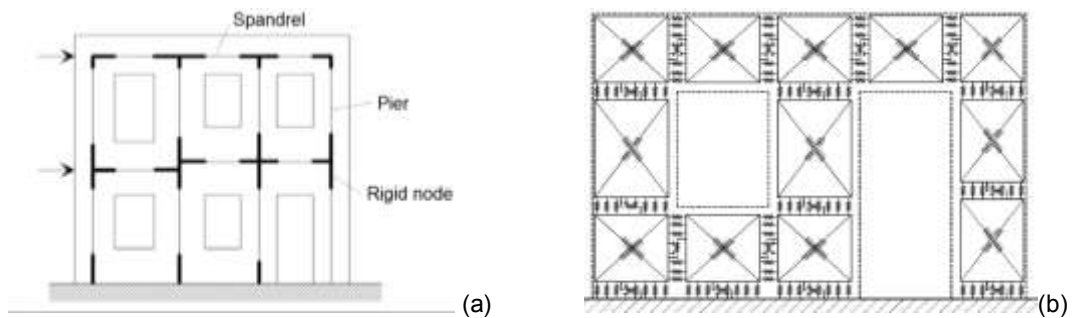


Figure 2.10 – Examples of macro-element models based on (a) monodimensional (Magenes & al., 2000) or (b) bidimensional elements (Caliò, 2005)

Nonlinear finite-element incremental static analyses based on macro-element modeling is proved a useful tool for the description of the global seismic behavior of existing masonry buildings, allowing to obtain, with low computational request, quite good predictions of the resistance and displacement capacity of the structures, when a proper calibration of the mechanical parameters and a reasoned schematization of the resistant elements is attained (Galasco & al., 2006; Marques & Lourenco, 2014).

In regard to the study of the out-of-plane masonry performances, a different, simplified approach, based on the study of the kinetics of collapse through the limit equilibrium analysis is commonly adopted, assuming the masonry wall as a kinematic chain of rigid blocks with infinite compressive strength and no tensile resistance - Figure 2.11 (Giuffrè, 1993; D'Ayala & Speranza, 2002). As this simplified method does not take into account neither the elastic deformation nor the post-elastic behavior of the wall, finite element micro-modeling strategies are often employed for such a purpose (Ferreira & al., 2015; Sorrentino & al., 2017).

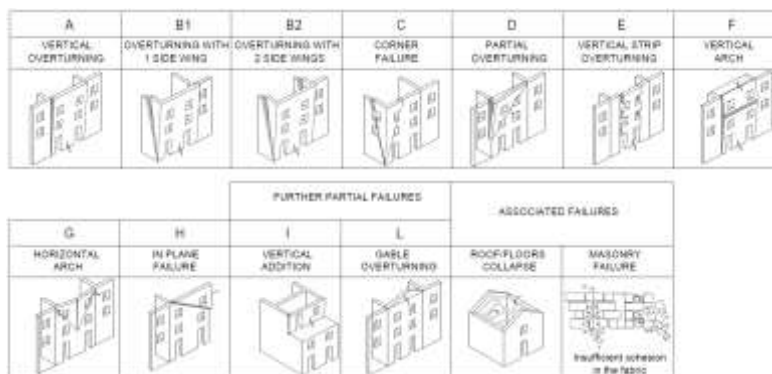


Figure 2.11 – Out-of-plane mechanisms typically considered in the limit equilibrium analysis of masonry walls (D'Ayala & Speranza, 2002)

## 2.2 Modern techniques for reinforcing masonry buildings

Since the systematic study on the seismic vulnerability of historic unreinforced masonry buildings has begun, in late Seventies, several researchers and professionals in the field have developed, tested and applied different reinforcing techniques to improve the capacities of masonry structures in resisting earthquakes (Martellotta & al., 2015).

Traditional techniques to achieve structural integrity included mainly the diaphragm stiffening, the connection of walls to floor diaphragms and the application of steel or reinforced concrete tiles (Karantoni & Fardis, 1992; Tomazevic & al., 1993; Tomazevic & al., 1996), so to encourage the global response of the structure and oppose to the independent response of the components. In such cases, masonry walls typically exhibit in-plane failure mechanisms, depending on the wall geometry, the mechanical properties of the masonry units and mortar, the interactions between them and the type of loads applied. The most diffuse traditional strengthening systems for masonry resisting elements concerned steel-reinforced concrete coatings, grout injections and unreinforced or steel-reinforced repointing of mortar joints (Hutchinson & al., 1984; Hamid & al., 1994; Binda & al. 1997; Tomazevic, 1999; Franklin & al., 2001; ElGawady & al., 2004a).

Different steel-reinforced concrete coatings were designed and investigated (Abrams & al. 2007). In ferrocement technique (Reinhorn & Prawel, 1985; Prawel & al. 1988; Chen, 2011, Ashraf & al. 2011) multiple layers of hardware cloths are embedded in a 10-20 mm thick cement mortar layer. Reinforced plasters concern thin cement layers (15-40 mm) reinforced by means of steel bars or welded meshes (Jabarov & al., 1980; Sheppard & Terceelj 1980; Churilov & Dumova-Jovanoska, 2012; Kadam & Singh, 2012). Shotcrete overlays (Kahn, 1984; Karantoni & Fardis, 1992; ElGawady & al., 2006) consist in spraying 50-100 mm thick concrete coatings on the masonry surface over steel welded meshes; shear steel dowels fixed with cement grout into holes drilled into the masonry are employed to connect the reinforced layers with the masonry. The experimental investigations performed on these techniques evidenced that their effectiveness in the enhancement on both the in-plane and out-of-plane performances of masonry walls depends on both the cement (strength and thickness) and steel (reinforcement percentage) characteristics. In particular, the presence of the steel reinforcement permits the improvement of the deformability capacity. However, the contribution of the reinforcement can be compromised by the plaster-masonry premature detachment, as the distribution of the seismic actions depends of the stiffness ratio between the two materials. It is thus of fundamental relevance to provide a good bond of the coating (e.g. cleaning, saturation, mechanical or chemical treatment of the masonry surface) and, if necessary, an adequate dimensioning of connectors.

The aim of grout injections in drilled holes in masonry (Binda & al., 1993; Tomazevic & Apih, 1993; Calvi & Magenes, 1994; Modena, 1994; Schuller & al. 1994; Vintzielou & Tassios, 1995;

Mazzon & al., 2010) is to fill voids and cracks present in unreinforced masonry, due to construction deficiencies, empty collar joints in multiple leafs masonry, mortar deterioration or masonry adjustments. The effectiveness of the injections depends on the compatibility of physical, chemical and mechanical properties of the original masonry and the injected material. Different injection mixtures (based mostly on cement) and methods were practiced and led, in general, to increments in masonry stiffness, compressive resistance and also shear strength, as able to prevent the separation of leaves and to improve the masonry cohesion. However, some critical aspects has to be considered in the application, mostly related to the difficulties in providing and controlling the uniformity of the injection (Binda & al., 1994). Moreover, the technique is not adequate for some types of walls such as single leaf walls or masonry with a low voids percentage within the core.

In applying the repointing technique (Corradi & al., 2008a; Valluzzi & al., 2005), weak mortars in regular courses masonry are partially removed from the bed joints and replaced with stronger, cement-based mixtures, able to improve the in-plane stiffness and resistance of masory walls. The introduction of steel rods or laminates in the the joints or in cuts created near the masonry surface before repointing was also employed to increase the walls resistance and deformation capacities.

Though extensively used in the past, traditional techniques using cement and steel elements have evidenced some critical aspects concerning deterioration, incompatibility with the historic materials and distortion of the structure seismic response, compromising the effectiveness of the intervention and the building appearance and integrity. For example, the steel elements showed, in the long term, severe problems of corrosion; the use of cement-based mortars and concrete reduced the vapor permeability of the masonry resulting, sometimes, in a damage of the surface finishes; heavy interventions, such as shotcrete, may add considerably masses to the building, increasing the earthquake induced inertia forces. In addition, the growing attention towards in the protection of the architectural heritage (Vecco, 2010) has led to the use of reinforcing materials characterised by an appropriate compatibility with those employed in historic buildings.

For these reasons, innovative strengthening techniques were proposed: in particular, non-corrosive reinforcements based on Fiber-Reinforced Polymers (FRPs) have been introduced (Ehsani & Saasatmanesh, 1996; Triantafillou & Fardis, 1997); moreover, the use of natural binders instead cement-based mixtures or organic resins has allowed a better mechanical and chemical compatibility with the masonry support, complying structural and conservation needs.

### *2.2.1 Characteristics and classification*

FRP is a composite material made of a organic, polymeric matrix (usually epoxy, vinylester or polyester thermosetting plastic) with addition of inorganic (mostly glass, carbon and basalt) or

synthetic (e.g. aramid, PBO – poliparafenilenbenzobisoxazole, PP - polypropylene) reinforcing fibers. Recently also natural fibers (such as flax, hemp, jute, sisal, kenaf, coir, kapok, banana, henequen...) have attracted the attention of many researchers (Ku & al., 2011; Codispoti & al., 2015; Ghiassi & al., 2015; Yan & al., 2016), although their mechanical properties significantly lower than those of other fibers, due to the growing concerns regarding the environmental impact of building materials.

Typically, reinforcing fibers are characterized by high rigidity and tensile resistance, with brittle behavior, and provide the tensile load-bearing portion of the composite. The polymer matrix protects the fibers and transfers stresses between the fibers and the surrounding structure (ACI 440, 2002). Thus, the performances of FRP composites depends on several aspects, such as the fibers characteristics (composition - Figure 2.12.a, orientation, length, shape...), the matrix chemical and mechanical properties, the fibers arrangement in the matrix and the fibers-matrix interaction. So, the FRP composite typically exhibits an intermediate tensile behavior between that of the fibers and of the matrix (Figure 2.12.b).

Commercially, the fibers are available arranged and woven in different forms: monofilaments (basic element, with dimensions of about 10  $\mu\text{m}$  diameter), tows, spun yarns, rovings (Figure 2.12.c). The filaments are classified by their chemical composition and their linear density (measured in “Tex”, equivalent to 1 g per km of fiber - ISO 1144:2016). FRP with uni-, bi- or multi-directional fiber orientation are available.

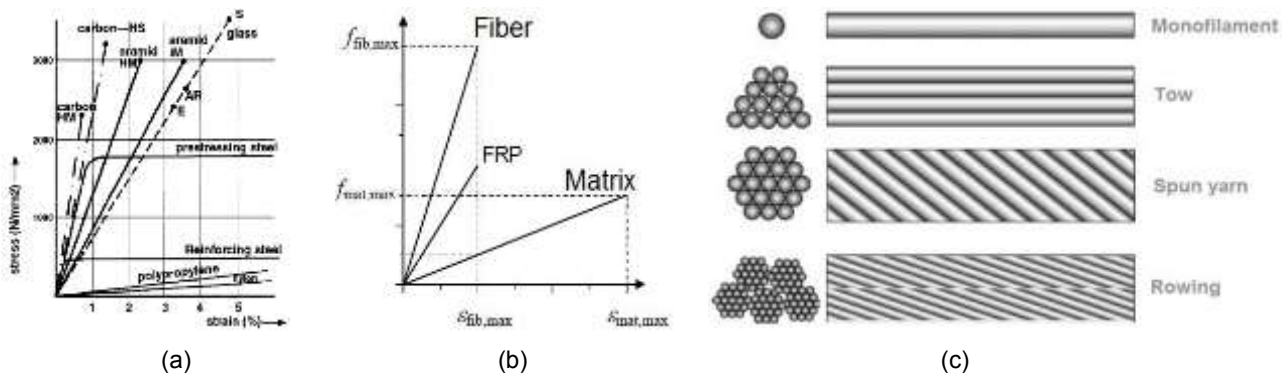


Figure 2.12 – Example of (a) typical tensile stress-strain behavior of various reinforcing fibers (ACI 440) and (b) behavior of FRP composites in respect to that of reinforcing fibers and matrix (CNR DT 200 R1/2013) and (c) typical fiber arrangements (CNR DT 200 R1/2013)

The development of FRPs began in 1930s and regarded mostly glass fiber composites; carbon and aramid fiber composites production started in the late 1950s. Their employment, however, concerned mainly aviation, shipbuilding, automotive and aerospace industries, sporting goods applications and specific structural components (tanks, pipes...). The systematic use of FRPs in civil engineering dates back to 1980s, finding application, as an alternative to steel, in the

realization of framed structures or in the production of reinforcing bars. Moreover, from 1990s, an exponential growth occurred in the application of this composite materials for the strengthening of reinforced concrete structures, at first, and then also of masonry buildings (Bakis & al., 2002; Mirmiran & al., 2003; Zoghi, 2013). The use of FRPs in the last 20 years has become a very common intervention practice to improve the performances of beams, pillars, columns, frame nodes, walls, floors... against both static and seismic loads (Shrive & al., 2001; Babatunde, 2017).

Actually, the use of FRPs in the enhancement of masonry structures is widespread because of the great mechanical properties (high strength to weight ratio), able to provide to masonry both high strength and a properly ductile behaviour, and of the low sensitivity to environmental agents (in particular, corrosion resistance), which makes the reinforcing system suitable for applications even under severe operating conditions (Triantafillou, 1998a; Tumialan & al., 2001a; Aldea & al., 2007).

Different retrofitting methods based on FRPs have been developed; depending on the elements employed (fabrics, meshes, laminates, bars...), the reinforcements can be externally bonded (EB) to the masonry surface, through either epoxy resin or inorganic matrix, or near surface mounted (NSM) in the masonry mortar joints (reinforced repointing) or in thin slots cut into the surface and bonded with resins or grouts (Corradi & al., 2008b; Kadam & al., 2014).

A first strategy, derived from previous experiences on reinforced concrete elements (Nanni, 1993; Ehsani & Saadatmanesh, 1996; Khalifa & al., 1998; Triantafillou, 1998a; Triantafillou, 1998b), concerns the bonding, through epoxy resins, of thin FRP elements (fabrics or laminates) on the masonry surface. Several experimental campaigns were aimed to assess the in-plane and out-of-plane effectiveness of this technique and to evaluate the influence of different parameters as the fiber type and amount, the type of resin, the reinforcement arrangement and the boundary conditions. Sometimes FRP spike anchors were introduced to improve the adhesion with the masonry.

In particular, experimental investigations showed that, for masonry walls subjected to in-plane loads, the shear performances can be significantly improved (Schwegler, 1994; Valluzzi & al., 2002; Chuang & al., 2003; Al-Salloum & Almusallam, 2004; Stratford & al., 2004; Lucciconi & Rougier, 2011; Tomazevic & al., 2011; Arifuzzaman and Saatcioglu, 2012; Umair & al., 2012; Bui & al., 2015). Other experimentations, concerning out-of-plane behavior, demonstrated also substantial increasing in the flexural resistance and displacement capacity of the strengthened walls (Ehsani et al., 1998; Gilstrap & Dolan; 1998; Velazquez-Dimas & al., 2000; Accardi & al., 2007; Hamed & Rabinovitch, 2010; Anil & al., 2012; Umair & al., 2015). Moreover, the benefits of the FRP reinforcement emerged also in testing masonry arches and vaults: FRP reinforcements, bonded at the intrados and/or extrados surface of vaulted structures, modify their collapse

mechanism, increasing the corresponding load carrying capacity, preventing the formation of localized structural hinges (Briccoli Bati & Rovero, 2001; Valluzzi & al., 2001; Foraboschi, 2001; Briccoli Bati & al., 2007; Cancelliere & al., 2010; Oliveira & al., 2010; Rovero & al., 2013).

Typically, the benefits of the FRP reinforcement are related to the ability of the composite material in contrasting the opening of masonry cracks, due to the high tensile strength. However, some drawbacks have to be considered: some tests evidenced that FRP is not totally compatible with the masonry (due to the differences between stiffness, strengths and thermal coefficients). In fact, in the application on masonry surfaces, the technique frequently evidenced a poor bond to the substrate (due to the higher surface roughness and irregularity, in respect to concrete) which may induce the reinforcement delamination, reducing the effectiveness of the intervention. In addition the epoxy resins, besides being high-costs and requiring special handling equipment and skilled installation staff, have very scarce resistance to high-temperatures and fire and are affected by ultraviolet (UV), water and alkaline degradation, needing therefore adequate protection systems (Frigione & al., 2006; Karbhari & al., 2007; Ghiassi & al., 2013; Sciolti & al., 2015); moreover, their application on wet surfaces or at low temperatures is not possible. Furthermore, the difficulty in removal the intervention (irreversibility of the retrofitting) lead heritage conservation authorities to avoid its application on listed historical buildings.

More recent EB methods, introduced to overcome most of these limits (Triantafillou, 2011), concerned Fiber-Reinforced Cementitious Matrix (FRCM) and Fiber-Reinforced Mortars (FRMs – known also as FRGs - Fiber Reinforced Grouts - or TRMs - Textile Reinforced Mortars), where the fiber-reinforced elements are embedded in a inorganic matrix (Kolsch, 1998; Faella & al., 2004; Papanicolaou & al., 2011). The various proposed systems differ in the type and thickness of the matrix (ranging from high strength cement-based mixtures to natural mortars, from an about 10 mm thin scratch coat to a 30-40 mm thick layer) and in the characteristics of the embedded reinforcement (mostly textile or meshes). The installation approach is quite simple, as requires the same skills and instruments of a traditional reinforced coating intervention, such as ferrocement or steel-reinforced plasters. These strengthening systems generally exhibit a more effective bond with the substrate in respect to the epoxy glued FRPs technique and also better performances at elevated temperatures (Bisby & al., 2013; Donnini & al., 2017). Inorganic matrices have a higher compatibility with historic masonry and, especially when lime-based mortars are employed, do not prejudice its water and vapour permeability (avoiding, thus, dangerous moisture accumulation at the interface) and the reversibility of the intervention.

Experimental investigations concerning composite textiles or meshes embedded in a mortar coating and applied on both wall faces evidenced the ability of these reinforcement systems to increase the in-plane (Prota & al., 2006; Aldea & al., 2007; Papanicolaou & al., 2007; Faella & al., 2010; Babaeidarabad, 2013; Corradi & al., 2014; Borri & al, 2015c; Gattesco & al., 2015a,

Garofano & al., 2016; Yardim & Lalaj O, 2016; Marcari & al., 2017) and out-of-plane (Manzoni & al., 2008; Papanicolaou & al., 2008; D'Ambrisi & al., 2013; Ismail & Ingham, 2016) resistance of masonry, also raising significantly the plastic deformation capacity. Moreover, promising results were obtained in testing reinforced masonry vaults (Panizza, 2010; Bednarz & al., 2011; Borri & al. 2011; Hojdys & Krajewski 2012; Alecci & al., 2016; Girardello & al., 2013; Garmendia & al. 2015).

However, the masonry-matrix bonding performances still remain a key topic for an effective design of the material (Carbone I., 2010). To avoid the detachment of wall coatings, the separation of wall leaves and improve the reinforcement effectiveness, transversal connectors were also introduced in some applications.

As an extension of the traditional steel reinforced repointing technique, the use of FRP NSM bars or strips located in mortar joints or thin slots cut in the masonry surfaces and injected with thixotropic cementitious grouts was proposed. Besides FRPs elements, also stainless steel bars and strands reinforcements were employed (Ismail & al., 2011).

The NSM technique performed good results in terms of in-plane strength and deformation capacity of masonry, permitting also to preserve the aspect of fair-face walls (Tumialan & al., 2001b; Petersen & al., 2010a; Mahmood & Ingham, 2011; Dizhur & al., 2013; Gams & al., 2015; Hracov & al., 2016; Parvin & Shah, 2016). Moreover, NSM reinforcements are able to provide resistance against out-of-plane actions in walls (Tinazzi & al. 2000; Turco & al., 2006; Willis & al., 2010) and vaults (Zlamal and Stepanek, 2009). However, the technique is suitable only for regular textures and it is not effective for multiple leaf masonry, if no transversal connections are planned; in addition, its effectiveness is limited by debonding failure. To overcome these deficiencies, considering also the application on irregular and multi-wythe walls, innovative structural repointing methods based on stainless steel or synthetic chords (with carbon fiber or polyethylene core) were proposed or both masonry walls and vaults (Borri & al., 2009; Borri & al., 2014; Csikai & al., 2014).

### *2.2.2 Testing, design and modeling reinforced masonry*

Successful retrofit strategies requires the understanding of the expected response mechanisms of the reinforced masonry elements and how they can affect the whole building response.

The experimental investigations aimed to the evaluation of the effectiveness of a reinforcement technique are based on the comparison between the performances of plain and enhanced masonry samples tested under the same boundary and loading conditions. Typically, tests on full-scale masonry resisting elements concern in-plane shear-compression and diagonal compression tests and out-of-plane four point-bending or air-bag tests (in-situ or laboratory, subsection 2.1.2), as able to provide information on the resistance, displacement and dissipative capacities

improvements due to retrofitting (ElGawady & al., 2004b). Besides, some laboratory dynamic tests (shaking table tests based on an acceleration history of increasing intensity) on masonry resisting elements and on whole buildings were also experienced (ElGawady, 2004; De Santis & al., 2016; Urban & Stempniewski, 2012; Xu & al., 2012) reproducing the behavior of reinforced masonry under actual seismic conditions and proving the reliability of the more simplified experimental models.

The fundamental benefits of the reinforcement with a composite material are strictly related to its great performances when subjected in tension. Thus, specific tensile tests aimed to assess the failure mode and the equivalent constitutive law of the fibers embedded in the matrix (organic or inorganic) were developed. Tests typically concern in rectangular strips of composite materials clamped at the ends with tabs and subjected to a monotonically increasing tensile elongation (displacement control test); the elongation in the central, undisturbed area of the sample is measured. A proper design of the clamping method and of the sample length are essential to obtain representative results (slippage from clamping heads and localized damage at ends has to be avoided and the base length for the elongation monitoring has to be adequate to provide representative measurements).

FRP typically exhibit an elastic brittle behavior. Differently, the tensile performances of FRCM and FRM composites materials are generally articulated into three stages (Figure 2.13): a pre-cracking, elastic stage, influenced mainly by the inorganic matrix characteristics, a multiple cracking formation stage, with sequential onset of cracks in the matrix, in the direction orthogonal to that of the loading, and a post-cracking stage, as the crack pattern stabilizes and the material behavior is mainly governed by the embedded fiber textile, which carries the load up to failure. In general, the stiffness of this third stage can be approximately parallel to that of the textile alone. The possible gap between the third stage of the composite and the textile alone behavior represents the stiffening contribution of the matrix between adjacent cracks. A wide range of experimental setting and results concerning tensile characterization tests of FRCM and FRM are available in the literature (Babaeidarabad, 2013; Carozzi & al., 2014; Garmendia & al., 2014; De Santis & De Felice, 2015a; Ascione & al., 2015; Arboleda & al., 2016); the relevance and recognisability of the stages depend on the geometrical and mechanical characteristics of the two components and on their interaction.

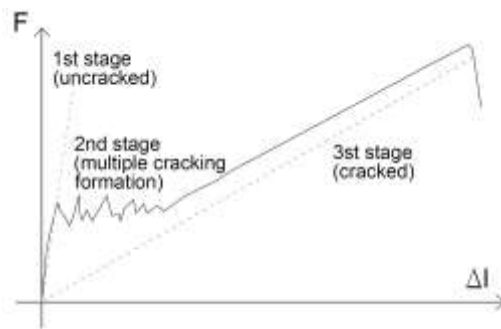


Figure 2.13 – Typical three-stages behavior of a FRM sample subjected to tensile test

Moreover, tests on masonry panels evidenced that, among the main aspects to be considered in the retrofitting design, is the possibility of reinforcement debonding, which may lead to an ineffective use of the material, and its potential reactivity to some environmental components that can affect its characteristics (durability).

Shear bond tests (CNR DT 200 R1/2013, ACI 440.7R-10), aimed to evaluate the interaction between the composite material and the masonry substrate are typically based on small masonry samples (single brick or stone units, or masonry wallets) to which the composite is applied on one or both sides, for a determined area. The extension of the reinforcing fibers component, outside both the matrix and the substrate, and the creation of an appropriate clamping system allow the application of a monotonic tensile load parallel to the masonry sample surface. The collapse may occur as a consequence of the failure of the different components: debonding of the masonry substrate, of the masonry-matrix or of the matrix-reinforcing fibers interface, slippage of reinforcing fibers within the matrix (eventually accompanied by the matrix tensile cracking) and tensile rupture of the composite out of the bonded area. Variations in the nature and roughness of the masonry surface, in the bond area and in the characteristics of the material composite influence the resistance and the type of collapse (Valluzzi & al., 2012; Capozucca, 2013; Carrara & al., 2013; De Felice & al., 2014; Ghiassi & al., 2015; Mazzotti & al., 2015; Leone & al., 2016). Besides shear bond, tensile bond tests, which consider load acting in the direction normal to the substrate, were performed (pull-off tests - EN 1015-12:2016, ASTM C1583).

The performances of the composite materials after the exposure to different environmental conditions were also investigated experimentally, due to the need to evaluate deterioration effects on the load carrying capacities of the reinforcement (Oliveira & al., 2014; De Santis & De Felice, 2015b; Sciolti & al. 2015; Corradi & al., 2016). The most relevant recognised degrading environmental agents are moisture, thermal cycling, freeze-thaw cycling, creep, fatigue, alkaline environment and ultraviolet light. The level of deterioration (physical, chemical and mechanical) depends on a series of factors such as type of fibers and matrix, manufacturing process and severity of exposure; furthermore the interaction with the masonry substrate has also to be

considered. Actually, tests are based on accelerated ageing procedures, but the connection of the results with those of real time exposures is still an open issue (Karbhari, 2007; Zorzi, 2014).

Based on experimental evidences, analytical models have been developed for the prediction of the strength characteristics of reinforced masonry walls. In particular, the most of the available strategies proposed in guidelines and building codes (ACI 440.7R-10; ACI 549.4R-13; AC434; CNR-DT 200/R1 2013) to evaluate the in-plane shear strength of FRP or FRM reinforced masonry walls are typically based on the linear effects superposition, considering the load carried by the unreinforced masonry and that carried by the reinforcement. Out-of-plane flexural resistance evaluations (and also in-plane bending strength) are performed through the well-known relations to design reinforced elements subjected to combined axial and bending action. It is worth note that in applying all these methods a particular attention has to be paid to possible premature failure due to the debonding of the reinforcement, which can reduce its contribution.

In regard to the numerical modeling, in analogy with strategies developed for unreinforced masonry (2.1.2), reinforced masonry can be modelled according to both micro-element and macro-element approaches, depending on the goal of the investigation, such as micro-mechanisms of masonry-reinforcement assemblages or basic, global structural response of walls and buildings (Gabor & al., 2006).

In particular, in micro-element approach based on discretization, the behavior of the reinforcement and that of interface are considered separately (Petersen & al., 2010b; Carozzi & al., 2014; Mazzotti & Murgio, 2015; Monaco & al., 2016). Diversely, according to a continuum approach, the reinforcement and the interface with the substrate are homogenised (Lignola & al., 2009; Lucciconi & Rougier, 2011; Melotto, 2013; Corradi & al., 2014; Gattesco & al., 2015b; Basili & al., 2016; Garofano & al., 2016). Homogenised strategies were typically adopted for the simulations on single wall panels or vaults and in such a models the reinforcement and tensile characteristics are calibrated on the bases of experimental results concerning tensile and bond tests or of theoretical formulations.

Some research works addressed to the numerical study of reinforced masonry buildings; homogenised strategies prevailed on simplified macro-element approaches based on mono-dimensional or bi-dimensional schematization of masonry resisting elements (Sacco & al., 2009; Maruccio, 2010), due to the lack of exhaustive, simplified strategies to account for their behavior and interaction.

### 3 GFRM TECHNIQUE AND CHARACTERISATION

The description and the main mechanical characteristics of the considered Glass Fiber-Reinforced Mortar (GFRM) technique, assessed experimentally, are summarised in the following.

#### 3.1 Reinforcement technique

The GFRM strengthening technique considered consists in the application of a GFRP (Glass Fiber-Reinforced Polymer) mesh, on both faces of the masonry wall, embedded mortar layer having a minimum thickness of 30 mm (Figure 1).

The application procedure of the strengthening technique concerns the following phases:

- removal of the existing plaster and of the mortar from the joints between elements, 10-20 mm deep, on both wall faces;
- optional application of a layer of scratch coat;
- drilling passing through holes in the masonry, to allow for connectors insertion (about 25 mm diameter);
- application of the GFRP mesh on both faces;
- positioning of additional GFRP mesh devices in correspondence of the holes, so to improve the anchorage of the connectors in the mortar layer;
- insertion of couples of L-shaped GFRP connectors, lap spliced inside the holes for a minimum of 120 mm, and injection of thixotropic cementitious mortar inside the holes, so to fix the connectors to the masonry;
- application of the new mortar coating (minimum thickness 30 mm), taking care to positioning the GFRP mesh in the middle of the mortar thickness.

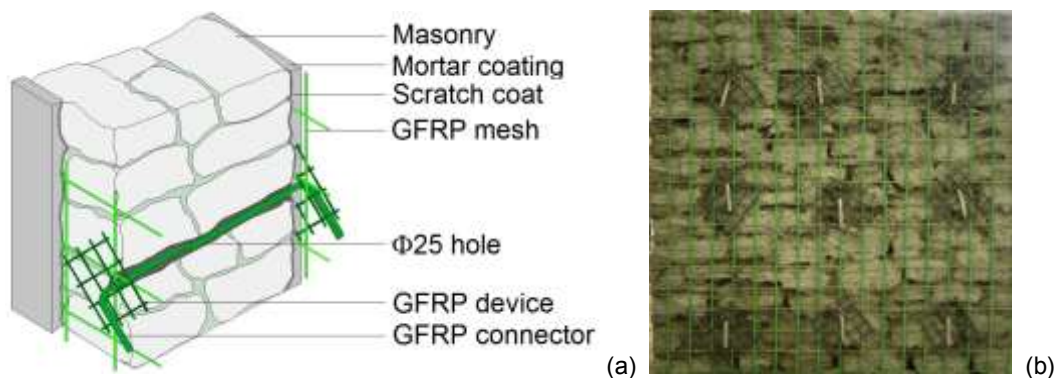


Figure 3.1 – GFRM reinforcement technique (a) schematization and (b) illustration during installation on a stone masonry wall, before the application of the mortar coating

### 3.2 Characteristics of GFRP elements

The wires of the GFRP meshes (Figure 3.2.a) are composed of Alkali-Resistant glass fibers (ASTM C1666/C1666M-07).

The dry fibers wires are soaked in a thermosetting resin made of epoxy vinyl ester with benzoyl peroxide as catalyst (Figure 3.2.b), then, before resin toughen, the mesh is formed by twisting the wires in one direction (warp) across the wires in the perpendicular direction, which fibers, differently, remain parallels (weft).

Preformed GFRP meshes are produced in rolls (Figure 3.2.c), with twisted fibers wires in the warp direction and parallel fibers wires in the weft one. Thus, for simplicity and speed of installation, the twisted fibers wires are commonly oriented in the vertical direction of a masonry wall. Preformed GFRP mesh angle brackets are employed to ensure the continuity of the reinforcement in correspondence of wall corners (Figure 3.2.d).

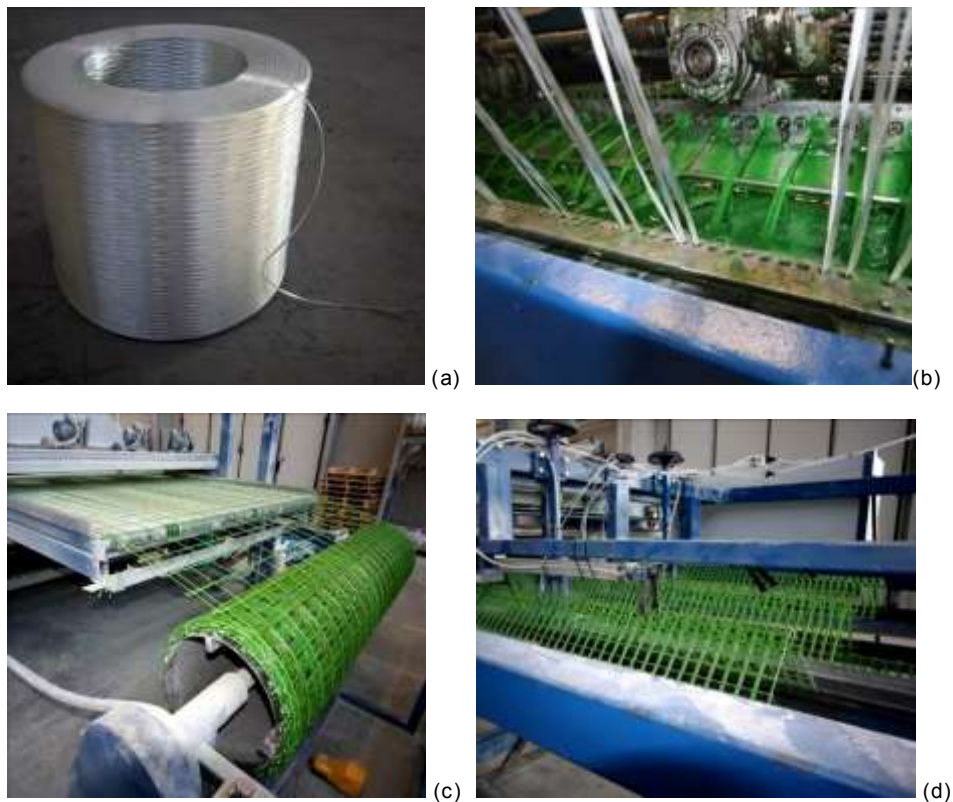


Figure 3.2 – Production of the GFRP meshes: (a) spools of dry Alkali-Resistant glass fibers wires, (b) soaking of dry fibers wires in the thermosetting resin, (c) storage of the GFRP mesh in rolls and (d) production of the angle brackets for corner devices

The GFRP meshes available in practice have grid dimensions of 33x33 mm<sup>2</sup>, 66x66 mm<sup>2</sup> and 99x99 mm<sup>2</sup> and have a net dry fiber cross section in a wire of 3.8 mm<sup>2</sup> (type “S”). A doubled fiber cross section (7.6 mm<sup>2</sup>, named type “D”) is also available for 66x66 mm<sup>2</sup> and 99x99 mm<sup>2</sup> meshes. However, the most widely used for the reinforcement of existing masonry buildings is the 66x66 mm<sup>2</sup>, type “S”, GFRP mesh (Figure 3.3).

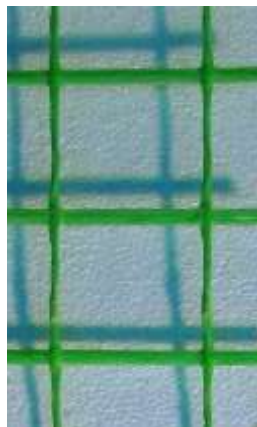


Figure 3.3 – Details of typical 66x66 mm<sup>2</sup> type “S” GFRP mesh used in practice: the warp (twisted fibers wires) is vertical and the weft (parallel fibers wires) is horizontal

The main geometrical and mechanical characteristics of the GFRP wires are summarized in Table 3.1.

The global equivalent cross section of the wires  $A_{tot}$  was detected, according to the procedure presented in CNR DT 203/2006, Appendix B. The tests consisted in immersing some portions of the wires (minimum total length of 200 mm) in a graduated cylinder filled with water and measuring the volume increase of the liquid (Figure 3.4.a).

Tensile tests were performed according to CNR DT 203/2006, Appendix B. The samples were constituted by single wires having a length of about 500 mm extracted from the mesh by cutting in half the transversal wires. The clamping heads were created by inserting the ends of the wire in aluminium cylinders (diameter 19 mm, thickness 1.5 mm, length 100 mm) injected with a high-performances bi-component epoxy anchoring. A universal testing machine “Galileo” (capacity 20 kN) was used (Figure 3.4.b); the load was measured using a pressure transducer, connected with a digital acquisition system interfaced with a laptop. To survey the axial elongation during test, a linear potentiometer transducer was applied (10 mm, error lin.  $\pm$  0.10%, base length 63 mm).

The twisted fibers wires reached tensile loads  $T_w$  lower than that of parallel fibers wires. This is probably due to the different tension occurring in each fiber during the tensile test, because of the twisting, so that not all fibers reached the ultimate resistance at the same time. During the tensile tests on twisted fibers wires, a gradual untwisting was noted at the increasing of the load.

The durability of the GFRP wires exposed to fatigue and ageing treatments was investigated by Corradi & al. (2016). From this preliminary study, it emerged that fatigue treatments did not produce relevant alterations in the GFRP physic-mechanical properties; differently, a significant GFRP tensile strength decrease emerged after a seven-month period of immersion in deionised water or in NaCl solutions.

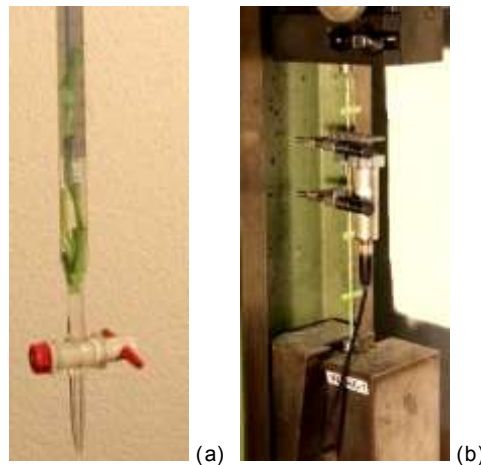


Figure 3.4 – Characterization of GFRP wires: (a) equivalent cross section evaluation and (b) tensile tests

Table 3.1 – Tensile characterization test on single GFRP wires: dry fiber cross section  $A_{fib}$ , equivalent cross section  $A_{tot}$ , tensile resistance  $T_w$  and axial stiffness  $EA_{tot}$  (the coefficients of variation, c.o.v., are also reported for  $T_w$  and  $EA_{tot}$ )

Grid dimensions	$A_{fib}$ [mm <sup>2</sup> ]	Fiber orientation	$A_{tot}$ [mm <sup>2</sup> ]	$T_w$ [kN]	C.o.v. [%]	$EA_{tot}$ [kN]	C.o.v. [%]
33x33 mm <sup>2</sup>	3.8	Twisted	7.29	3.97	9	219	9
		Parallel	9.41	4.88	12	285	12
66x66 mm <sup>2</sup>	3.8	Twisted	7.29	4.22	14	219	14
		Parallel	9.41	4.71	8	264	1
	7.6	Twisted	21.64	5.78	4	556	11
		Parallel	22.13	8.22	6	539	2
99x99 mm <sup>2</sup>	3.8	Twisted	7.29	4.01	18	207	15
		Parallel	9.41	4.65	15	245	4
	7.6	Twisted	21.64	6.06	19	457	13
		Parallel	22.13	8.52	3	612	6

The GFRP L-shaped connectors (Figure 3.5) are composed of Alkali-Resistant glass fibers, oriented in parallel across the longitudinal direction. The fibers are embedded in a thermosetting resin made of epoxy vinylester with benzoyl peroxide as catalyst. The global cross section is 7x10 mm<sup>2</sup> and the net fiber percentage is 60% (42 mm<sup>2</sup>). Experimental tensile tests (CNR DT 203/2006, Appendix B) provided an average tensile strength of 25.9 kN (c.o.v. 7%).



Figure 3.5 – A GFRP L-shaped connector

Also the resistance performances of the GFRP angle brackets were tested experimentally. Samples consisted in “L-shaped” GFRP mesh portions (side 530 mm) embedded at the ends in a 150 mm thick reinforced concrete basement, so to avoid slippage. Parallel fibers wires were oriented in the transversal direction (Figure 3.6.a) Two grid dimensions were considered: 66x33 mm<sup>2</sup> type “S” GFRP mesh, with 66 mm spaced wires oriented in the transversal direction (ID.: 66x33S) and 66x66 mm<sup>2</sup> type “D” GFRP mesh (ID.: 66x66D). 8 and 4 longitudinal twisted fiber wires were considered, respectively, with radius of curvature at the corner equal to 15 mm. Two tests for each type were performed.

A monotonic, vertical load was applied in correspondence of the corner by an hydraulic jack (ENERPAC mod. RC-154, 142 kN each, stroke 101 mm) governed by an hand pump (ENERPAC, mod. P84, 700 bar). A metallic device was interposed, so to allow a uniform load distribution. The load was measured with a pressure transducer (AEP Transducers, LAB TP14, error f.s. 0.05%) connected to an electronic acquisition unit (PCMCi National Instruments, mod. DAQ Card-AI-16-XE-50). The samples collapsed for the failure of the longitudinal, twisted fiber wires. The results of the four tests are reported in Table 3.2 in terms of vertical peak load  $V_{max}$  and equivalent axial force  $P_{max}$  acting on the single longitudinal wire ( $P_{max} = V_{max} / n_w \sqrt{2}$ , being  $n_w$  the number of longitudinal wires). The ratios between  $P_{max}$  and the wire tensile resistance  $T_w$  deduced from characterization tests (Table 3.1) are also calculated: these values resulted significantly lower than unit, indicating that the L-shaping weakens the wires resistance.

Table 3.2 – Characterization tests on GFRP angle brackets: Vertical peak load  $V_{max}$ , number of longitudinal wires  $n_w$ , equivalent axial force acting on the single longitudinal wire  $P_{max}$  and ratios between  $P_{max}/T_w$  (being  $T_w$  the single wire tensile resistance)

ID	Sample	$V_{max}$ [kN]	$n_w$ [-]	$P_{max}$ [kN]	$P_{max}/T_w$
66x33S	01	13.42	8	1.19	0.30
	02	11.38	8	1.01	0.25
66x66D	01	13.57	4	2.40	0.42
	02	12.32	4	2.18	0.38

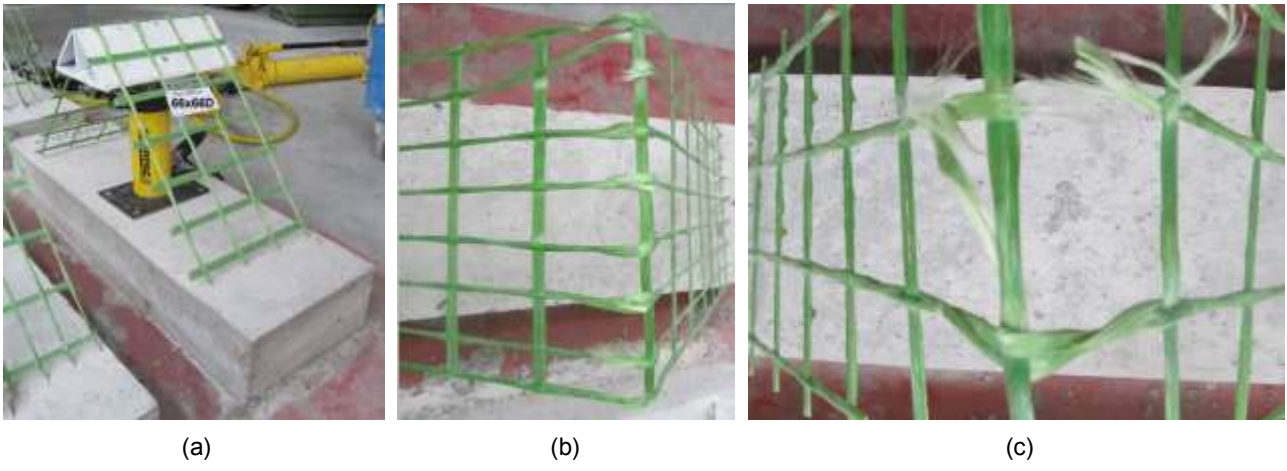


Figure 3.6 – Tests on GFRP angle brackets: (a) test setup and detail of wire failure at corner in (b) 66x33S and (c) 66x66D samples

### 3.3 Characterization tests on GFRM

This subsection collects the results of some experimental investigations conducted so to assess the mechanical characteristics of the proposed GFRM technique in terms of tensile properties and bond performances on masonry substrate, useful to provide correct design procedures for an effective application, and thus operation, of the strengthening system (Gattesco & Boem, 2017a).

The presence of a mesh grid dimension and a mortar thickness outside of the usual standards for FRMs (typically 10-15 mm) required the execution of some preliminary tests (pull-out and lap-splice tests) on elemental samples, to check the interaction between the GFRP mesh and the mortar matrix. The results had the intent to detect the main aspects which has to be taken into account in the proper design of the characterization tests for the considered reinforcement technique. It is observed that tests focused on twisted fibers wires oriented in the loading direction, accounting for the typical mesh positioning in masonry walls and vaults (subsection 3.1). However, some comparisons with the parallel fibers wires were also made.

Then, the shear and tensile characterization tests performed on GFRP reinforced mortar samples are described and discussed in detail. In particular, observations on the different failure mechanisms occurred in bond test at the varying of the bond length and of the mesh pitch and in tensile tests at the varying of the sample dimensions, gripping system and mesh grid dimensions are made. Characterization tests permitted the assessment of the anchorage length to make effective the reinforcement and the definition of the stress-strain curve of the reinforced material (GFRM), suitable also for numerical modeling.

It is evidenced that, in the considered reinforcement technique, different types of mortar may be utilized for the coating, such as natural binders, cement, pozzolanic additives. As an example, a lime and cement mortar commonly used in practice for plaster (dosage 300 kg of hydraulic lime and 100 kg of cement per  $m^3$  of mortar) was considered for the characterization tests ("Type C4").

Experimental tests performed on prismatic samples (40x40  $mm^2$  cross section, 160 mm length) by means of a universal testing machine Galdabini PM/50 sn 21645 – 47, evidenced for this mortar a flexural tensile strength  $f_{f,c} = 1.7$  MPa (Figure 3.7.a) and a compressive strength  $f_{c,c(prism)} = 6.1$  MPa, (EN196-1:2005 - Figure 3.7.b).

Indirect tensile (EN12390-6:2009 - Figure 3.7.c) and compression (EN12390-3:2009/AC:2011 - Figure 3.7.d) tests on cylindrical samples (100 mm diameter, 200 mm height) were also performed and the Young modulus was evaluated according to "Method B" proposed in EN12390-13:2013. In particular, to detect the deformation of the samples, three potentiometer transducers (stroke 25 mm) were placed on the side surface of the cylinders, at  $120^\circ$  one from the other, on a base length

of 100 mm (Figure 3.7.c). It resulted a tensile strength  $f_{t,c} = 1.1$  MPa, a compressive strength  $f_{c,c} = 6.9$  MPa and an average Young modulus  $E_c = 14.4$  GPa.

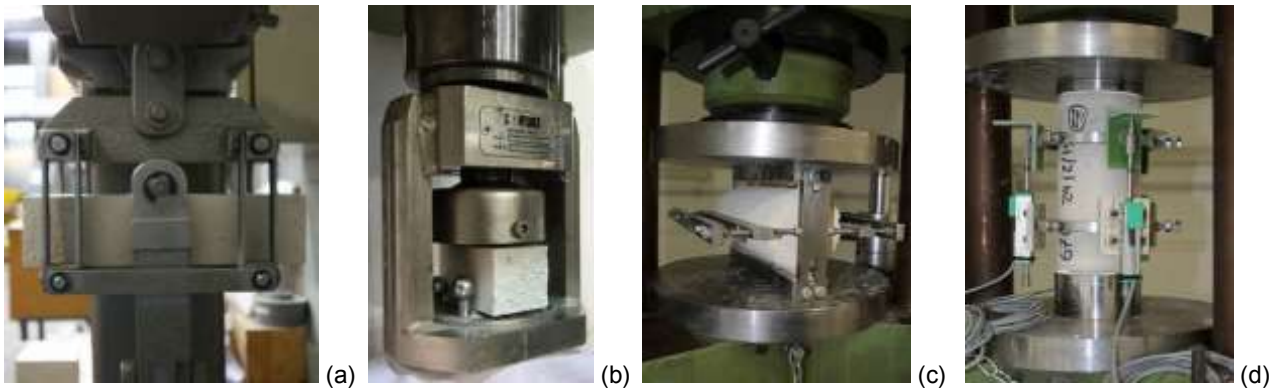


Figure 3.7 – Mortar characterization tests: (a) flexural tensile and (b) compressive strength tests on prisms and (c) indirect tensile and (d) Young modulus and compressive strength tests on cylinders

The performed tensile and bond characterization tests constitute a part of a research project promoted by the Rilem Technical Committee 250-CSM “Composites for Sustainable Strengthening of Masonry”, which involved 15 European laboratories for testing 8 GFRP grid products coupled with different lime or cement matrices (Leone & al., 2016). In fact, among the primary aims of the Committee, there is the identification and promotion of standardized experimental procedures for tensile and debonding tests on FRMs and the dissemination of proper application procedures for mortar-based composite materials on existing masonry structures.

### 3.3.1 Pull-out tests

The pull-out test samples consist in  $30 \times 180 \times 180$  mm<sup>2</sup> mortar plates with  $66 \times 66$  mm<sup>2</sup> GFRP mesh embedded, centred in the mortar thickness. Two transversal, parallel fibers, wires and three longitudinal, twisted fibers, wires were considered; the central longitudinal wire was extended outside the mortar, for about 260 mm, so to permit the application of the tensile force.

The preparation procedure consisted in the positioning of a first frame of wooden slats (cross section  $15 \times 15$  mm<sup>2</sup>) on a plywood base covered with a plastic film; specific grooves in the slats facilitated the positioning of the GFRP mesh on the frame. A second frame of wooden slats (section  $15 \times 15$  mm<sup>2</sup>) was screwed on the one below, blocking the mesh. Then, the mortar was casted inside the wooden formwork, taking care to vibrate the cast so to compact adequately the mould. During the casting phase, two rubble tubes (30 mm length) were used as spacers, in correspondence of the central wire, so to avoid the local damage of the mortar in correspondence of the mortar layer edges. The actual bond length between the central GFRP wire and the mortar was, thus, equal to 120 mm. The extrados surface of the casted mortar was levelled by float and

covered with cotton fabrics maintained wet, so to avoid the accelerated evaporation of the water in the mixture. The formwork was removed after three days of curing. The specimens were maintained in a temperature controlled room ( $23^{\circ}\text{C} \pm 2^{\circ}\text{C}$ ) until the achievement of maturation (about 30 days from the cast). Then, at the free end of the central longitudinal wire, the clamping head of the sample was created by means of aluminium cylinder injected with anchoring resin (see tensile tests on GFRP wires, in subsection 3.2).

The same testing machine and measurement equipment employed in tensile tests on GFRP wires (subsection 3.2) were used. The tests setup and the main specimen characteristics are illustrated in Figure 3.8. A contrast frame, composed by two horizontal “C-shaped” metallic elements jointed with two vertical steel bars, was connected to the lower clamp of the machine. For the installation of the specimen, the free end of the central wire was inserted in a central hole created in the upper metallic element of the contrast frame and the aluminium cylinder was fixed to the upper clamp of the machine. A potentiometer transducer was pinned to the central GFRP wire and was used to monitor the relative displacement between the mesh and the upper steel element. The base length was 105 mm thus, at the beginning of the test, the transducer was able to survey the elongation of a 140 mm portion of the wire.

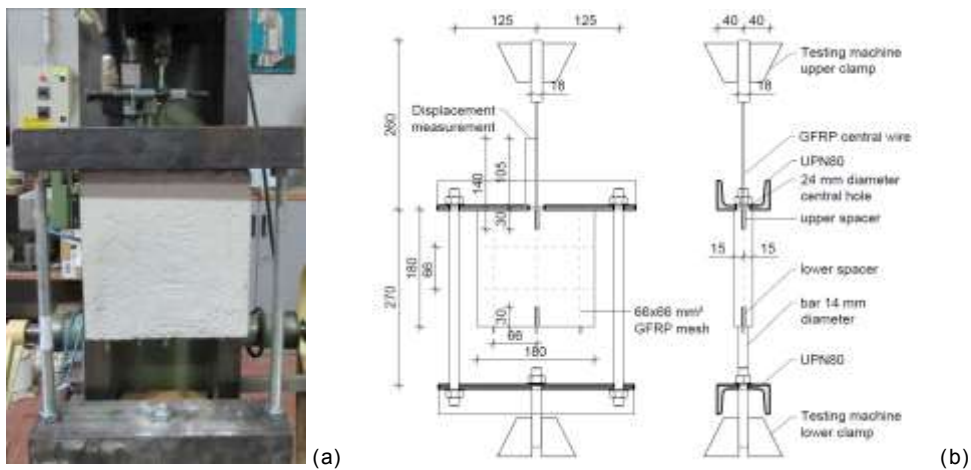


Figure 3.8 - Test setup for pull-out tests on plate samples: (a) picture before the beginning of a test and (b) main geometrical characteristics in frontal and lateral vertical sections

Six specimens were tested: the samples were signed through an identifier which indicates the type of tests (PO for pull-out tests), the geometry of the mortar coating (P for plate), the fibers orientation of the central wire (T for twisted fibers) and distinguishes through numbers (1 to 6) specimens with identical characteristics. The maximum pull-out force,  $T_{max}$ , the wire-mortar slip corresponding to maximum load,  $\Delta(T_{max})$ , and the failure mode are reported in Table 3.3; the curves representing the tensile load  $T$  in function of the global displacement monitored by the transducer  $\Delta$  are plotted in Figure 3.9. The load-displacement curve of a GFRP twisted fibers wire,

referred to a base length of 140 mm, is also reported, so to evaluate the contribution to the global displacement due to the wire deformation in the initial base length and detect the beginning of the wire slip.

Table 3.3 - Pull-out tests on GFRM layers: maximum pull-out load  $T_{max}$ , wire-mortar slip corresponding to maximum load  $\Delta(T_{max})$  and failure mode

ID	$T_{max}$ [kN]	$\Delta(T_{max})$ [mm]	Failure mode
PO-PT1	3.81	3.22	Central wire rupture
PO-PT2	3.71	3.35	Mortar splitting and mesh nodes failure
PO-PT3	4.88	5.57	Central wire rupture
PO-PT4	4.21	4.63	Mortar splitting and mesh nodes failure
PO-PT5	3.94	3.84	Central wire rupture
PO-PT6	4.30	4.16	Mortar splitting and mesh nodes failure
PO-CT1	4.98	4.58	Wire rupture
PO-CT2	4.02	2.48	Wire rupture
PO-CT3	3.69	3.40	Wire rupture
PO-CT4	4.70	4.35	Wire rupture
PO-CT5	4.39	3.61	Wire rupture
PO-CT6	4.41	3.82	Wire rupture
PO-PP1	3.96	3.32	Mortar splitting and central wire extraction
PO-PP2	5.05	4.00	Mortar splitting and central wire extraction
PO-PP3	3.92	2.61	Mortar splitting and central wire extraction
PO-PP4	3.42	2.82	Mortar splitting and central wire extraction
PO-PP5	4.46	2.97	Mortar splitting and central wire extraction
PO-PP6	3.71	2.83	Mortar splitting and central wire extraction

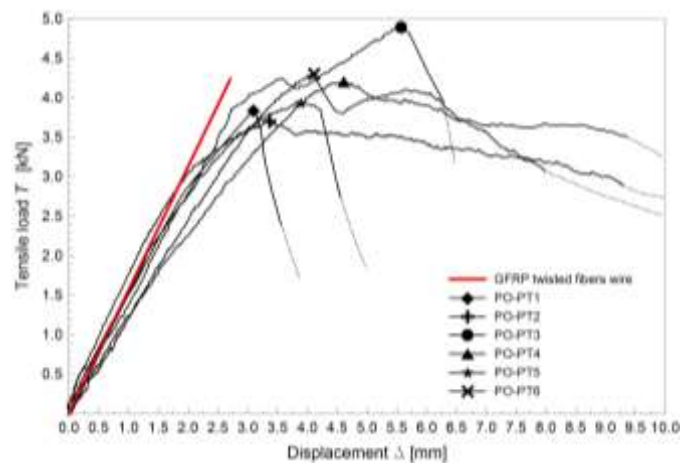


Figure 3.9 - Load vs. displacement curves of the pull-out tests performed of GFRM plate samples with twisted fibers wires oriented in the longitudinal direction

In general, the specimens manifested an initial linear behavior, which is in good agreement with the GFRP wire stiffness until a load of 2.2 kN; then, a gradual decreasing of stiffness emerged, due to the slip of the central wire with respect to the mortar (starting loss of chemical adherence at wire-mortar interface). Specimens attained to similar peak values (4.14 kN, c.o.v. 10%).

In specimens PO-PT1, PO-PT3 and PO-PT5 the wire rupture emerged (Figure 3.10.a) after reaching the maximum resistance; then the load rapidly dropped down. Differently in specimen PO-PT2, PO-PT4 and PO-PT6 the gradual formation of a vertical crack, in correspondence of the central wire, occurred (Figure 3.10.b); however the load continue to increase; the collapse was achieved in consequence of the mesh central nodes rupture, which determined a gradual load decrease. At the end of the tests it was possible to inspect the failure mode of the mesh nodes: it emerged the cutting through of the transversal wires (Figure 3.10.c).

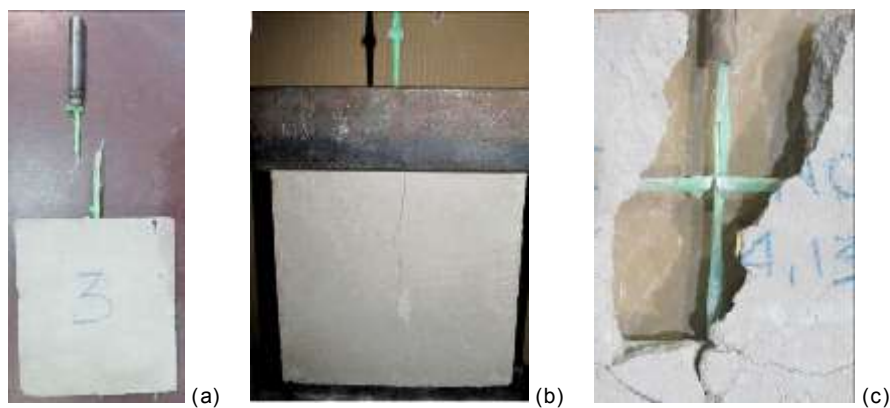


Figure 3.10 - Pull-out tests performed of GFRM plate samples with twisted fibers wires oriented in the longitudinal direction: (a) failure of the GFRP central wire in PO-PT3 and (b) vertical cracking of the mortar and (c) failure of the mesh nodes at the end of the test in PO-PT4

It is evidenced that the cracking formation was probably induced by the geometry of the specimen: in fact, the slightly bending deformation of the upper steel element of the contrast frame and possible minor irregularity in the mortar plate edge in contact with the frame caused a concentration of the reactions at the lateral ends of the mortar layer, producing a parasitic bending moment which caused the splitting of the matrix. Thus, for comparison, pull-out test were performed on samples of different geometry, avoiding the splitting.

In particular, mortar cylinders (100 mm in diameter and 200 mm in height) with a single longitudinal twisted fibers wire (of a 66x66 mm<sup>2</sup> GFRP mesh) were tested (Figure 3.11.a). The wire was centred in the cylinder cross section and two transversal wires embedded in the mortar and cut in half at both ends were considered. The mortar was casted in PVC cylindrical formworks and 40 mm length rubble tubes were used as spacers (actual bond length equal to 120 mm, as in plate samples).

The same test setup used for plate samples was adopted. A 5x120x120 mm<sup>3</sup> steel plate, with a central hole, was interposed between the upper “C-shaped” element of the contrast frame and the cylinder, so to uniformly distribute the reactions of the contrast frame to the upper base of the mortar sample. At the beginning of the test, the displacement transducer was able to monitor the elongation of a 140 mm portion of the GFRP wire.

Six specimens were tested; the main results are reported in Table 3.3 and the curves representing the load in function of the global slip monitored by the transducer are plotted in Figure 3.12. In the second part of the sample identifier, the letter “C” refers to the cylindrical shape of the mortar. An average maximum load of about 4.37 kN was attained (c.o.v. 11%) and the wire rupture always occurred (Figure 3.11.b); then the load rapidly dropped down. No significant differences emerged in the load-displacement curves in respect to those concerning plate samples collapsed for the wire rupture.

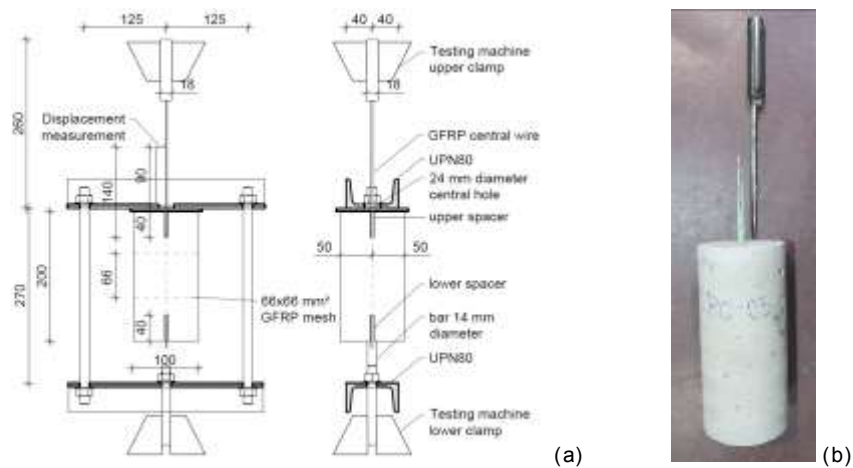


Figure 3.11 - Pull-out tests performed of GFRM cylindric samples with twisted fibers wires oriented in the longitudinal direction: (a) test setup and (b) failure of the GFRP wire in PO-CT5

The comparison of the results of plate and cylindrical samples (Figure 3.12) evidenced that the splitting failure mode is related to the particular test setup used for plate samples. Actually, the stress state of the GFRP reinforced mortar coating applied on masonry does not affect a single mesh wire, involving a wider area of reinforcement. Thus, it is important to perform characterization tests reproducing as close as possible the actual stress state of the mesh and reinforcement boundary conditions.

However, some important findings emerged. At first, the results showed that, from a tensile load of about 2.2 kN, a gradual detachment of the GFRP wire from the mortar occurs. Nevertheless, a wire-mortar bond length of at least 120 mm may ensure the exploitation of the whole mesh resistance, avoiding the premature reinforcement collapse for composite slippage. Actually, the tests permitted to evidence that the mesh nodes are able to provide an effective contribution

against the wire slippage: the resistance of two mesh nodes (deduced from the tests PO-PT2, PO-PT4 and PO-PT6, where the chemical adhesion between the central wire and the mortar was completely nullified by the occurrence of splitting) resulted quite close to the tensile resistance of the wire.

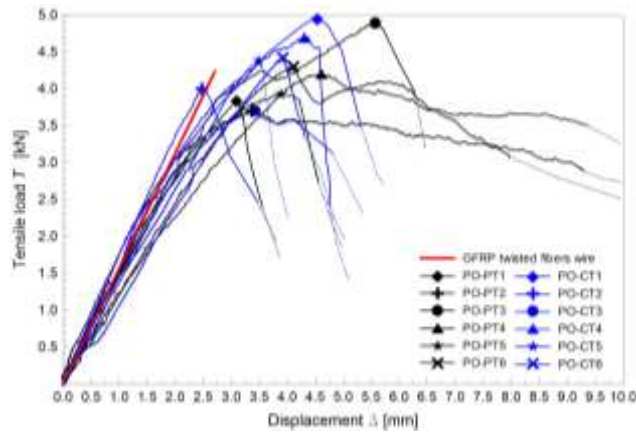


Figure 3.12 – Pull-out tests: comparison between PO-CT and PO-PT samples (load vs. displacement curves)

Six additional plate samples were tested so to check the performances of the reinforcement when the parallel fibers wire is loaded in tension (PO-PP tests in Table 3.3). The tests (Figure 3.13.a) evidenced the beginning of the loss of chemical adherence at wire-mortar interface of the central parallel fibers wire in correspondence of a load of about 1.8 kN; this value resulted lower than that emerged from PO-PT tests, where the wire roughness is realistically higher, due to twisting.

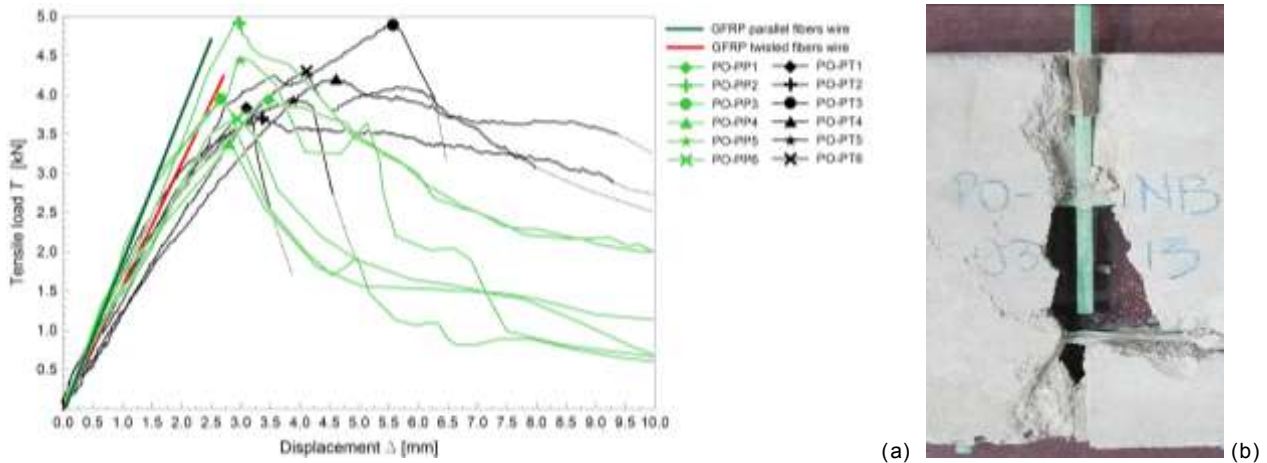


Figure 3.13 - Pull-out tests performed of GFRM plate samples with parallel fibers wires oriented in the longitudinal direction: (a) comparison between PO-PP and PO-PT samples (load vs. displacement curves) and (b) detail of the slippage of the central wire from the transversal ones at the end of the test PO-PP2

At the increasing of the load, also the gradual vertical mortar splitting occurred; the local bend of the wire in correspondence of the intersection with the transversal wires (twisted) caused an

increase of the bond resistance. The collapse was achieved with the extraction of the central wire from transversal ones (Figure 3.13.b) in correspondence of an average maximum load of about 4.09 kN (c.o.v. 14%). This load is lower than the tensile resistance of a parallel fibers wire (Table 3.1) but it is quite close to the peak load attained in PO-PT samples.

### 3.3.2 Lap-splice tests

Lap-splice samples (Figure 3.14.a) consisted in 30x180x180 mm<sup>3</sup> mortar plates with embedded two GFRP meshes having the same characteristics of pull-out plate samples. The meshes were overlapped and centred in the mortar thickness and an offset of about 10-12 mm was created between the transversal wires. The actual bond length was 180 mm. The longitudinal central wires were centred in the plate width and extended outside the mortar at opposite sides for about 200 mm, so to permit the application of the tensile force by clamping the injected aluminium cylinders installed at the wire ends to the universal testing machine “Galileo”. Two linear potentiometer transducers monitored the displacement between the wires and the mortar on a base lengths of 100 mm.

Six specimens were tested: the samples were signed through an identifier indicating the type of tests (LS for lap-splice tests), the geometry of the mortar coating (P for plate), the fibers orientation in longitudinal wires (T for twisted fibers wires) and distinguishing, through sequential numbers, specimens with identical characteristics. The maximum force,  $T_{max}$ , the wire-mortar slip corresponding to maximum load,  $\Delta(T_{max})$ , and the failure mode are reported in Table 3.4

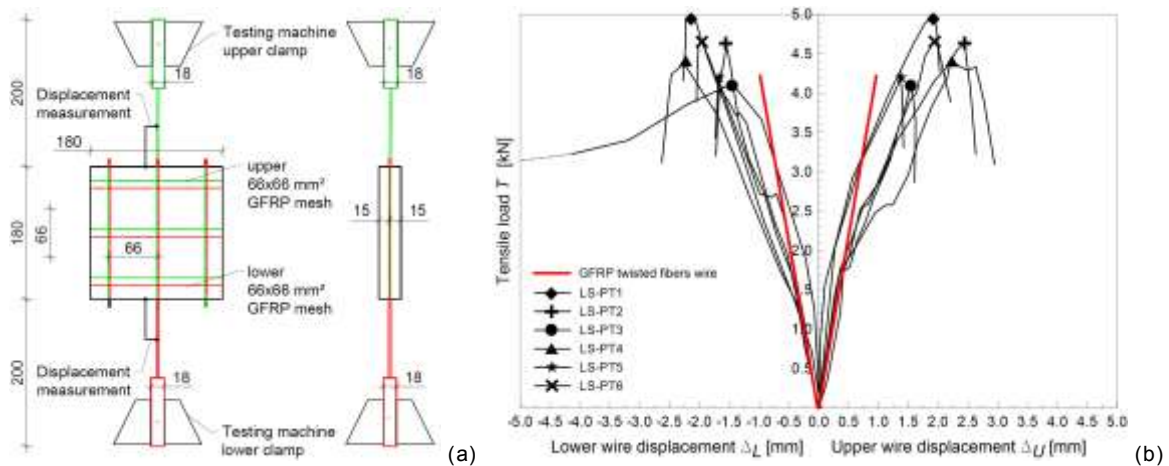


Figure 3.14 – Lap-splice tests on plate samples: main geometrical characteristics in frontal and lateral vertical section and (b) load vs. average displacement curves

The load-displacement performances (Figure 3.14.b) show a first linear branch up to a tensile load of 2.0-2.2 kN; then a stiffness reduction occurred, due to the slip of the central wire with respect to the mortar (starting loss of chemical adherence at wire-mortar interface). The collapse occurred at an average load of 4.49 kN (c.o.v. 7%), generally in consequence of the tensile rupture of a central wire, outside of the mortar (Figure 3.15.a). Exception for LS-PT3, where a horizontal cracking of the mortar occurred in correspondence of a transversal wire, then the progressive central nodes failure occurred (Figure 3.15.b). In LS-PT5, a local damage of the mortar at the graft of the central wire emerged, however this did not change appreciably the sample behavior.

Table 3.4 – Lap-splice tests on GFRM layers: maximum force  $T_{max}$ , average wire-mortar slip corresponding to maximum load  $\Delta(T_{max})$  and failure mode

ID	$T_{max}$ [kN]	$\Delta(T_{max})$ [mm]	Failure mode
LS-PT1	4.97	2.04	Central wire rupture
LS-PT2	4.62	1.73	Central wire rupture
LS-PT3	4.10	1.54	Mortar splitting and mesh nodes failure
LS-PT4	4.40	2.25	Central wire rupture
LS-PT5	4.19	1.56	Central wire rupture
LS-PT6	4.65	1.97	Central wire rupture
LS-CT1	4.36	1.79	Wire rupture
LS-CT2	4.94	1.77	Wire rupture
LS-CT3	-	-	<i>Premature wire failure at clamping</i>
LS-CT4	4.78	2.23	Wire rupture
LS-CT5	4.91	1.73	Wire rupture
LS-CT6	4.47	1.71	Wire rupture
LS-PP1	4.05	1.93	Central wire extraction
LS-PP2	3.63	1.65	Central wire extraction
LS-PP3	3.72	2.19	Central wire extraction
LS-PP4	3.63	1.65	Central wire extraction
LS-PP5	-	-	<i>Premature wire failure at clamping</i>
LS-PP6	-	-	<i>Premature wire failure at clamping</i>

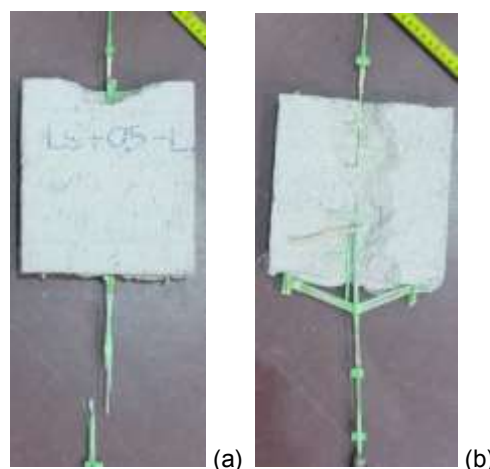


Figure 3.15 – Lap-splice tests on plate samples: (a) failure of the GFRP central wire in LS-PT5 and (b) failure mode of the mesh nodes at the end of the test in LS-PT3,

Six cylindrical samples (LS-CT in Table 3.4) with the same overlapping length were tested for comparisons: the load-displacement curves resulted comparable to those obtained in LS-PT specimens (Figure 3.16.a) and the wire rupture (Figure 3.16.b) was always attained (average load 4.69 kN, c.o.v. 6%).

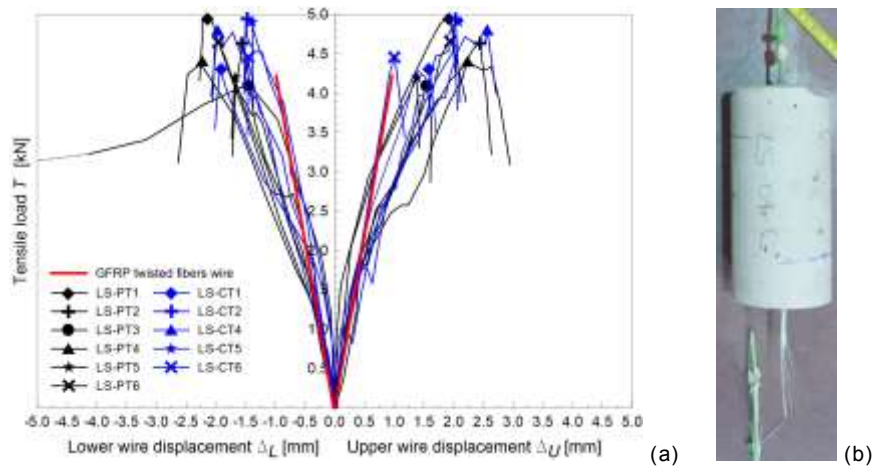


Figure 3.16 – Lap-splice tests performed of GFRM cylindrical samples with twisted fibers wires oriented in the longitudinal direction: (a) comparison between LS-CT and LS-PT samples in terms of load vs. displacement curves and (b) failure of the GFRP central wire in LS-CT1

Moreover, six additional tests on plate samples with GFRP parallel fibers wires loaded in tension were performed (LS-PP in Table 3.4). The tests evidenced the starting of loss of adherence at wire-mortar interface at a load of about 1.8 kN but, due to the local bend of the wire in correspondence of the intersection with the transversal wires (twisted), further bond resistance was obtained (Figure 3.17.a). The collapse, in fact, was achieved for an average load of 3.76 kN (c.o.v. 5%), with the extraction of the central wire from transversal ones (Figure 3.17.b).

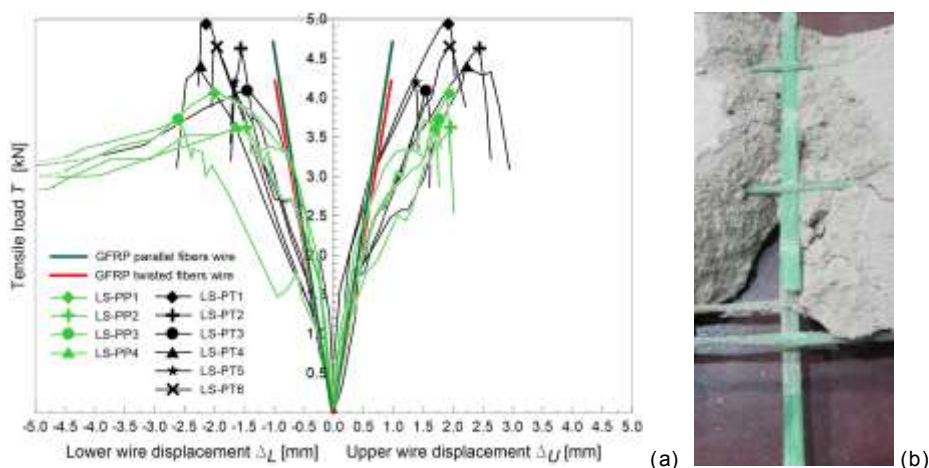


Figure 3.17 – Lap-splice tests performed of GFRM plate samples with parallel fibers wires oriented in the longitudinal direction: (a) comparison between LS-PP and LS-PT samples in terms of load vs. displacement curves and (b) failure of the GFRP central wire in LS-PP2

The results of lap-splice tests evidenced that an overlapping of 180 mm permits the exploitation of the whole GFRP mesh resistance, when the tensile direction is that of twisted fibers wires; on the contrary, the premature wire reinforcement slippage occurred when loading in tension the parallel fibers wires, but for values of the load almost equal to those obtained in tests with twisted wires. The comparison of the results of plate and cylindrical samples evidenced that both tests are suitable to reproduce with good accuracy the actual boundary conditions.

### 3.3.3 Tensile tests

Some tensile tests were carried out on mortar layers with GFRP meshes embedded, so to evaluate the performances of the reinforcement when subjected in tension and the effect of the intact mortar between cracks (tension stiffening effect).

The specimens consisted in a 132x900 mm<sup>2</sup> layer of mortar plaster, 30 mm thick, with a 66x66 mm<sup>2</sup> GFRP mesh embedded in the center of the mortar thickness, with the two twisted fibers wires disposed in the longitudinal direction and arranged symmetric to the specimen width (Figure 3.18).

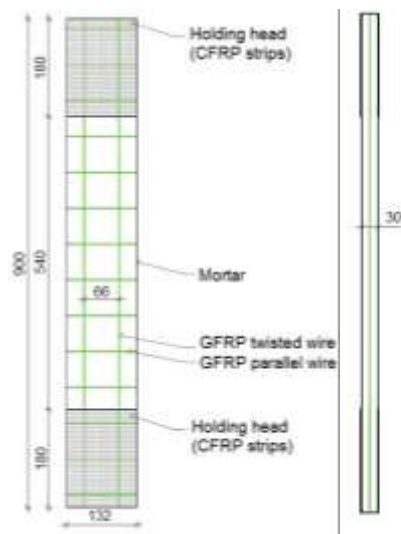


Figure 3.18 – Tensile tests: main geometrical characteristics of the GFRM samples TA66, in frontal and lateral vertical sections

Seven specimens were prepared (TA66-1 to 7); the packaging and the curing of the reinforced mortar layers followed the steps already described in subsection 3.3.1 for pull-out samples. Once the mortar curing was completed, the clamping heads of the samples were created. In particular, on the faces of each specimen, at both ends, two overlapped strips of CFRP (Carbon Fiber-Reinforced Polymer) were applied by the impregnation of the fabric with bicomponent epoxy resin. This reinforcement was aimed to avoid local load concentration and damage during the test in correspondence of the gripping areas. The width of this reinforcement was equal to that of the



The metallic pins used to join the different elements of the apparatus were calibrated to avoid tolerances. The test apparatus was dimensioned so to limit as close as possible the elastic deformation of the metallic elements and connections: the deformation of the apparatus associated to a tensile force on the specimen equal to 10 kN was estimated approximately equal to 0.04 mm.

The results of the tensile tests are summarized in Table 3.5 in terms of first cracking load  $T_{cr}$ , peak load  $T_{max}$  and displacements measured by the transducers T1 and T2 in correspondence of  $T_{cr}$  and  $T_{max}$  ( $\delta_{T1}(T_{cr})$ ,  $\delta_{T1}(T_{max})$ ,  $\delta_{T2}(T_{cr})$ ,  $\delta_{T2}(T_{max})$ ). The tensile stresses in correspondence of the first cracking ( $\sigma_{cr}$ ) and of the maximum resistance ( $\sigma_{max}$ ) were evaluated in respect to the cross section of dry fibers in the longitudinal direction ( $3.8 \text{ mm}^2 \times 2 = 7.6 \text{ mm}^2$ ); moreover the mean tensile strains  $\varepsilon_{cr}$  and  $\varepsilon_{max}$  were calculated by dividing the average displacements for the base length  $l_d$ . The number of transversal cracks noted at the end of the tests ( $n_{cr,tot}$ ) and detected by the transducers ( $n_{cr,mis}$ ) and the average values of the distance between adjacent cracks at failure ( $\Delta_{cr,m}$ ) were also provided.

Table 3.5 – Results of the tensile tests carried out on reinforced mortar coating layers: first cracking and peak loads ( $T_{cr}$ ,  $T_{max}$ ), stresses evaluated in respect to the cross section of dry fibers ( $\sigma_{cr}$ ,  $\sigma_{max}$ ), base length of the displacements transducers ( $l_d$ ), displacements monitored by the transducers T1 and T2 in correspondence of first cracking and peak loads ( $\delta_{T1}(T_{cr})$ ,  $\delta_{T1}(T_{max})$ ,  $\delta_{T2}(T_{cr})$ ,  $\delta_{T2}(T_{max})$ ), average strains in correspondence of  $T_{cr}$  and  $T_{max}$ , ( $\varepsilon_{cr}$ ,  $\varepsilon_{max}$ ), number total cracks ( $n_{tot,cr}$ ) and of cracks detected by the transducers ( $n_{tot,mis}$ ) and average crack distance ( $\Delta_{cr,m}$ )

ID	$T_{cr}$ [N]	$T_{max}$ [N]	$\sigma_{cr}$ [MPa]	$\sigma_{max}$ [MPa]	$l_d$ [mm]	$\delta_{T1}(T_{cr})$ [mm]	$\delta_{T2}(T_{cr})$ [mm]	$\varepsilon_{cr}$ [‰]	$\delta_{T1}(T_{max})$ [mm]	$\delta_{T2}(T_{max})$ [mm]	$\varepsilon_{max}$ [‰]	$n_{cr,tot}$ [-]	$n_{cr,mis}$ [-]	$\Delta_{cr,m}$ [mm]
TA66-1*	-	10094	-	1328	400	-	-	-	5.77	5.20	13.71	3 (+1)	3 (+1)	149
TA66-2	4923	9802	648	1290	400	0.005	0.058	0.08	6.97	5.56	15.66	4	2	154
TA66-3	4974	10072	654	1325	400	0.046	0.082	0.16	8.71	8.27	21.23	5	3	116
TA66-4	5172	11301	681	1487	400	0.013	0.072	0.11	8.31	8.96	21.59	5	3	116
TA66-5	4403	9573	579	1260	400	0.001	0.063	0.08	4.27	4.59	11.08	3	1	231
TA66-6	4852	13753	638	1810	400	0.079	0.029	0.14	10.78	10.24	26.28	5	3	132
TA66-7	4016	12498	528	1644	400	0.011	0.038	0.06	8.39	9.21	22.00	5	3	108
TB66-1	5828	12137	767	1597	830	0.038	-	0.05	8.90	-	12.26	7	7	110
TB66-2	5230	11055	688	1455	830	0.044	-	0.06	6.81	-	9.38	6	6	132
TB66-3	5088	11816	669	1555	830	0.060	-	0.08	9.04	-	12.45	7	7	110
TB66-4	3112	12367	409	1627	830	0.035	-	0.05	9.07	-	12.49	6	6	132

\* presence of a crack in the specimen before starting the test

The curves representing the tensile stress  $\sigma$  at the varying of the mean strain  $\varepsilon$  were plotted in Figure 3.20.a. A first elastic branch was generally detected by the displacement transducers, as the mortar was uncracked. Then, a first, horizontal crack formed, resulting in a sudden decrease of the load. The tensile force increased then again, until the formation of another crack. Other

horizontal cracks gradually appeared in the mortar, located, for the most, in correspondence of transversal mesh wires. As the number of cracks stabilized, the load increased until the rupture of the longitudinal wires (Figure 3.20.b), in correspondence of a crack, determining the sample failure at about 11.0 kN (c.o.v. 14%).

It is observed that in samples TA66-3, TA66-4, TA66-6 and TA66-7, five cracks formed and the couple of transducers were able to survey the opening of three cracks. Diversely, a lower number of cracks (two or one) were included in the measure length in TA66-1, TA66-2 and TA66-5. Moreover, the presence of an existing horizontal crack noted in specimen TA66-1 before testing, resulted in a lower initial stiffness of the  $\sigma$ - $\varepsilon$  curve.

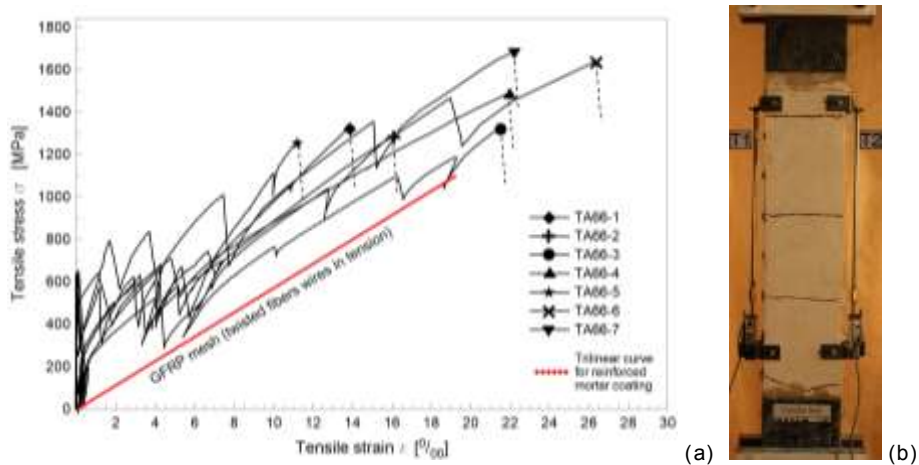


Figure 3.20 – Tensile tests on GFRM samples: (a) stress  $\sigma$  against strain  $\varepsilon$  curves and (b) crack pattern at the end of test TA66-4

To account for a possible influence of the gripping mechanism on the GFRM samples behavior (De Santis & De Felice, 2015a), a second set of tensile tests (“TB66”) was performed on reinforced mortar layers 860x132x30 mm<sup>3</sup>, with tensile load applied directly to the GFRP mesh, which exceeded from the ends of the mortar coating (Figure 3.21). To apply the load, reinforced concrete tabs (concrete compressive strength 25 MPa), wrapped with CFRP strips impregnated with epoxy resin, were created for embedding the GFRP mesh ends and clamping the specimens to the holding plates of the testing machine. The same preparation, curing and loading conditions considered in “TA66” samples were assumed. A single displacement transducer (T1) was applied on the samples, at the centre of the mortar layer face. The base length was approximately 830 mm.

Four samples were tested for “TB66” typology; the results are summarized in Table 3.5 and plotted in the stress-strain graph of Figure 3.22. The same collapse mechanism evidenced in type “TA66” specimens was noted and the  $\sigma$ - $\varepsilon$  curves are, in general, comparable. This indicates that even a possible slippage in the clamping heads of type “TA66” did not influenced the results and

that a base length of 400 mm can be sufficient to provide a quite accurate evaluation of the mean performances of the GFRP reinforced mortar layer.

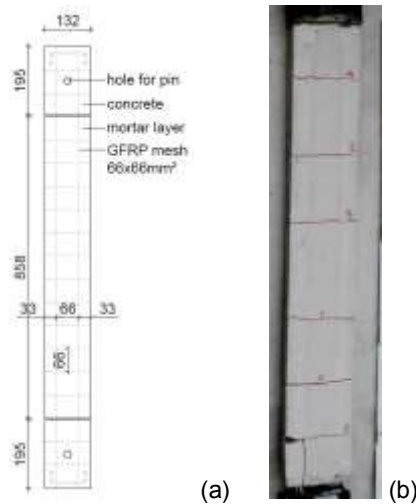


Figure 3.21 – Tensile tests on GFRM samples: (a) main characteristics of TB66 samples and (b) crack pattern at the end of test TB66-4

The higher scatters noted in the diagrams representing the behavior of specimens TA66-1 and TA66-5 were induced by the formation of only one crack along the base length. Thus, in these cases, the curve cannot be considered as representative on the average behavior of the reinforced material, as at least two cracks has to be detected by the transducers.

Generally, the performances of the specimens can be schematized by a trilinear behavior characterised by a pre-cracking, elastic branch, with stiffness dependent on the mortar Young modulus, a multiple cracking formation branch (assumed horizontal) and a post-cracking branch, until the tensile rupture of the wires. This last branch can be assumed parallel to the curve representing the tensile behavior of the GFRP wires alone. The horizontal gap between the third branch of the trilinear curve and that of the GFRP wires represents the tension stiffening effect of the mortar between the cracks.

For comparison, the stress-strain curve of a GFRP twisted wire was plotted in Figure 3.22. It is observed that, in general, the final slope of the  $\sigma$ - $\varepsilon$  curves well accords with the wire stiffness.

The average, simplified trilinear curve representing the global behavior of the GFRP reinforced mortar layer is plotted in Figure 3.22: the curve was derived considering only the specimens in which the transducers were able to detect at least two cracks.

It is worth note that the average maximum stress resulted higher than that derived from the wire resistance obtained in the characterization tests (Table 3.1). This was probably due to the different boundary condition applied on the GFRP wires. In fact, during the characterization test, a gradual straighten of the twisted wires was noted until the rupture. Differently, during the tensile tests on

the GFRP reinforced mortar layer, the presence of the transversal wires embedded in the mortar matrix partially opposed to this occurrence and may have improved the strength characteristics of the tensed wires.

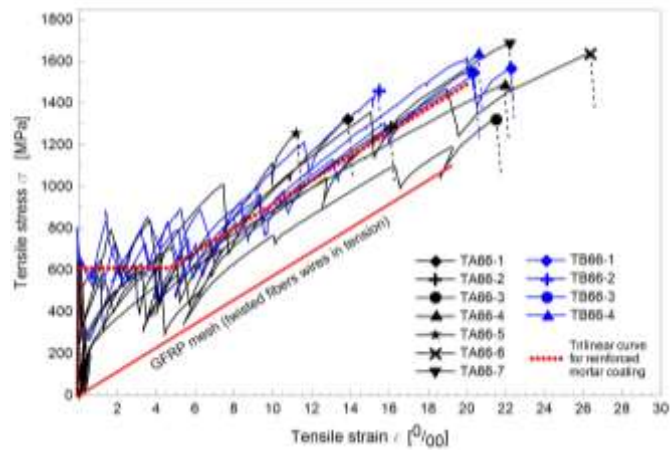


Figure 3.22 – Tensile tests on GFRM layers: comparison between TB66 and TA66 samples in terms of stress  $\sigma$  - strain  $\varepsilon$  curves

To evidence the importance of design tensile tests on reinforced mortar layers with an anchorage length adequate to the mesh and matrix characteristics, an example of a non-acceptable specimen failure is reported. It refers to samples  $30 \times 198 \times 900 \text{ mm}^3$  of mortar, with a  $99 \times 99 \text{ mm}^2$  GFRP mesh embedded (“TA99”) - Figure 3.23.a. A 180 mm anchorage length was considered, analogously to “TA66” specimens. The transducer T2 had a base length of 400 mm; diversely the transducer T1 was installed on a base length 580 mm, so to be able to measure the opening of all the cracks. An illustration of a “TA99” specimen at the end of the test is reported in Figure 3.23.b, as an example. Some horizontal cracks formed but, at the occurrence of cracking in the vicinity of the anchorage length, the gradual extraction of the longitudinal GFRP wires from a holding head emerged and induced the sample failure. The rupture of GFRP wires was never reached.

The amount of the mesh slippage from the lower clamping head can be estimated as difference between the displacements monitored by the two transducers at the varying of the tensile load (Figure 3.23.c); in fact, the lower crack formed outside the transducer T2 base length. Due to this slippage, which resulted of about 7.3 mm in correspondence of the peak load, it was not possible to detect a post-cracking branch parallel to the curve representing the tensile behavior of the GFRP wires alone. This type of collapse has to be considered not acceptable: in fact, is related to the test setup. In particular, the slippage emerged in these tests was due to the mesh arrangement: a single transversal wire was present in the anchorage length. Actually, pull-out tests (subsection 3.3.1) evidenced that transversal wires offer an important contribution against slippage.

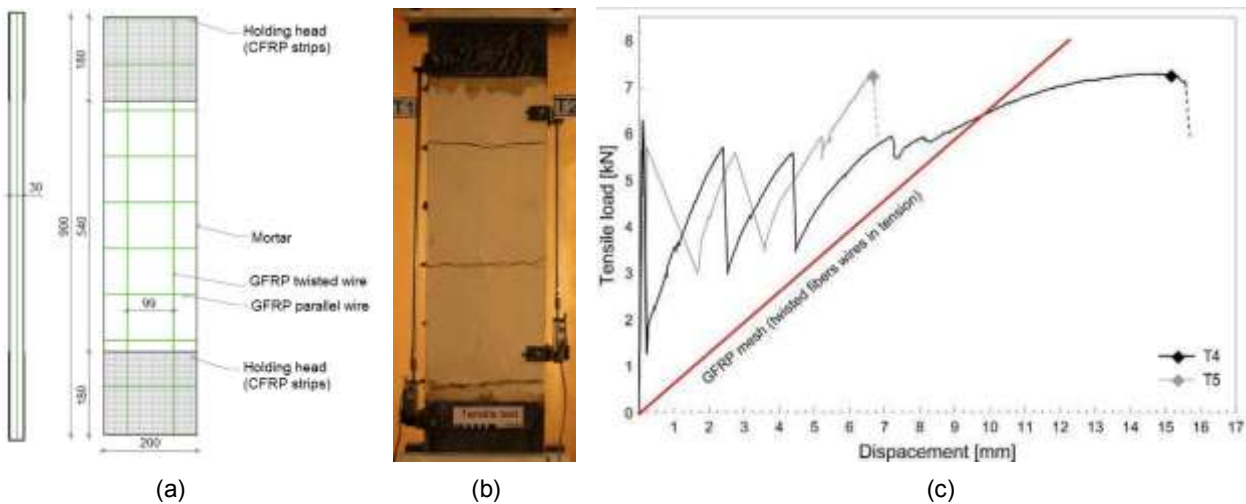


Figure 3.23 - Tensile tests TA99: (a) samples characteristics, (b) view at the end of the tests and (c) example of  $\sigma$ - $\varepsilon$  curve

### 3.3.4 Shear bond tests

Some bond tests were performed so to evaluate the shear performances of the GFRM layers applied on a masonry substrate. Specimens were composed by solid brick masonry wallets ( $250 \times 315 \times 120 \text{ mm}^3$  - Figure 3.24) to which a 30 mm thick GFRP reinforced mortar coating was applied on one face, leaving a distance from the wallet base of about 30 mm. The GFRP mesh, which exceeded from the mortar in correspondence of the bottom side of the layer, was placed in the center of the mortar thickness and the twisted wires were disposed in the longitudinal direction (Figure 3.25).

A  $66 \times 66 \text{ mm}^2$  GFRP mesh was applied, assuming different lengths for the mortar layer (120 mm, 180 mm and 240 mm) and keeping a constant width of 132 mm. The three dimensions were chosen, based on the findings of preliminary pull-out tests (subsection 3.3.1), so to check the influence of the bond length on the resistance and collapse mode of the GFRM reinforcement, which may occur for mesh wire failure, mesh wire slippage from mortar matrix or mortar slippage from the masonry substrate. Moreover, for the latter case, the presence of a  $33 \times 33 \text{ mm}^2$  GFRP mesh, instead of a  $66 \times 66 \text{ mm}^2$  one, was also considered. Five samples were tested for each of the four described layouts.

The packaging of the samples consisted in the preparation and curing of the masonry wallets, which were then arranged disposing face-up the surface to be reinforced. Then, the procedure followed the same steps described in subsection 3.3.1 for pull-out samples, taking care in wetting the masonry surface before casting, so to avoid the absorption of the water of the mortar. The tests were performed after about 78 to 93 days of mortar coating curing.

The average compressive strength of the solid bricks was determined in accordance with EN 772-1:2011+A1:2015. Each sample was composed of a single solid unit (Figure 3.24.b). The results of the six tests performed provided an average compressive strength of 20.8 MPa (c.o.v. 4 %). The normalized compressive strength resulted equal to 15.7 MPa.

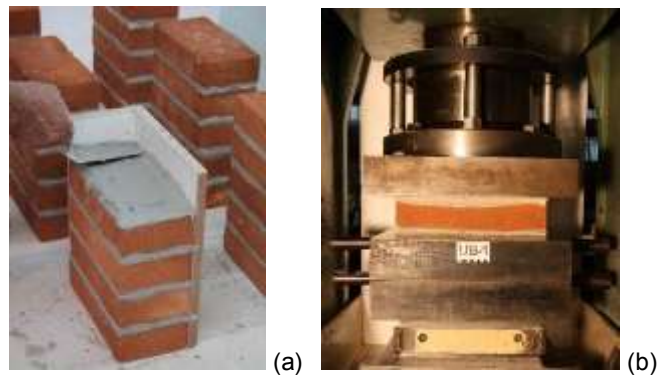


Figure 3.24 – Illustration of (a) the construction of a masonry wallet for bond tests and (b) compressive strength test on a solid brick unit

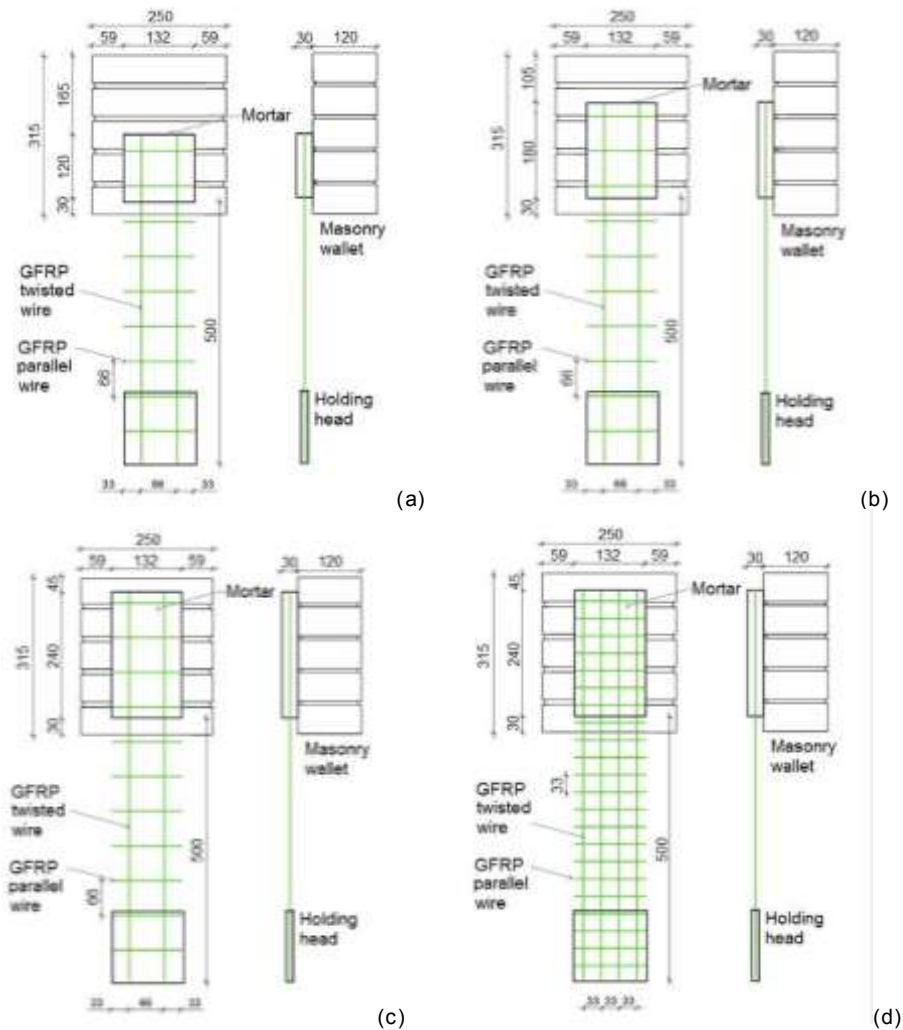


Figure 3.25 - Characteristics of the samples for bond tests: (a) type A66-1, (b) A66-2, (c) A66-3 and (d) type A33-1

To facilitate the execution of the experimental bond tests, a holding head in correspondence of the free end of the GFRP mesh was created once the curing was completed. In particular, two GFRP pultruded plates (dimensions 8 x 130 x 130 mm<sup>3</sup>) were coupled with the interposition of the GFRP mesh and the injection of a bicomponent epoxy resin.

The test apparatus (Figure 3.26.a) was for the most the same of that employed for tensile tests (subsection 3.3.3), replacing the upper couple of steel plates with a metallic device, shaped as a seat, so to support the masonry wallet. The device was set so to maintain the GFRP mesh in the vertical direction and it was properly designed so to guarantee a sufficient stiffness and ensure the vertical alignment of the load along the specimens, avoiding secondary forces, perpendicular to the masonry surface, which could anticipate the sample failure.

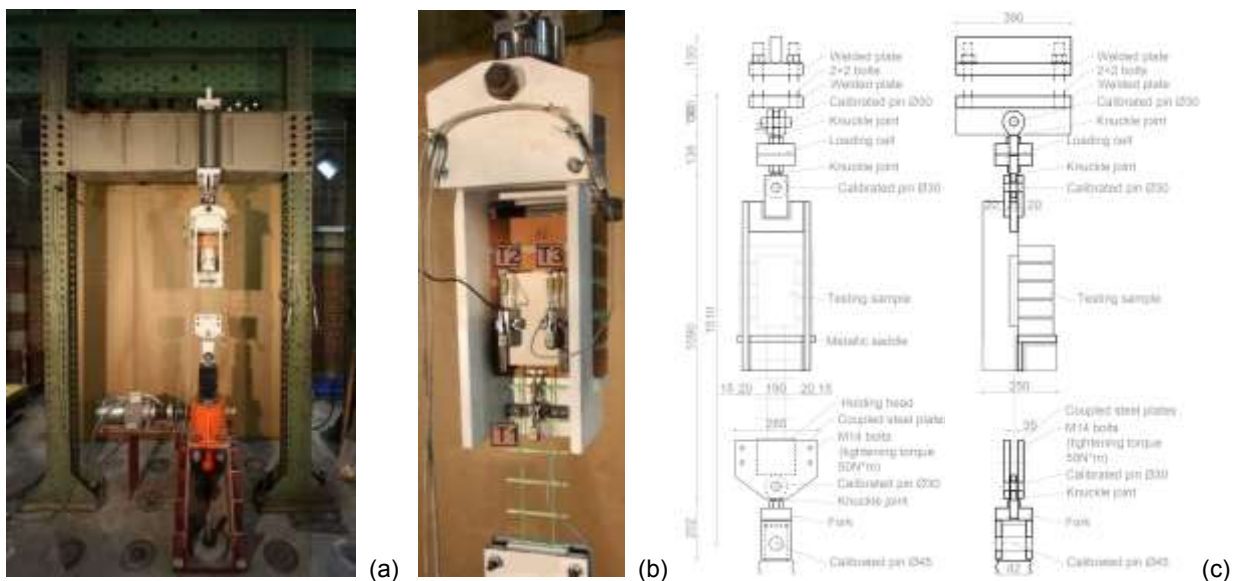


Figure 3.26 – Shear bond tests: (a) global and (b) detail views and (c) schematization of the test setup

Three potentiometer transducers were applied on the specimens, as illustrated in Figure 3.26.b. In particular, potentiometer T1 measured the displacement between the GFRP mesh and the base of the masonry wallet (wire-support slip and wire elongation); potentiometers T2 and T3 surveyed the displacement between the base of the masonry wallet and the upper edge of the mortar coating layer (mainly masonry shortening).

All the instruments were connected to an electronic acquisition unit, interfaced with a computer. The acquisition frequency was 1 Hz. The software allowed the real-time monitoring of the loading history, the displacement measured by the transducers and the load-displacement diagrams. Tests were performed at displacement control, on the basis of elongation detected by the potentiometer T1 (rate 0.5 mm/min).

The main characteristics and results of the tested samples are summarized in Table 3.6. The sample identifier distinguishes the GFRP grid dimensions (“A66” for 66x66 mm<sup>2</sup> and “A33” for

33x33 mm<sup>2</sup>) and the mortar coating length (“1” for 120 mm, “2” for 180 mm and “3” for 240 mm); a final number, from 1 to 5, differentiates specimens having the same features. The results are resumed in terms of peak load  $P_u$ , displacements  $\delta_{T1}$ ,  $\delta_{T2}$  and  $\delta_{T3}$  monitored by transducers T1, T2 and T3 at peak load and type of collapse.

The tensile load  $P$  at the varying of the mesh-mortar displacement ( $\delta_{t-m}$ ) is illustrated in Figure 3.27. The value of  $\delta_{t-m}$  was evaluated as the difference between the global mesh-support displacement ( $\delta_{T1}$ ) and the mortar-support displacement (average of the displacements  $\delta_{T2}$  and  $\delta_{T3}$ ). It is evidenced that the displacement  $\delta_{t-m}$  generally may be due to elongation of the mesh and to the relative mesh-mortar slippage. Actually, at the beginning of the test, there was the perfect adhesion between the mesh and the mortar, thus  $\delta_{t-m}$  was initially determined by the strain of the vertical GFRP tensed wires, in the portion of wires ranging from the clamping of transducer T1 on the mesh to the lower border of the mortar coating (about 100 mm). For comparison, the load vs. elongation curves of 2 and 4 twisted fibers GFRP wires were plotted in Figure 3.27. The curves were evaluated considering the results of the characterization tests on GFRP wires reported in Table 3.1, referring to a 100 mm wire length.

Table 3.6 – Main characteristics and results of the samples subjected to bond test in terms of peak load  $P_u$ , displacements  $\delta_{T1}$ ,  $\delta_{T2}$  and  $\delta_{T3}$  monitored by transducers T1, T2 and T3 in correspondence of the peak load and type of collapse.

ID	Mortar layer [mm <sup>3</sup> ]	GFRP mesh [mm <sup>2</sup> ]	$P_u$ [N]	$\delta_{T1}$ [mm]	$\delta_{T2}$ [mm]	$\delta_{T3}$ [mm]	Type of collapse
A66-1-1	120x132x30	66x66 - S	5529	3.30	0.011	0.045	Mesh slip and deboning of mortar from masonry
A66-1-2	120x132x30	66x66 - S	6180	4.11	0.022	0.022	Mesh slip within the mortar, with cracking of the mortar
A66-1-3	120x132x30	66x66 - S	-	-	-	-	Not performed, due to former damage of the sample
A66-1-4	120x132x30	66x66 - S	8165	4.76	0.012	-	Mesh slip and GFRP mesh rupture out of the bond area
A66-1-5	120x132x30	66x66 - S	6143	1.96	0.011	0.024	Mesh slip within the mortar, with cracking of the mortar
A66-2-1	180x132x30	66x66 - S	9101	3.41	0.035	0.054	Deboning of the mortar coating from the masonry
A66-2-2	180x132x30	66x66 - S	9330	3.03	0.026	0.037	GFRP mesh rupture out of the bond area
A66-2-3	180x132x30	66x66 - S	9173	3.33	-	0.029	Mesh slip within the mortar, with cracking of the mortar
A66-2-4	180x132x30	66x66 - S	9596	3.03	0.015	0.023	Deboning of the mortar coating from the masonry
A66-2-5	180x132x30	66x66 - S	9283	6.90	0.014	0.049	Deboning at mesh-to-mortar interface
A66-3-1	240x132x30	66x66 - S	9861	4.12	0.047	0.096	GFRP mesh rupture out of the bond area
A66-3-2	240x132x30	66x66 - S	8844	3.33	0.034	0.045	GFRP mesh rupture out of the bond area
A66-3-3	240x132x30	66x66 - S	9177	4.10	0.017	0.028	GFRP mesh rupture out of the bond area
A66-3-4	240x132x30	66x66 - S	10081	4.12	0.014	0.032	GFRP mesh rupture out of the bond area
A66-3-5	240x132x30	66x66 - S	9605	3.11	0.015	0.026	GFRP mesh rupture out of the bond area
A33-3-1	240x132x30	33x33 - S	17061	3.09	0.068	-	Deboning of the mesh-to-mortar interface
A33-3-2	240x132x30	33x33 - S	17807	3.30	0.032	-	Deboning of the mesh-to-mortar interface
A33-3-3	240x132x30	33x33 - S	15735	2.73	0.060	0.049	Deboning of the mesh-to-mortar interface
A33-3-4	240x132x30	33x33 - S	15169	3.04	0.048	0.074	Deboning of the mesh-to-mortar interface
A33-3-5	240x132x30	33x33 - S	16263	2.70	-	0.029	GFRP mesh rupture out of the bond area

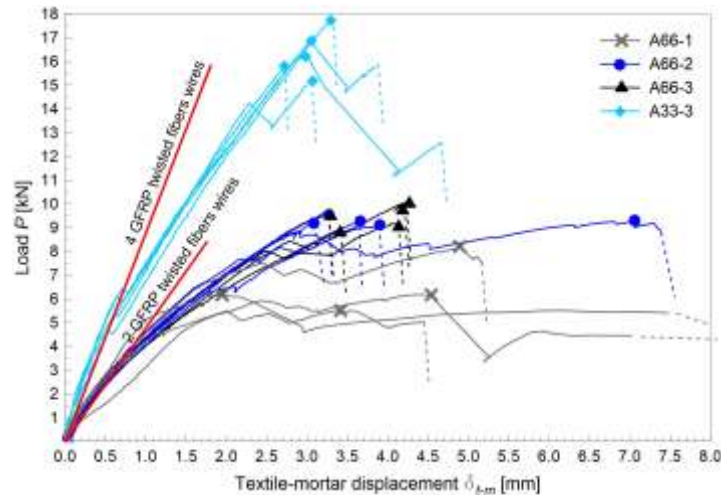


Figure 3.27 - Load  $P$  against displacement  $\delta_{t,m}$  of samples subjected to bond tests

The results of bond tests generally evidenced very low displacements between the masonry and the mortar coating ( $< 0.1$  mm, at peak load) in respect to those monitored between the mortar and the reinforcement ( $> 3$  mm, at peak load).

In samples “A66-1” an important mesh-mortar slippage was noted. The slip was, in general, so consistent that the deformation of the transversal wires induced a local cracking and detachment of the mortar covering the mesh (Figure 3.28.a), in correspondence of the lower transversal wire. The slippage affected the whole bond length: in fact, it was possible to clearly distinguish the slip of the vertical wires also at the upper edge of the mortar layer. Then, at the increasing of the slip, the load gradually decreased. Actually, the untwisting of the upper end of the longitudinal wires was noted at the end of the tests. The peak loads were quite similar for A66-1-1, A66-1-2 and A66-1-5 (about 6.0 kN, c.o.v. 6%); differently, an anomalous, higher value was obtained from A66-1-4 (8.2 kN), where the failure of the GFRP wires was attained.

Also in samples A66-2 the local, horizontal cracking of the mortar in correspondence of the lower transversal wire occurred, but then the load continued to increase until the abrupt debonding of the coating from the masonry (Figure 3.28.b) or the failure of the GFRP wires (Figure 3.28.c). The peak loads were quite similar and about 9.3 kN (c.o.v. 2%).

In specimens A66-3, in general, no mortar cracking emerged and the GFRP wires rupture (Figure 3.28.d) occurred for a mean value of 9.5 kN (c.o.v. 5%).

No visible wires slippage was noted at the end of the tests in correspondence of the upper edge of the mortar layer neither in A66-2 nor in A66-3 samples. It emerged, instead, a progressive deformation of the transverse wires in the free part of the mesh, as a consequence of the

untwisting of the longitudinal wires. This deformation, in some cases, also determined the failure of some of transversal wires during the test.

In specimens A33-3, after the horizontal cracking of the mortar portion covering the mesh in correspondence of the lower transversal wire, the debonding of the mesh-to-mortar interface occurred abruptly in four samples (Figure 3.28.e). Exception for specimen A33-3-5, where the GFRP wires collapsed. However, the values of maximum resistance were quite similar (16.4 kN, c.o.v. 6%).

Generally, the slope on the  $P-\delta_{t-m}$  curves initially resulted in good agreement with the stiffness of the GFRP wires so, at the beginning of the test, the mesh can be assumed as perfectly bonded to the mortar. Then, a decrease in the curves slope emerged, which indicates the occurrence of the mesh-mortar slip. Actually, the beginning of this slip occurred at a load value of about 4 kN for type A66 specimens and 5.5-6 kN for A33 ones. The value obtained from A66 samples resulted in agreement with that noted in preliminary pull-out tests (subsection 3.3.1). Due to the higher amount of reinforcement, lower values of displacements  $\delta_{t-m}$  were obtained from A33-3 specimens, in respect to A66-3 ones at the same load level.

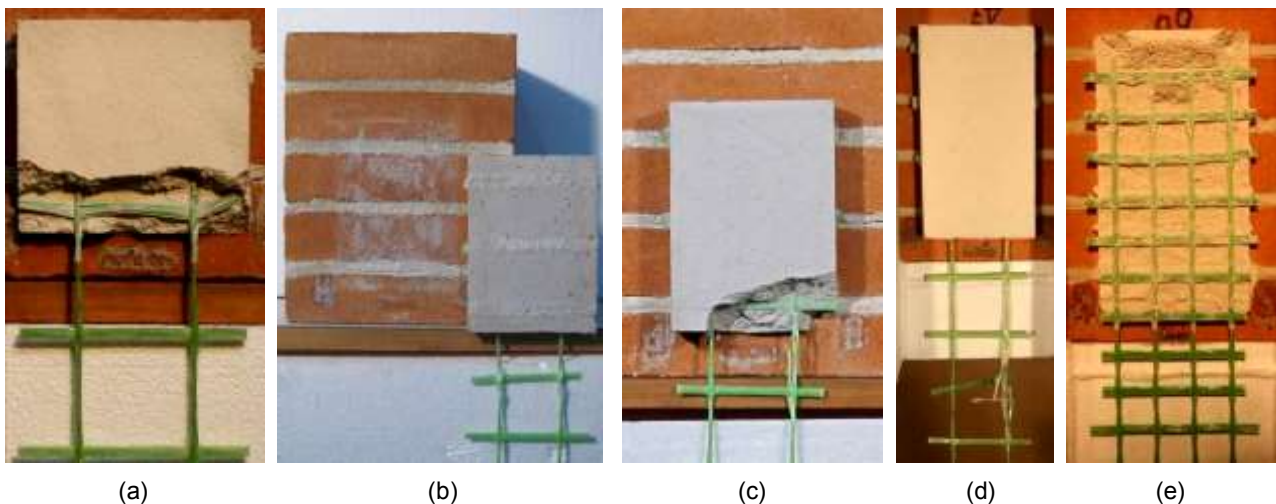


Figure 3.28 - Examples of failure mechanism emerged in bond tests: (a) mesh-mortar slip with cracking of the mortar in a A66-1 sample, (b) debonding at mortar-masonry interface and (c) GFRP wire rupture in A66-2 samples, (d) GFRP wire rupture in a A66-3 sample and (e) debonding of the mortar covering the mesh in a A33-3 sample

Some other interesting aspects can be observed from the results:

- the resistance of A66 samples associated to the GFRP wire rupture (which is independent from the bond length) resulted, on average equal to 9.5 kN. This value is quite higher than that derived from tests on single wires ( $2 \times 4.2 \text{ kN} = 8.4 \text{ kN}$ , Table 3.1). As already evidenced in subsection 3.3.3; this was probably due to the different boundary condition applied in bond

tests on the GFRP wires and, in particular, to the presence of the transversal wires in the mortar layer;

- the mesh-mortar slippage resistance, referred to a 120 mm bond length, resulted on average equal to 6.2 kN (A66-1-2 and A66-1-4 samples). This value is quite lower than that obtained from pull-out tests on plate samples ( $2 \times 4.1 \text{ kN} = 8.2 \text{ kN}$ , Table 3.3) as the effectiveness of the mesh nodes against the slippage was partially limited by the occurrence of the horizontal cracking in correspondence of the lower transversal wire and by the subsequent untwisting of the upper end of the longitudinal wires, once the chemical adhesion of the longitudinal wires to the mortar completely failed. Reasonably, at the increasing of the bond length, the mesh-mortar slippage should be more than linearly proportional to this parameter, as 4 or 8 mesh nodes in A66-2 and A66-3 specimens, respectively, offer effective resistance to sliding;
- the equivalent bond strength to the masonry substrate (deduced from specimens A66-2-1 and A66-2-4, by dividing the peak load for the whole bond area) resulted on average  $\tau_b = 0.39 \text{ MPa}$ . If a simplified linear trend of the bond resistance is assumed, a value of 6.2 kN and 12.4 kN for specimens having a 120 mm and a 240 mm length, respectively, emerged. Actually, the value for 120 mm bond length samples resulted quite close to that associated to the failure for mesh-mortar slippage. Diversely, the value for 240 mm bond length specimens resulted higher than that associated to the wires failure in A66-3 samples and lower than that associated both to the wires failure and to the debonding of the mesh-mortar interface in A33-3 samples. Actually, the debonding of the mortar coating from the masonry did not occur in the latter type of samples and load values higher than 12.4 kN were attained. Deeper investigations are needed on the mortar-masonry bond resistance, because many parameters, such as the presence of mortar joints and the actual distribution of the shear load, may affect this aspect (Faella & al. 2012; Kashyap & al., 2012; Carozzi & al., 2014; Napoli & al., 2016);
- the debonding at mesh-mortar interface in A33-3 specimens may have been induced by the weakening of the shear plane due to the high reinforcement ratio and to a greater non-planar configuration of the yarns (Bertolesi & al., 2014).

### 3.4 Summary

The main characteristics of the considered GFRM reinforcement technique were described and the results of some experimental tests of GFRP elements (single wires and angle brackets) were presented.

For the characterization of GFRM, some preliminary pull-out and lap-splice tests were performed so to investigate, through small samples, on the interaction between the composite mesh and the inorganic matrix and on the influence of the boundary conditions on the tests results.

The typical reinforcement configuration, consisting in a 66x66 mm<sup>2</sup> GFRP mesh embedded in a 30 mm thick lime and cement mortar coating, was considered for reference.

The tests permitted to evidence that the slip of the wire embedded in the mortar occurred for loads considerably lower than the bond resistance obtained, which was quite close to the wire tensile strength. So the bond resistance is guaranteed by the mechanical contribution due to transversal wires acting as dowels. The tests carried out on diverse specimens, plate and cylindrical, did not show appreciable differences in terms of resistance even though the type of collapse was different: the occurrence of a splitting crack in the plate elements in the wire direction emphasizes again the important role of transversal wires of the mesh for bond resistance. Preliminary tests indicated that a bond length of 120 mm, with at least two transversal wires, should be sufficient to guarantee the collapse of the specimen for twisted fibers wire rupture.

Tensile and bond tests were then performed with two twisted fibers wires oriented in the load direction. A particular attention was paid in the design of the test setup, especially regarding the correct alignment of the loading forces, so to avoid parasitic flexure, which may cause premature failures, and the adequate stiffness of the contrast device, so to permit the execution of the tests at displacement control.

Tensile tests permitted to evaluate the tensile performances of GFRM layers. In particular, a tension stiffening effect of the intact mortar between the cracks emerged. Moreover, it is observed that the average distance between cracks is approximately 125 mm and that different test setups, based on the mortar or on the GFRP mesh loading, provide similar results. Moreover, it is important to ensure an appropriate anchorage length so to achieve a type of collapse independent from the test setup. The deduced stress-strain curve is representative of the average behaviour of the reinforced material if at least two cracks occur inside the measurement length.

For bond tests on masonry substrate, three different bond length were considered: 120, 180 and 240 mm. In general, in the former case, the debonding of the mesh from the mortar matrix

emerged; in fact, the transversal cracking of the mortar occurred, compromising the contribution of the mesh nodes against the slippage. In the latter case, the failure for longitudinal wires rupture was obtained. In the intermediate case, different failure mechanisms manifested (wires rupture, debonding of the mortar, debonding of the composite); however, similar loads, close to the wires resistance, were attained. Thus, a bond length of at least 180 mm has to be guaranteed in order to exploit the maximum resistance of the considered reinforcement. On the contrary, shear tests performed on 240 mm bond length specimens considering a 33x33 mm<sup>2</sup> GFRP mesh evidenced the premature failure for mortar debonding at mesh-to-mortar interface. However, the reached load resulted very close to the wires resistance.

From both tensile and bond tests emerged a tensile resistance of the GFRP twisted fibers wires higher than that evaluated through characterization tests on single wires, due to the presence of mesh transversal wires which oppose to the progressive un-twisting of tensed wires at the increasing of the load.

Further shear and tensile tests should be performed so to investigate on the bond and tensile performances of the reinforcement technique when the parallel fibers wires are oriented in the loading direction. Also 99x99 mm<sup>2</sup> GFRP mesh in bond and tension and 33x33mm<sup>2</sup> GFRP mesh in tension should be investigated. Moreover, different masonry supports and mortar types could also be considered. However, the obtained results provide some important advices for the definition of correct testing procedures for characterization tests of GFRM strengthening systems and permitted to evaluate the mechanical properties of the considered reinforcement technique useful for numerical simulations and analytical design purposes.



## 4 IN-PLANE BEHAVIOUR

This section focuses on the in-plane behavior of GFRM reinforced masonry. In particular, a collection of experimental results concerning diagonal compression tests is reported and discussed, evidencing the effectiveness of the GFRM technique at the varying of different geometric and mechanic parameters, by comparison with unreinforced masonry. Analytical formulations, supported also by some considerations derived from a simplified numerical Finite Element model, are then proposed to predict the stiffness and the resistance of reinforced masonry specimens. The results of a preliminary, numerical study on the global behavior of reinforced masonry structures, based on pushover analyses on an Equivalent Frame model, is also presented.

### 4.1 Experimental diagonal compression tests

In this subsection, the characteristics and the results an extensive experimental campaign concerning diagonal compression tests on unreinforced and reinforced masonry specimens are described and discussed. The tests were performed so to assess the effectiveness of the considered reinforcing technique in terms of resistance and displacement capacity, by comparing the results of unreinforced and reinforced masonry samples. The influence of several masonry and reinforcement parameters on the effectiveness of the reinforcement were investigated (Gattesco & al., 2015a; Gattesco & Boem, 2015a; Gattesco & Boem, 2016a). The characteristics of the specimens, the test setup, the loading procedure and measurements, the tests results and the results discussion are reported in the following.

#### 4.1.1 Specimens characteristics

Diagonal compression tests were performed on full-scale square masonry specimens, 1160x1160 mm<sup>2</sup>. Different masonry types were considered (Figure 4.1 - Figure 4.2):

- solid brick, 250 mm thick (S);
- solid brick, 380 mm thick (S2);
- two-leaf solid brick, with small rubble conglomerate infill, 120 + 140 + 120 mm thick (I)
- rubble stones, 400mm thick (R and R2);
- rubble stones, 700 mm thick (R3);
- cobblestones, 400 mm thick (C).

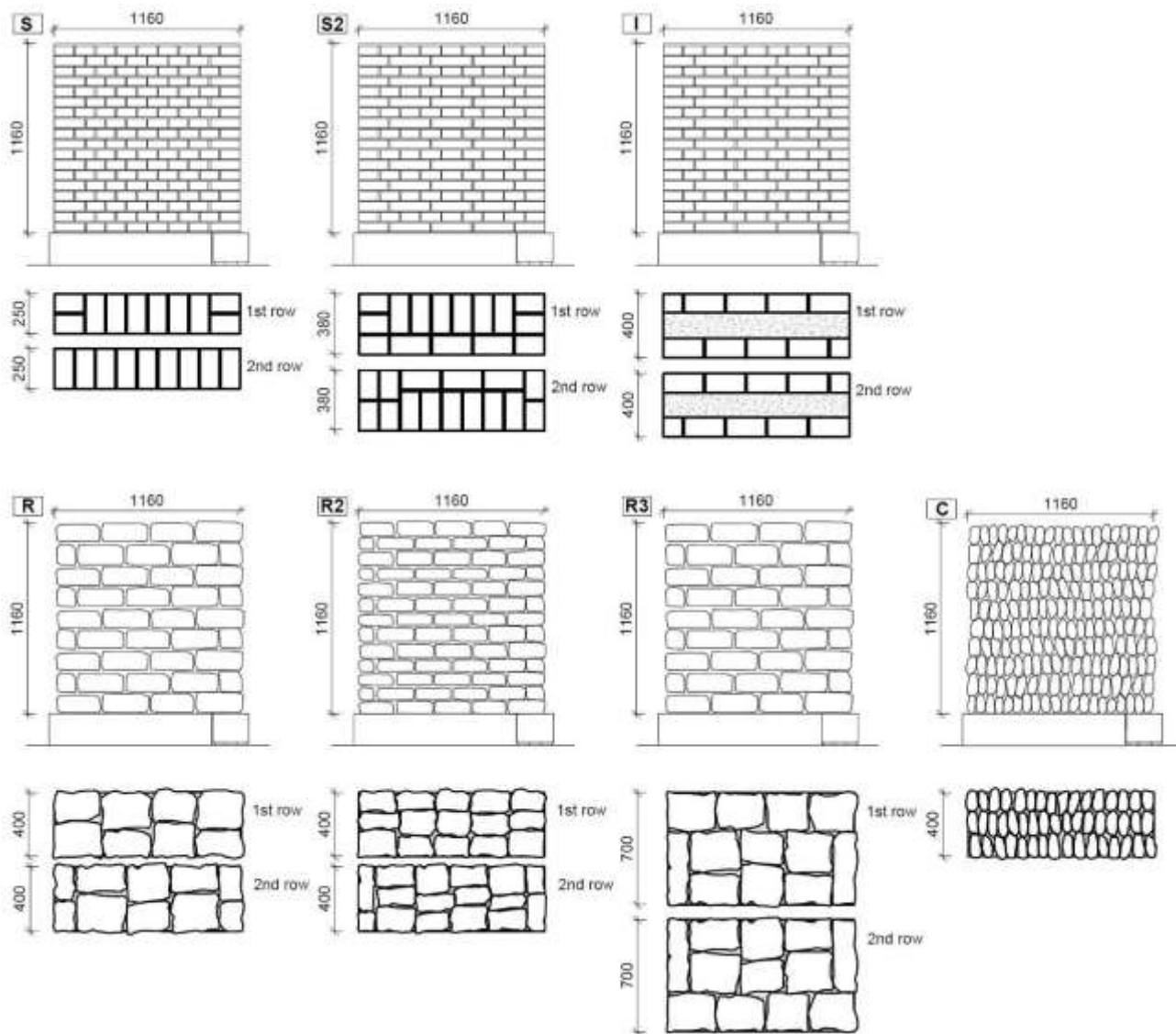


Figure 4.1 – Specimens of different masonry types subjected to diagonal compression tests: solid brick 250 mm thick (S), solid brick 380 mm thick (S2), two-leaf solid brick with small rubble conglomerate infill 120 + 140 + 120 mm thick (I), rubble stones 400mm thick (R and R2), rubble stones 700 mm thick (R3) and cobblestones 400 mm thick (C)

The average resistance of solid bricks ( $55 \times 120 \times 250 \text{ mm}^3$ ) subjected to compression tests was 44.0 MPa (EN 772-1:2011+A1:2015, c.o.v. 16%). The mortar bed joints and vertical joints were 10 mm thick and had a flush profile. In 250 mm thick solid brick masonry specimens (S), the bricks were arranged according to the header bond pattern (single skin walls); 3/4 bat bricks were used at the lateral edges.

Stone elements were all sandstones (specific weight about  $23 \text{ kN/m}^3$ ) and were arranged as close as possible so to limit the mortar joints dimensions. In rubble stones masonry R and R3 the unit dimensions were roughly  $130 \times 230 \times 200 \text{ mm}^3$  (respectively height, width and depth). Differently,

the average units dimensions in R2 rubble stone masonry specimens were 90x160x200 mm<sup>3</sup>. Cobblestones specimens (C) had elements with average dimensions 90 x 90 x 130 mm<sup>3</sup>.

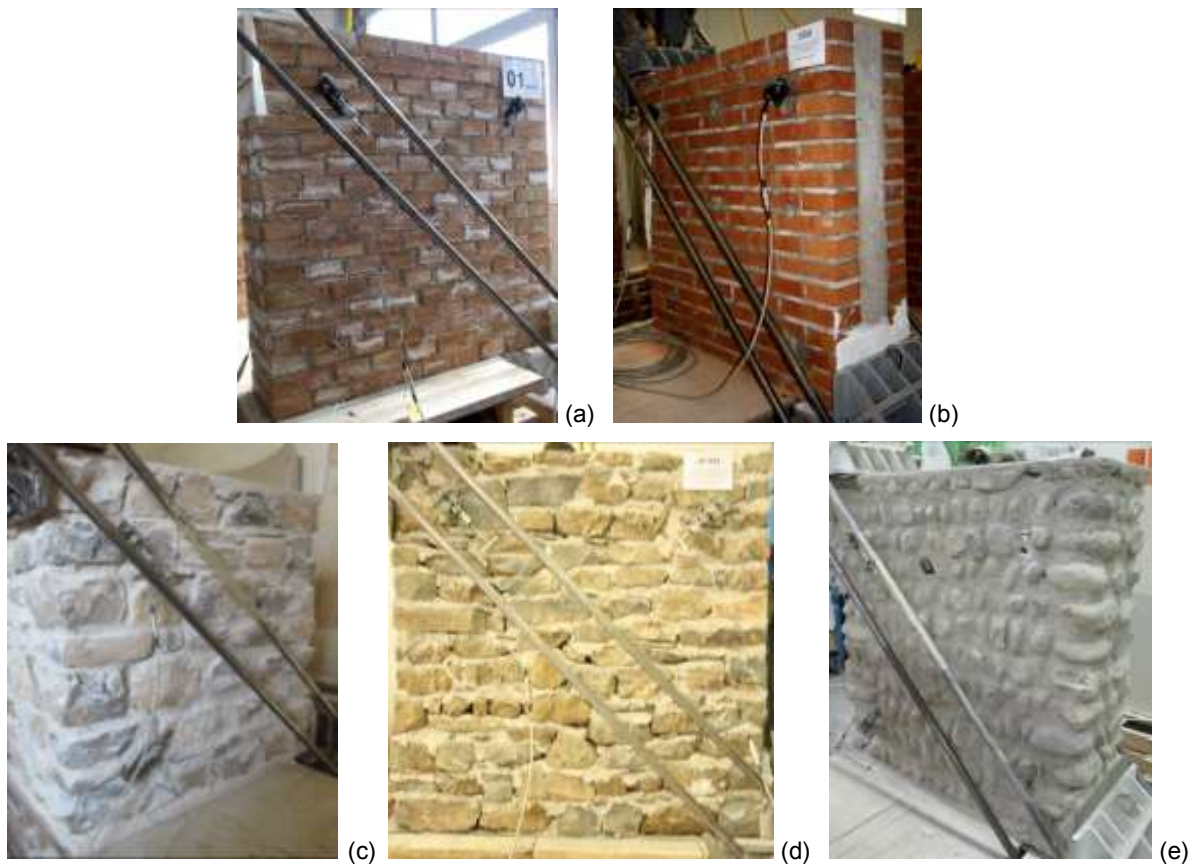


Figure 4.2 – Texture details of the masonry in specimens subjected to diagonal compression tests: (a) solid brick masonry S and S2, (b) solid brick infill masonry I, (c) R-R3 and (d) R2 rubble stone masonry and (e) cobblestones masonry C

Different types of hydraulic lime mortar were used for masonry: Table 4.1 resumes, for the six different mixtures employed, the binder dosage, the compressive and tensile strengths, obtained from cylindrical samples (100 mm diameter, 200 mm height - Figure 3.7.c-d) tested at about 60 days air curing (EN12390-3:2009/AC:2011, EN12390-6:2009). At least six samples were tested for each mortar type. The average compressive strengths,  $f_{c,b}$ , ranged from 1.3 to 5.3 MPa, the tensile strengths,  $f_{t,b}$ , from 0.2 to 1.1 MPa. It is observed that the mortars of some samples performed resistances quite different to those of other samples made with the same dosage. As specimens were made on different days, these differences are attributable to small dissimilarities in the particle size distribution of the sand and mainly to slightly diverse environmental conditions during the setting/curing of the mortar. For this reason, type B4 and type B5 mortars are kept separate, even having the same binder dosage.

Table 4.1 - Characteristics of the hydraulic lime mortars used for the masonry ( $f_{c,b}$  is the compressive strength,  $f_{t,b}$  the tensile strength, the coefficients of variation, c.o.v., are also reported)

Mortar type	Binder dosage	$f_{c,b}$ [MPa]	C.o.v. [%]	$f_{t,b}$ [MPa]	C.o.v. [%]
B1	200kg of hydraulic lime per m <sup>3</sup> of mortar	1.30	10.0	0.20	11.2
B2	250kg of hydraulic lime per m <sup>3</sup> of mortar	2.41	3.6	0.47	7.2
B3	320kg of hydraulic lime per m <sup>3</sup> of mortar	2.93	9.9	0.70	8.4
B4	350kg of hydraulic lime per m <sup>3</sup> of mortar	3.52	6.5	0.66	5.4
B5	350kg of hydraulic lime per m <sup>3</sup> of mortar	4.09	4.5	0.72	6.5
B6	390kg of hydraulic lime per m <sup>3</sup> of mortar	5.26	3.3	1.10	6.2

A preliminary experimental investigation on the masonry performances in terms of compressive strength,  $f_{c,m}$ , and Young modulus,  $E_m$ , was performed through compression tests carried out on masonry samples 500 mm wide and 1000 mm high (Figure 4.3.a). In particular, three of the considered masonry types were tested: two tests concerned solid brick masonry, type “S”, made with “B3” mortar (Figure 4.3.b), two rubble stone masonry, type “R”, made with “B5” mortar (Figure 4.3.c) and one cobblestones masonry, type “C”, made with “B2” mortar (Figure 4.3.d). The compression tests were made inserting the specimens inside a robust steel, closed frame; the compression force was applied through four hydraulic jacks (ENERPAC, 718 kN each one), connected in parallel to a hand pump (ENERPAC, mod. P84, 700 bar). The load was surveyed with a pressure transducer (AEP Transducers, LAB TP14, error f.s. 0.05%) connected to a data acquisition unit (PCMCi National Instruments, mod. DAQ Card-AI-16-XE-50). Teflon sheets were introduced in correspondence of the contact areas of the sample with the contrast frame, to reduce friction and avoid the local confinement of the masonry. Two potentiometer transducers were arranged vertically on each side of the panel, measuring specimen vertical strains (average measurement base length  $l_b = 700$  mm); some other potentiometer transducers were arranged horizontally to monitor the horizontal strains. The loading procedure included a sequence of loading-unloading cycles (step about 150 kN for solid brick and rubble stone specimens, 50 kN for cobblestones specimens) up the reaching of the peak load, then the tests were controlled at displacement steps. The results are reported in Figure 4.4 in terms of compressive stress  $\sigma_c$  (ratio between the applied load and the sample transversal cross section) against average compressive strain  $\varepsilon_c$  (ratio between the average displacement monitored by the vertical transducers and the base length  $l_b$ ) curves and are summarized in Table 4.2 in terms of masonry compressive strength  $f_{c,m}$  and Young modulus  $E_m$ . The Young modulus was estimated as secant stiffness at 10% and 40% of the compressive strength (peak stress in the diagram). The specimens are distinguished by an identifier split in three parts: the first refers to the type of test (C for compression) and to the masonry group (S, R or C), the second refers to the mortar type (Table 4.1) and the latter indicates

unreinforced masonry (U) and differentiates with a number (01 or 02) samples with identical characteristics.

It emerged, on average,  $f_{c,m} = 7.88$  MPa and  $E_m = 4266$  MPa for solid brick masonry S,  $f_{c,m} = 4.51$  MPa and  $E_m = 2430$  MPa for rubble stone masonry R and  $f_{c,m} = 1.04$  MPa and  $E_m = 1256$  MPa for cobblestones masonry C.

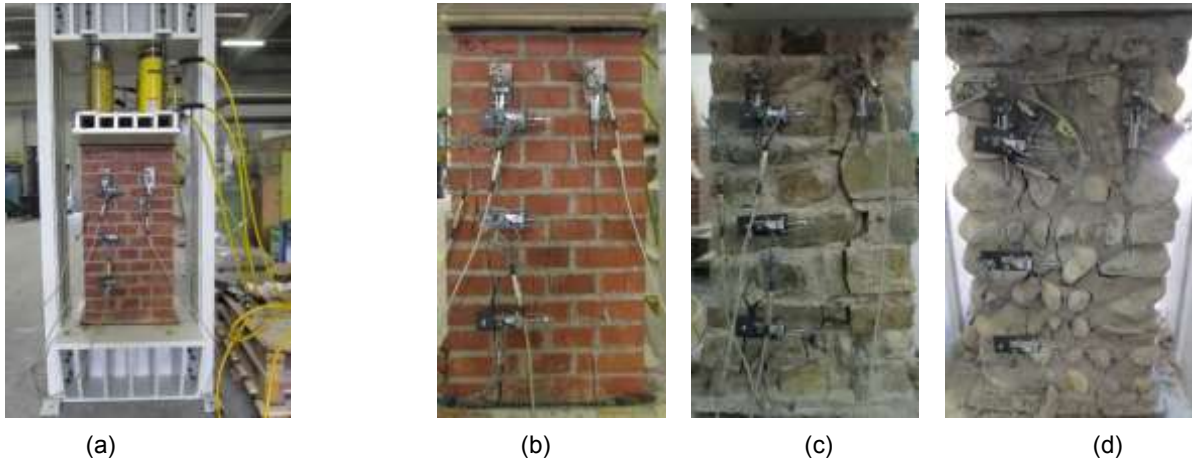


Figure 4.3 - Compression tests on masonry specimens: (a) test setup and failure mode of (b) solid brick S, (b) rubble stone R and (c) cobblestones C specimens

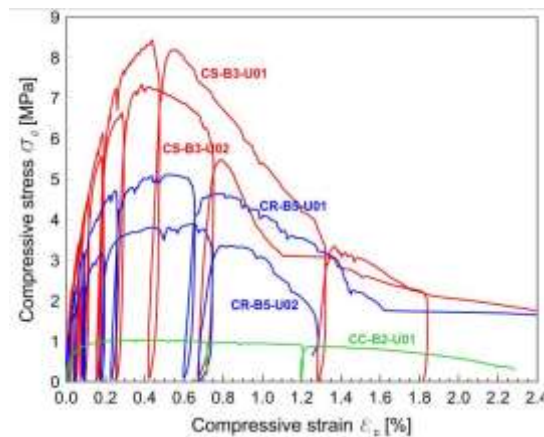


Figure 4.4 - Compression tests on masonry specimens: compressive stress  $\sigma_c$  vs. strain  $\epsilon_c$  curves

Table 4.2 - Mechanical characteristics of masonry samples subjected to compression tests: compressive strength  $f_{c,m}$  and Young modulus  $E_m$ .

ID	Mortar type	$f_{c,m}$ [MPa]	$E_m$ [MPa]
CS-B3-U01	B3	8.43	4377
CS-B3-U02	B3	7.34	4154
CR-B5-U01	B5	5.12	2711
CR-B5-U02	B5	3.89	2149
CC-B2-U01	B2	1.04	1256

In the diagonal compression experimental campaign, one or more unreinforced specimen were tested for each considered masonry type, so to directly compare the results with those obtained from reinforced samples.

The masonry samples were built on a timber basement (Figure 4.5.a); the reinforcement was applied after about 8 days from the building of the masonry panel (Figure 4.5.b-c), with or without the application of a cement based scratch coat (dosage 600 kg of cement per m<sup>3</sup> of mortar). Passing through holes, 25 mm diameter, were drilled in the masonry, then the GFRP mesh was applied on both faces, spacing from the masonry surface for about 15 mm. Couples of L-shaped GFRP connectors were inserted in the holes, assuring a lap splice of 120 mm; additional GFRP mesh devices (130x130 mm<sup>2</sup> square pieces of a GFRP mesh, 33x33 mm<sup>2</sup> grid pitch) were introduced in correspondence of the connectors, above the main mesh. The holes were then injected with a thixotropic cementitious mortar; then, the mortar layer was applied, assuring a minimum thickness of 30 mm.

It is evidenced that, in solid brick masonry, the thickness of the mortar coating resulted approximately constant, due to the high planarity of the masonry surface (Figure 4.2.a-b); thus an average thickness about 30 mm can be assumed. Differently, in stone masonry, as the faces were more irregular, due to the blocks geometry, an average thickness higher than 30 mm resulted. In fact, the average thickness of the mortar coating in rubble stone (Figure 4.2.c-d) and cobblestones reinforced samples (Figure 4.2.e) was estimated equal to 35 and 45 mm, respectively.

It is worth note that, in the application of the GFRM layers, a particular attention was devoted to the wetting the masonry surface, so to avoid the absorption of the water of the mortar.

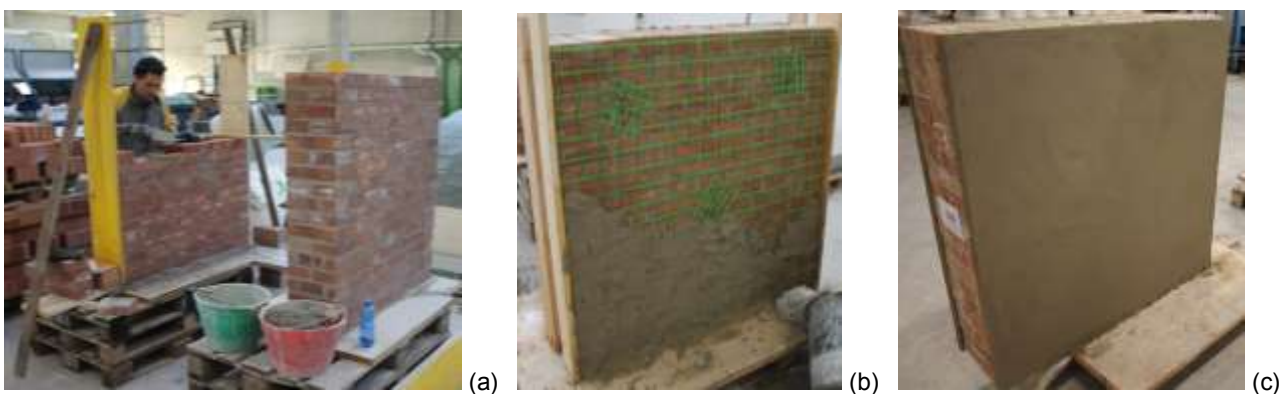


Figure 4.5 – Main realization stages of a sample for diagonal compression test (DS-B3-R19): (a) building of the masonry panel, (b) installation of the GFRP mesh and connectors and (c) application of the mortar coating

The tests were performed after at least 40 days of mortar coating curing. Several type of plasters and of reinforcements were applied, so to investigate on the influence of the different parameters on the technique effectiveness.

The different mortars used for the coating are summarised in Table 4.3. The mechanical characteristics (tensile strength  $f_{t,c}$ , compressive strength  $f_{c,c}$  and Young modulus  $E_c$ ), were determined through indirect tensile (EN12390-6:2009) and compression (EN12390-3:2009/AC:2011, EN12390-13:2013) tests performed on at least three cylindrical samples (100 mm diameter, 200 mm height - Figure 3.7.c-d). Tensile strengths ranged from 0.6 to 2.8 MPa, while compressive strengths varied from 3.6 to 25.6 MPa.

Table 4.3 – Main characteristics of the mortars used for the coating ( $f_{t,c}$  and  $f_{c,c}$  are the tensile and the compressive strengths,  $E_c$  is the Young modulus, the coefficients of variation, c.o.v., are also reported)

Mortar type	$f_{t,c}$ [MPa]	C.o.v. [%]	$f_{c,c}$ [MPa]	C.o.v. [%]	$E_c$ [GPa]	C.o.v. [%]	Description
C1	0.55	10.9	3.64	4.5	14.5	3.3	300 kg of hydraulic lime per m <sup>3</sup> of mortar
C2	0.77	5.2	4.66	13.0	13.8	11.8	Premixed mortar (based on hydraulic lime and additives)
C3	0.80	3.8	6.71	3.9	14.3	9.4	300 kg of hydraulic lime and 100 kg of cement per m <sup>3</sup> of mortar
C4	1.10	7.6	6.90	11.1	14.4	14.2	300 kg of hydraulic lime and 100 kg of cement per m <sup>3</sup> of mortar
C5	1.20	13.2	4.82	11.1	6.0	3.8	Premixed mortar (based on hydraulic lime)
C6	1.36	14.4	10.14	2.7	14.4	1.5	Premixed mortar (based on lime and cement, fiber-reinforced)
C7	1.40	6.8	7.15	13.1	7.7	1.1	Premixed mortar (based on cement and expanded clay)
C8	1.44	9.0	11.66	12.4	13.4	13.8	Premixed mortar (based on lime and pozzolanic additives)
C9	1.76	12.5	11.16	11.4	17.7	7.2	Premixed mortar (based on hydraulic lime)
C10	2.80	8.3	19.57	14.9	13.4	0.7	Premixed bicompo. mortar (hydraulic lime, cement, pozzolanic, fiber-reinforced)
C11	2.81	10.0	19.65	2.3	11.9	4.4	Premixed mortar (hydraulic lime, cement, pozzolanic, fiber-reinforced)
C12	2.97	3.4	25.74	13.2	23.3	4.9	Premixed mortar (based on lime, cement, fiber-reinforced)

By plotting the results in a  $f_{t,c} - f_{c,c}$  graph, emerged that the relationship between the tensile and compressive strength of the analysed mortars can be expressed with quite accuracy by a power function curve, as reported in Figure 4.6.a. Diversely it was not possible to find a clear correlation between the compressive (or tensile) resistance and the Young modulus (Figure 4.6.b); this is probably related to the different mortars compositions, which significantly influenced the material stiffness, even in conglomerates having very similar resistance characteristics.

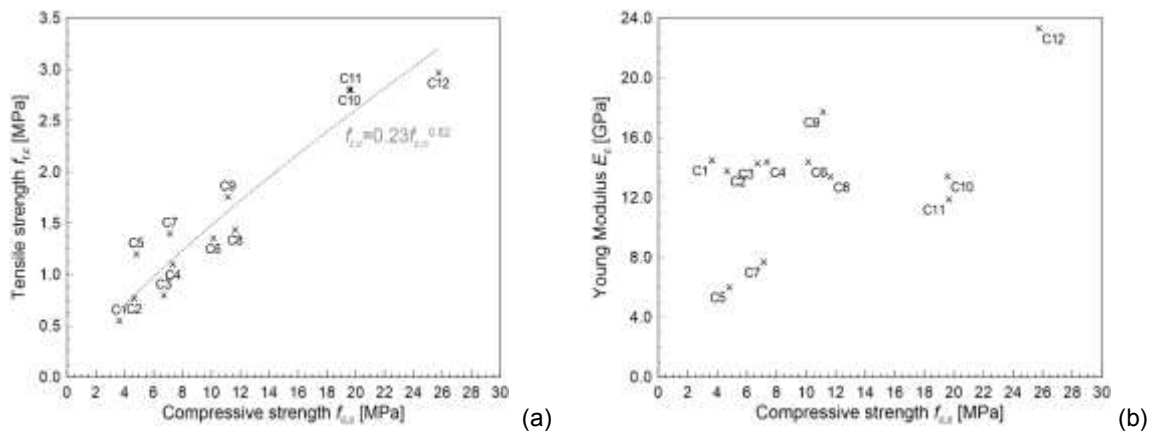


Figure 4.6 – Correlation between mortar coating characteristics: (a) compressive against tensile strengths and (b) compressive strength against Young modulus

It is observed that, before the application of the C6 and C12 mortar coatings, a preliminary treatment of the masonry surface, aimed to increase its roughness, was performed through a sand-blasting machine. Moreover, in solid brick masonry samples “S” enhanced with C5, C6, C7, C9, C10, C11 and C12 mortar coatings, the cement-based scratch coat was not applied.

Different reinforcement percentages were considered (grid dimensions 33x33 mm<sup>2</sup>, 66x66 mm<sup>2</sup> and 99x99 mm<sup>2</sup> with single “S” or doubled “D” dry fibers amount in a wire – subsection 3.2). Moreover, also the performances of a reinforcement with ribbed steel bars welded mesh (150x150 mm<sup>2</sup>, 5 mm diameter or 200x200 mm<sup>2</sup>, 6 mm diameter, B450C – D.M. 14.01.2008) were investigated, so to compare the GFRM performances with those of a traditional reinforcement technique.

In specimens reinforced with steel meshes, 9 steel passing-through ribbed bars (6 mm diameter) were introduced as connectors (Figure 4.7a), according to the indication made by Tomazevic (1999) for reinforced-cement coatings (4-6 connectors per m<sup>2</sup> of wall’s surface). Similarly, the GFRM reinforced panels were provided by 9 or 5 passing-through connections, made with couples of L-shape GFRP elements (Figure 3.5), respecting thus a limitation of 6 (Figure 4.7a) or 4 (Figure 4.7b) connectors / m<sup>2</sup>, respectively.

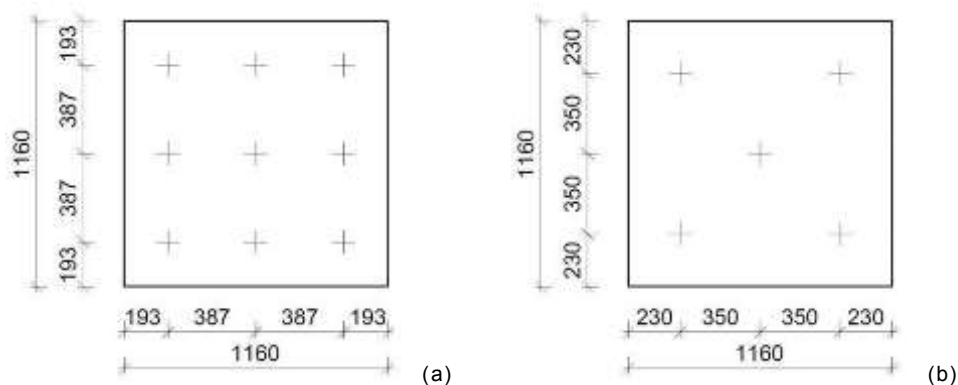


Figure 4.7 - Connectors arrangement in reinforced samples: (a) 6 and (b) 4 connectors / m<sup>2</sup>.

The list and the main characteristics of the specimens subjected to the diagonal compression tests are reported in Table 4.4 - Table 4.8. The specimens are distinguished by an identifier split in three parts: the first refers to the type of test (D for diagonal compression) and to the masonry group (S, S2, I, R, R2, R3 and C), the second indicates the type of mortar used for the masonry (Table 4.1) and the latter distinguishes unreinforced (U) and reinforced (R) masonry and differentiates the samples with a number (01, 02, 03, ...). Generally, two specimens were tested for each reinforcement asset, so to check the repeatability of the results.

A wide experimental campaign was performed on solid brick masonry, type “S” (Table 4.4): a first study concerned the influence of the mortar used for the masonry (B3 or B6) and the

reinforcement amount (varying the grid dimension) and material (considering both GFRP and steel); a reduction in the number of connections was also investigated. Then, the incidence on the masonry behavior of the mortar coating mechanical characteristics was deeply analyzed. Also for solid brick masonry “S2” (Table 4.5), infill masonry “I” (Table 4.6) and rubble stone masonry “R2” (Table 4.7), the effects of a variation in the masonry mortar characteristics (B3 or B2) and in the reinforcement embedded in the plaster were analyzed. A comparison between different mortar coatings was made for rubble stone masonry “R” and “R3” (Table 4.7); moreover, a variation of the dry fibers amount in the GFRP mesh was considered for “R3”. Lastly, in cobblestones masonry “C” (Table 4.8), a variation of both the masonry mortar (B2 and B1) and the plaster mortar was examined.

Table 4.4 - Main characteristics of the solid brick masonry samples, 250 mm thick (S) tested to diagonal compression

ID	Masonry mortar	Mortar coating	Reinforcement	Connections
DS-B3-U01 DS-B3-U02 DS-B3-U03 DS-B3-U04 DS-B3-U05 DS-B3-U06	B3	-	-	-
DS-B3-R01 DS-B3-R02	B3	C3	GFRP 33X33S	GRFP 6/m <sup>2</sup>
DS-B3-R03 DS-B3-R04	B3	C3	GFRP 66X66S	GRFP 6/m <sup>2</sup>
DS-B3-R05 DS-B3-R06	B3	C3	GFRP 99X99S	GRFP 6/m <sup>2</sup>
DS-B3-R07 DS-B3-R08	B3	C3	Steel 150x150 $\phi$ 5	Steel 6/m <sup>2</sup> $\phi$ 6
DS-B3-R09 DS-B3-R10	B3	C3	Steel 200x200 $\phi$ 6	Steel 6/m <sup>2</sup> $\phi$ 6
DS-B3-R11 DS-B3-R12	B3	C2	GFRP 66X66S	GRFP 4/m <sup>2</sup>
DS-B3-R13 DS-B3-R14	B3	C4	GFRP 66X66S	GRFP 4/m <sup>2</sup>
DS-B3-R15 DS-B3-R16	B3	C5	GFRP 66X66S	GRFP 4/m <sup>2</sup>
DS-B3-R17 DS-B3-R18	B3	C6*	GFRP 66X66S	GRFP 4/m <sup>2</sup>
DS-B3-R19 DS-B3-R20	B3	C7	GFRP 66X66S	GRFP 4/m <sup>2</sup>
DS-B3-R21 DS-B3-R22	B3	C8	GFRP 66X66S	GRFP 4/m <sup>2</sup>
DS-B3-R23 DS-B3-R24	B3	C9	GFRP 66X66S	GRFP 4/m <sup>2</sup>
DS-B3-R25 DS-B3-R26	B3	C10	GFRP 66X66S	GRFP 4/m <sup>2</sup>
DS-B3-R27 DS-B3-R28	B3	C11	GFRP 66X66S	GRFP 4/m <sup>2</sup>
DS-B3-R29 DS-B3-R30	B3	C12*	GFRP 66X66S	GRFP 4/m <sup>2</sup>
DS-B3-R31	B3	C4	GFRP 66X66S	-
DS-B3-R32	B3	C4	-	-
DS-B6-U01 DS-B6-U02	B6	-	-	-
DS-B6-R01 DS-B6-R02	B6	C3	GFRP 33X33S	GRFP 6/m <sup>2</sup>
DS-B6-R03 DS-B6-R04	B6	C3	GFRP 66X66S	GRFP 6/m <sup>2</sup>
DS-B6-R05 DS-B6-R06	B6	C3	GFRP 99X99S	GRFP 6/m <sup>2</sup>

\* Preliminary surface sand-blasting

Table 4.5 - Main characteristics of the solid brick masonry samples, 380 mm thick (S2) tested to diagonal compression

ID	Masonry mortar	Mortar coating	Reinforcement	Connections
DS2-B3-U01 DS2-B3-U02	B3	-	-	-
DS2-B3-R01 DS2-B3-R02	B3	C3	GFRP 33X33S	GRFP 6/m <sup>2</sup>
DS2-B3-R03 DS2-B3-R04	B3	C3	GFRP 66X66S	GRFP 6/m <sup>2</sup>
DS2-B3-R05 DS2-B3-R06	B3	C3	GFRP 66X66D	GRFP 6/m <sup>2</sup>
DS2-B3-R07 DS2-B3-R08	B3	C3	GFRP 99X99D	GRFP 6/m <sup>2</sup>
DS2-B3-R09 DS2-B3-R10	B3	C3	Steel 150x150 $\phi$ 5	Steel 6/m <sup>2</sup> $\phi$ 6
DS2-B2-U01 DS2-B2-U02	B2	-	-	-
DS2-B2-R01 DS2-B2-R02	B2	C3	GFRP 99X99D	GRFP 6/m <sup>2</sup>

Table 4.6 - Main characteristics of the infill solid brick masonry samples (I) tested to diagonal compression

ID	Masonry mortar	Mortar coating	Reinforcement	Connections
DI-B3-U01 DI-B3-U02	B3	-	-	-
DI-B3-R01 DI-B3-R02	B3	C3	GFRP 66X66S	GRFP 6/m <sup>2</sup>
DI-B3-R03 DI-B3-R04	B3	C3	GFRP 99X99S	GRFP 6/m <sup>2</sup>
DI-B2-U01 DI-B2-U02	B2	-	-	-
DI-B2-R01 DI-B2-R02	B2	C3	GFRP 33X33S	GRFP 6/m <sup>2</sup>
DI-B2-R03 DI-B2-R04	B2	C3	GFRP 66X66S	GRFP 6/m <sup>2</sup>

Table 4.7 - Main characteristics of the rubble stone masonry samples (R, R2 and R3) tested to diagonal compression

ID	Masonry mortar	Mortar coating	Reinforcement	Connections
DR-B5-U01 DR-B5-U02	B5	-	-	-
DR-B5-R01 DR-B5-R02	B5	C2	GFRP 66X66S	GRFP 4/m <sup>2</sup>
DR-B5-R03 DR-B5-R04	B5	C4	GFRP 66X66S	GRFP 4/m <sup>2</sup>
DR-B5-R05 DR-B5-R06	B5	C10	GFRP 66X66S	GRFP 4/m <sup>2</sup>
DR2-B3-U01 DR2-B3-U02	B3	-	-	-
DR2-B3-R01 DR2-B3-R02	B3	C3	GFRP 33X33S	GRFP 6/m <sup>2</sup>
DR2-B3-R03 DR2-B3-R04	B3	C3	GFRP 66X66S	GRFP 6/m <sup>2</sup>
DR2-B3-R05 DR2-B3-R06	B3	C3	GFRP 66X66D	GRFP 6/m <sup>2</sup>
DR2-B2-U01 DR2-B2-U02	B2	-	-	-
DR2-B2-R01 DR2-B2-R02	B2	C3	GFRP 66X66S	GRFP 6/m <sup>2</sup>
DR3-B4-U01 DR3-B4-U02	B4	-	-	-
DR3-B4-R01 DR3-B4-R02	B4	C4	GFRP 66X66S GFRP 66X66D	GRFP 4/m <sup>2</sup>
DR3-B4-R03 DR3-B4-R04	B4	C10	GFRP 66X66S GFRP 66X66D	GRFP 4/m <sup>2</sup>

Table 4.8 - Main characteristics of the cobblestones masonry samples (C) tested to diagonal compression

ID	Masonry mortar	Mortar coating	Reinforcement	Connections
DC-B2-U01 DC-B2-U02	B2	-	-	-
DC-B2-R01 DC-B2-R02	B2	C4	GFRP 66X66S	GRFP 4/m <sup>2</sup>
DC-B1-U01 DC-B1-U02	B1	-	-	-
DC-B1-R01 DC-B1-R02	B1	C1	GFRP 66X66S	GRFP 4/m <sup>2</sup>

#### 4.1.2 Tests apparatus

To facilitate the testing operations and avoid the damage to the masonry, the samples were built on a wooden base with a removable part, so to allow the preparation of the testing machine without moving the specimens, but re-arranging the apparatus. An illustration of a sample set for the diagonal compression test is illustrated in Figure 4.8.a.

The experimental apparatus, schematized in Figure 4.8.b, was constituted by two independent steel elements "1" and "2", placed along a diagonal of the sample, in correspondence of the two edges. An hydraulic jack was placed at the top of element "2" and was contrasted by a third steel element ("3"), connected with element "1" by means of four bolted steel bars (two at each side). A double-effect hydraulic jack (ENERPAC, mod.RR-1006, capacity 950 kN, stroke 170 mm) governed by means of an hand pump (ENERPAC, mod. P84, high pressure 700 bar) was used.

All metallic elements were made of steel S235 (EN10027-1:2005, 2005). Element "1" (Figure 4.9) was composed by two plates welded at a right angle and placed in contact with the sample, and by a HEB steel profile, stiffened so to prevent local deformations. Also element "2" was made of a steel profile at a right angle, provided by welded stiffening steel devices and a circular slot for the positioning of the actuator. Element "3" was made with a HEB profile on which some plates are welded as stiffening.

To limit the confinement action by friction in the contact areas between the apparatus and the specimen, a sheet made of anti-friction material (Teflon) was interposed.

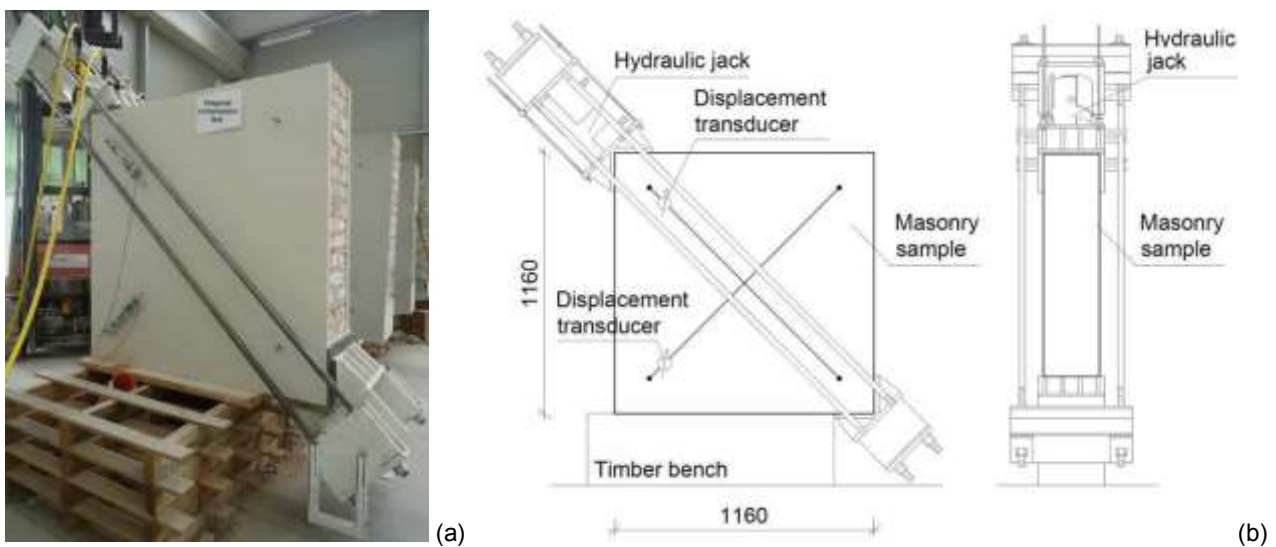


Figure 4.8 - Test setup for diagonal loading: (a) illustration of the apparatus, set on a reinforced sample and (b) schematization of frontal and lateral views

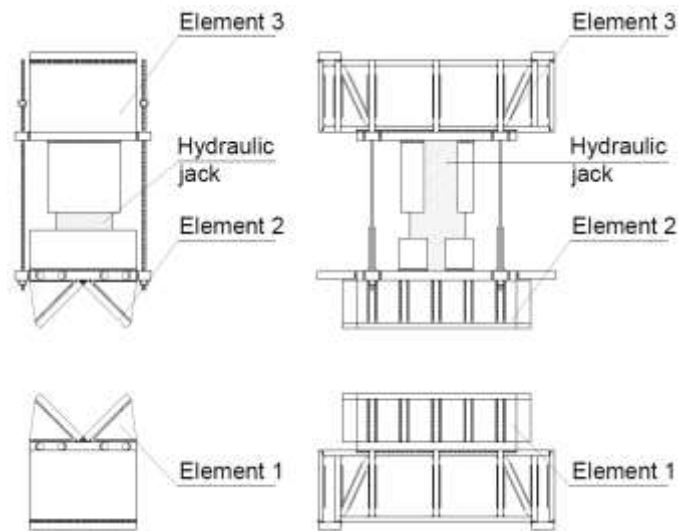


Figure 4.9 – Details of the steel contrast devices used for diagonal compression tests: frontal and lateral views

#### 4.1.3 Loading procedure and measurements

The loading procedure followed a sequence of loading and unloading cycles with constant amplitude, until reaching the resistance peak value, so to detect possible hysteresis loops (Figure 4.10). Then, the test was controlled at displacement steps. The load was measured with a pressure transducer (AEP Transducers, LAB TP14, error f.s. 0.05%).

On both sides of the specimen, couples of potentiometer transducers (Gefran LT, mod. PA1, stroke 50 mm) provided by two thin metallic wires were placed along the diagonals, on a base length  $l_b = 1150$  mm, for monitoring the displacements during the loading procedure. In particular, transducers T1 and T2 were placed on the front face of the masonry panels (Figure 4.11.a), while T3 and T4 on the back face (Figure 4.11.b). T1 and T3 detected shortenings along the compressed diagonal, in the direction of the load application, while transducers T2 and T4 monitored elongations along the diagonal in tension.

All the measurement equipment was connected to an electronic acquisition unit (PCMCI National Instruments, mod. DAQ Card-AI-16-XE-50), interfaced with a computer, permitting a real-time monitoring of the load-displacements story.

The steps adopted for the loading were, in general, of 25 kN until the reaching of 200 kN and then of 50 kN up to the cracking load. The load speed was manually governed as to be maintained constant, both in the loading and unloading phases, and equal to about 3 kN/s. Tests were stopped when the displacement of the compressed diagonal exceeded about 25 mm and, in any case, when the residual resistance was less than 20% of the maximum one.

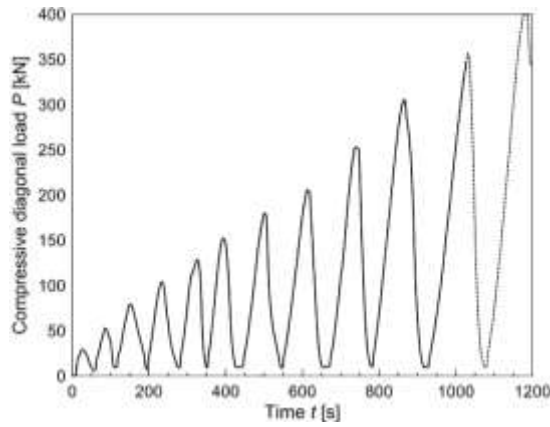


Figure 4.10 - Example of a loading-unloading sequence applied to samples subjected to diagonal compression tests

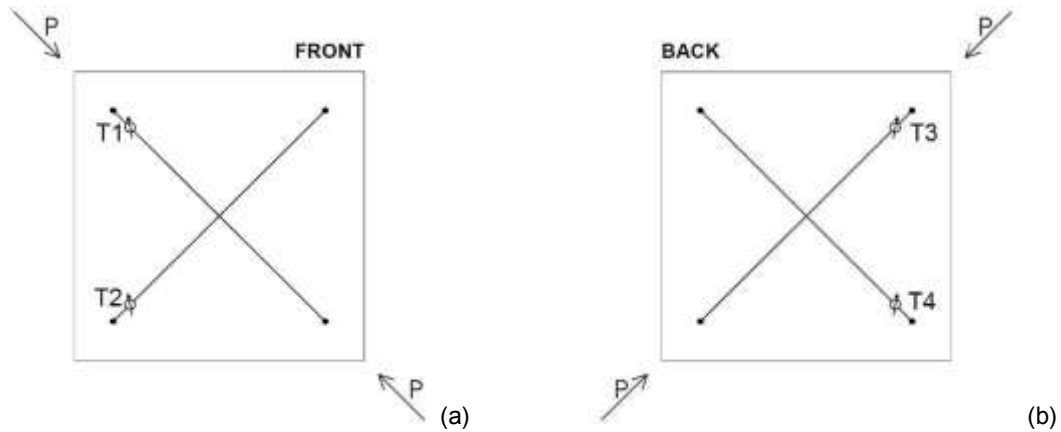


Figure 4.11 – Displacement transducers arrangement on the (a) front and (b) back side of the specimens

Through the displacements measurement during the tests, it was thus possible to evaluate the average compressive  $\varepsilon_c$  and tensile  $\varepsilon_t$  strains along the diagonals:

$$\varepsilon_c = \frac{\delta_c}{l_b} \quad (4.1)$$

$$\varepsilon_t = \frac{\delta_t}{l_b} \quad (4.2)$$

where  $\delta_c$  is the average relative displacement monitored by transducers T1 and T3 along the loading direction,  $\delta_t$  is the average relative displacement monitored by transducers T2 and T4 and  $l_b$  is the base length.

Thus, the shear strain  $\gamma$  can be evaluated, as

$$\gamma = |\varepsilon_t| + |\varepsilon_c| \quad (4.3)$$

#### 4.1.4 Results and discussion

The experimental results concerning the diagonal compression tests are expressed in the following in terms of curves representing the diagonal load  $P$  (assumed positive, for simplicity) in function of the average compressive ( $\varepsilon_c$ ) and tensile ( $\varepsilon_t$ ) strains. The unloading and reloading branches of the curves were not displayed in the graphs, so to allow for a clearer comparison among many curves.

However, as an example, two  $P-\varepsilon_c$  and  $P-\varepsilon_t$  curves complete of the loading and unloading branches, are reported in Figure 4.12.

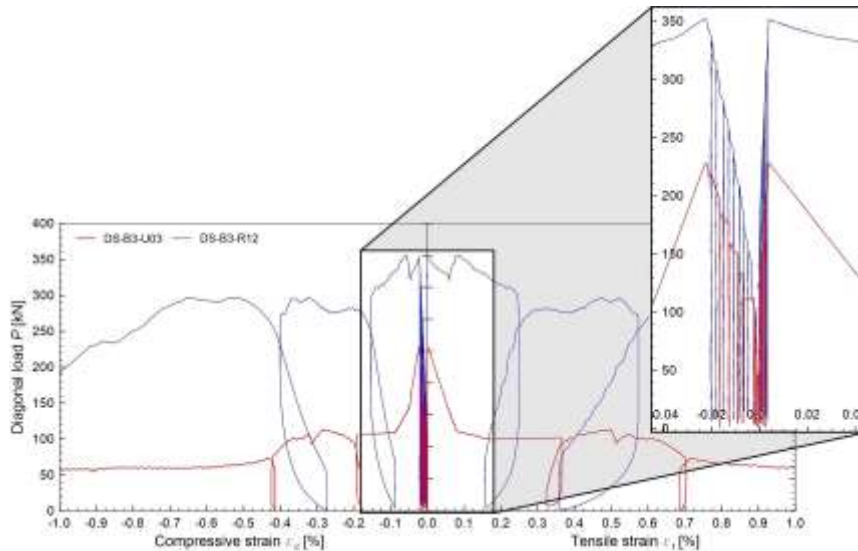


Figure 4.12 – Example of  $P-\varepsilon_c$  and  $P-\varepsilon_t$  curves complete of the loading and unloading branches obtained from experimental diagonal compression tests

The experimental performances of the different masonry types subjected to diagonal compression tests are described in the following paragraphs. Moreover, all the experimental results are resumed in Table 4.9 - Table 4.13 for the different masonry types in terms of:

- $P_m$ : maximum diagonal load;
- $\varepsilon_{cp}$ : average compressive strain in correspondence of the maximum load;
- $G$ : shear modulus;
- $P_{m(R)} / P_{m(U)}$ : ratio between the maximum load of the reinforced sample and average maximum load of the unreinforced specimens made with the same masonry type;
- $G_{(R)} / G_{(U)}$ : ratio between the shear modulus of the reinforced sample and average shear modulus of the unreinforced specimens made with the same masonry type;
- $\gamma_{0.8}$  and  $\gamma_{0.6}$ : shear strains associated to a resistance value after the peak of 80% and 60% of the maximum, respectively (Figure 4.13).
- ratios  $\mu_{0.8} = \gamma_{0.8}/\gamma_y$  and  $\mu_{0.6} = \gamma_{0.6}/\gamma_y$ , providing an indication of the capacity of the panels to deform in the post-elastic range maintaining significant levels of resistance;

It is observed that the shear modulus  $G$  was calculated by means of Equation ( 4.4 ), considering the value of the secant stiffness between the origin and the 70% of the shear stress  $\sigma_{xy}$  vs. shear strain  $\gamma$  curve (Park, 1989) and, however, fitting as close as possible the slope of the first elastic branch of the curve.

$$G = 1.1 \frac{\Delta P}{b t \Delta \gamma} \tag{ 4.4 }$$

$b$  and  $t$  are, respectively, the width and thickness of the wall (unreinforced masonry thickness) and  $1.1\Delta P/bt$  represents the shear stress at the centre of the panel  $\sigma_{xy}$  (subsection 4.1.5).

Moreover, the value of shear strain associated to the conventional yield strength  $\gamma_y$  (Figure 4.13) was evaluated by means of Equation ( 4.5 ):

$$\gamma_y = \frac{\sigma_{xy,max}}{G} = 1.1 \frac{P_m}{b t G} \tag{ 4.5 }$$

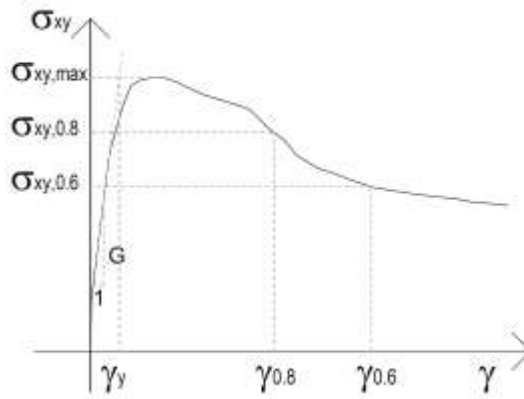


Figure 4.13 – Illustration of the shear strains  $\gamma_y$ ,  $\gamma_{0.8}$  and  $\gamma_{0.6}$

Table 4.9 - Main results concerning solid brick masonry samples, 250 mm thick (S): maximum diagonal load ( $P_m$ ), average compressive strain in correspondence of  $P_m$  ( $\varepsilon_{cp}$ ), shear modulus ( $G$ ), ratios between  $P_m$  ( $P_{m(R)} / P_{m(U)}$ ) and between  $G$  ( $G_{(R)} / G_{(U)}$ ) of the reinforced and the unreinforced specimens, shear strains associated to a resistance value after the peak of 80% and 60% of  $P_m$  ( $\gamma_{0.8}$  and  $\gamma_{0.6}$ ) and ratios  $\mu_{0.8} = \gamma_{0.8}/\gamma_y$  and  $\mu_{0.6} = \gamma_{0.6}/\gamma_y$ , being  $\gamma_y$  the shear strain associated to the conventional yield strength

ID	$P_m$ [kN]	$\varepsilon_{cp}$ [%]	$G$ [MPa]	$P_{m(R)}/$ $P_{m(U)}$	$G_{(R)}/$ $G_{(U)}$	$\gamma_y$ [%]	$\gamma_{0.8}$ [%]	$\gamma_{0.6}$ [%]	$\mu_{0.8}$ [-]	$\mu_{0.6}$ [-]
DS-B3-U01	214.2	-0.0208	2123	-	-	0.0365	0.1176	0.1472	3.22	4.03
DS-B3-U02	169.5	-0.0239	2118	-	-	0.0290	0.0930	0.1629	3.21	5.62
DS-B3-U03	228.2	-0.0340	2097	-	-	0.0394	0.1118	0.1987	2.84	5.04
DS-B3-U04	254.5	-0.0197	2484	-	-	0.0371	0.1248	0.2105	3.36	5.67
DS-B3-U05	179.9	-0.0141	2198	-	-	0.0296	0.0962	0.1862	3.25	6.28
DS-B3-U06	257.7	-0.0205	2930	-	-	0.0318	0.0906	0.1506	2.85	4.73
DS-B3-R01	389.4	-0.0518	3563	1.79	1.53	0.0396	0.5417	0.8907	13.69	22.51
DS-B3-R02	371.7	-0.0320	3398	1.71	1.46	0.0396	0.7870	1.2196	19.87	30.79
DS-B3-R03	372.5	-0.0418	3063	1.71	1.32	0.0440	0.4456	1.2980	10.12	29.48
DS-B3-R04	419.8	-0.0413	3228	1.93	1.39	0.0471	0.2604	0.7731	5.53	16.42
DS-B3-R05	423.0	-0.0333	2923	1.95	1.26	0.0524	0.2106	0.4726	4.02	9.02
DS-B3-R06	400.3	-0.0377	2982	1.84	1.28	0.0486	0.2591	0.4759	5.33	9.79
DS-B3-R07	324.6	-0.0763	3991	1.49	1.72	0.0294	0.4676	0.7720	15.88	26.22
DS-B3-R08	339.3	-0.0974	4237	1.56	1.82	0.0290	0.4776	0.8412	16.47	29.01
DS-B3-R09	406.8	-0.0761	3754	1.87	1.61	0.0392	0.3931	0.8113	10.02	20.68
DS-B3-R10	398.0	-0.0300	3904	1.83	1.68	0.0369	0.3185	0.2469	8.63	6.69
DS-B3-R11	363.4	-0.0283	3799	1.67	1.63	0.0346	0.6961	1.5099	20.10	43.60
DS-B3-R12	355.2	-0.0601	3797	1.63	1.63	0.0339	0.7214	2.1810	21.30	64.40
DS-B3-R13	315.9	-0.0802	3428	1.45	1.47	0.0334	0.5072	1.8885	15.20	56.60
DS-B3-R14	332.4	-0.0271	3534	1.53	1.52	0.0341	0.9671	1.9308	28.40	56.70
DS-B3-R15	312.9	-0.0295	3025	1.44	1.30	0.0375	1.1686	1.8427	31.20	49.20
DS-B3-R16	336.2	-0.0227	2934	1.55	1.26	0.0415	0.4771	0.9086	11.50	21.90
DS-B3-R17	424.1	-0.0287	3824	1.95	1.64	0.0402	0.8713	1.9715	21.70	49.10
DS-B3-R18	419.5	-0.0220	4033	1.93	1.73	0.0377	0.2599	0.9303	6.90	24.70
DS-B3-R19	401.5	-0.2288	3178	1.85	1.37	0.0457	1.4179	1.8570	31.00	40.60
DS-B3-R20	318.5*	-0.0298	3266	-	-	-	-	-	-	-
DS-B3-R21	269.1*	-0.2109	3174	-	-	-	-	-	-	-
DS-B3-R22	345.3	-0.0335	3622	1.59	1.56	0.0345	0.9045	1.7088	26.20	49.50
DS-B3-R23	400.1	-0.1218	4067	1.84	1.75	0.0356	1.1933	1.6493	33.50	46.30
DS-B3-R24	404.3	-0.0502	4065	1.86	1.75	0.0360	0.4033	1.1380	11.20	31.60
DS-B3-R25	494.8	-0.0292	3819	2.28	1.64	0.0469	0.1510	0.2167	3.22	4.62
DS-B3-R26	493.1	-0.0368	3692	2.27	1.59	0.0484	0.2118	0.2423	4.38	5.01
DS-B3-R27	540.6	-0.0341	3509	2.49	1.51	0.0558	0.2237	0.2103	4.01	3.77
DS-B3-R28	556.6	-0.0408	3406	2.56	1.46	0.0592	0.1763	0.2047	2.98	3.46
DS-B3-R29	574.5	-0.0459	4060	2.64	1.75	0.0512	0.2818	0.9120	5.50	17.80
DS-B3-R30	603.0	-0.0380	4615	2.77	1.98	0.0473	0.4352	1.0171	9.20	21.50
DS-B3-R31	384.0	-0.0198	3508	1.77	1.51	0.0396	0.1385	0.2306	3.49	5.82
DS-B3-R32	350.6	-0.0190	3415	1.61	1.47	0.0372	0.5122	1.6192	13.78	43.56
DS-B6-U01	275.1	-0.0188	3530	-	-	0.0282	0.0965	0.1476	3.42	5.23
DS-B6-U02	238.8	-0.0212	3307	-	-	0.0261	0.1022	0.1600	3.91	6.12
DS-B6-R01	420.8	-0.1168	5257	1.64	1.54	0.0290	0.4411	0.8077	15.22	27.87
DS-B6-R02	412.9	-0.1045	5073	1.61	1.48	0.0295	0.4647	0.9333	15.77	31.67
DS-B6-R03	474.6	-0.0449	4723	1.85	1.38	0.0364	0.1976	0.6723	5.43	18.48
DS-B6-R04	506.0	-0.0397	4842	1.97	1.42	0.0378	0.1937	0.5936	5.12	15.69
DS-B6-R05	469.6	-0.0363	4451	1.83	1.30	0.0382	0.1612	0.3442	4.22	9.01
DS-B6-R06	539.7	-0.0587	4574	2.10	1.34	0.0427	0.2362	0.6186	5.53	14.48

\* Premature failure due to local damage

Table 4.10 - Main results concerning solid brick masonry samples, 380 mm thick (S2): maximum diagonal load ( $P_m$ ), average compressive strain in correspondence of  $P_m$  ( $\varepsilon_{cp}$ ), shear modulus ( $G$ ), ratios between  $P_m$  ( $P_{m(R)} / P_{m(U)}$ ) and between  $G$  ( $G_{(R)} / G_{(U)}$ ) of the reinforced and the unreinforced specimens, shear strains associated to a resistance value after the peak of 80% and 60% of  $P_m$  ( $\gamma_{0.8}$  and  $\gamma_{0.6}$ ) and ratios  $\mu_{0.8} = \gamma_{0.8}/\gamma_y$  and  $\mu_{0.6} = \gamma_{0.6}/\gamma_y$ , being  $\gamma_y$  the shear strain associated to the conventional yield strength

ID	$P_m$ [kN]	$\varepsilon_{cp}$ [%]	$G$ [MPa]	$P_{m(R)}/$ $P_{m(U)}$	$G_{(R)}/$ $G_{(U)}$	$\gamma_y$ [%]	$\gamma_{0.8}$ [%]	$\gamma_{0.6}$ [%]	$\mu_{0.8}$ [-]	$\mu_{0.6}$ [-]
DS2-B3-U01	258.9	-0.0186	2542	-	-	0.0243	0.0893	0.1504	3.68	6.20
DS2-B3-U02	312.6	-0.0237	2654	-	-	0.0281	0.0906	0.1271	3.23	4.53
DS2-B3-R01	478.8	-0.0670	3925	1.68	1.51	0.0291	0.5233	0.8947	18.01	30.79
DS2-B3-R02	478.1	-0.0510	3761	1.67	1.45	0.0303	0.4052	0.7940	13.38	26.22
DS2-B3-R03	530.4	-0.0505	3477	1.86	1.34	0.0363	0.1533	0.8764	4.22	24.12
DS2-B3-R04	434.6	-0.0470	3534	1.52	1.36	0.0293	0.1857	0.8721	6.34	29.77
DS2-B3-R05	548.3	-0.1111	4106	1.92	1.58	0.0318	0.4068	0.8489	12.79	26.69
DS2-B3-R06	575.4	-0.0324	4409	2.01	1.70	0.0311	0.2835	0.7262	9.12	23.36
DS2-B3-R07	457.3	-0.0368	3988	1.60	1.54	0.0273	0.2103	0.4404	7.70	16.12
DS2-B3-R08	414.4	-0.0343	3980	1.45	1.53	0.0248	0.1543	0.5749	6.22	23.18
DS2-B3-R09	498.0	-0.0175	4475	1.74	1.72	0.0265	0.2442	0.6460	9.21	24.37
DS2-B3-R10	404.1	-0.0355	4533	1.41	1.74	0.0212	0.4156	0.5413	19.57	25.49
DS2-B2-U01	242.7	-0.0077	1785	-	-	0.0324	0.0978	0.1622	3.02	5.01
DS2-B2-U02	286.0	-0.0205	1822	-	-	0.0374	0.1051	0.1540	2.81	4.12
DS2-B2-R01	413.9	-0.0582	2793	1.57	1.55	0.0353	0.2295	0.5433	6.50	15.39
DS2-B2-R02	315.7	-0.0377	2860	1.19	1.59	0.0263	0.1557	0.5435	5.92	20.67

Table 4.11 - Main results concerning infill solid brick masonry samples (I): maximum diagonal load ( $P_m$ ), average compressive strain in correspondence of  $P_m$  ( $\varepsilon_{cp}$ ), shear modulus ( $G$ ), ratios between  $P_m$  ( $P_{m(R)} / P_{m(U)}$ ) and between  $G$  ( $G_{(R)} / G_{(U)}$ ) of the reinforced and the unreinforced specimens, shear strains associated to a resistance value after the peak of 80% and 60% of  $P_m$  ( $\gamma_{0.8}$  and  $\gamma_{0.6}$ ) and ratios  $\mu_{0.8} = \gamma_{0.8}/\gamma_y$  and  $\mu_{0.6} = \gamma_{0.6}/\gamma_y$ , being  $\gamma_y$  the shear strain associated to the conventional yield strength

ID	$P_m$ [kN]	$\varepsilon_{cp}$ [%]	$G$ [MPa]	$P_{m(R)}/$ $P_{m(U)}$	$G_{(R)}/$ $G_{(U)}$	$\gamma_y$ [%]	$\gamma_{0.8}$ [%]	$\gamma_{0.6}$ [%]	$\mu_{0.8}$ [-]	$\mu_{0.6}$ [-]
DI-B3-U01	221.9	-0.0289	1076	-	-	0.0491	0.1385	0.2078	2.82	4.23
DI-B3-U02	202.6	-0.0155	1139	-	-	0.0424	0.1411	0.2178	3.33	5.14
DI-B3-R01	354.7	-0.0372	1699	1.67	1.53	0.0497	0.2054	0.8359	4.13	16.81
DI-B3-R02	338.9	-0.0344	1750	1.60	1.58	0.0461	0.1670	0.4530	3.62	9.82
DI-B3-R03	370.5	-0.0361	1629	1.75	1.47	0.0542	0.2021	0.4513	3.73	8.33
DI-B3-R04	309.6	-0.0334	1580	1.46	1.43	0.0467	0.2352	0.6664	5.04	14.28
DI-B2-U01	207.5	-0.0224	981	-	-	0.0504	0.1320	0.2186	2.62	4.34
DI-B2-U02	200.4	-0.0216	601	-	-	0.0794	0.2550	0.3662	3.21	4.61
DI-B2-R01	285.2	-0.0421	1577	1.40	1.99	0.0431	0.2163	0.5178	5.02	12.02
DI-B2-R02	301.1	-0.0716	1670	1.48	2.11	0.0429	0.3233	0.6385	7.53	14.87
DI-B2-R03	249.9	-0.0399	1528	1.23	1.93	0.0390	0.2081	0.7505	5.34	19.26
DI-B2-R04	252.8	-0.0822	1515	1.24	1.92	0.0398	0.3061	0.6512	7.70	16.38

Table 4.12 - Main results concerning rubble stone masonry samples (R, R2 and R3): maximum diagonal load ( $P_m$ ), average compressive strain in correspondence of  $P_m$  ( $\varepsilon_{cp}$ ), shear modulus ( $G$ ), ratios between  $P_m$  ( $P_{m(R)} / P_{m(U)}$ ) and between  $G$  ( $G_{(R)} / G_{(U)}$ ) of the reinforced and the unreinforced specimens, shear strains associated to a resistance value after the peak of 80% and 60% of  $P_m$  ( $\gamma_{0.8}$  and  $\gamma_{0.6}$ ) and ratios  $\mu_{0.8} = \gamma_{0.8}/\gamma_y$  and  $\mu_{0.6} = \gamma_{0.6}/\gamma_y$ , being  $\gamma_y$  the shear strain associated to the conventional yield strength

ID	$P_m$ [kN]	$\varepsilon_{cp}$ [%]	$G$ [MPa]	$P_{m(R)}/$ $P_{m(U)}$	$G_{(R)}/$ $G_{(U)}$	$\gamma_y$ [%]	$\gamma_{0.8}$ [%]	$\gamma_{0.6}$ [%]	$\mu_{0.8}$ [-]	$\mu_{0.6}$ [-]
DR-B5-U01	238.0	-0.0178	1666	-	-	0.0323	0.3971	1.0020	12.28	31.00
DR-B5-U02	236.9	-0.0333	1743	-	-	0.0308	0.2469	0.4429	8.03	14.40
DR-B5-R01	427.6	-0.1014	2513	1.80	1.47	0.0385	0.8391	1.4368	21.79	37.31
DR-B5-R02	449.6	-0.0352	2269	1.89	1.33	0.0448	0.6612	1.6814	14.75	37.50
DR-B5-R03	464.6	-0.0785	2560	1.96	1.50	0.0411	0.7796	1.3322	18.98	32.44
DR-B5-R04	457.6	-0.0233	2779	1.93	1.63	0.0373	1.1901	1.5985	31.94	42.90
DR-B5-R05	473.4	-0.1971	2588	1.99	1.52	0.0414	1.3601	2.1037	32.86	50.82
DR-B5-R06	402.8	-0.1356	2895	1.70	1.70	0.0315	1.8064	2.7234	57.38	86.51
DR2-B3-U01	126.4	-0.0847	815	-	-	0.0351	0.5508	0.8245	15.70	23.50
DR2-B3-U02	135.7	-0.0282	718	-	-	0.0428	0.7098	1.1159	16.60	26.10
DR2-B3-R01	388.0	-0.0948	1365	3.34	1.78	0.0643	1.1964	1.9683	18.60	30.60
DR2-B3-R02	360.0	-0.0937	1374	3.10	1.79	0.0593	0.9841	1.9386	16.60	32.70
DR2-B3-R03	331.9	-0.1084	1205	2.86	1.57	0.0623	1.0658	1.6018	17.10	25.70
DR2-B3-R04	366.4	-0.0690	1285	3.16	1.68	0.0645	0.8065	1.6774	12.50	26.00
DR2-B3-R05	410.7	-0.1032	1478	3.54	1.93	0.0629	1.6223	2.2699	25.80	36.10
DR2-B3-R06	398.2	-0.1220	1496	3.43	1.95	0.0602	1.1807	1.5903	19.60	26.40
DR2-B2-U01	117.2	-0.0677	638	-	-	0.0416	0.7024	0.8562	16.90	20.60
DR2-B2-U02	115.0	-0.0224	801	-	-	0.0325	0.4938	0.7829	15.20	24.10
DR2-B2-R01	368.9	-0.0115	1252	2.82	1.74	0.0667	1.4802	2.1069	22.20	31.60
DR2-B2-R02	393.0	-0.0856	1293	3.00	1.80	0.0688	1.0181	1.5408	14.80	22.40
DR3-B4-U01	439.5	-0.0550	1872	-	-	0.0304	0.8093	0.9137	26.66	30.10
DR3-B4-U02	376.0	-0.0331	1798	-	-	0.0270	0.7251	1.2823	26.81	47.41
DR3-B4-R01	702.1	-0.0736	2476	1.72	1.32	0.0367	1.4837	1.9350	40.46	52.77
DR3-B4-R02	749.5	-0.0894	2187	1.84	1.17	0.0443	0.8580	2.1370	19.36	48.22
DR3-B4-R03	617.4	-0.1587	2513	1.51	1.34	0.0318	1.0789	1.7820	33.96	56.09
DR3-B4-R04	717.1	-0.3570	2264	1.76	1.21	0.0410	1.9236	2.7210	46.96	66.43

Table 4.13 - Main results concerning cobblestones masonry samples (C): maximum diagonal load ( $P_m$ ), average compressive strain in correspondence of  $P_m$  ( $\varepsilon_{cp}$ ), shear modulus ( $G$ ), ratios between  $P_m$  ( $P_{m(R)} / P_{m(U)}$ ) and between  $G$  ( $G_{(R)} / G_{(U)}$ ) of the reinforced and the unreinforced specimens, shear strains associated to a resistance value after the peak of 80% and 60% of  $P_m$  ( $\gamma_{0.8}$  and  $\gamma_{0.6}$ ) and ratios  $\mu_{0.8} = \gamma_{0.8}/\gamma_y$  and  $\mu_{0.6} = \gamma_{0.6}/\gamma_y$ , being  $\gamma_y$  the shear strain associated to the conventional yield strength

ID	$P_m$ [kN]	$\varepsilon_{cp}$ [%]	$G$ [MPa]	$P_{m(R)}/$ $P_{m(U)}$	$G_{(R)}/$ $G_{(U)}$	$\gamma_y$ [%]	$\gamma_{0.8}$ [%]	$\gamma_{0.6}$ [%]	$\mu_{0.8}$ [-]	$\mu_{0.6}$ [-]
DC-B2-U01	110.4	-0.0315	799	-	-	0.0313	0.3955	0.7710	12.65	24.67
DC-B2-U02	126.0	-0.0491	800	-	-	0.0356	0.5715	1.1851	16.03	33.24
DC-B2-R01	379.4	-0.0630	1863	3.21	2.33	0.0461	1.4526	2.1670	31.52	47.02
DC-B2-R02	371.5	-0.0818	1722	3.14	2.16	0.0488	0.9694	1.8235	19.86	37.35
DC-B1-U01	46.7	-0.0231	276	-	-	0.0383	0.3552	0.5252	9.28	13.73
DC-B1-U02	49.8	-0.0503	203	-	-	0.0555	0.5114	1.1153	9.22	20.10
DC-B1-R01	209.2	-0.0364	1093	4.34	4.56	0.0433	0.5446	0.7635	12.57	17.63
DC-B1-R02	227.4	-0.1077	1102	4.72	4.60	0.0467	0.9817	1.3113	21.03	28.08

- Solid brick masonry (S, S2 and I)

74 diagonal compression tests on unreinforced and reinforced solid brick masonry were performed.

46 tests concerned 250 mm thick masonry (DS) made of two different types of mortar (B3 and B6). A broad investigation was performed on DS-B3 masonry: at first, 5 different type of reinforcement were considered (GFRP meshes 33x33S, 66x66S and 99x99S and steel meshes 150x150 mm<sup>2</sup>  $\phi$ 5 and 200x200 mm<sup>2</sup>  $\phi$ 6), maintaining the same type of mortar for the coating (C3). Then, the characteristics of the mortar coating were varied, keeping constant the reinforcement (GFRP 66x66S meshes). Moreover, the cases of both reinforcement with no connections and unreinforced mortar coating were analysed. A total of 6 unreinforced masonry samples were tested for comparison. Tests on DS-B6 masonry concerned 2 unreinforced samples and 3 couples of reinforced samples enhanced with C3 mortar plaster and 3 different types of GFRP meshes (33x33S, 66x66S and 99x99S).

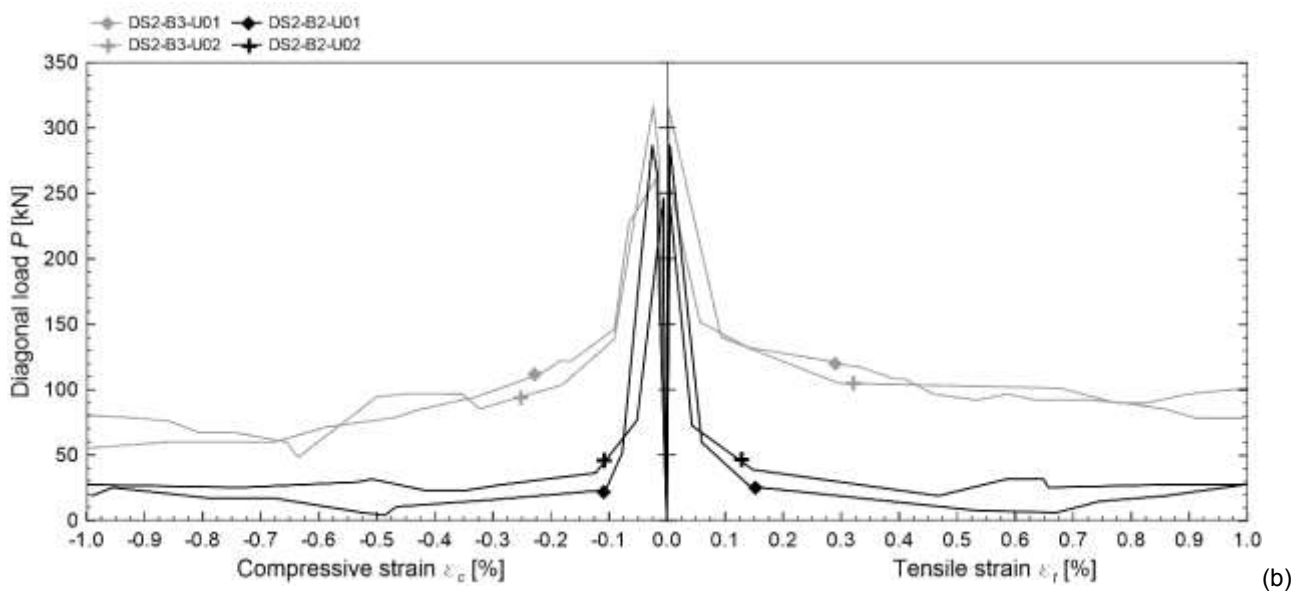
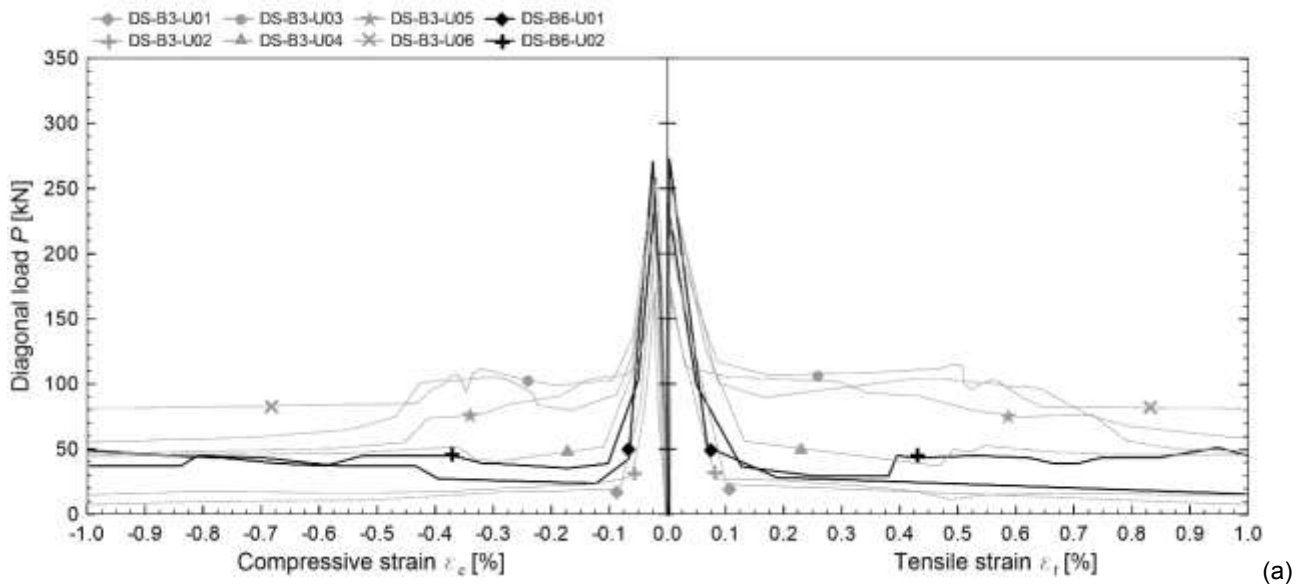
The experimental investigations on 380 mm thick solid brick masonry (DS2) involved 16 specimens, made of 2 different mortars, B3 and B2. 2 tests for each type were made on unreinforced masonry. Investigations on DS2-B3 masonry concerned couples of samples enhanced with different type of reinforcement (GFRP meshes 33x33S, 66x66S, 66x66D and 99x99D and steel meshes 150x150 mm<sup>2</sup>  $\phi$ 5). For DS2-B2 case, a single type of reinforcement (GFRP meshes 99x99D) was considered.

Also for the infill solid brick masonry specimens, B3 and B2 mortars were considered; 6 samples were tested for both. In particular, tests concerned a couple of unreinforced samples and two couples of reinforced specimens with different GFRP mesh grid dimensions (66x66S and 99x99S for DI-B3 and 33x33S and 66x66S for DI-B2).

The same type of mortar for the coating (C3) was employed for both DS2 and DI reinforced specimens.

Unreinforced solid brick masonry samples (Figure 4.14) developed an approximately linear trend up to the maximum value of the load; then, a sudden drop in resistance occurred after the appearance of a diagonal cracking. In general, the cracks had a stair-stepped pattern, typical of regular masonry composed of strong blocks and weak mortar: the cracks followed mainly head and bed mortar joints, involving specially the brick-mortar interface, but sometimes also some bricks were broken (Figure 4.15.a-b). In DI samples, also the detachment of a masonry leaf a from the rubble conglomerate infill emerged (Figure 4.15.c). The cracks involved the whole masonry thickness; the residual load was related to friction between elements across the cracks and the compressive strength of the masonry struts.

Actually, some notable differences emerged in peak loads reached by samples having same characteristics; this variability was probably due to some little differences during the executive stages, both in terms of construction and curing environmental conditions. The brittle behavior of the masonry emphasised this effect, resulting then in a marked variability in the specimens resistances. However, some observations on unreinforced solid brick masonry samples can be done: by comparing the average shear modulus  $G$  and peak resistance  $P_m$  of the different masonry types, emerged that the greater was the masonry mortar resistance, the higher values of both shear modulus and resistance were attained. Moreover, similar maximum loads were reached by DS-B3 and DI-B3 samples, evidencing that the rubble conglomerate infill was not able to provide any additional resistance contribution, but only a slightly more gradual strength decay. However, significant lower shear modulus (almost halved) resulted for DI-B3.



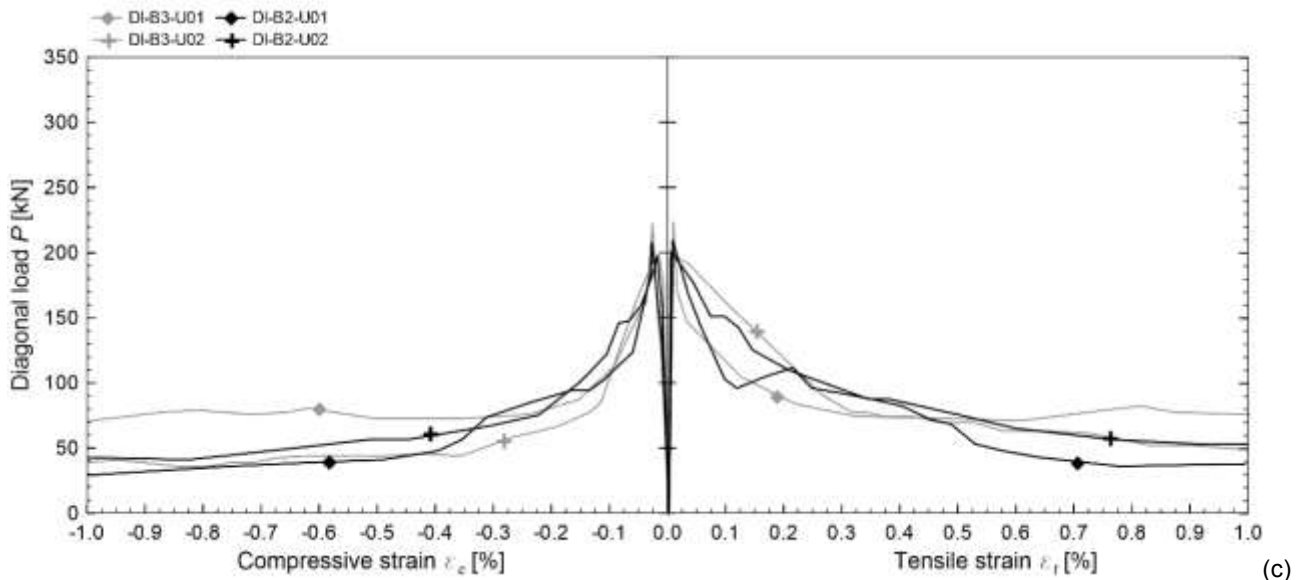


Figure 4.14 –  $P-\varepsilon_c$  and  $P-\varepsilon_t$  envelope curves of unreinforced solid brick masonry samples: (a) DS, (b) DS2 and (c) DI

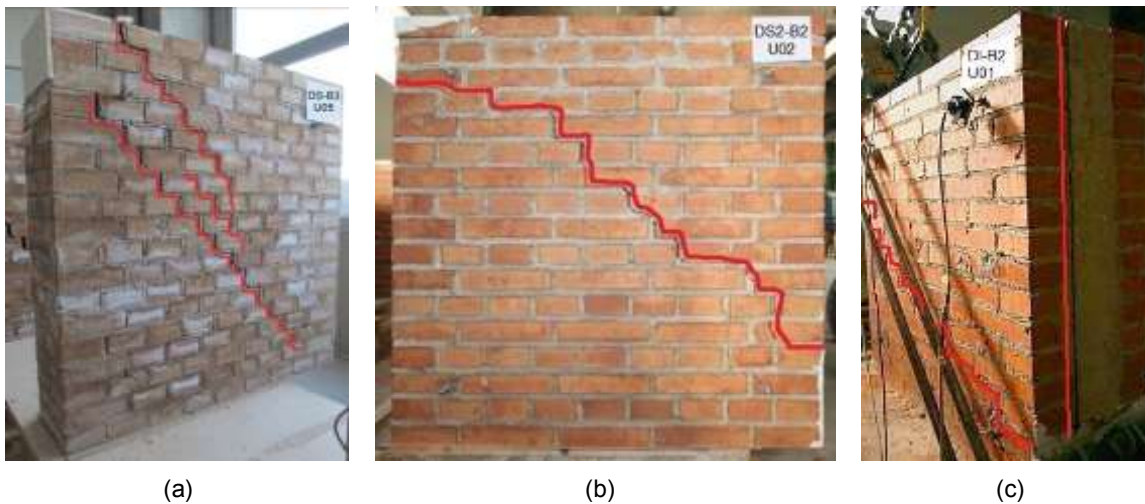


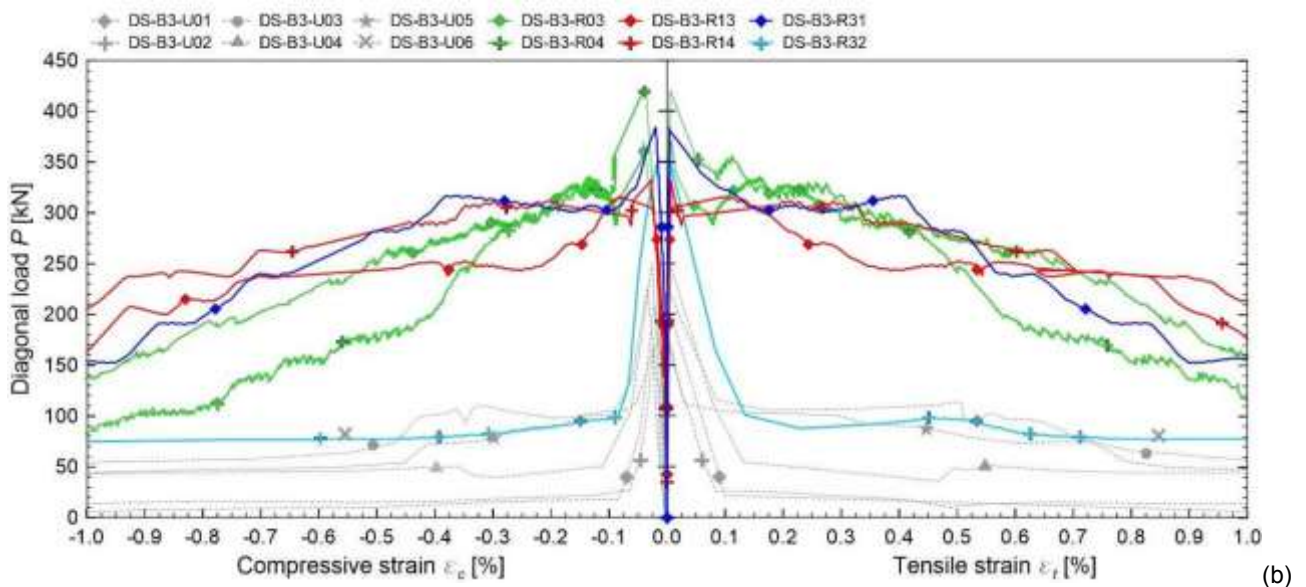
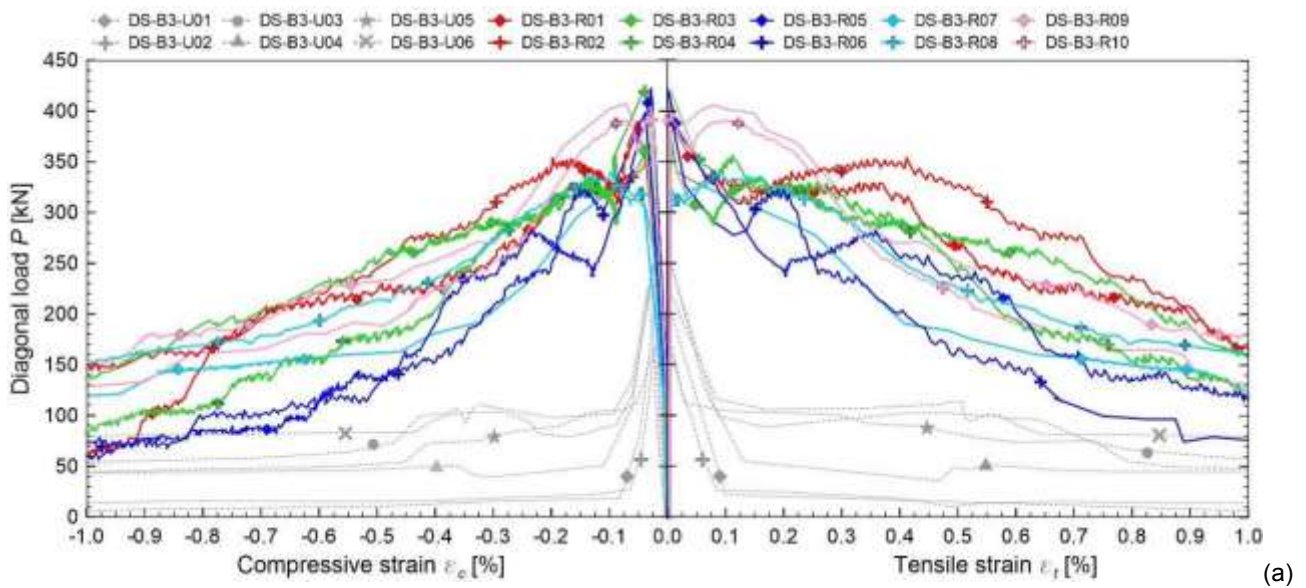
Figure 4.15 – Examples of typical crack patterns in unreinforced solid brick masonry samples at the end of the diagonal compression test: (a) DS-B3-U05, (b) DS2-B2-U02 and (c) DI-B2-U01

The  $P-\varepsilon_c$  and  $P-\varepsilon_t$  curves concerning reinforced solid brick masonry specimens are plotted in Figure 4.16-Figure 4.18; the behavior of unreinforced samples is also reported for comparison.

In general, in reinforced specimens, a diagonal crack formed in the mortar coating, in the force direction, just before reaching the maximum diagonal force; gradually the cracking zone spared, with the formation of other cracks, almost parallel to the first one (Figure 4.19). The cracking involved also the masonry, with a trend similar to that evidenced in unreinforced specimens. The GFRP mesh intervened in the cracked areas of mortar coating: it contrasts the opening of cracks supporting tensile stresses, resulting in a gradual and moderate decrease of the resistance in the post-peak branch. No evident out-of-plane swellings in the masonry or slips between the masonry

and the mortar coating generally occurred for tensile strains  $\varepsilon_t$  lower than 0.5-0.6%. The progressive collapse of several GFRP wires in the widely damaged area occurred from values of tensile deformation  $\varepsilon_t$  of about 0.6-0.7%. At the increasing of the strains, an augmenting damage of the mortar among cracks (with local detachments of mortar portions covering the GFRP mesh) was also observed.

The sensitivity of the reinforcement technique effectiveness at the varying of the different masonry and reinforcement characteristics is discussed in detail in the following; however, significant performance improvements were in general observed in reinforced masonry samples, in respect to unreinforced ones, both in terms of peak load and deformation capacity before collapsing (gradual instead abrupt decrease of resistance).



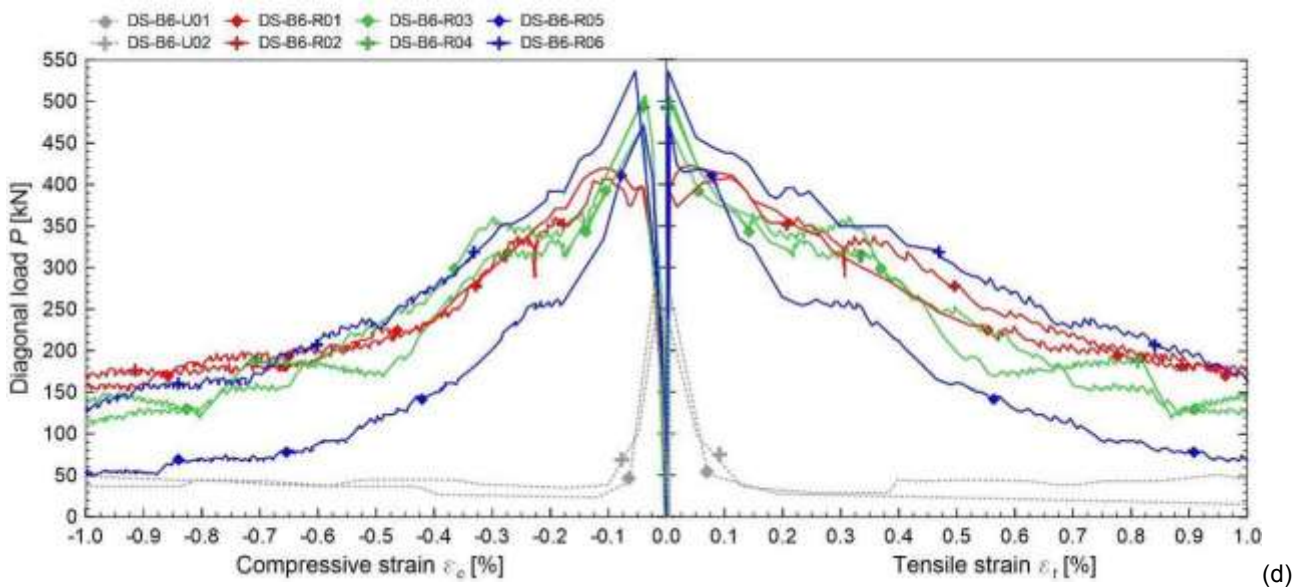
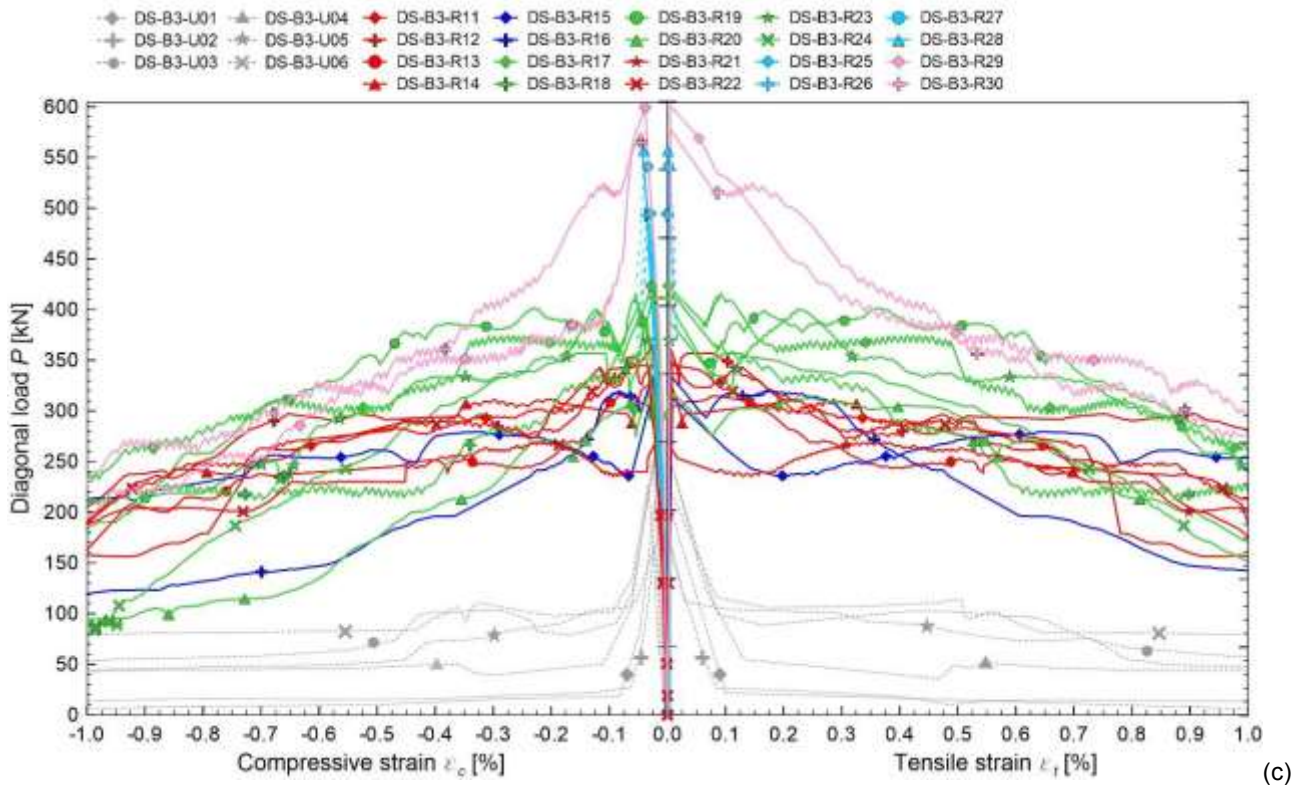


Figure 4.16 – Comparison between  $P$ - $\varepsilon_c$  and  $P$ - $\varepsilon_t$  envelope curves concerning samples made of 250 mm thick solid brick masonry DS

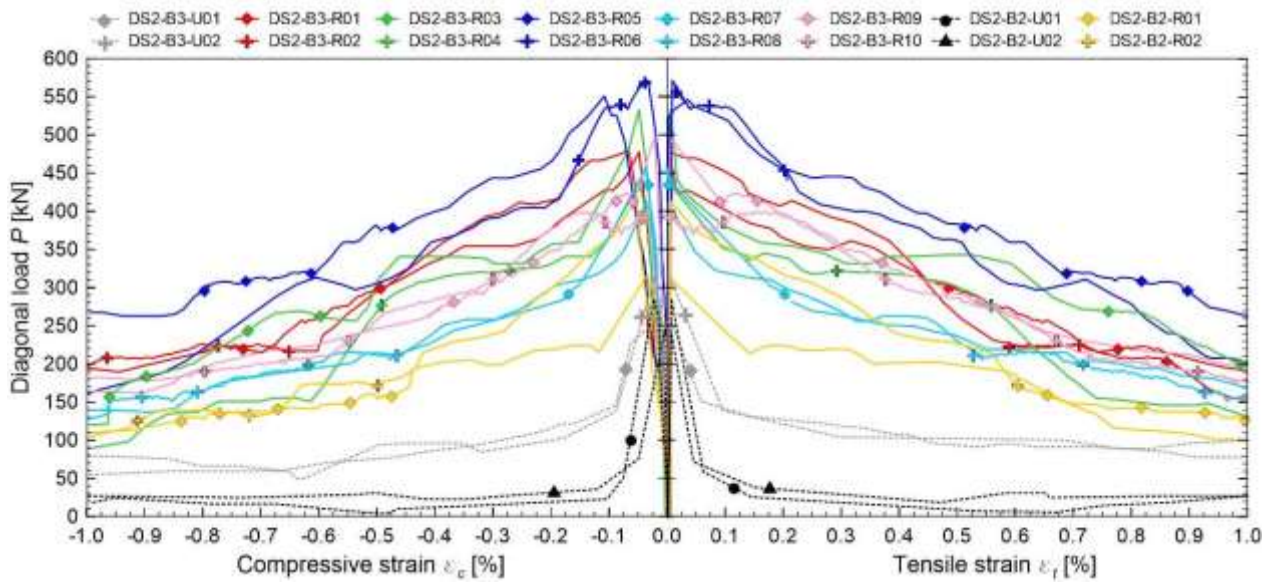


Figure 4.17 – Comparison between  $P-\varepsilon_c$  and  $P-\varepsilon_t$  envelope curves concerning samples made of 380 mm thick solid brick masonry DS2

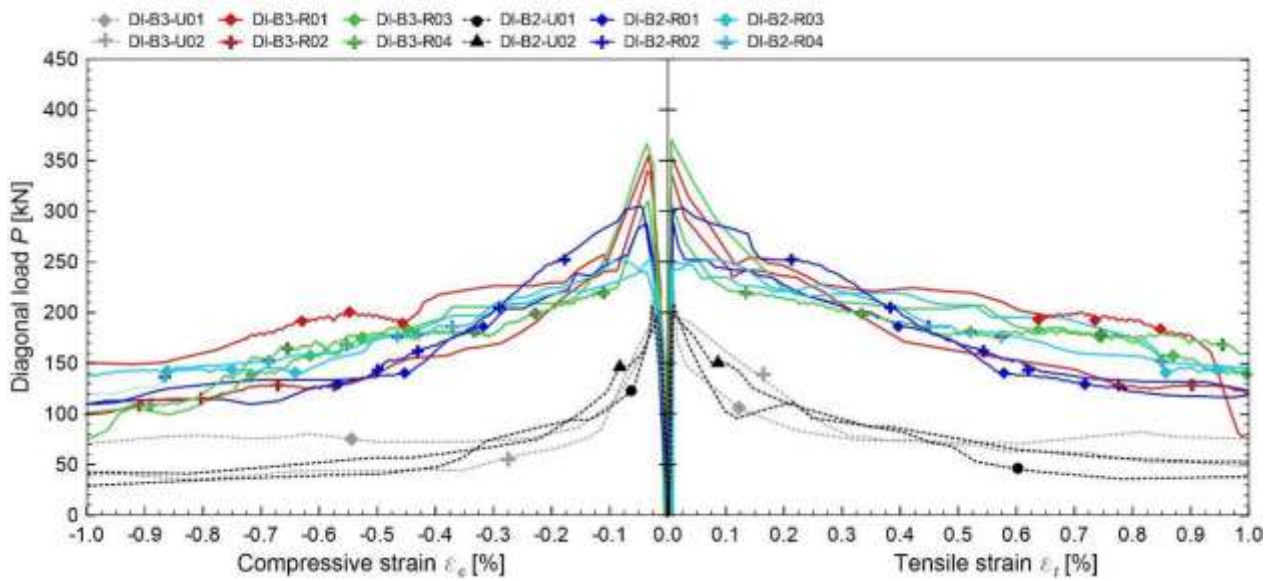


Figure 4.18 – Comparison between  $P-\varepsilon_c$  and  $P-\varepsilon_t$  envelope curves concerning samples made of two-leaf solid brick with conglomerate infill masonry DI.

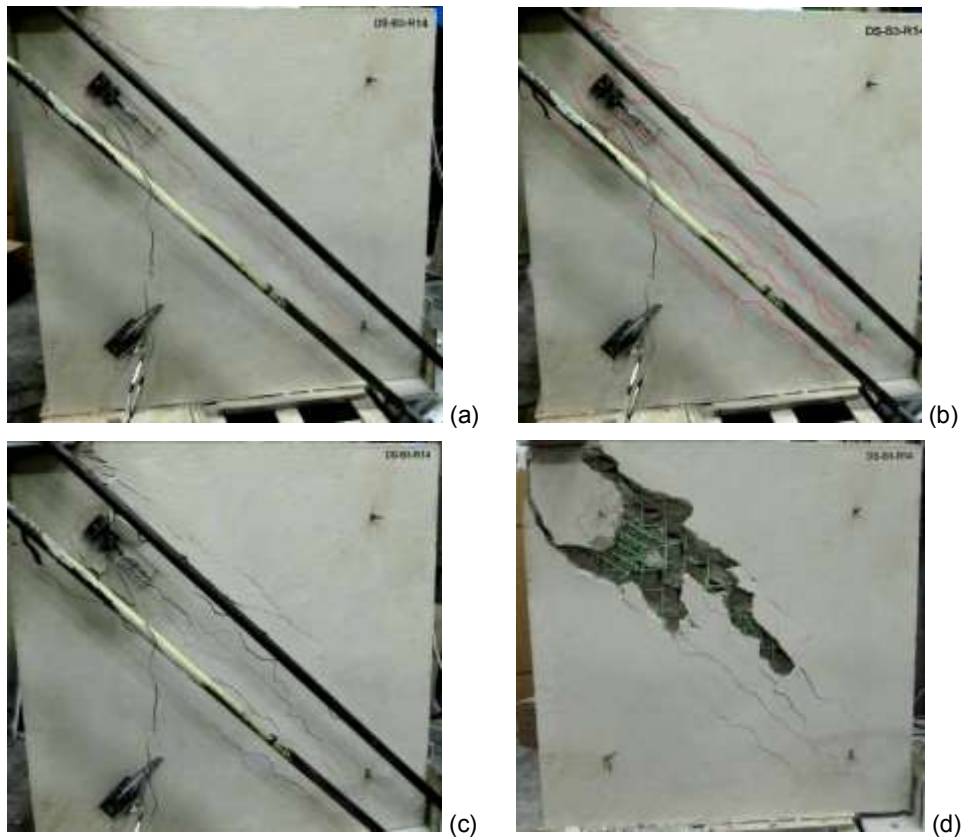


Figure 4.19 – Example of typical crack pattern evolution in a reinforced solid brick masonry specimen: sample DS-B3-R14 at (a)  $\varepsilon_c = 0.18\%$ , (b)  $\varepsilon_c = 0.43\%$ , (c)  $\varepsilon_c = 0.65\%$  and (a) at the end of the test, after removing some damaged mortar portions

Considering the specimens enhanced with C3 mortar coating (curves in Figure 4.16.a, Figure 4.16.d, Figure 4.17 and Figure 4.18), it can generally be observed that the elastic deformability and the peak resistance of solid brick reinforced masonry is very limitedly affected by the type of GFRP mesh used, because the tensile strength of the reinforced coating is very little influenced by the composite before cracking, as evidenced in tensile tests on reinforced mortar coating (subsection 3.3.3). This is due to due to the low geometrical percentage and to the low modular ratio of the composite. The main differences among specimens are rather due to the incidental occurrence of some voids in the coating in correspondence of mesh intersections, which can anticipate the crack formation. The void presence in the coating may reasonably be more pronounced where a mesh with a small grid pitch (such as  $33 \times 33 \text{ mm}^2$ ) is employed, inducing a premature cracking.

The ratios  $P_{m(R)}/P_{m(U)}$  generally ranged from 1.5 to 2.1 both in 250 mm and in 380 mm thick solid brick masonry (DS and DS2). Lower values (about 1.2-1.7) emerged for infill masonry (DI). Ratios  $G_{(R)}/G_{(U)}$  resulted on average equal to 1.5 (C.o.v. 10%), exception for DI-B2, where quite higher values (about 2, C.o.v. 4%) emerged.

After cracking, the presence of the GFRP mesh permitted in general to maintain good resistance performances also at higher values of deformation ( $\mu_{0.8}$  and  $\mu_{0.8}$  in Table 4.9 - Table 4.11). Comparing the results of specimens reinforced using the same plaster, a lower mesh grid dimension resulted in an higher diffusion of cracks. In DS-B3 and DS-B6, the use of 99x99S mesh grid (Figure 4.20.a) instead of 66x66S (Figure 4.20.b) induced, on average, a more pronounced resistance degradation, due to the lower reinforcement percentage.

Also in specimens enhanced by means of 33x33S GFRP mesh a more gradual resistance decrease after peak, in respect to 66x66S mesh reinforced samples, was initially observed till  $\varepsilon_t \cong 0.6\%$  (DS-B3 and DS2-B3). However, after the reaching of this deformation level, the results provided by the two types of reinforcement became comparable. This was due to the premature failure of the 33x33S reinforced mortar coating, as a result of the progressive delamination of the plaster covering the mesh (Figure 4.20.c). This occurrence did not allow the exploitation of the whole resistant contribution of the GFRP wires crossing the cracks, which only in very few cases broke up. This delamination phenomenon already emerged during the shear test performed for the reinforcement characterization (subsection 3.3.4, Figure 3.28.e) and is related to the weakening of the mortar layer in the plane of the embedded reinforcement, as the higher GFRP mesh density further prejudice the effective continuity of the inorganic matrix.

A comparison between specimens with the same reinforcement percentage but a different mesh grid dimension (33x33S and 66x66D) was performed for DS2-B3: the delamination did not occur when the 66x66D mesh was employed (Figure 4.20.d), thus higher deformation performances, also in respect to 66x66S, were attained. Diversely, the use of 99x99D mesh grids (Figure 4.20.e) did not permit to reach behavior similar to 33x33S and 66x66S, even if the reinforcement percentage was intermediate between these two cases. This aspect, was probably related the higher mesh-mortar slippage for the 99x99 grid, governed mainly by transversal wires (as evidenced in characterization tests on GFRM, discussed in subsection 3.3). Thus, the lower crack diffusion induced a concentration of the mesh tensile stress.

The specimens strengthened with steel weld fabric showed almost similar performances as those specimens arranged with GFRP meshes (DS-B3 and DS2-B3). However, the bars yielding did not occur: the progressive resistance degradation was due to the increasing damage and delamination of the mortar among cracks. Better performances were attained by increasing the grid dimension from 150 to 200 mm, maintaining the same reinforcement percentage (DS-B3).

The important role of an effective reinforcement embedded in the mortar plaster was clearly evidenced in Figure 4.16.b, considering specimens DS-B3-R31 and DS-B3-R32, where the C4 mortar coating was applied, respectively, with and without the GFRP mesh embedded. An abrupt

drop of the resistance suddenly occurred after peak in the latter case (Figure 4.20.f) and a limited number of cracks formed in the plaster.

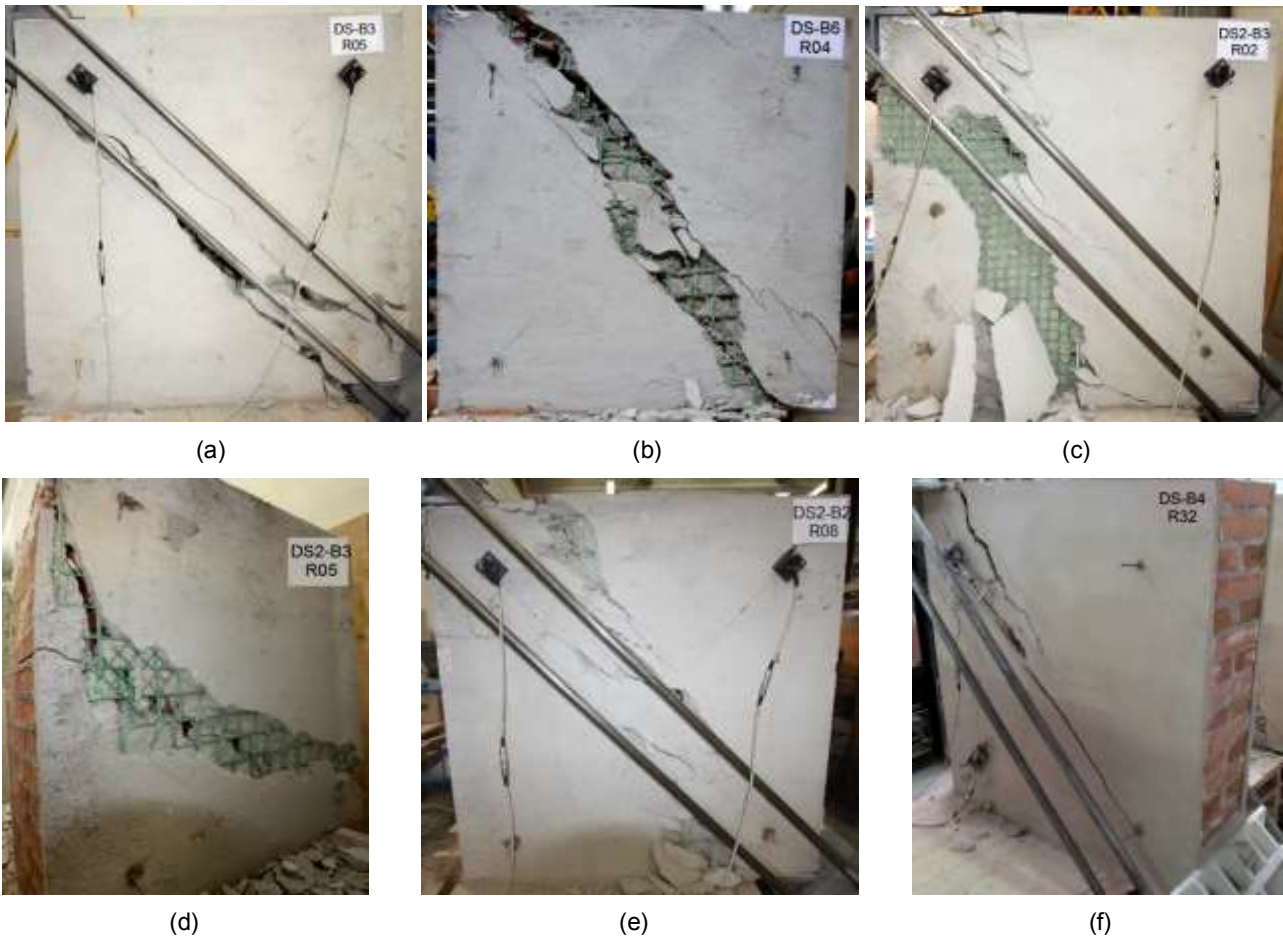


Figure 4.20 – Comparison among solid brick masonry specimens enhanced by means of (a) 99x99S, (b) 66x66S (c) 33x33S, (d) 66x66D and (e) 99x99D GFRP meshes at the end of the tests and (f) sample without any reinforcement embedded in the plaster

In the same graph (Figure 4.16.b) an evaluation of the sensitivity of the test results to the connector amount was illustrated: the introduction of 4 connections/m<sup>2</sup> (DS-B3-R13, DS-B3-R14) did not change appreciably the global  $P-\varepsilon$  behavior in respect to the sample without connections (DS-B3-R31). These results, compared also with those of samples DS-B3-R03 and DS-B3-R04 (6 connections/m<sup>2</sup> and similar mortar used for the coating), seem to indicate that the number of connections between reinforcement and masonry does not affect appreciably the performances of the reinforced specimens. However, the important role of the connectors emerged in samples made of two-leaf solid bricks masonry with conglomerate infill: the detachment of the brick facing emerged in testing unreinforced panels (Figure 4.15.c) did not occurred in reinforced panels, although significantly higher stress levels were achieved.

In general, it is important to evidence that the connectors play a fundamental role when an axial compression is also present, intervening in confining of masonry and connecting the reinforcement to the masonry substrate when the adhesion fails, as evidenced by Gattesco & al. (2013, 2015b) through experimental shear compression tests and numerical investigations. Diagonal compression tests are not able to evidence clearly this aspect.

Figure 4.16.c is aimed to evidence the influence of the mortar of the coating on specimens DS-B3. Five different groups, for similar performances, can be distinguished:

- 1) Samples reinforced with C2, C4 and C8 mortars (red curves in the graph of Figure 4.16.c);
- 2) Samples reinforced with C5 mortar (blue);
- 3) Samples reinforced with C6, C7 and C9 mortars (green);
- 4) Samples reinforced with C10 and C11 mortars (light blue);
- 5) Samples reinforced with C12 mortars (pink).

The mortars of group 1 have different tensile strengths ( $f_{t,c}$  ranging from 0.77 to 1.44 MPa) but a similar Young modulus ( $E_c$  about 14.4 GPa). An average shear modulus  $G = 3559$  MPa (C.o.v. 7%) resulted; moreover, excluding DS-B3-21 for premature cracking of the plaster (due to a local defect), samples attained to an average a peak load  $P_m$  of 342 kN (C.o.v. 5%). The post-peak branches were very similar (also the DS-B3-21 curves tended to align, at the increasing of the deformations).

The tensile strength of C5 mortar - group 2 - is in the resistance range of group 1 ( $f_{t,c} = 1.20$  MPa), but the elastic modulus is more than halved ( $E_c = 6$  GPa). Actually, before cracking, samples of group 2 manifested an higher deformability ( $G = 2980$  MPa, C.o.v. 2%) and also the average peak load ( $P_m = 325$  kN, C.o.v. 5%) and post-peak trend were a little lower.

At the end of the tests it was possible to note some differences in crack patterns: more diffused cracks resulted for group 1 (Figure 4.21), in respect to group 2 (Figure 4.22).

The samples of group 3 (tensile strength range  $f_{t,c} = 1.36 - 1.76$  MPa) performed similar resistances ( $P_m = 410$  kN, C.o.v. 3% - excluding DS-B3-20 for premature cracking of the plaster due to a local defect) and post peak-branches. However, some differences in terms of shear modulus emerged; in fact, the value of  $G$  (mean value 3793 MPa, C.o.v. 11%) tended to increase at the increasing of the mortar Young modulus: 3222 MPa for C7 ( $E_c = 7.7$  GPa), 3929 MPa for C6 ( $E_c = 14.4$  GPa) and 4066 MPa for C9 ( $E_c = 17.7$  GPa). Diversities emerged also in the crack patterns: a wider cracks diffusion was noted for the C6 (Figure 4.23.a) and C9 (Figure 4.23.c) mortar coatings, while a modest number of cracks formed in the C7 plasters (Figure 4.23.b). Moreover, cracks almost rectilinear were observed in the C6 cases, while a more irregular pattern in C9 ones.

It is worth note the higher performances manifested by samples reinforced through C6 mortar in respect to C8 one, although characterised by very similar mechanical parameters. Actually, the difference may be related to the preliminary sand-blasting of the masonry surface (subsection 4.1.1), which could have improved the interaction between layers.

The samples of both group 4 and 5 (tensile strength range  $f_{t,c} = 2.80 - 2.97$  MPa) reached very high values of both shear modulus and peak resistance (mean values  $P_m = 544$  – C.o.v. 8% - and  $G = 3850$  – C.o.v. 11%), which resulted directly dependent from the mortar Young modulus and tensile strength. However, in the specimens of group 4, a sudden drop of the resistance emerged just after the peak load, due to the diffuse detachment of the mortar layers from the masonry surface (Figure 4.24.a-b). It is supposed that this premature failure did not occurred in the samples of the group 5 (Figure 4.24.c) due to the surface sand-blasting (subsection 4.1.1), which could reasonably have improved the bond performances of the masonry-mortar interface, permitting the formation and diffusion of the diagonal cracks.

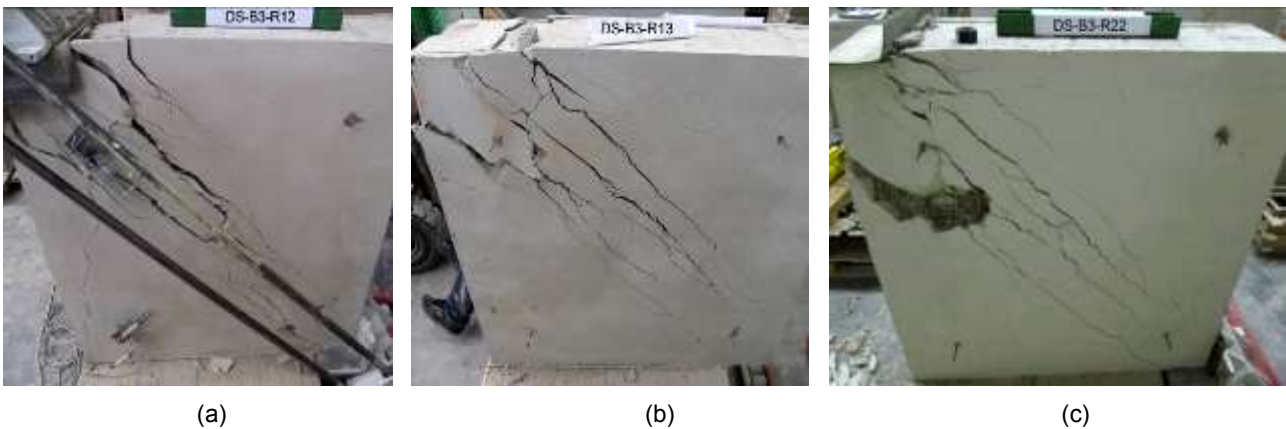


Figure 4.21 – Typical crack patterns at the end of the test in samples of group 1: coatings made of (a) C2, (b) C4 and (c) C8 mortars



Figure 4.22 – Typical crack pattern at the end of the test in samples of group 2 (coating made of C5 mortar)

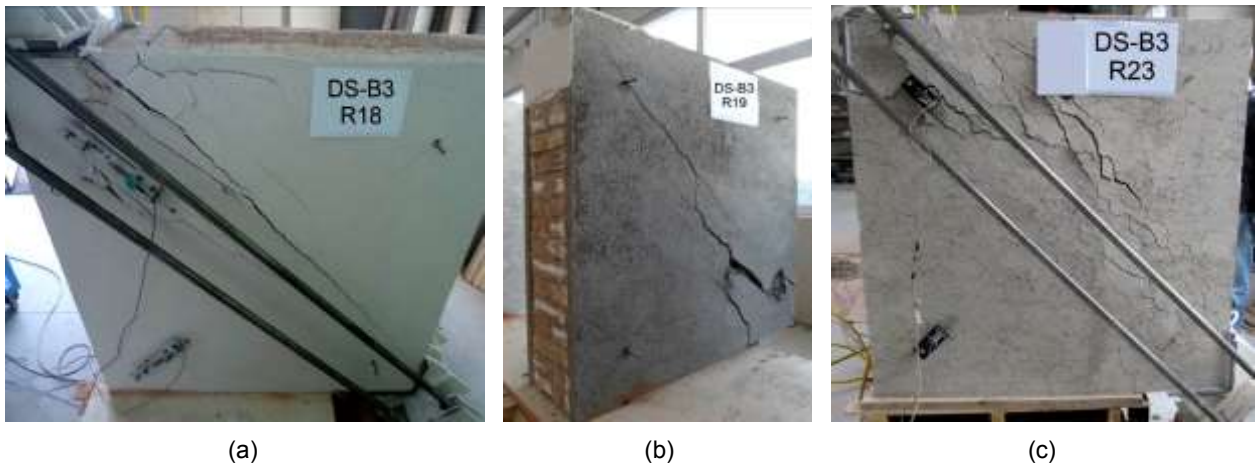


Figure 4.23 – Typical crack patterns at the end of the test in samples of group 3: coatings made of (a) C6, (b) C7 and (c) C8 mortars

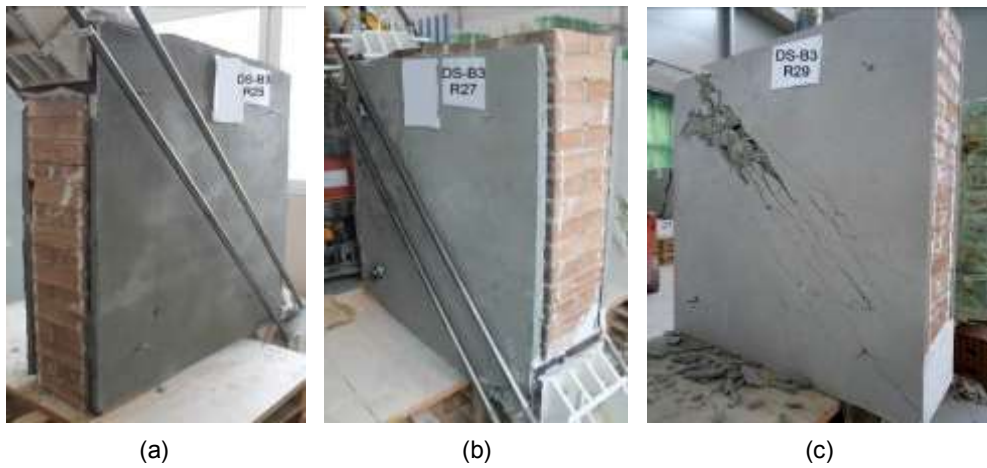


Figure 4.24 – Typical crack patterns at the end of the test in samples of group 4 and 5: coatings made of (a) C10, (b) C11 and (c) C12 mortars

In general, it is observed that the mortar mechanical characteristics influenced the ratios  $G_{(R)}/G_{(U)}$  (range 1.3-1.7) and  $P_{m(R)}/P_{m(U)}$  (range 1.5-2.5). For example, in Figure 4.25 the values of  $P_{m(R)}/P_{m(U)}$  are plotted against the tensile resistance of the mortar coating  $f_{t,c}$ ; the best fitting tendency line was also drawn. In general, an increasing of  $P_{m(R)}/P_{m(U)}$  at the increasing of  $f_{t,c}$  was observed; however the scatters from the tendency line are quite consistent in some cases. The dependence from a single mechanical parameter (i.e. the mortar tensile strength or Young modulus) is not clear; so, it is likely a combined effect of the main parameters of the reinforced coating that affects the reinforced masonry performances.

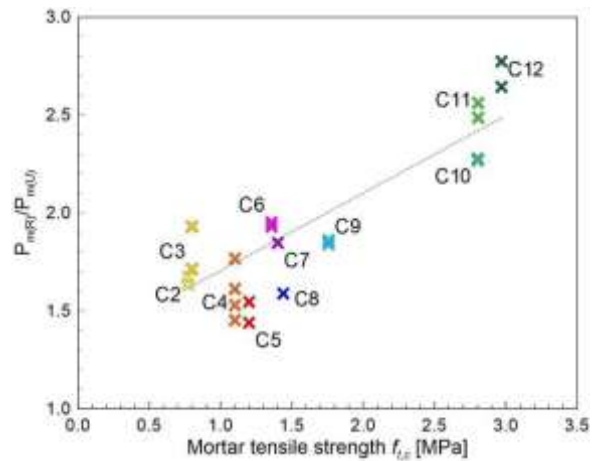


Figure 4.25 – Ratios  $P_{m(R)}/P_{m(R)}$  against the mortar coating tensile strength in solid brick DS-B3 samples.

Moreover, by analysing the curves in Figure 4.16.c, it can in general be observed that the decrease of resistance (slope of the post-peak branch) occurred more rapidly in specimens which attained to higher peak loads and that the curves tended to converge at the increase of the deformations.

- Behaviour of rubble stone and cobblestones masonry (R, R2, R3 and C)

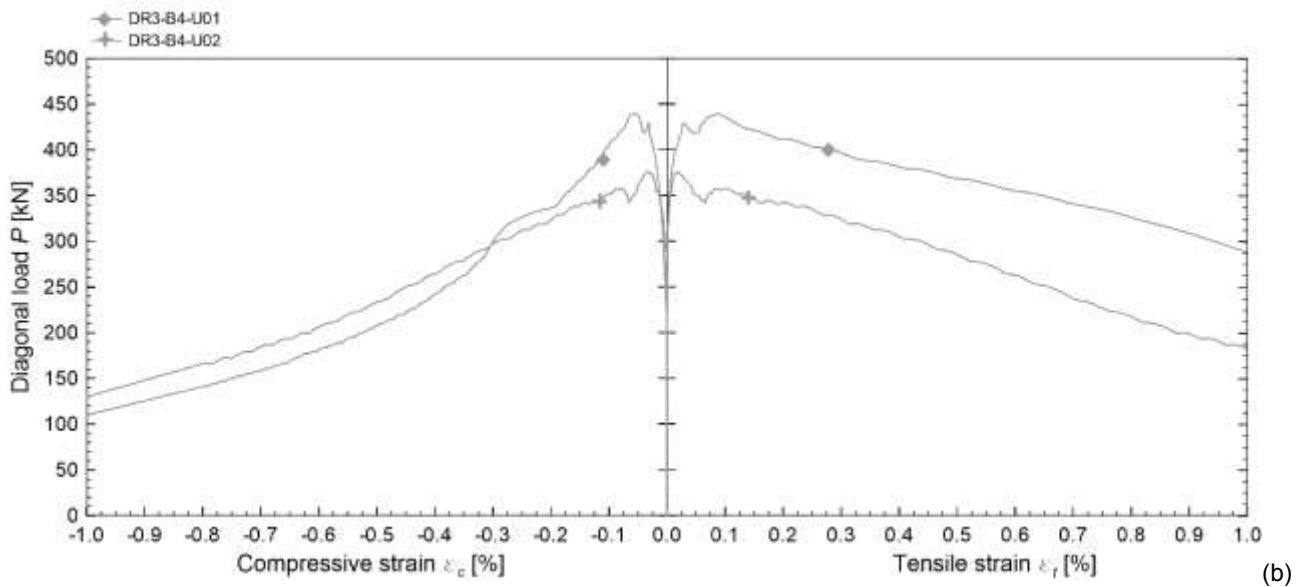
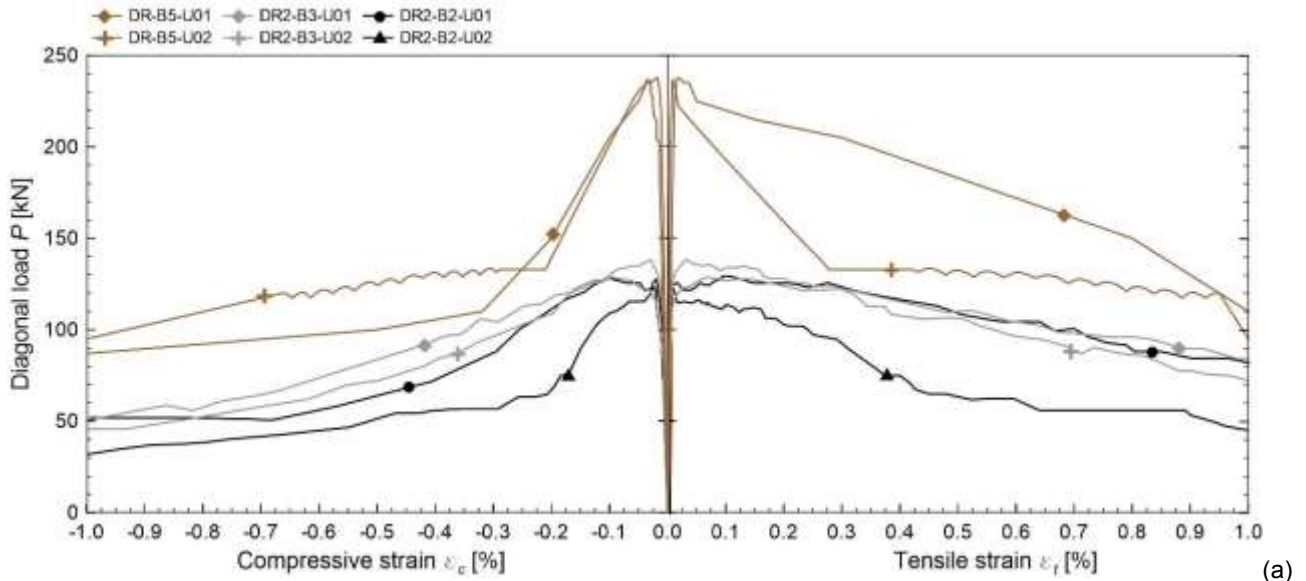
34 diagonal compression tests on unreinforced and reinforced stone masonry samples were performed. In particular, 8 tests concerned 400mm thick rubble stone masonry DR (average units dimension 130x230x200 mm<sup>3</sup>), 12 tests concerned 400mm thick rubble stone masonry DR2 (average units dimension 90x160x200 mm<sup>3</sup>), 6 tests considered 700mm thick rubble stone masonry DR3 (average units dimension 130x230x200 mm<sup>3</sup>) and 8 cobblestones masonry C.

Investigations on DR samples referred to three different types of mortar coating, assuming a 66x66S GFRP mesh reinforcement. Differently, in DR2 reinforced samples, the characteristics of the mortar coating were maintained constant, while a variation in both the masonry mortar (B3 or B2) and in the reinforcement (33x33S, 66x66S and 66x66D GFRP meshes) were investigated. Two different mortar plasters and both 66x66S and 66x66D GFRP meshes were applied on DR3 reinforced panels; B2 and B1 masonry mortars were considered for cobblestones specimens. A couple of unreinforced samples was tested for each typology, for comparison.

Unreinforced stone specimens manifested an approximately linear trend up to the formation of a diagonal crack along the force direction. Then, even if a stiffness reduction was noted, the load still continue to increase. Afterwards, the progressive spread and opening of other cracks along the force direction occurred; however, the samples did not show any sudden drop of the load, after peak, but a gradual decrease in resistance as the deformation increased (Figure 4.26). This behavior was due to the irregular shape of the stone units, which generated an important

interlocking effect, contrasting effectively the crack opening. According to the unit dimensions and nature, this effect resulted less marked in rubble stone masonry DR and DR3 (Figure 4.27.a and Figure 4.27.c), while more pronounced in rubble stone DR2 and cobblestones DC specimens (Figure 4.27.b and Figure 4.27.d). The cracks involved for the most the mortar joints (in particular, the mortar-blocks interface) and affected the whole masonry thickness.

By comparing the results in terms of peak resistance, it emerged that the greater was the masonry mortar resistance, the higher values of both masonry shear modulus and resistance were attained (DR2-B3 / DR2-B2 and DC-B2 / DC-B1).



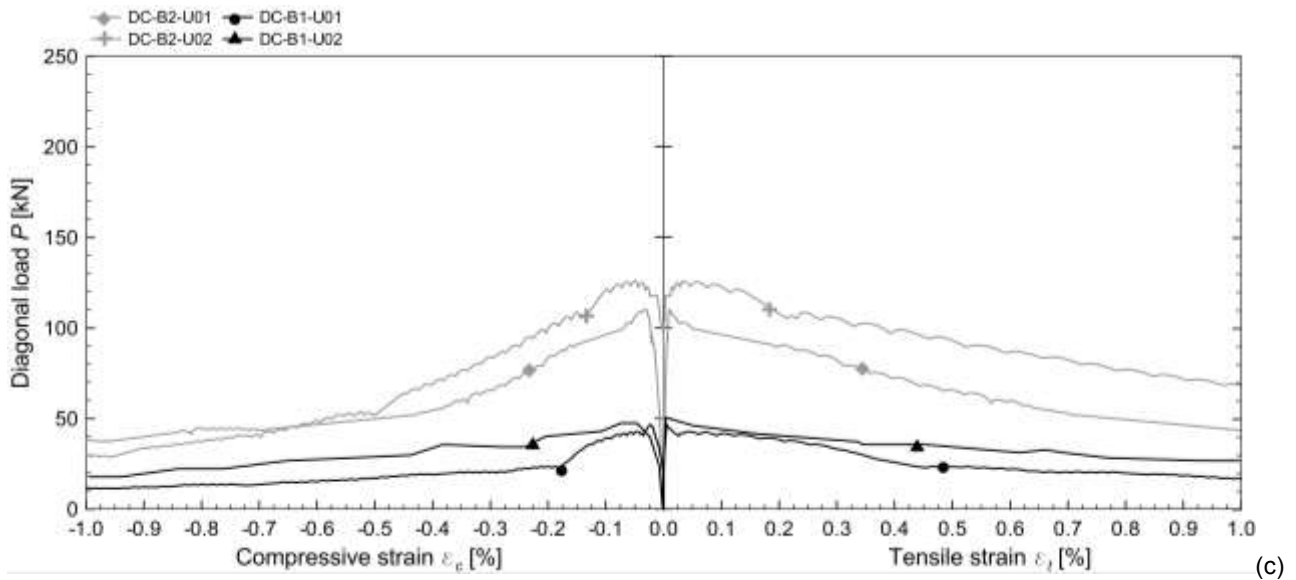


Figure 4.26 –  $P$ - $\varepsilon_c$  and  $P$ - $\varepsilon_t$  envelope curves of unreinforced stone masonry samples: (a) DR and DR2, (b) DR3 and (c) DC

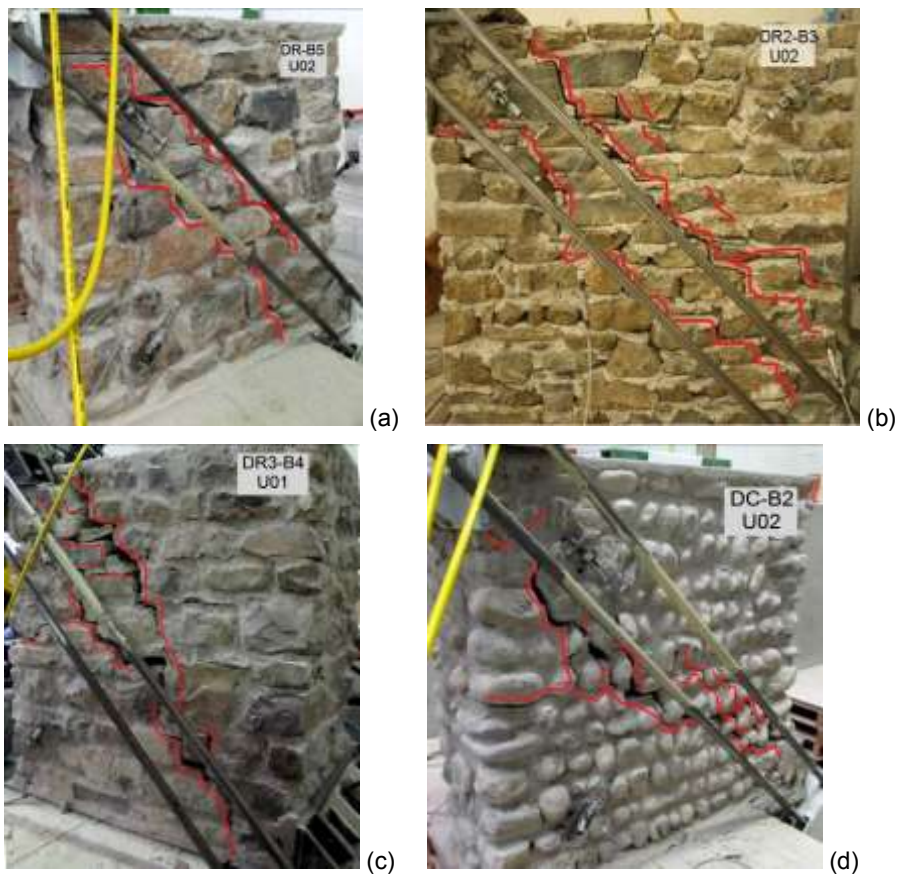
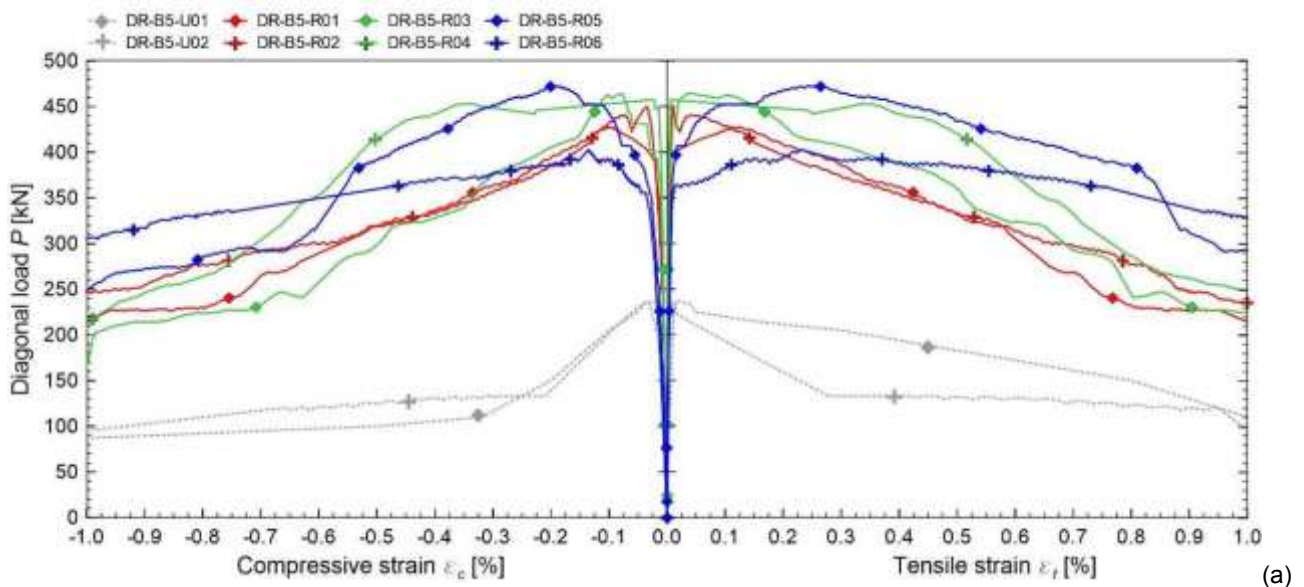


Figure 4.27 – Examples of typical crack patterns in unreinforced stone masonry samples at the end of the diagonal compression test: (a) DR-B5-U02, (b) DR2-B3-U02, (c) DR3-B4-U01 and (D) DC-B2-U02

The  $P-\varepsilon_c$  and  $P-\varepsilon_t$  curves concerning reinforced rubble stone and cobblestones masonry specimens are plotted, respectively, in Figure 4.28 and Figure 4.29. The behavior of unreinforced samples is also reported, for comparison. According to the performances of solid brick specimens, also in reinforced stone masonry samples a diagonal crack formed in the mortar coating, in the force direction, just before reaching the maximum diagonal force. Gradually, the crack opening increased and the cracking zone spread with the formation of other cracks. The cracking of the masonry, inspected at the end of the tests, showed the same trend evidenced in unreinforced specimens. The GFRP mesh intervened in the cracked areas of the mortar coating, contrasting the opening of cracks until collapsing (GFRP wires rupture in the central panel area started at  $\varepsilon_t \cong 0.6-0.7\%$ ); this resulted in a gradual and moderate decrease of the resistance in the post-peak branch. No evident out-of-plane swellings or masonry – plaster slips emerged. However, at high deformations levels ( $\varepsilon_t > 0.9-1.0\%$ ), an extensive damage of the mortar among cracks emerged along the compressed diagonal, resulting in local detachments of mortar portions covering the GFRP mesh.

Notable stiffness and resistance improvements emerged in reinforced masonry samples, in respect to unreinforced ones: in particular, the peak load resulted on average 1.7 (C.o.v. 8%) and 1.9 (C.o.v. 9%) times that of unreinforced masonry for DR3 and DR, respectively, and reached 3.2 times (C.o.v. 8%) in DR2. For cobblestones samples, the average ratio  $P_{M(R)}/P_{M(U)}$  was 3.2 (C.o.v. 1%) for DC-B2 and 4.5 (C.o.v. 6%) for DC-B1. Moreover, the presence of the GFRP mesh permitted to maintain the good deformation capacities of unreinforced stone masonry panels.



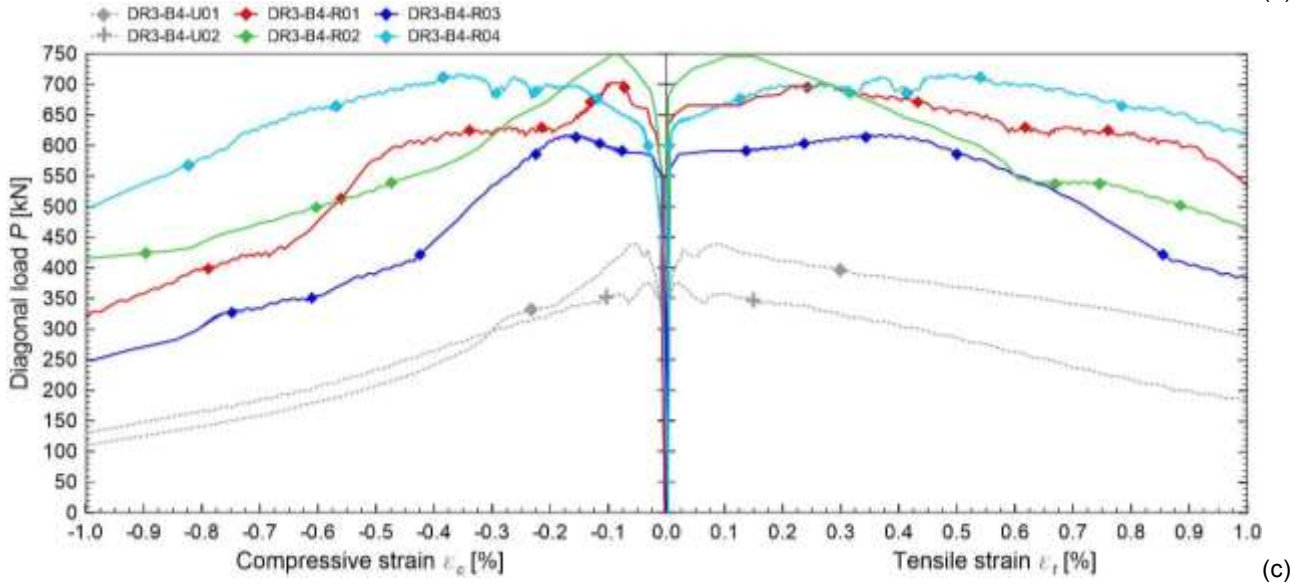
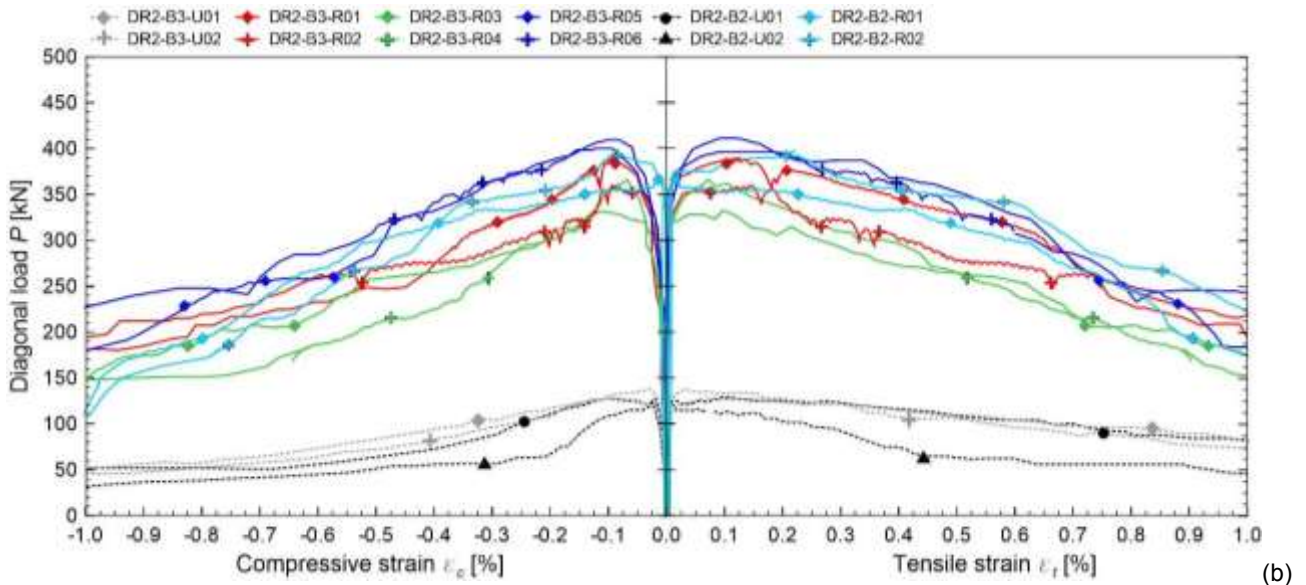


Figure 4.28 – Comparison between  $P-\varepsilon_c$  and  $P-\varepsilon_t$  envelope curves concerning rubble stones samples

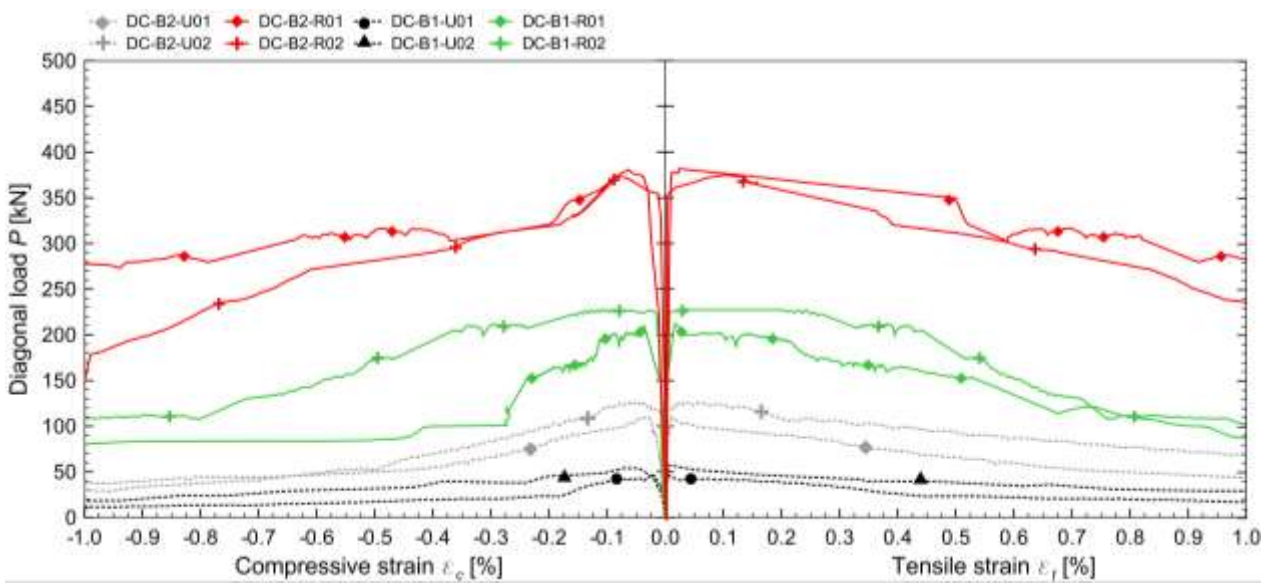


Figure 4.29 – Comparison between  $P-\varepsilon_c$  and  $P-\varepsilon_t$  envelope curves concerning cobblestones samples DC

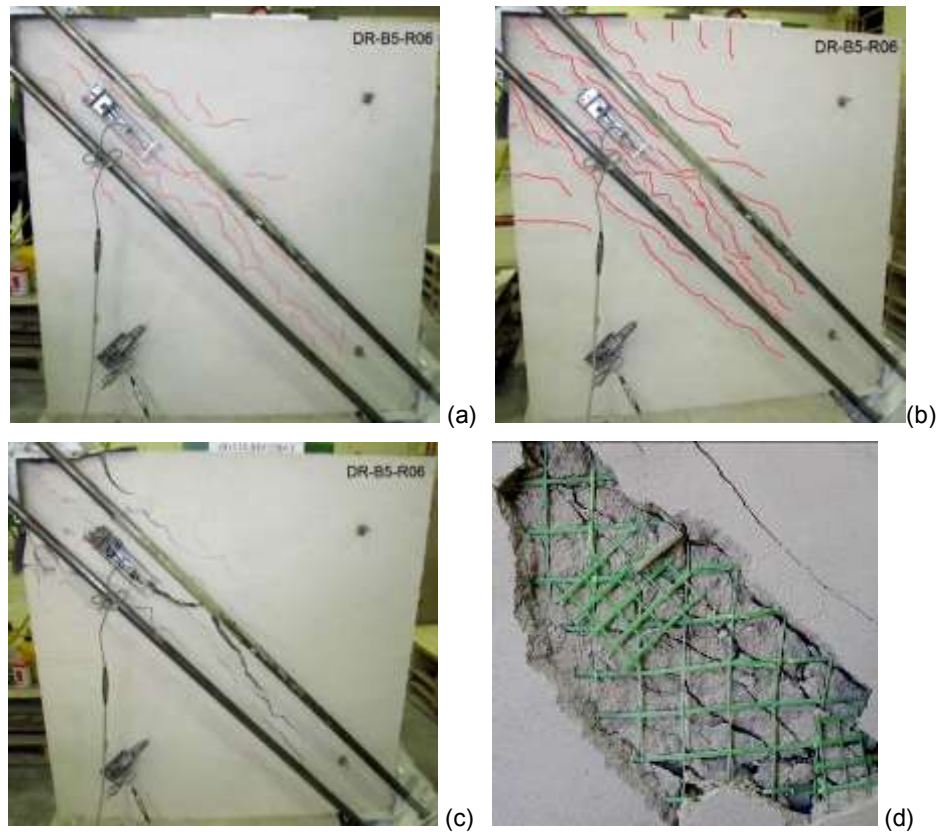


Figure 4.30 – Example of typical crack pattern evolution in a reinforced stone masonry specimen (sample DR-B5-R06): (a) at  $\varepsilon_c = 0.3\%$ , (b)  $\varepsilon_c = 0.5\%$ , and (c)  $\varepsilon_c = 1.1\%$  and (d) detail of the GFRP mesh rupture at the end of the test, after removing some pieces of the cracking mortar

It is observed that a difference in the reinforcement embedded in the mortar coating, as experimented for DR2-B3 masonry, resulted in a variation of the deformation capacities of the samples. In particular, the presence of a 66x66D GFRP mesh, instead of a 66x66S one, improved the post-peak performances of the reinforced masonry. A 33x33S GFRP mesh (Figure 4.31.a) did not permit to attain to the same performances of the 66x66D mesh (Figure 4.31.b), because of the premature delamination of the mortar covering the mesh (as evidenced in solid brick reinforced samples), due to the excessive weakening of the mortar layer in correspondence of the embedded reinforcement plane. This delamination did not permit the exploitation of the whole resistant contribution of the GFRP wires crossing the cracks, which became ineffective as no longer retained by the mortar cover (see also subsection 3.3.4).

However, also the reinforcement by means of 66x66D GFRP meshes incurred sometimes in a premature plaster delamination before the wires rupture ( $\varepsilon_c \cong 0.3\%$ ) in 700 mm thick rubble stone samples (DR3-B4-R02, Figure 4.31.c), where higher diagonal compression loads were attained. This induced results almost comparable to that provided by the 66x66S GFRP mesh reinforced sample (DR3-R4-R01, Figure 4.31.d). Differently, in DR3-B4-R04, the mortar coating delamination

occurred at higher deformation levels ( $\varepsilon_c \cong 0.6-0.7\%$ ), thus the resistance degradation resulted more gradual than that of DR3-B4-R03 sample.

Comparing the results of DR, DR2 and DC, it emerged an higher effectiveness of the technique for weaker masonry.

Not significant differences attributable to the different plaster applied seems to emerge in the results of DR-B5 reinforced samples. However, some differences in the interaction with the GFRP mesh may arise in the degradation branch and further investigation are necessary (e.g. tensile and bond characterization tests).

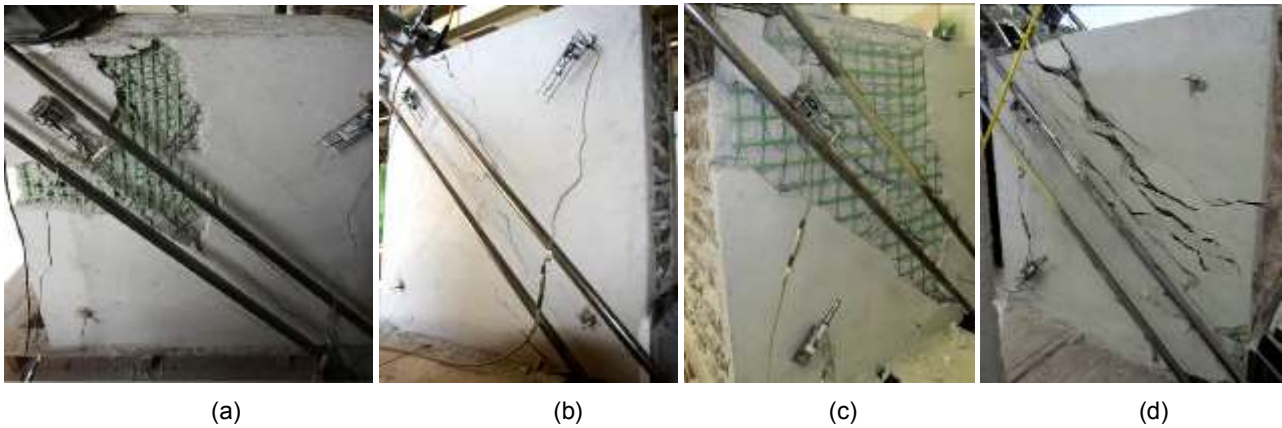


Figure 4.31 – Comparison among stone masonry specimens enhanced by means of (a) 33x33S and (b) 66x66D GFRP meshes, for 400 mm thick masonry, and by means of (c) 66x66D and (d) 66x66S GFRP meshes, for 700 mm thick samples

#### 4.1.5 Interpretation of the results

The diagonal compression tests permitted to assess the principal tensile strength of the specimens. In particular, reference was made to the stress state obtained by Frocht (1931) through a photoelastic model in the hypothesis of a continuous, elastic, homogeneous and isotropic material. In that study emerged that the stress state in the center of the panel is not of pure shear. In fact, the principal tensile stress  $\sigma_I$ , in the direction orthogonal to that of the compressed diagonal can be calculated through equation ( 4.6 ) and the principal compressive stress  $\sigma_{III}$ , in the direction parallel to that of the compressed diagonal, by means of equation ( 4.7 ):

$$\sigma_I = 0.52 \frac{P}{bt} \quad (4.6)$$

$$\sigma_{III} = -1.68 \frac{P}{bt} \quad (4.7)$$

where  $P$  is the diagonal compressive load,  $b$  and  $t$  the width and the thickness of the panel, respectively. It thus results that, in the centre of the panel,  $\sigma_1$  is equal to  $-3.2\sigma_{III}$ .

The values obtained by Frocht (1931) are also confirmed with a good approximation by the results of some numerical simulations (Yokel & Fattal, 1975 - Figure 4.32). Yokel & Fattal (1975) evidenced also that both Poisson's Ratio and elastic orthotropy do not affect significantly the solution.

A Mohr Circle representation of the corresponding stress state is illustrated in Figure 4.33.

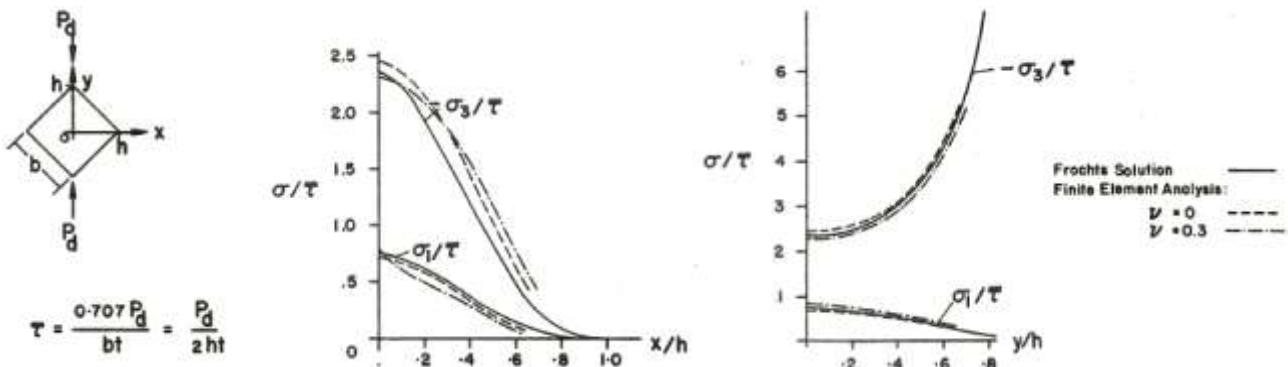


Figure 4.32 – Elastic stress on a square plate loaded by diagonal load: comparison between the Frocht's solution and numerical results (Yokel & Fattal, 1975)

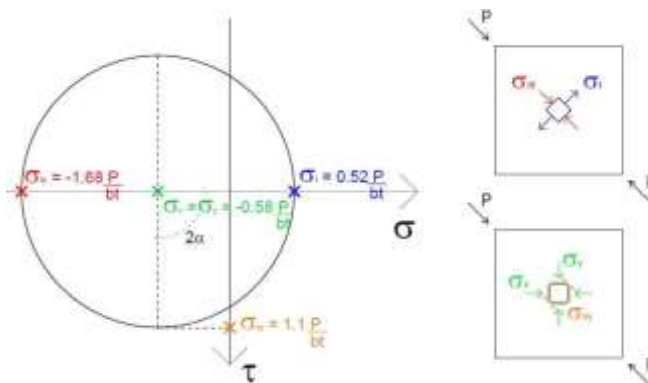


Figure 4.33 - Representation of the stress state at the centre of the panel in the Mohr's circle

The described approach was applied to the results of diagonal compression tests. In particular, by considering the masonry as a continuum and assuming, in a simplified way, both reinforced and unreinforced masonry as equivalent homogeneous materials, the values of the diagonal tensile strength  $f_t$  of the different specimens were calculated according to Equation ( 4.8 ):

$$f_t \cong 0.5 \frac{P_m}{bt} \tag{ 4.8 }$$

The values were reported in Table 4.14-Table 4.18. The unreinforced masonry thickness was considered in the calculations also for reinforced masonry.

It is worth note that the value of  $f_t$  calculated through Equation ( 4.8 ) corresponds to the tensile strength of masonry associated to a ratio between the principle stresses  $\sigma/\sigma_{III}$  equal to -3.2 - Equations ( 4.6 ) and ( 4.7 ) - and referred to a loading direction angle of  $45^\circ$  with respect to the orientation of the bed joints.

A recent study by Brignola et al. (2009), based on experimental tests and numerical nonlinear simulations, evidenced that the assessment of the tensile resistance by using the results of diagonal compression tests is function of the type of masonry. In fact, while in solid brick masonry the maximum diagonal load is reached approximately when the masonry cracks at the center of the sample, in rubble stone masonry a relevant redistribution of the stresses due to the interlocking effect occurs in the specimen, resulting in a further appreciable increase of the diagonal load after the local failure at the center of the specimen. Thus, to evaluate the principal tensile strength associated to this local crack, a coefficient lower than 0.5 has to be used in Equation ( 4.8 ) for stone masonry (in particular, a value of 0.4 is suggested for simple stone masonry, 0.35 for rubble stone masonry).

However, with the aim to estimate the average equivalent principle tensile strength of the masonry associated to the maximum load, the value 0.5 used in Equation ( 4.8 ) results more appropriate, so to consider the additional contribution to the global resistance due to the interlocking effect.

Also to estimate the average equivalent principle tensile strength associated to the maximum load of RM specimens, the value 0.5 is here utilized. In fact, the experimental tests evidenced after the local damage (first crack) of the plaster a further increase of the diagonal load, due to the presence of the GFRP mesh that determinates a stress redistribution.

Table 4.14 – Evaluation on the equivalent principal tensile tests  $f_t$  from the peak load  $P_m$  obtained from diagonal compression tests for solid brick masonry samples, 250 mm thick (S) and calculation of the masonry shear strength  $\tau_0$

ID	$P_m$ [kN]	$f_t$ [MPa]	$\tau_0$ [MPa]
DS-B3-U01	214.2	0.37	0.25
DS-B3-U02	169.5	0.29	0.19
DS-B3-U03	228.2	0.39	0.26
DS-B3-U04	254.5	0.44	0.29
DS-B3-U05	179.9	0.31	0.21
DS-B3-U06	257.7	0.44	0.30
DS-B3-R01	389.4	0.67	0.45
DS-B3-R02	371.7	0.64	0.43
DS-B3-R03	372.5	0.64	0.43
DS-B3-R04	419.8	0.72	0.48
DS-B3-R05	423.0	0.73	0.49
DS-B3-R06	400.3	0.69	0.46
DS-B3-R11	363.4	0.63	0.42
DS-B3-R12	355.2	0.61	0.41
DS-B3-R13	315.9	0.54	0.36
DS-B3-R14	332.4	0.57	0.38
DS-B3-R15	312.9	0.54	0.36
DS-B3-R16	336.2	0.58	0.39
DS-B3-R17	424.1	0.73	0.49
DS-B3-R18	419.5	0.72	0.48

ID	$P_m$ [kN]	$f_t$ [MPa]	$\tau_0$ [MPa]
DS-B3-R19	401.5	0.69	0.46
DS-B3-R22	345.3	0.60	0.40
DS-B3-R23	400.1	0.69	0.46
DS-B3-R24	404.3	0.70	0.46
DS-B3-R25	494.8	0.85	0.57
DS-B3-R26	493.1	0.85	0.57
DS-B3-R27	540.6	0.93	0.62
DS-B3-R28	556.6	0.96	0.64
DS-B3-R29	574.5	0.99	0.66
DS-B3-R30	603.0	1.04	0.69
DS-B3-R31	384.0	0.66	0.44
DS-B3-R32	350.6	0.60	0.40
DS-B6-U01	275.1	0.47	0.32
DS-B6-U02	238.8	0.41	0.27
DS-B6-R01	420.8	0.73	0.48
DS-B6-R02	412.9	0.71	0.47
DS-B6-R03	474.6	0.82	0.55
DS-B6-R04	506.0	0.87	0.58
DS-B6-R05	469.6	0.81	0.54
DS-B6-R06	539.7	0.93	0.62

Table 4.15 – Evaluation on the equivalent principal tensile tests  $f_t$  from the peak load  $P_m$  obtained from diagonal compression tests for solid brick masonry samples, 380 mm thick (S2) and calculation of the masonry shear strength  $\tau_0$

ID	$P_m$ [kN]	$f_t$ [MPa]	$\tau_0$ [MPa]
DS2-B3-U01	258.9	0.29	0.20
DS2-B3-U02	312.6	0.35	0.24
DS2-B3-R01	478.8	0.54	0.36
DS2-B3-R02	478.1	0.54	0.36
DS2-B3-R03	530.4	0.60	0.40
DS2-B3-R04	434.6	0.49	0.33
DS2-B3-R05	548.3	0.62	0.41
DS2-B3-R06	575.4	0.65	0.44
DS2-B3-R07	457.3	0.52	0.35
DS2-B3-R08	414.4	0.47	0.31
DS2-B2-U01	242.7	0.28	0.18
DS2-B2-U02	286.0	0.32	0.22
DS2-B2-R01	413.9	0.47	0.31
DS2-B2-R02	315.7	0.36	0.24

Table 4.16 – Evaluation on the equivalent principal tensile tests  $f_t$  from the peak load  $P_m$  obtained from diagonal compression tests for infill solid brick masonry samples (I) and calculation of the masonry shear strength  $\tau_0$

ID	$P_m$ [kN]	$f_t$ [MPa]	$\tau_0$ [MPa]
DI-B3-U01	221.9	0.25	0.17
DI-B3-U02	202.6	0.23	0.15
DI-B3-R01	354.7	0.40	0.27
DI-B3-R02	338.9	0.38	0.26
DI-B3-R03	370.5	0.42	0.28
DI-B3-R04	309.6	0.35	0.23
DI-B2-U01	207.5	0.24	0.16
DI-B2-U02	200.4	0.23	0.15
DI-B2-R01	285.2	0.32	0.22
DI-B2-R02	301.1	0.34	0.23
DI-B2-R03	249.9	0.28	0.19
DI-B2-R04	252.8	0.29	0.19

Table 4.17 – Evaluation on the equivalent principal tensile tests  $f_t$  from the peak load  $P_m$  obtained from diagonal compression tests for rubble stone masonry samples (R, R2 and R3) and calculation of the masonry shear strength  $\tau_0$

ID	$P_m$ [kN]	$f_t$ [MPa]	$\tau_0$ [MPa]
DR-B5-U01	238.0	0.26	0.17
DR-B5-U02	236.9	0.26	0.17
DR-B5-R01	427.6	0.46	0.31
DR-B5-R02	449.6	0.48	0.32
DR-B5-R03	464.6	0.50	0.33
DR-B5-R04	457.6	0.49	0.33
DR-B5-R05	473.4	0.51	0.34
DR-B5-R06	402.8	0.43	0.29
DR2-B3-U01	126.4	0.14	0.09
DR2-B3-U02	135.7	0.15	0.10
DR2-B3-R01	388.0	0.42	0.28
DR2-B3-R02	360.0	0.39	0.26
DR2-B3-R03	331.9	0.36	0.24
DR2-B3-R04	366.4	0.39	0.26
DR2-B3-R05	410.7	0.44	0.30
DR2-B3-R06	398.2	0.43	0.29

ID	$P_m$ [kN]	$f_t$ [MPa]	$\tau_0$ [MPa]
DR2-B2-U01	117.2	0.13	0.08
DR2-B2-U02	115.0	0.12	0.08
DR2-B2-R01	368.9	0.40	0.27
DR2-B2-R02	393.0	0.42	0.28
DR3-B4-U01	439.5	0.27	0.18
DR3-B4-U02	376.0	0.23	0.15
DR3-B4-R01	702.1	0.43	0.29
DR3-B4-R02	749.5	0.46	0.31
DR3-B4-R03	617.4	0.38	0.25
DR3-B4-R04	717.1	0.44	0.29

Table 4.18 – Evaluation on the equivalent principal tensile tests  $f_t$  from the peak load  $P_m$  obtained from diagonal compression tests for cobblestones masonry samples (C) and calculation of the masonry shear strength  $\tau_o$

ID	$P_m$ [kN]	$f_t$ [MPa]	$\tau_o$ [MPa]
DC-B2-U01	110.4	0.12	0.08
DC-B2-U02	126.0	0.14	0.09
DC-B2-R01	379.4	0.41	0.27
DC-B2-R02	371.5	0.40	0.27
DC-B1-U01	46.7	0.05	0.03
DC-B1-U02	49.8	0.05	0.04
DC-B1-R01	209.2	0.23	0.15
DC-B1-R02	227.4	0.25	0.16

The estimation of the diagonal tensile strengths permitted a comparison between DS-B3 and DS2-B3 samples and also between DR-B5 and DR3-B4 samples, evidencing a similar value of diagonal tensile strength for the unreinforced masonry. This indicates, for the considered masonry, that the tensile strength is not significantly influenced by the masonry thickness.

Moreover, some observations can be made from the analysis of the results of reinforced samples. In particular, in Figure 4.34, the curves representing the trend of the equivalent principal tensile stress - calculated through Equation ( 4.6 ) - at the varying of the diagonal strains are plotted. From Figure 4.34.a emerged quite higher peak and post peak values of tensile stress for the 250 mm thick solid brick masonry (DS-B3), in respect to 380 mm thick one (DS2-B3). Similarly, in Figure 4.34.b, the performances of the 400 mm thick rubble stone masonry (DR-B5) resulted a little better than those of the 700 mm thick one (DR3-B4). It can thus be deduced that the effectiveness of the reinforcement technique tended to decrease with increasing the masonry thickness, because of the lower incidence of both the mortar coating and the GFRP mesh.

In Figure 4.34.a the curves of DI-B3 reinforced specimens are also reported. It is observed that the performances of the infill masonry samples are considerably reduced in respect to those of DS2-B3 samples, evidencing the negligible contribution of the conglomerate filling. Moreover, referring the equivalent principal tensile stresses to the two single wythe masonry layers (assuming, thus,  $t = 250$  mm), the stress-strain diagrams (dotted lines) are comparable to those of DS2-B3 reinforced samples.

It is worth note, once again, that the evaluated equivalent principal tensile stresses are based on the simplified assumption of an equivalent, fictitious homogeneous, isotropic material. Actually, a significant redistribution on the tensile stresses (both in amount and orientation), due to cracking, occurred in the panel.

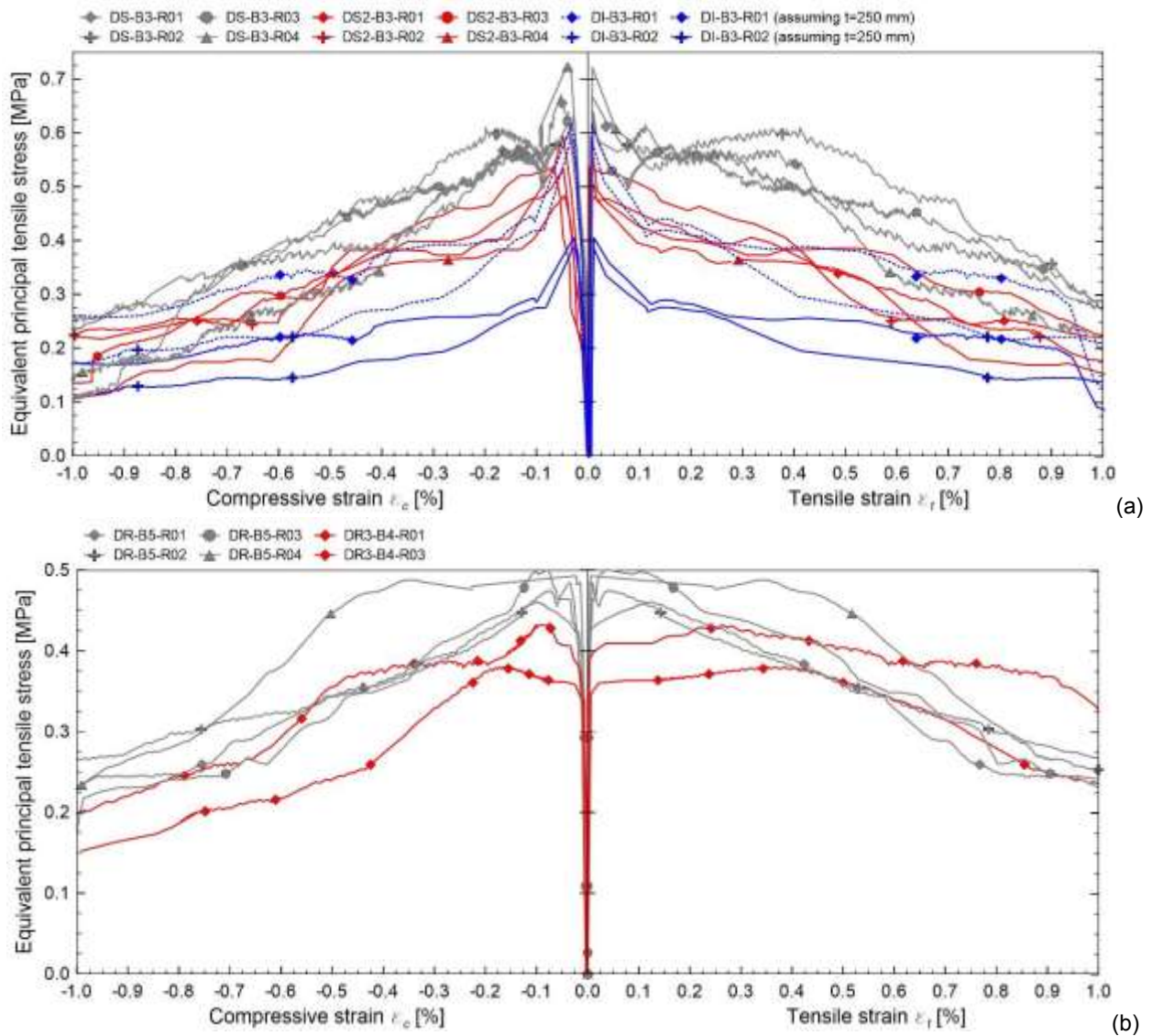


Figure 4.34 – Curves representing the equivalent principal tensile stress at the varying of the diagonal strains  $\varepsilon_c$ - $\varepsilon_t$ : comparison between some reinforced samples made of (a) solid brick and (b) rubble stone masonry

The value of the equivalent principal tensile strength deduced from diagonal compression tests was adopted by several authors (es. Tubi, 1993; Calderoni B, 1996; Borri & al., 2015b) for the evaluation of the masonry referential shear strength without normal stresses  $\tau_0$  ( 4.9 ). The coefficient 1.5 in Equation ( 4.9 ) takes into account for the variability of the shear stresses distribution in the panel (according to the Jourawsky's approximate solution for shear in rectangular section). The value of  $\tau_0$  is currently adopted for the evaluation of the shear strength of masonry walls subjected to the combined action of horizontal and axial loads, according to the Turnsek & Cacovic approach (1971).

$$\tau_0 = \frac{f_t}{1.5} \quad (4.9)$$

The values of  $\tau_0$  calculated for the different masonry sample subjected to diagonal compression tests are reported in Table 4.14-Table 4.18.

## 4.2 Analytical estimations

A first analytical evaluation was performed on the shear modulus of the reinforced masonry panels  $G_{(R)}$ , which was evaluated as the weighted sum of that of unreinforced masonry,  $G_{(U)}$ , and that of the mortar coating  $G_c$ , assuming no-slip between the masonry layer and the mortar coating and neglecting the contribution of the GFRP mesh:

$$G_{(R)} = G_{(U)} + G_c \cdot \frac{2t_c}{t} \quad (4.10)$$

being  $t$  and  $t_c$  the masonry and the coating thicknesses, respectively.

The mortar coating shear modulus  $G_c$  was deduced from the mortar Young modulus  $E_c$ , assuming a Poisson modulus  $\nu = 0.2$  and applying the well know relationship:

$$G_c = \frac{E_c}{2(1+\nu)} \quad (4.11)$$

The calculated values of  $G_{(R)}$  (suffix “calc”) were compared with the experimental ones (suffix “exp”) in Table 4.19-Table 4.23 and in Figure 4.35. Quite good predictions generally emerged, considering the scatter of the experimental results.

Table 4.19 – Analytical evaluation of the shear modulus concerning reinforced solid brick masonry samples, 250 mm thick (S) tested to diagonal compression: experimental shear modulus of reinforced ( $G_{(R),exp}$ ) and unreinforced ( $G_{(U)}$ ) samples, mortar shear modulus ( $G_c$ ), calculated shear modulus of reinforced samples ( $G_{(R),calc}$ ) and error percentage between  $G_{(R),calc}$  and  $G_{(R),exp}$  ( $\Delta_{err}$ )

ID	$G_{(R),exp}$ [MPa]	$G_{(U)}$ [MPa]	$G_c$ [MPa]	$G_{(R),calc}$ [MPa]	$\Delta_{err}$ [%]	ID	$G_{(R),exp}$ [MPa]	$G_{(U)}$ [MPa]	$G_c$ [MPa]	$G_{(R),calc}$ [MPa]	$\Delta_{err}$ [%]
DS-B3-R01	3563	2325	5958	3755	5%	DS-B3-R23	4067	2325	7391	4099	1%
DS-B3-R02	3398	2325	5958	3755	11%	DS-B3-R24	4065	2325	7391	4099	1%
DS-B3-R03	3063	2325	5958	3755	23%	DS-B3-R25	3819	2325	5594	3668	-4%
DS-B3-R04	3228	2325	5958	3755	16%	DS-B3-R26	3692	2325	5594	3668	-1%
DS-B3-R05	2923	2325	5958	3755	28%	DS-B3-R27	3509	2325	4958	3515	0%
DS-B3-R06	2982	2325	5958	3755	26%	DS-B3-R28	3406	2325	4958	3515	3%
DS-B3-R11	3799	2325	5750	3705	-2%	DS-B3-R29	4060	2325	9719	4658	15%
DS-B3-R12	3797	2325	5750	3705	-2%	DS-B3-R30	4615	2325	9719	4658	1%
DS-B3-R13	3428	2325	6000	3765	10%	DS-B3-R31	3508	2325	6000	3765	7%
DS-B3-R14	3534	2325	6000	3765	7%	DS-B3-R32	3415	2325	6000	3765	10%
DS-B3-R15	3025	2325	2513	2928	-3%	DS-B6-R01	5257	3419	5958	4849	-8%
DS-B3-R16	2934	2325	2513	2928	0%	DS-B6-R02	5073	3419	5958	4849	-4%
DS-B3-R17	3824	2325	6003	3766	-2%	DS-B6-R03	4723	3419	5958	4849	3%
DS-B3-R18	4033	2325	6003	3766	-7%	DS-B6-R04	4842	3419	5958	4849	0%
DS-B3-R19	3178	2325	3210	3095	-3%	DS-B6-R05	4451	3419	5958	4849	9%
DS-B3-R22	3622	2325	5583	3665	1%	DS-B6-R06	4574	3419	5958	4849	6%

Table 4.20 – Analytical evaluation of the shear modulus concerning reinforced solid brick masonry samples, 380 mm thick (S2) tested to diagonal compression: experimental shear modulus of reinforced ( $G_{(R),exp}$ ) and unreinforced ( $G_{(U)}$ ) samples, mortar shear modulus ( $G_c$ ), calculated shear modulus of reinforced samples ( $G_{(R),calc}$ ) and error percentage between  $G_{(R),calc}$  and  $G_{(R),exp}$  ( $\Delta_{err}$ )

ID	$G_{(R),exp}$ [MPa]	$G_{(U)}$ [MPa]	$G_c$ [MPa]	$G_{(R),calc}$ [MPa]	$\Delta_{err}$ [%]
DS2-B3-R01	3925	2598	5958	3539	-10%
DS2-B3-R02	3761	2598	5958	3539	-6%
DS2-B3-R03	3477	2598	5958	3539	2%
DS2-B3-R04	3534	2598	5958	3539	0%
DS2-B3-R05	4106	2598	5958	3539	-14%
DS2-B3-R06	4409	2598	5958	3539	-20%
DS2-B3-R07	3988	2598	5958	3539	-11%
DS2-B3-R08	3980	2598	5958	3539	-11%
DS2-B2-R01	2793	1804	5958	2744	-2%
DS2-B2-R02	2860	1804	5958	2744	-4%

Table 4.21 – Analytical evaluation of the shear modulus concerning reinforced infill solid brick masonry samples (I) tested to diagonal compression: experimental shear modulus of reinforced ( $G_{(R),exp}$ ) and unreinforced ( $G_{(U)}$ ) samples, mortar shear modulus ( $G_c$ ), calculated shear modulus of reinforced samples ( $G_{(R),calc}$ ) and error percentage between  $G_{(R),calc}$  and  $G_{(R),exp}$  ( $\Delta_{err}$ )

ID	$G_{(R),exp}$ [MPa]	$G_{(U)}$ [MPa]	$G_c$ [MPa]	$G_{(R),calc}$ [MPa]	$\Delta_{err}$ [%]
DI-B3-R01	1699	1108	5958	2048	21%
DI-B3-R02	1750	1108	5958	2048	17%
DI-B3-R03	1629	1108	5958	2048	26%
DI-B3-R04	1580	1108	5958	2048	30%
DI-B2-R01	1577	791	5958	1732	10%
DI-B2-R02	1670	791	5958	1732	4%
DI-B2-R03	1528	791	5958	1732	13%
DI-B2-R04	1515	791	5958	1732	14%

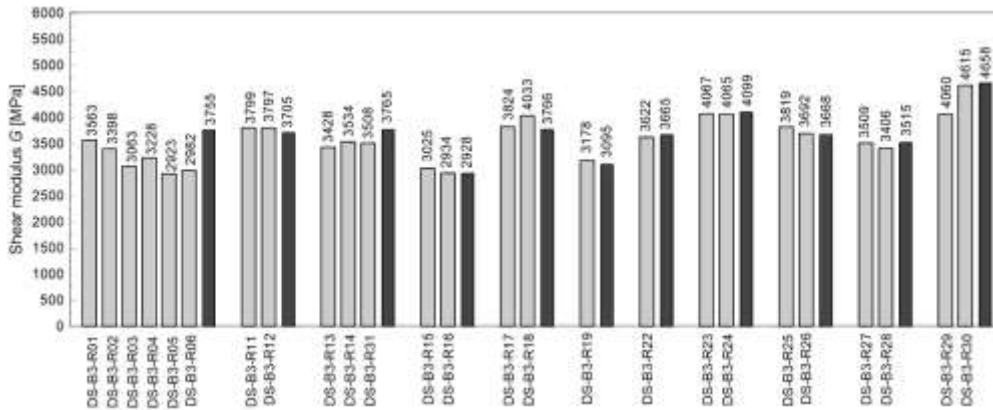
Table 4.22 – Analytical evaluation of the shear modulus concerning reinforced rubble stone masonry samples (R, R2 and R3) tested to diagonal compression: experimental shear modulus of reinforced ( $G_{(R),exp}$ ) and unreinforced ( $G_{(U)}$ ) samples, mortar shear modulus ( $G_c$ ), calculated shear modulus of reinforced samples ( $G_{(R),calc}$ ) and error percentage between  $G_{(R),calc}$  and  $G_{(R),exp}$  ( $\Delta_{err}$ )

ID	$G_{(R),exp}$ [MPa]	$G_{(U)}$ [MPa]	$G_c$ [MPa]	$G_{(R),calc}$ [MPa]	$\Delta_{err}$ [%]
DR-B5-R01	2513	1705	5750	2567	2%
DR-B5-R02	2269	1705	5750	2567	13%
DR-B5-R03	2560	1705	6000	2605	2%
DR-B5-R04	2779	1705	6000	2605	-6%
DR-B5-R05	2588	1705	5583	2542	-2%
DR-B5-R06	2895	1705	5583	2542	-12%
DR2-B3-R01	1365	767	5958	1660	22%
DR2-B3-R02	1374	767	5958	1660	21%
DR2-B3-R03	1205	767	5958	1660	38%
DR2-B3-R04	1285	767	5958	1660	29%
DR2-B3-R05	1478	767	5958	1660	12%
DR2-B3-R06	1496	767	5958	1660	11%

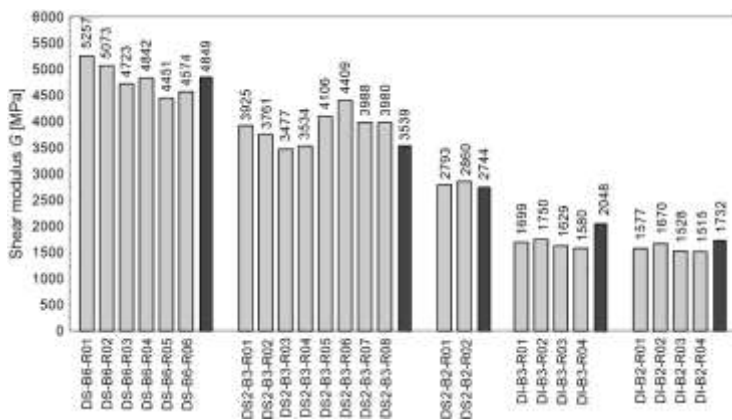
ID	$G_{(R),exp}$ [MPa]	$G_{(U)}$ [MPa]	$G_c$ [MPa]	$G_{(R),calc}$ [MPa]	$\Delta_{err}$ [%]
DR2-B2-R01	1252	720	5958	1613	29%
DR2-B2-R02	1293	720	5958	1613	25%
DR3-B4-R01	2476	1835	6000	2349	-5%
DR3-B4-R02	2187	1835	6000	2349	7%
DR3-B4-R03	2513	1835	5583	2314	-8%
DR3-B4-R04	2264	1835	5583	2314	2%

Table 4.23 – Analytical evaluation of the shear modulus concerning reinforced cobblestones masonry samples (C) tested to diagonal compression experimental shear modulus of reinforced ( $G_{(R),exp}$ ) and unreinforced ( $G_{(U)}$ ) samples, mortar shear modulus ( $G_c$ ), calculated shear modulus of reinforced samples ( $G_{(R),calc}$ ) and error percentage between  $G_{(R),calc}$  and  $G_{(R),exp}$  ( $\Delta_{err}$ )

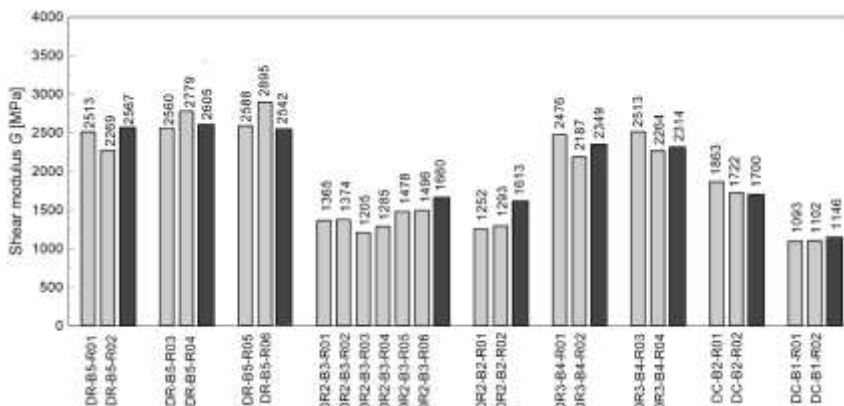
ID	$G_{(R),exp}$ [MPa]	$G_{(U)}$ [MPa]	$G_c$ [MPa]	$G_{(R),exp}$ [MPa]	$\Delta_{err}$ [%]
DC-B2-R01	1863	800	6000	1700	-9%
DC-B2-R02	1722	800	6000	1700	-1%
DC-B1-R01	1093	240	6042	1146	5%
DC-B1-R02	1102	240	6042	1146	4%



(a)



(b)



(c)

Figure 4.35 – Comparisons between experimental values (light grey) and analytical estimations (dark grey) of shear modulus  $G_{(R)}$  of reinforced masonry panels subjected to diagonal compression tests: (a) DS-B3, (b) DS-B6, DS and DI and (c) DR, DR2, DR3 and DC

The analysis of the results of the experimental campaign allowed also to developing analytical formulation for the prediction of the diagonal compression peak resistance of reinforced masonry panels.

Assuming the hypothesis of no-slip between the masonry layer and the mortar coating, at least until the reaching of the peak load, an estimate of the diagonal compression resistance of the reinforced samples was at first conducted by the summation of the average resistance of unreinforced specimens  $P_{m(U)}$  and the resistance of the mortar coating  $P_c$ .

$P_c$  was derived from the tensile strength of mortar  $f_{t,c}$  (Table 4.3) through Equation ( 4.8 ), assuming as  $t$  the thickness of the two layers of plaster ( $2t_c$ ). Due to the low geometrical percentage and modular ratio of the GFRP mesh, its contribution was assumed negligible up to the crack formation in the mortar coating.

Comparing these preliminary analytical values with the experimental results (Table 4.24 - Table 4.28), some observations can be done in terms of error percentage  $\Delta_{err(1)}$ .

In particular, in regard to solid brick samples:

- for DS and DS2 masonry enhanced using C3 mortar, consistent underestimations, ranging from about -10% to -30%, emerged;
- infill masonry (DI) results showed quite good prediction of the experimental resistances in case DI-B3 (mean error -5%) and notable overestimation for DI-B2 ( $\cong +17\%$ );
- considering the results of DS-B3 samples at the varying of the mortar coating type, overestimations generally resulted for weaker plasters and underestimations for stronger ones.

Moreover, referring to stone masonry, it is observed that:

- rubble stone specimens DR2 attained on average to a -36% underestimation;
- very high underestimations resulted also for cobblestones DC-B2 (-28%) and DC-B1 (-43%);
- the results of DR and DR3 rubble stone samples indicate some underestimations (attaining at least to -25%) which however tend to reduce at the improvement of the mortars characteristics.

Then, a modification factor  $\beta$  was defined as the ratio between the experimental resistance of reinforced sample  $P_{m(R),exp}$  and the preliminary analytical prediction ( $P_{m(U)} + P_c$ ):

$$\beta = \frac{P_{m(R),exp}}{(P_{m(U)} + P_c)} \quad ( 4.12 )$$

The values of the  $\beta$  coefficient are reported in Table 4.24-Table 4.28.

Table 4.24 – Analytical evaluation concerning solid brick masonry samples, 250 mm thick (S) tested to diagonal compression: experimental resistance of reinforced ( $P_{m(R),exp}$ ) and unreinforced samples ( $P_{m(U),exp}$ ), calculated diagonal compression resistance of the mortar coating ( $P_c$ ), preliminary analytical prediction of reinforced samples resistance ( $P_{m(U)} + P_c$ ) with error percentage ( $\Delta_{err(1)}$ ), coefficients  $\beta$  and  $\beta^*$  and calculated resistance of reinforced samples ( $P_{m(R),calc}$ ) with error percentage ( $\Delta_{err(2)}$ )

ID	$P_{m(R),exp}$ [kN]	$P_{m(U),exp}$ [kN]	$P_c$ [kN]	$P_{m(U),exp}+P_c$ [kN]	$\Delta_{err(1)}$ [%]	$\beta$ [-]	$\beta^*$ [-]	$P_{m(R),calc}$ [kN]	$\Delta_{err(2)}$ [%]
DS-B3-R01	389.4	217.3	111.4	328.7	-16%	1.18	1.13	372.9	-4%
DS-B3-R02	371.7	217.3	111.4	328.7	-12%	1.13	1.13	372.9	0%
DS-B3-R03	372.5	217.3	111.4	328.7	-12%	1.13	1.13	372.9	0%
DS-B3-R04	419.8	217.3	111.4	328.7	-22%	1.28	1.13	372.9	-11%
DS-B3-R05	423.0	217.3	111.4	328.7	-22%	1.29	1.13	372.9	-12%
DS-B3-R06	400.3	217.3	111.4	328.7	-18%	1.22	1.13	372.9	-7%
DS-B3-R11	363.4	217.3	107.2	324.5	-11%	1.12	1.17	380.2	5%
DS-B3-R12	355.2	217.3	107.2	324.5	-9%	1.09	1.17	380.2	7%
DS-B3-R13	315.9	217.3	153.1	370.5	17%	0.85	0.92	339.7	8%
DS-B3-R14	332.4	217.3	153.1	370.5	11%	0.90	0.92	339.7	2%
DS-B3-R15	312.9	217.3	167.0	384.4	23%	0.81	0.88	339.2	8%
DS-B3-R16	336.2	217.3	167.0	384.4	14%	0.87	0.88	339.2	1%
DS-B3-R17	424.1	217.3	188.8	406.2	-4%	1.04	0.85	344.3	-19%
DS-B3-R18	419.5	217.3	188.8	406.2	-3%	1.03	0.85	344.3	-18%
DS-B3-R19	401.5	217.3	195.1	412.5	3%	0.97	0.84	346.8	-14%
DS-B3-R22	345.3	217.3	200.4	417.8	21%	0.83	0.84	349.1	1%
DS-B3-R23	400.1	217.3	244.7	462.1	15%	0.87	0.81	375.0	-6%
DS-B3-R24	404.3	217.3	244.7	462.1	14%	0.88	0.81	375.0	-7%
DS-B3-R25	494.8	217.3	390.2	607.6	23%	0.81	0.80	486.2	-2%
DS-B3-R26	493.1	217.3	390.2	607.6	23%	0.81	0.80	486.2	-1%
DS-B3-R27	540.6	217.3	390.7	608.0	12%	0.89	0.80	486.6	-10%
DS-B3-R28	556.6	217.3	390.7	608.0	9%	0.92	0.80	486.6	-13%
DS-B3-R29	574.5	217.3	413.4	630.8	10%	0.91	0.80	504.7	-12%
DS-B3-R30	603.0	217.3	413.4	630.8	5%	0.96	0.80	504.7	-16%
DS-B3-R31	384.0	217.3	153.1	370.5	-4%	1.04	0.92	339.7	-12%
DS-B6-R01	420.8	257.0	111.4	368.3	-12%	1.14	1.28	470.6	12%
DS-B6-R02	412.9	257.0	111.4	368.3	-11%	1.12	1.28	470.6	14%
DS-B6-R03	474.6	257.0	111.4	368.3	-22%	1.29	1.28	470.6	-1%
DS-B6-R04	506.0	257.0	111.4	368.3	-27%	1.37	1.28	470.6	-7%
DS-B6-R05	469.6	257.0	111.4	368.3	-22%	1.27	1.28	470.6	0%
DS-B6-R06	539.7	257.0	111.4	368.3	-32%	1.47	1.28	470.6	-13%

Table 4.25 - Analytical evaluation concerning solid brick masonry samples, 380 mm thick (S2) tested to diagonal compression: experimental resistance of reinforced ( $P_{m(R),exp}$ ) and unreinforced samples ( $P_{m(U),exp}$ ), calculated diagonal compression resistance of the mortar coating ( $P_c$ ), preliminary analytical prediction of reinforced samples resistance ( $P_{m(U)} + P_c$ ) with error percentage ( $\Delta_{err(1)}$ ), coefficients  $\beta$  and  $\beta^*$  and calculated resistance of reinforced samples ( $P_{m(R),calc}$ ) with error percentage ( $\Delta_{err(2)}$ )

ID	$P_{m(R),exp}$ [kN]	$P_{m(U),exp}$ [kN]	$P_c$ [kN]	$P_{m(U),exp}+P_c$ [kN]	$\Delta_{err(1)}$ [%]	$\beta$ [-]	$\beta^*$ [-]	$P_{m(R),calc}$ [kN]	$\Delta_{err(2)}$ [%]
DS2-B3-R01	478.8	285.7	111.4	397.1	-17%	1.21	1.23	489.7	2%
DS2-B3-R02	478.1	285.7	111.4	397.1	-17%	1.20	1.23	489.7	2%
DS2-B3-R03	530.4	285.7	111.4	397.1	-25%	1.34	1.23	489.7	-8%
DS2-B3-R04	434.6	285.7	111.4	397.1	-9%	1.09	1.23	489.7	13%
DS2-B3-R05	548.3	285.7	111.4	397.1	-28%	1.38	1.23	489.7	-11%
DS2-B3-R06	575.4	285.7	111.4	397.1	-31%	1.45	1.23	489.7	-15%
DS2-B3-R07	457.3	285.7	111.4	397.1	-13%	1.15	1.23	489.7	7%
DS2-B3-R08	414.4	285.7	111.4	397.1	-4%	1.04	1.23	489.7	18%
DS2-B2-R01	413.9	264.3	111.4	375.7	-9%	1.10	0.97	364.8	-12%
DS2-B2-R02	315.7	264.3	111.4	375.7	19%	0.84	0.97	364.8	16%

Table 4.26 - Analytical evaluation concerning infill solid brick masonry samples (I) tested to diagonal compression: experimental resistance of reinforced ( $P_{m(R),exp}$ ) and unreinforced samples ( $P_{m(U),exp}$ ), calculated diagonal compression resistance of the mortar coating ( $P_c$ ), preliminary analytical prediction of reinforced samples resistance ( $P_{m(U)} + P_c$ ) with error percentage ( $\Delta_{err(1)}$ ), coefficients  $\beta$  and  $\beta^*$  and calculated resistance of reinforced samples ( $P_{m(R),calc}$ ) with error percentage ( $\Delta_{err(2)}$ )

ID	$P_{m(R),exp}$ [kN]	$P_{m(U),exp}$ [kN]	$P_c$ [kN]	$P_{m(U),exp}+P_c$ [kN]	$\Delta_{err(1)}$ [%]	$\beta$ [-]	$\beta^*$ [-]	$P_{m(R),calc}$ [kN]	$\Delta_{err(2)}$ [%]
DI-B3-R01	354.7	212.3	111.4	323.6	-9%	1.10	1.06	343.4	-3%
DI-B3-R02	338.9	212.3	111.4	323.6	-4%	1.05	1.06	343.4	1%
DI-B3-R03	370.5	212.3	111.4	323.6	-13%	1.14	1.06	343.4	-7%
DI-B3-R04	309.6	212.3	111.4	323.6	5%	0.96	1.06	343.4	11%
DI-B2-R01	285.2	203.9	111.4	315.3	11%	0.90	0.86	272.3	-5%
DI-B2-R02	301.1	203.9	111.4	315.3	5%	0.95	0.86	272.3	-10%
DI-B2-R03	249.9	203.9	111.4	315.3	26%	0.79	0.86	272.3	9%
DI-B2-R04	252.8	203.9	111.4	315.3	25%	0.80	0.86	272.3	8%

Table 4.27 - Analytical evaluation concerning rubble stone masonry samples (R, R2 and R3) tested to diagonal compression: experimental resistance of reinforced ( $P_{m(R),exp}$ ) and unreinforced samples ( $P_{m(U),exp}$ ), calculated diagonal compression resistance of the mortar coating ( $P_c$ ), preliminary analytical prediction of reinforced samples resistance ( $P_{m(U)} + P_c$ ) with error percentage ( $\Delta_{err(1)}$ ), coefficients  $\beta$  and  $\beta^*$  and calculated resistance of reinforced samples ( $P_{m(R),calc}$ ) with error percentage ( $\Delta_{err(2)}$ )

ID	$P_{m(R),exp}$ [kN]	$P_{m(U),exp}$ [kN]	$P_c$ [kN]	$P_{m(U),exp}+P_c$ [kN]	$\Delta_{err(1)}$ [%]	$\beta$ [-]	$\beta^*$ [-]	$P_{m(R),calc}$ [kN]	$\Delta_{err(2)}$ [%]
DR-B5-R01	427.6	237.5	107.2	344.7	-19%	1.24	1.29	445.3	4%
DR-B5-R02	449.6	237.5	107.2	344.7	-23%	1.30	1.29	445.3	-1%
DR-B5-R03	464.6	237.5	153.1	390.6	-16%	1.19	1.16	453.1	-2%
DR-B5-R04	457.6	237.5	153.1	390.6	-15%	1.17	1.16	453.1	-1%
DR-B5-R05	473.4	237.5	200.4	437.9	-7%	1.08	1.02	448.4	-5%
DR-B5-R06	402.8	237.5	200.4	437.9	9%	0.92	1.02	448.4	11%
DR2-B3-R01	388.0	131.0	111.4	242.4	-38%	1.60	1.55	375.9	-3%
DR2-B3-R02	360.0	131.0	111.4	242.4	-33%	1.49	1.55	375.9	4%
DR2-B3-R03	331.9	131.0	111.4	242.4	-27%	1.37	1.55	375.9	13%
DR2-B3-R04	366.4	131.0	111.4	242.4	-34%	1.51	1.55	375.9	3%
DR2-B3-R05	410.7	131.0	111.4	242.4	-41%	1.69	1.55	375.9	-8%
DR2-B3-R06	398.2	131.0	111.4	242.4	-39%	1.64	1.55	375.9	-6%
DR2-B2-R01	368.9	116.1	111.4	227.4	-38%	1.62	1.67	381.0	3%
DR2-B2-R02	393.0	116.1	111.4	227.4	-42%	1.73	1.67	381.0	-3%
DR3-B4-R01	702.1	407.8	153.1	560.9	-20%	1.25	1.24	695.5	-1%
DR3-B4-R02	749.5	407.8	153.1	560.9	-25%	1.34	1.24	695.5	-7%
DR3-B4-R03	617.4	407.8	200.4	608.2	-1%	1.02	1.04	630.1	2%
DR3-B4-R04	717.1	407.8	200.4	608.2	-15%	1.18	1.04	630.1	-12%

Table 4.28 - Analytical evaluation concerning cobblestones masonry samples (C) tested to diagonal compression: experimental resistance of reinforced ( $P_{m(R),exp}$ ) and unreinforced samples ( $P_{m(U),exp}$ ), calculated diagonal compression resistance of the mortar coating ( $P_c$ ), preliminary analytical prediction of reinforced samples resistance ( $P_{m(U)} + P_c$ ) with error percentage ( $\Delta_{err(1)}$ ), coefficients  $\beta$  and  $\beta^*$  and calculated resistance of reinforced samples ( $P_{m(R),calc}$ ) with error percentage ( $\Delta_{err(2)}$ )

ID	$P_{m(R),exp}$ [kN]	$P_{m(U),exp}$ [kN]	$P_c$ [kN]	$P_{m(U),exp}+P_c$ [kN]	$\Delta_{err(1)}$ [%]	$\beta$ [-]	$\beta^*$ [-]	$P_{m(R),calc}$ [kN]	$\Delta_{err(2)}$ [%]
DC-B2-R01	379.4	118.2	153.1	271.3	-28%	1.40	1.38	375.5	-1%
DC-B2-R02	371.5	118.2	153.1	271.3	-27%	1.37	1.38	375.5	1%
DC-B1-R01	209.2	48.2	76.6	124.8	-40%	1.68	1.75	218.3	4%
DC-B1-R02	227.4	48.2	76.6	124.8	-45%	1.82	1.75	218.3	-4%

For solid brick masonry, it is observed that the values of  $\beta$  resulted approximately constant at the varying of the masonry thickness (compare, for example, DS2-B3 and DS-B3 enhanced with C3 mortar in Figure 4.36) and tended to increase at the increasing of the masonry mortar characteristics (DS-B3 / DS-B6, DS2-B2 / DS2-B3, DI-B2 / DI-B3). Mean values of  $\beta < 1$  resulted for both for DS2-B2 and DI-B2.

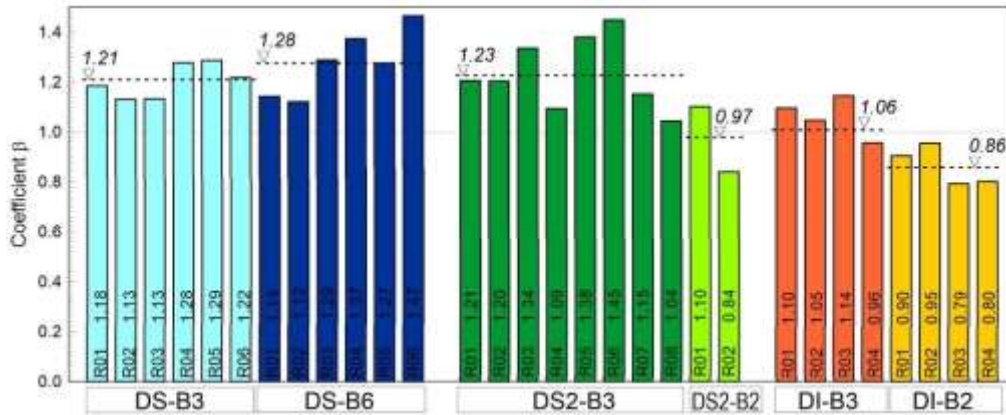


Figure 4.36 – Coefficient  $\beta$  in solid brick masonry samples enhanced with C3 mortar; mean values are also reported for each category

An evaluation of the trend of  $\beta$  coefficient at the varying of the tensile strength of the mortar used for the coating  $f_{t,c}$ , maintaining the same type of GFRP reinforcement, was performed for DS-B3 samples (Figure 4.37). It emerged that  $\beta$  ranges from 0.8 to 1.3. A significant scatter in the results occurred, however a quite clear dependence from the tensile strength of the mortar coating resulted: the higher the tensile strength, the lower the coefficient  $\beta$ . The characteristic curve (5<sup>th</sup> percentile) in the  $\beta$ - $f_{t,c}$  graph can be approximated with quite accuracy by an exponential curve having a decreasing trend at the tensile strength increasing and a horizontal asymptote in correspondence of a value of  $\beta$  of about 0.8, that is:

$$\beta_{5\%} = 0.8 + 5.5 \cdot e^{-3.5 \cdot f_{t,c}} \quad (4.13)$$

This curve, plotted in Figure 4.37, clearly evidences that for values of the tensile strength of the mortar coating greater than 0.9-1.0 MPa the values of the coefficient  $\beta$  are lower than unity. This means that the resistance of the strengthened masonry is lower than the sum of the resistances of the bare masonry and of the coating.

In regard to the stone masonry, the values of coefficient  $\beta$  generally resulted  $> 1$  (Figure 4.38). Moreover, it was noted that for masonry with equal mechanical characteristics (e.g. BD-B5 and DR3-B4) and for the range of mortar coatings tested, the coefficient assumed a decreasing trend as the mortar strength increases (Figure 4.39). The best fitting tendency lines are also displayed in Figure 4.39.

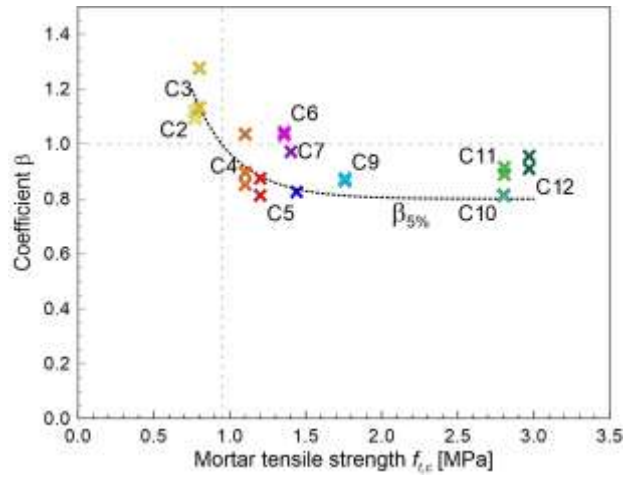


Figure 4.37 – Coefficient  $\beta$  at the varying of the mortar coating tensile resistance  $f_{t,c}$  in solid brick DS-B3 masonry

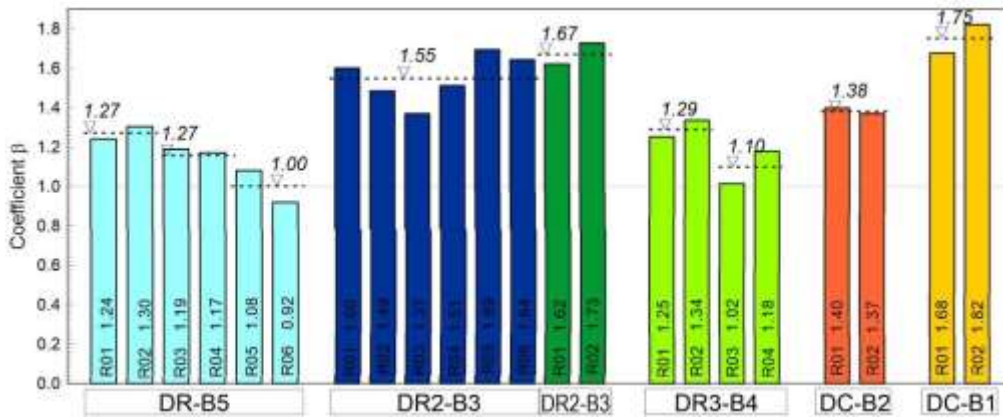


Figure 4.38 – Coefficient  $\beta$  in stone masonry samples; mean values are also reported for each category

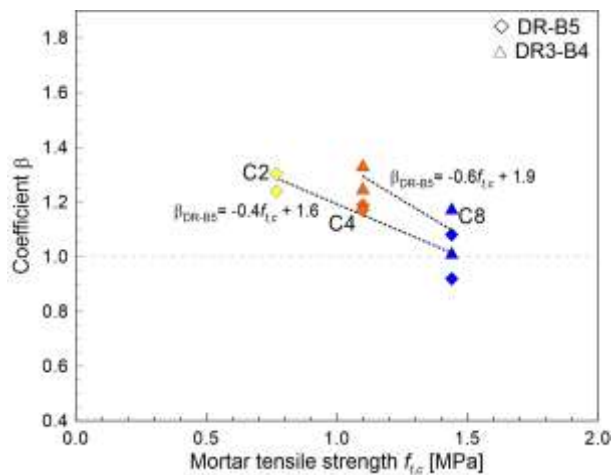


Figure 4.39 – Coefficient  $\beta$  at the varying of the mortar coating tensile resistance  $f_{t,c}$  in rubble stone DR-B5 and DR3-B4 reinforced masonry samples

In general, it can be observed that the tendency of the coefficient  $\beta$  is strictly related to the dissipative capacity of both the plain masonry and the reinforced mortar coating. To better understand their contribution, it can be useful to deduce the behaviour of the reinforced mortar coating by subtracting, for each strain value of the  $P$ - $\varepsilon$  curves, the ordinates of the unreinforced masonry curve to the reinforced masonry one.

As an example, in Figure 4.40, the average  $P$ - $\varepsilon_c$  curves referred to 250 mm thick solid brick masonry are schematized (DS-B3). In particular, Figure 4.40.a refers to type C4 mortar coating, Figure 4.40.b to type C8, Figure 4.40.c to type C2, Figure 4.40.d to type C12.

C4, C8 and C2 mortars are characterised by quite different tensile and compressive strengths, but similar Young modulus (Table 4.3). As observed in subsection 4.1.4, experimental results evidenced a similar behavior for samples reinforced with these three mortar types (Figure 4.16.c). By comparing Figure 4.40.a-c it can be observed that in a masonry with a brittle behaviour, such as solid brick, the resistance of the reinforced specimens,  $P_{m(R)}$ , can be evaluated as the sum of the resistances of the masonry,  $P_{m(U)}$ , and of the plain coating,  $P_c$ , only in case of simultaneous cracking of both components. This type of collapse is evidenced in Figure 4.40.a, where  $AD = AC + AB$  (with  $AC = P_{m(U)}$  and  $AB = P_c$ ) and, thus,  $\beta \approx 1$ . Otherwise, if the cracking occurs first in the masonry, the maximum load of the specimen is reached without exploiting the whole resistance of the plaster, as emerges in Figure 4.40.b, where  $AD = AC + AB$  but  $AB < EF (= P_c)$ , therefore  $\beta < 1$ . In the two cases of collapse described above, the resistance of the reinforced coating, although higher than that of the plain plaster, does not affect the resistance of the reinforced masonry, as the abrupt decrease of the load in the unreinforced masonry is larger than the load increment in the reinforced coating after the cracking. On the contrary, when the cracking occurs first in the coating, the post cracking resistance of the reinforced mortar coating is partially exploited before the masonry cracking is reached, as shown in Figure 4.40.c where  $AD = AC + AB$  and  $AB > EF (= P_c)$ , so  $\beta > 1$ .

In the light of these considerations, it emerged that a mortar tensile strength higher than that of  $AB$  would not provide any adjunctive peak resistance increment in the reinforced specimen. Differently, when higher Young modulus are considered, higher resistance mortars can provide further benefits to the sample peak load, as emerged, for example, for C12 mortar (Figure 4.40.d)

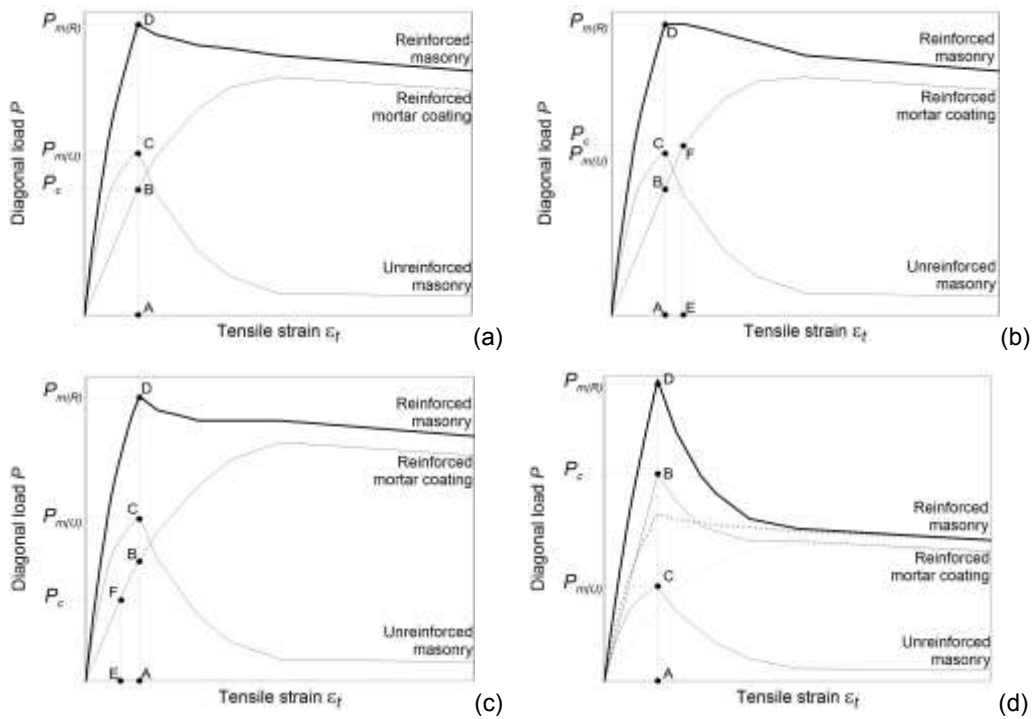


Figure 4.40 – Schematization of different collapse cases in solid brick reinforced specimens DS-B3: (a) simultaneous cracking of masonry and reinforced coating, (b) cracking occurs first in the masonry, (c) cracking occurs first in the mortar coating and (d) simultaneous cracking with higher stiffness mortar

Differently, as evidenced in subsection 4.1.4, in unreinforced specimens made with stone units a significant interlocking effect caused an attenuated decrease of the resistance after the peak load (Figure 4.26). These aspect affects the resistance of reinforced samples, as the gradual decrease of the load in the masonry allows to exploit the whole or part of the post cracking resistance of the reinforced mortar coating, as evidenced in Figure 4.41 ( $P_{m(R)} = AD = AC + AB$ ). In particular Figure 4.41.a and Figure 4.41.b schematically represent the behaviour of rubble stone specimens 400 mm thick strengthen with a type C2 and type C8 reinforced mortar coating, respectively. In Figure 4.41.a the reinforced masonry resistance ( $AD = AC + AB$ ) is much higher than the summation of  $P_{m(U)}$  and  $P_c$  ( $GH + EF$ ), while in Figure 4.41.b  $AC + AB \approx GH + EF$ .

Therefore, considering for example DR-B5 reinforced masonry, in reinforced specimens employing type C2 mortar resulted  $\beta > 1$ , while for specimens reinforced with type C8 mortar the coefficient is approximately unitary. The behavior of the specimens strengthen with type C4 mortar and the value of the corresponding modification factor is intermediate between the cases of Figure 4.41.a-b.

Comparing Figure 4.41.a to Figure 4.41.c, it is evidenced that the exploitation of the post cracking resistance of the reinforced mortar coating (AB) is significantly influenced by the softening branch after the maximum resistance of the unreinforced masonry.

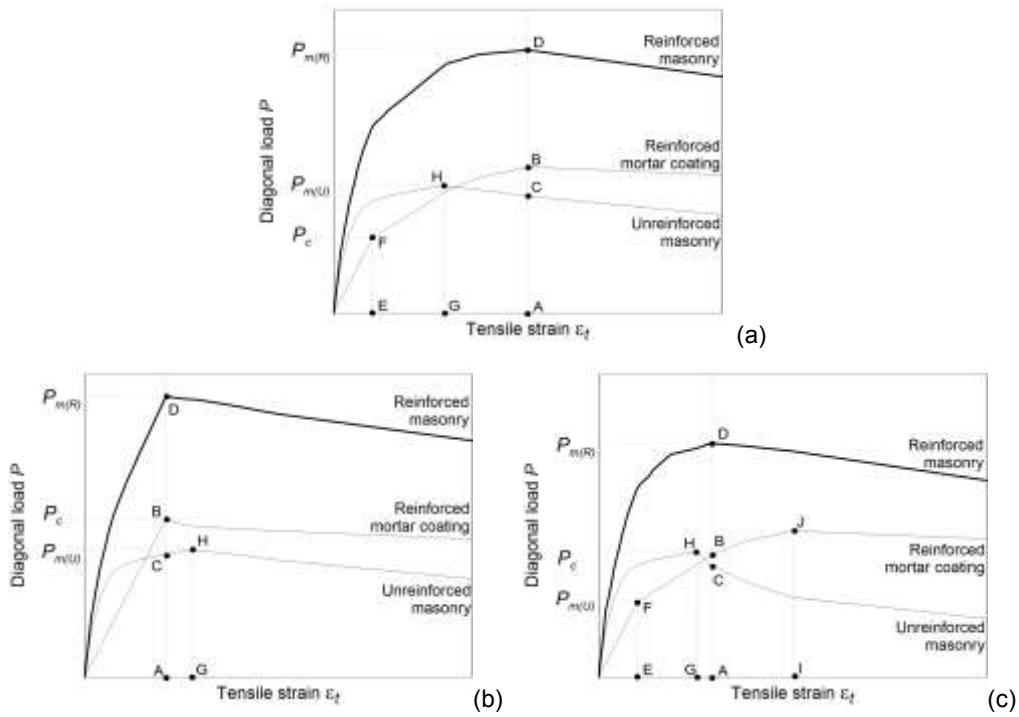


Figure 4.41 – Schematization of possible collapse mechanism in stone masonry specimens

In general, the different collapse cases are strictly related to the characteristics of both the masonry and the coating (i.e., stiffness, thicknesses, tensile strengths, post cracking behavior etc.), thus the values of the coefficient  $\beta$  depends on the type of masonry and of reinforcement analysed. The use of similar formulations is obviously allowed also for different materials, but it is necessary to determine the correct value of the modification factor through experimental tests or numerical simulations.

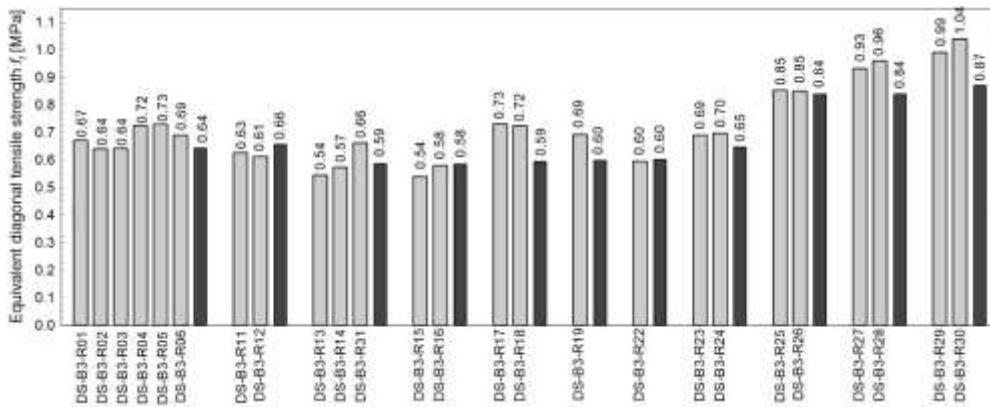
So, the resistance of reinforced masonry specimens was calculated analytically through the relationship:

$$P_{m(R),calc} = \beta^* \cdot (P_{m(U)} + P_c) \quad (4.14)$$

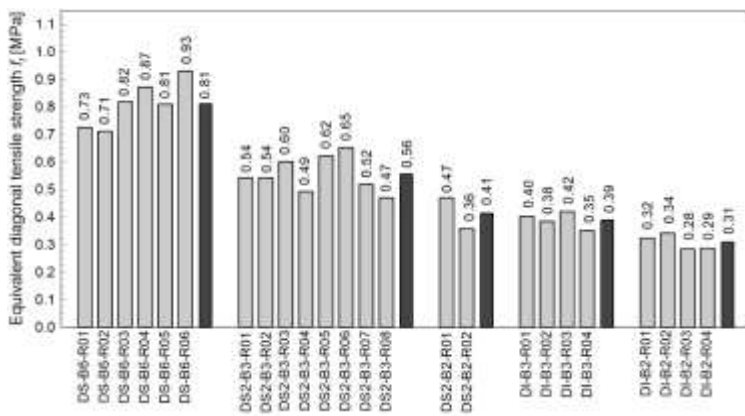
where  $\beta^*$  refers to values calculated by means of Equation ( 4.13 ) for DS-B3, through the tendency lines reported in Figure 4.39 for DR-B5 and DR3-B4 and adopting the mean values deduced from Equation ( 4.12 ) for the other masonry types (Figure 4.36 and Figure 4.38). The values of  $\beta^*$ ,  $P_{m(R),calc}$  and the error percentages  $\Delta_{err(2)}$  are reported in Table 4.24-Table 4.28.

It is worth note that, from  $P_{m(R),calc}$ , it is also possible to derive, through Equation ( 4.8 ), the predicted equivalent principal tensile strength of reinforced masonry samples,  $f_{t(R),calc}$ , and compare this values with the experimental results, to check the accuracy of the analytical formulation. The analytical calculation of the principal tensile strength  $f_{t(R),calc}$  and the comparisons with the experimental results are illustrated in Figure 4.42. The evaluations are very good for all specimens

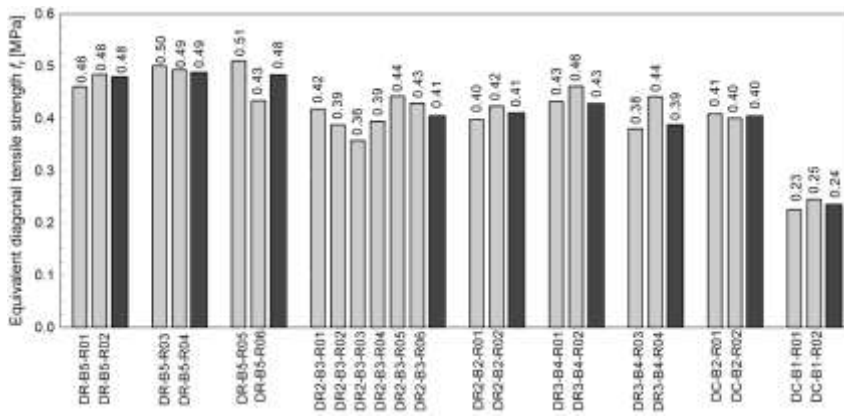
considering the scatter in the resistance of the unreinforced masonry: the error percentage ranges between -19% and +18%, with a coefficient of variation equal to 9 percentage points.



(a)



(b)



(c)

Figure 4.42 – Comparisons between experimental values (light grey) and analytical estimations (dark grey) of equivalent diagonal tensile strength  $f_{t(R)}$  of reinforced masonry panels subjected to diagonal compression tests: (a) DS-B3, (b) DS-B6, DS and DI and (c) DR, DR2, DR3 and DC

### 4.3 Numerical simulation of diagonal compression tests

To support the interpretation of the diagonal compression tests results provided in subsection 4.1.5, some numerical simulation were performed through the software Midas FEA (2015, v.1.1) on a preliminary, simplified finite element numerical model based on continuum.

The adopted numerical model is schematised in Figure 4.43: 8-node “Solid” elements were employed for the masonry, while 4-node “Plane Stress” elements (30 mm nominal thickness) for the mortar coating. The mesh dimensions were 66 x 66 mm<sup>2</sup>; the thickness of the solid mesh elements was assumed 1/4 of the global masonry thickness. The perfect adhesion between plaster and masonry layers was assumed for simplicity (coincident nodes). 8-node “Solid” elements were considered also to reproduce the presence of the loading heads.

A diagonal displacement was applied in correspondence of one head, while the other was assumed fixed. Non-linear static analysis were performed incrementing then step-by-step the imposed displacement. The Newton-Rapshon iterative method was considered (energy convergence criteria 0.001).

All the implemented materials were assumed being homogeneous and isotropic and a Smear Crack, rotating model (TNO Building and Construction Research, 2002) was considered both for the masonry and for the mortar coating.

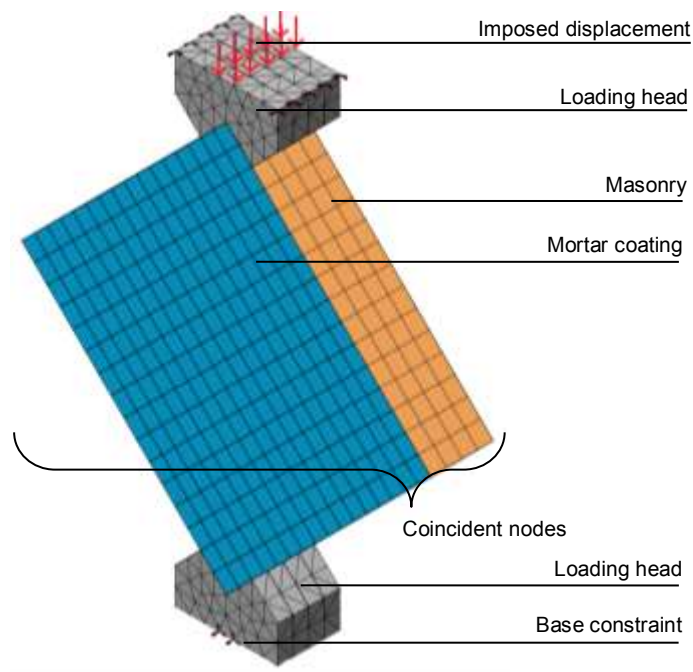


Figure 4.43 – Schematization of the numerical model adopted for the preliminary simulations of diagonal compression tests

DS-B3 solid brick masonry was investigated: the shear modulus  $G_m$  was deduced from the results of diagonal compression tests (subsection 4.1.4) and a Poisson modulus equal to 0.25 was considered. For the compressive behaviour, a parabolic relationship was applied (Figure 4.44); it is evidenced that a compressive strength almost halved in respect to that deduced from the compression tests on masonry wallets (Figure 4.4) was considered: this was due to the different orientation of the principal compressive strain in diagonal compression tests, which are not oriented in the direction perpendicular to bed joint but, mainly, at  $45^\circ$  (Samarasinghe, 1980; Hendry, 1981). The equivalent tensile strength was derived from the average values deduced from the experimental diagonal compression tests on unreinforced specimens (subsection 4.1.5); a brittle behavior was assumed. The masonry mechanical characteristic are resumed in Table 4.29.

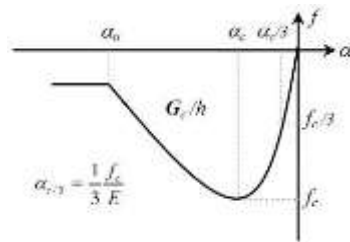


Figure 4.44 – Schematization of the parabolic softening law adopted for masonry in compression (TNO Building and Construction Research, 2002)

Table 4.29 – Main characteristics assumed for DS-B3 in the preliminary numerical simulations of diagonal compression tests ( $G_m$  and  $\nu$  are the shear and Poisson modulus,  $f_{t,m}$  and  $f_{c,m}$  the tensile and compressive strengths of unreinforced masonry,  $G_{f/h}$  the fracture energy)

<b>DS-B3</b>	
$G_m$ [MPa]	2325
$\nu$ [-]	0.25
Tensile behavior	Brittle
	$f_{t,m} = 0.374$ MPa
Compressive behavior	Parabolic
	$f_{c,m} = 3.94$ MPa
	$G_{f/h} = 0.05$ N/mm <sup>2</sup>

A first simulation on the solid brick unreinforced masonry was performed (Figure 4.45). A good accordance with the experimental results emerged both in terms of initial stiffness and peak load (Figure 4.14.a). The analysis of the stress state at the center of the panel (Figure 4.46) showed, for a diagonal compressive load equal to 220 kN (numerical peak load), a principal tensile stress equal to 0.374 MPa and a principal compressive stress equal to 1.298 MPa. It follows  $\sigma_I = 0.49 P/bt$  and  $\sigma_{III} = -1.71 P/bt$ . These values resulted in good accordance with those provided by Frocht (1931) – subsection 4.1.5. The trend of the principal stresses is also reported in Figure 4.46: it is observed

that, at the center of the panel, the compressive stresses  $\sigma_{III}$  are oriented in the loaded diagonal direction and the tensile stresses  $\sigma_I$  in the orthogonal direction.

Once the masonry tensile strength was exceeded at the center of the panel and then rapidly spread along the loaded diagonal, the load suddenly dropped down.

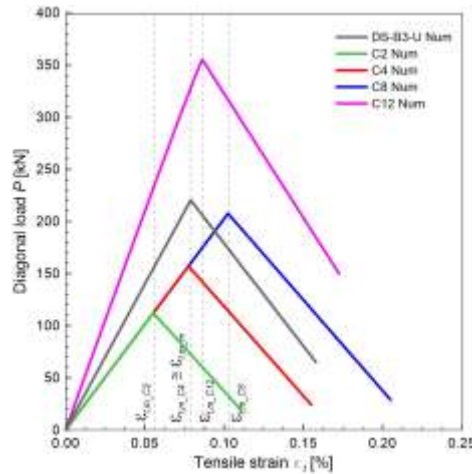


Figure 4.45 –  $P$ - $\epsilon_t$  numeric curves concerning unreinforced masonry and unreinforced mortar layers

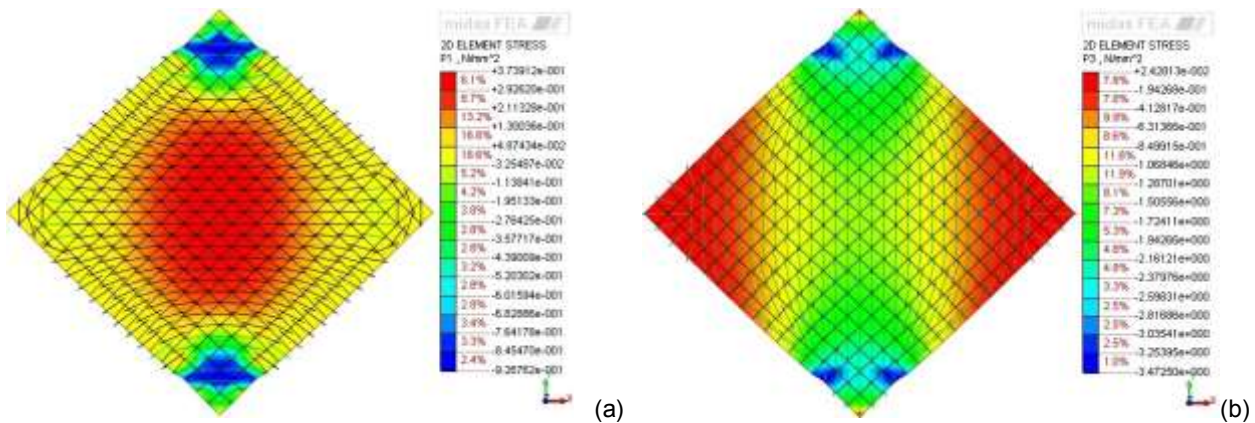


Figure 4.46 - Finite element numerical simulations on a square panel type DS-B3 subject to diagonal compression: principal stresses (a) in tension  $\sigma_I$  and (b) in compression  $\sigma_{III}$  (b) at peak load

So to assess the first cracking load  $P_c$  of the mortar coating, some numerical simulations were performed according to the model illustrated in Figure 4.43, by assuming a fictitious, low Young modulus for the masonry ( $E = 10^{-6}$  MPa).

In particular, C2, C4, C8 and C12 mortars were analysed; the assumed compressive and tensile strengths were those deduced from characterization tests (Table 4.3). An elastic-plastic relationship was considered in compression, while a brittle behavior in tension, according to the actual behavior of plain mortar.

Table 4.30 – Main characteristics of the mortar considered in the numerical simulation

	Mortar type			
	C2	C4	C8	C12
E [GPa]	13.8	14.4	13.4	23.3
$\nu$ [-]	0.2	0.2	0.2	0.2
Tensile behavior	$f_{t,m} = 0.77$ MPa	$f_{t,m} = 1.10$ MPa	$f_{t,m} = 1.44$ MPa	$f_{t,m} = 2.97$ MPa
Compressive behavior	Elastic-plastic $f_{c,m} = 4.66$ MPa	Elastic-plastic $f_{c,m} = 6.90$ MPa	Elastic-plastic $f_{c,m} = 11.66$ MPa	Elastic-plastic $f_{c,m} = 25.74$ MPa

The diagonal load against tensile strain curves of the four considered mortar coatings are reported in Figure 4.45. It is observed (Table 4.31) that the experimental peak loads attained numerically are in agreement with the analytical predictions of  $P_c$ .

In Figure 4.45, it can also be observed that the C4 mortar coating reached the diagonal peak load at a value of the tensile strain  $\varepsilon_{t,m\_C4}$  quite close to that of the plain masonry,  $\varepsilon_{t,m\_m}$ . Differently,  $\varepsilon_{t,m\_C2}$  and  $\varepsilon_{t,m\_C8}$  resulted, respectively, lower and higher than  $\varepsilon_{t,m\_m}$ . Also the value  $\varepsilon_{t,m\_C12}$  resulted greater than  $\varepsilon_{t,m\_m}$ .

Table 4.31 – Comparisons between analytical (suffix “calc”) and numerical (suffix “num”) results in terms of first cracking load  $P_c$  of unreinforced mortar layers

	Mortar type			
	C2	C4	C8	C12
$P_{c,calc}$ [kN]	107.2	153.1	200.5	413.4
$P_{c,num}$ [kN]	112.2	157.1	207.6	427.8
$\Delta_{err}$	+4.7%	+2.6%	+3.5%	+3.5%

Then, the behavior of the solid brick masonry panel with unreinforced mortar layers applied on both faces was investigated. The four mortar types already mentioned were considered. The results were reported in Figure 4.47. The experimental results can be compared to those of some experimental DS-B3 samples reinforced with C2 (DS-B3-R11, DS-B3-R12), C4 (DS-B3-R13, DS-B3-R14, DS-B3-R31, DS-B3-R32), C8 (DS-B3-R22) and C12 (DS-B3-R29, DS-B3-R30) mortars (Figure 4.16.b-c).

According to the experimental results provided by sample DS-B3-R31 (C4 plain mortar coating), the  $P$ - $\varepsilon_t$  numerical curves showed a brittle behavior due to the characteristics assumed for both the masonry and the mortar. Some considerations on the peak loads can be conducted: in particular, it emerged that the models which considered type C4, C8 and C12 mortars (Figure 4.47.b, c and d) approximated very good to the experimental medium resistances. Differently, a significant underestimation emerged for DS+C2 case (Figure 4.47.a).

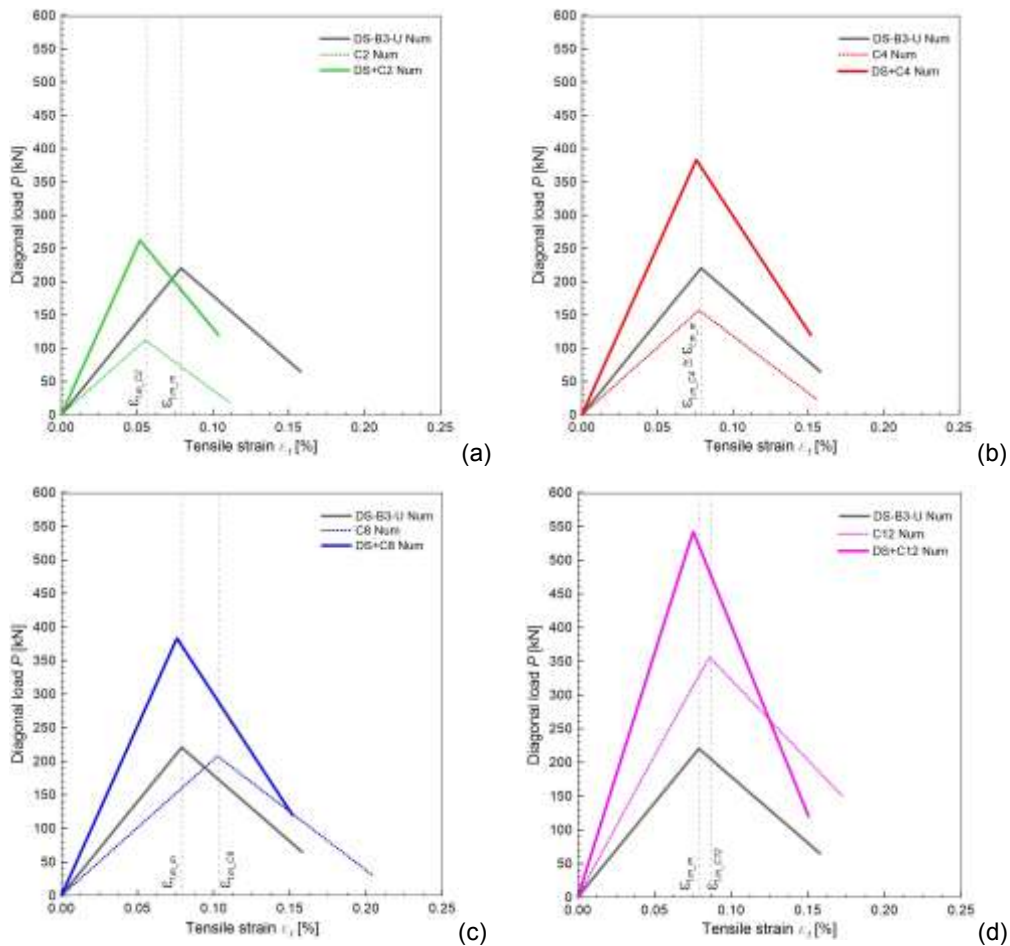


Figure 4.47 –  $P$ - $\epsilon_1$  numeric curves concerning a solid brick masonry panel DS-B3-U with unreinforced mortar layers at both faces, at the varying of the mortar type: (a) DS+C2, (b) DS+C4, (c) DS+C8 and (d) DS+C12

The values of principal tensile stress in the center of the panel at peak both in the masonry and in the mortar coating were compared in Table 4.36 for the four different cases: the contemporary masonry and mortar cracking emerged in case C4. Differently, in case C8 and C12, the masonry tensile failure occurred when the principal tensile stresses in the mortar coating were lower than the mortar strength; however, once the masonry cracks, losing load-bearing capacity, the consequent, immediate failure of the mortar layers occurred. Contrarily, in case C2, the tensile failure of the mortar layers emerged first.

In general, by comparison also with the experimental results, it can be deduced that, in the cases C4, C8 and C12, the presence of the GFRP mesh embedded in the mortar coating does not affect appreciably the panel resistance, but is fundamental to maintain significant resistance reserves after cracking. However, when weaker mortars are considered (as in case C2), the GFRP mesh provides a contribution also to the reinforced panel peak resistance.

Table 4.32 – Main numerical results concerning solid brick masonry samples with unreinforced mortar layers applied at both faces: peak load  $P_{m,num}$  and principal tensile stress at the center of the panel in masonry  $\sigma_{_m}$  and in mortar layer  $\sigma_{_c}$  at peak

	Mortar type			
	C2	C4	C8	C12
$P_{m,num}$ [kN]	262.3	383.1	383.1	568.9
$\sigma_{_m}$ [MPa]	$0.27 < f_{t,m}$	$0.37 = f_{t,m}$	$0.37 = f_{t,m}$	$0.37 = f_{t,m}$
$\sigma_{_c}$ [MPa]	$0.77 = f_{t,c}$	$1.10 = f_{t,c}$	$1.10 < f_{t,c}$	$2.22 < f_{t,c}$

The simulations were then extended to GFRM reinforced solid brick masonry samples, modeling also the presence of the GFRP mesh, by introducing only tension reagent truss elements solidarized to the mortar layer (mesh dimension 66 mm). By performing the numerical simulations (considering, for example, a C4 mortar type), it emerged that, to fit adequately the experimental results, a modification to the mortar softening law, in respect to the brittle behavior of plain mortar, is necessary. The nonlinear behavior assumed in tension for mortar is resumed in Table 4.33. For the GFRP wires, a Young modulus of 30 GPa and an ultimate strain of equal to 2.4 % were considered.

Table 4.33 – Constitutive relationships adopted for the tensile behaviour of the mortar of the coating (C4)

$\epsilon_t$ [‰]	$\sigma_t$ [MPa]
0.000	0.00
0.008	1.10
0.200	0.84
0.300	0.78
0.460	0.70
0.920	0.50
1.430	0.42
2.400	0.42
2.500	0.00

Actually, in characterization tests on GFRM layers (subsection 3.3.3), a not negligible tension stiffening effect of the mortar between adjacent cracks emerged. Thus, although in diagonal compression tests the mesh position, in respect to the principal tensile stress direction, is not the same of the tensile tests on GFRM layers and that the mechanical characteristics of the wires in the two mesh main directions are different, quite similar performances of the reinforced mortar coating in tension are expected (Vecchio & Collins, 1986).

A comparison with experimental results evidenced a good reliability of the numerical results, considering the simplifications assumed in the model (Figure 4.48.a). It was possible to distinguish a first linear-elastic stage then, as both the masonry and the mortar coating cracked, almost

simultaneously, a stress re-distribution occurred in the mortar and in the GFRP mesh. At the increasing of the imposed displacement, the GFRP wires stresses gradually increase till rupture, in the central area, at  $\varepsilon_t \approx 0.7\%$  (Figure 4.48.b).

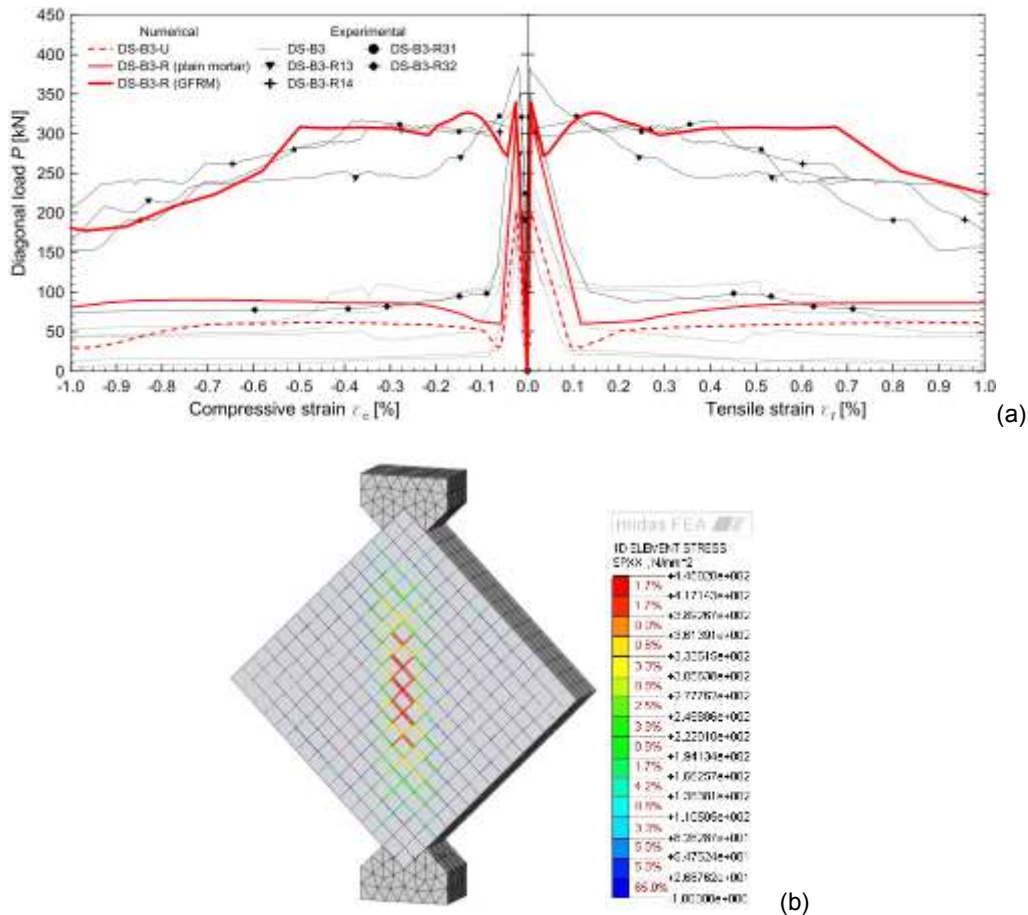


Figure 4.48 – DS-B3: (a) comparison between experimental and numerical capacity curves ( $P-\varepsilon_c$ ,  $P-\varepsilon_t$ ) and (b) GFRP mesh stress state just before failure

The simplified modeling was also adopted for the simulation of DR-B5 and DC-B2 reinforced masonry samples. The shear modulus  $G_m$  were deduced from the diagonal compression tests results on plain samples. A parabolic relationship was assumed in compression (Figure 4.4), while the nonlinear softening law proposed by Hordijk (1991) in tension. According to the interpretation of diagonal compression tests provided by Brignola et al. (2009), the masonry tensile resistance associated to the first cracking in the center of the panel was evaluated by assuming, in Equation (4.8), a coefficient of 0.4 for rubble stone and of 0.35 for cobblestones, instead 0.5. The values of fracture energy in tension, accounting for the interlocking effect between units after first cracking, were calibrated trying to fitting the behavior of unreinforced samples. The considered masonry characteristics are summarised in Table 4.34.

The results of the numerical simulation simulations are illustrated in Figure 4.50, in comparisons with the experimental curves: a good agreement of the predictions was noted.

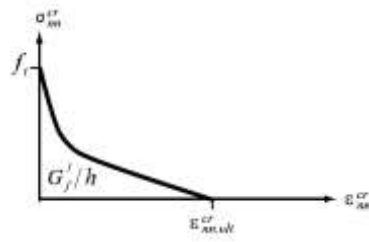


Figure 4.49 – Schematization of the Hordijk softening law adopted for masonry (TNO Building and Construction Research, 2002)

Table 4.34 – Main characteristics assumed for DR-B5 and DC-B2 samples in the preliminary numerical simulations of diagonal compression tests ( $G_m$  and  $\nu$  are the shear and Poisson modulus,  $f_{t,m}$  and  $f_{c,m}$  the tensile and compressive strengths of unreinforced masonry,  $G_f/h$  the fracture energy)

	DR-B5	DC-B2
$G_m$ [MPa]	1640	800
$\nu$ [-]	0.25	0.25
Tensile behavior	Hordijk $f_{t,m} = 0.182$ MPa $G_f/h = 0.0009$ N/mm <sup>2</sup>	Hordijk $f_{t,m} = 0.089$ MPa $G_f/h = 0.0011$ N/mm <sup>2</sup>
Compressive behavior	Parabolic $f_{c,m} = 3.5$ MPa $G_f/h = 0.025$ N/mm <sup>2</sup>	Parabolic $f_{c,m} = 1.04$ MPa $G_f/h = 0.06$ N/mm <sup>2</sup>

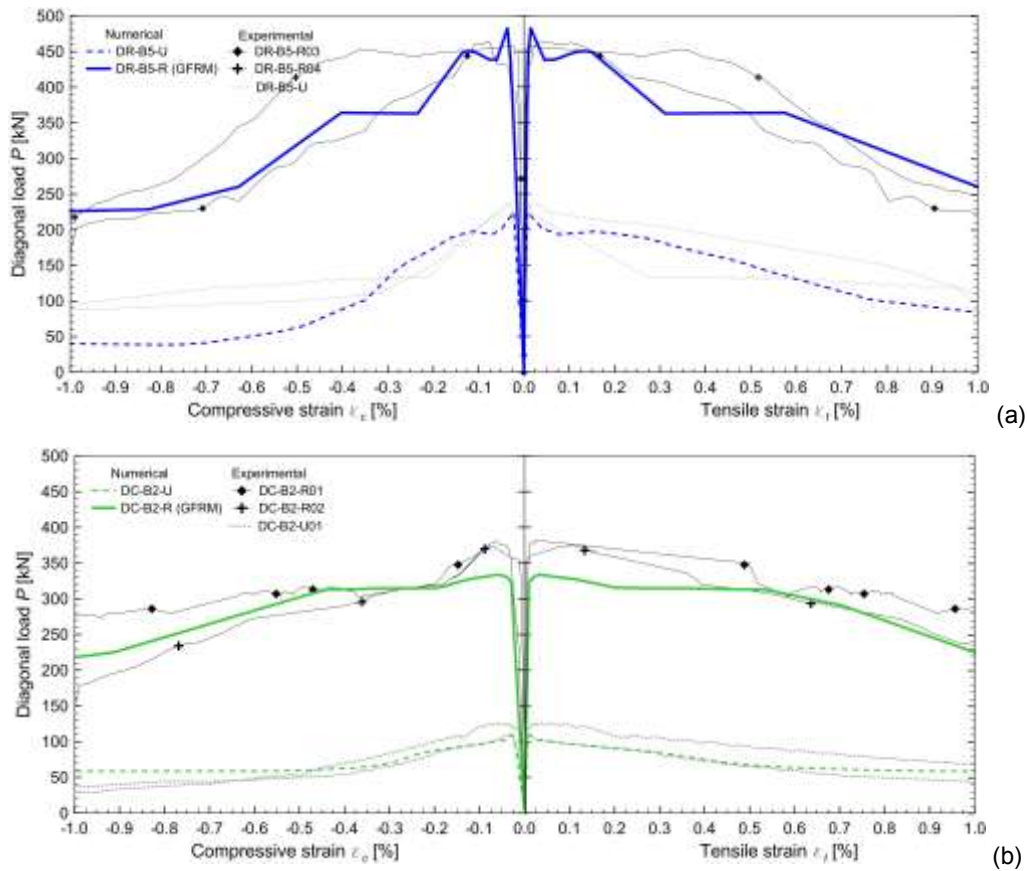


Figure 4.50 – Comparison between experimental and numerical capacity curves ( $P_{-c_c}$ ,  $P_{-c_t}$ ): (a) DR-B5 and (b) DC-B2

It is observed that two previous numerical studies, based on 2D (Melotto, 2013; Gattesco & al., 2016b) and 3D (Gattesco & al., 2015b) simplified models, were developed for GFRM reinforced mortar samples subjected to diagonal compression. Both models considered continuous, homogeneous, smeared crack materials. In particular, in the former model (software Midas FEA), plane stress elements were employed for modeling both the masonry and the mortar layers; truss elements represented the mesh wires. In the latter model (software ABAQUS/Standard), solid elements were considered for the masonry, while shell and truss elements for the mortar coating and the GFRP wires, respectively. The numerical results derived from plain and GFRM reinforced masonry were analysed and compared; however, in both cases, the simulation were limited to a single masonry type: cobblestones for the 2D model, rubble stones for the 3D one.

The results of the preliminary numerical simulations presented in this study are promising, as the same modeling of the reinforcement is valid for different masonry types. In future development of the research, the model could be extended to other types of mortars used for the coating, once the mesh-mortar interaction under the actual stress state has been evaluated. Moreover, for a detailed study on the post-peak behavior of reinforced panels, it will necessary a refinement of the model, as experimental evidences showed the not negligible influence of local mechanisms such as the interaction between masonry and mortar layers, the cracking and delamination of the mortar between cracks and the compressive plasticization of both masonry and mortar.

#### **4.4 Numerical investigations on reinforced masonry buildings**

The effectiveness of the considered GFRM technique in the enhancement of the mechanical response of unreinforced masonry samples subjected to in-plane action was experimentally assessed, but the designer needs to evaluate the global improvement of the seismic response of strengthened buildings and, for such a goal, it is necessary to use numerical simulation tools.

In this first approach to the study on the effects of a GFRM coating on the global seismic behavior of masonry buildings, a user-friendly commercial computer code, based on nonlinear static analysis performed on an Equivalent Frame model, was considered to make an initial assessment of the global effectiveness of the technique. Some difficulties needed to be faced for strengthened masonry, so to consider the effect of the reinforcement in available commercial computer codes (Gattesco & Boem, 2015b; Gattesco & Boem, 2017b).

Four building configurations were modelled, as an example: two and three storey structures, both regular and non-regular in plan. Solid brick and rubble stone masonry were considered. The deduced capacity curves permitted to make comparisons between unreinforced and reinforced structures in terms of horizontal shear resistance and displacement capacity. Moreover, by applying the modified Capacity Spectrum Method based on equivalent viscous damping, the seismic resistances in terms of ground acceleration were assessed, permitting to evaluate the seismic enhancement obtainable through the application of the reinforcement.

##### *4.4.1 Modeling*

The numerical simulations were carried out on an Equivalent Frame model (Tomazevic, 1999; Magenes, 2000), using the structural program Midas Gen (2015, v1.1) to evaluate the seismic behavior of masonry structures, both unreinforced and reinforced with the proposed GFRM technique. This modeling method constitutes a simplified macro-modeling strategy based on one-dimensional elements. According to such an approach, the masonry acts as a fictitious isotropic and homogeneous material, with elastic behavior dependent from both the flexural and shear deformations and nonlinearities concentrated in so called “plastic hinges” that take into account for the in-plane nonlinear behavior of masonry resisting elements (piers and spandrels) both in shear and in bending. Calibrations on the basis of the experimental results were necessary for the parameters describing the plastic hinges, as indicated in the following.

It is worth note that masonry typically exhibits a nonlinear, brittle behavior due to the limited dissipative properties in tension and shear, mostly related to the weakness at the masonry-mortar interface level. However, experimental tests on piers and spandrels (e.g. Anthoine & al., 1995; Magenes & Calvi, 1997; Chiostriani & Vignoli, 1994; Corradi & al., 2003; Beyer & Dazio, 2012, Graziotti & al., 2012; Gattesco & al., 2016a) evidenced some resistance reserves after peak, due to the presence of axial loads and to the interlocking effect among blocks, once the masonry cracks. The global result of these effects is a more gradual decrease of the wall panel resistance capacity, even if no real plasticization occurs in the masonry components. Thus, the nonlinear response provided to the masonry resisting elements takes account of their ability to deform even after reaching the peak resistance, simulating a progressive stiffness degradation before collapse.

- Buildings characteristics and modeling approach

Four different building configurations were considered: two and three storey buildings, both regular and non-regular in plan. The regular plan (Figure 4.51.a) had a rectangular shape 29880 x 16350 mm<sup>2</sup> and was assumed symmetric in both X and Y directions. The non-regular plan differed from the regular one for the absence of a corner room (Figure 4.51.b). The inter-storey height was 3800 mm.

For each configuration, two different masonry types were analyzed: solid brick and rubble stone. The thickness of the solid brick masonry was 380 mm (three-wythe), for the two storey buildings, and 510 mm (four-wythe), for the three storey ones; in the case of rubble stone masonry, a 400 mm and a 550 mm thickness were assumed, respectively. Actually the thickness of the masonry of the third floor was 380 mm, in case of solid bricks, and 400 mm, in case of rubble stones.

In order to estimate the actual structural enhancement due to the application of the reinforcement, out-of-plane mechanisms were assumed prevented both in unreinforced and reinforced structures: the walls were effectively connected to the floors by means of steel angles (90x150x12 mm<sup>3</sup>, S275 steel - EN 10027-1:2005, anchor bolts 16 mm diameter, 500 mm spaced – Rinaldin & al., 2017). The floors were made with unidirectional timber joists and wooden boards, to which CFRP strips are glued so to provide an adequate in-plane stiffness of the diaphragm (Gattesco & Macorini, 2014). The intermediate floors were completed with light concrete subfloor, concrete screed over floor heating system, deck with marble tiles, gypsum suspended ceiling with lighting and ventilation plant systems incorporated and thermal insulation; a quote for the partition walls made with hollow bricks was also considered. For the roof floor, elastomeric waterproof membrane, roof tiles, gypsum suspended ceiling with the plant systems and thermal insulation were considered. The storey load distribution related to the seismic combination was equal to 6.80 kN/m<sup>2</sup>, for the intermediate storeys (dead load = 5.00 kN/m<sup>2</sup> and live load = 3.00 kN/m<sup>2</sup>, quasi-

permanent factor = 0.6 for live loads), and equal to 2.85 kN/m<sup>2</sup>, for the roof (dead load = 2.85 kN/m<sup>2</sup> and live load = 1.2 kN/m<sup>2</sup>, quasi permanent factor equal to zero for live loads).

A 66x66 mm<sup>2</sup> GFRP mesh, type “S” (subsection 3.2) embedded in a 30 mm thick lime and cement mortar coating (type “C4” in Table 4.3) applied of both masonry surface was considered for the reinforcement, as an example.

Nonlinear-static analysis (pushover) were performed on a three-dimensional Equivalent Frame model composed by vertical and horizontal beams connected by rigid nodes; the effective piers lengths were evaluated according to the practice rule of Dolce (1989). Plastic hinges at the end nodes and in the central section of the resisting elements were considered so to take into account for the in-plane bending and shear nonlinear behavior, respectively. A rigid plane constraint was introduced at each storey. For the global seismic analysis, a material safety factor equal to  $\gamma_M = 1.0$  was considered.

The application of the Equivalent Frame model adopted for the numerical simulations is illustrated in Figure 4.52, for the external and the internal masonry walls. It is observed that the same model was adopted for both unreinforced and reinforced buildings. In fact, according to the experimental behavior of reinforced panels, reinforced resisting elements could be realistically modelled as masonry panels with improved stiffness, resistance and displacement capacity. In fact, as the stiffness of the masonry and that of the mortar coating are comparable, the in-plane action is distributed among the layers, so that they collaborate in the development of the wall panel strength.

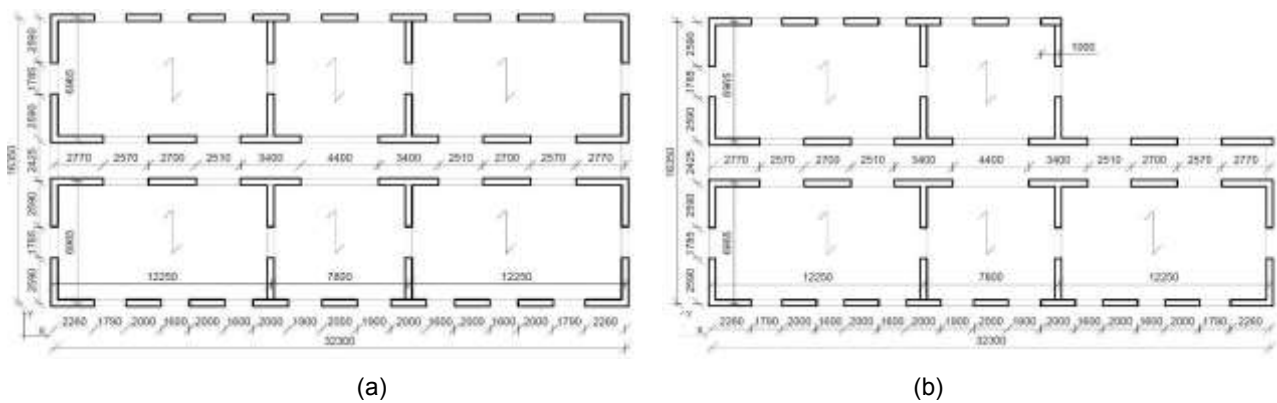


Figure 4.51 – Main in-plan geometrical characteristics of the (a) regular and (b) non-regular buildings

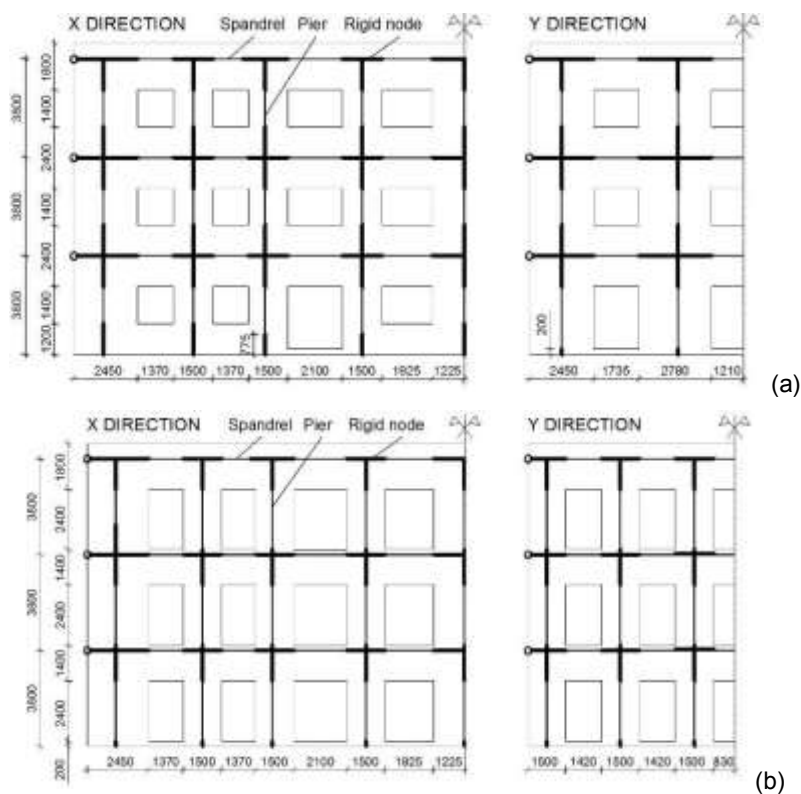


Figure 4.52 – Main geometrical characteristics of (a) external and (b) internal masonry walls, with indication of the Equivalent Frame schematization adopted for the numerical simulations

#### - Mechanical characteristics

The main mechanical characteristics assumed for solid brick and rubble stone masonry are summarized in Table 4.35. In particular, for unreinforced masonry, they referred to the values indicated in the Italian Recommendations “Circolare 2 febbraio 2009, n. 617”, annex of the Italian building code D.M. 14.01.2008; for the reinforced masonry, the shear strengths were derived by applying the analytical formulation proposed in subsection 4.2 - equation ( 4.14 ) - for the equivalent tensile resistance of reinforced masonry. The masonry referential shear strength without normal stresses,  $\tau_0$ , was assumed as the equivalent tensile strength,  $f_t$ , divided by 1.5, according to equation ( 4.9 ). The compressive strength in the horizontal direction ( $f_{hc,m}$ ) was assumed half that in the vertical direction ( $f_{c,m}$ ) (Hendry, 1981).

The shear and bending resistances were evaluated by applying the equations summarised in Table 4.36. In particular, it is observed that the same value of shear strength ( $\tau_0$ ) was assumed for piers and spandrels. The shear resistance of the spandrels,  $V_s$ , was evaluated by means of equation ( 4.16 ); differently, the shear resistance of piers,  $V_p$ , was considered affected by the axial compressive stress,  $p$ , according to the Turnsek and Cacovic (1971) interpretation for existing masonry ( 4.15 ). The bending resistance of the piers,  $M_p$ , was assumed influenced by the axial compressive stress,  $p$ , and by the masonry compressive strength in the vertical direction,

neglecting the tensile resistance of the masonry ( 4.17 ), while the contribution of the tie beam at floor level to the bending resistance of spandrels  $M_S$  was considered ( 4.18 ).

Actually the model does not account for the sliding shear failure mechanisms of masonry piers. However, in the considered structures, this type of collapse does not occur, due to the consistent axial load at the ground floor.

Table 4.35 – Mechanical characteristics of the masonry resisting elements: Young and shear modulus ( $E_m$ ,  $G_m$ ), specific weight ( $\gamma_m$ ), compressive resistance in the vertical ( $f_{c,m}$ ) and horizontal ( $f_{hc,m}$ ) directions and shear resistance ( $\tau_0$ ).

	Solid brick masonry			Rubble stone masonry		
	Unreinforced	Reinforced (380 mm)	Reinforced (510 mm)	Unreinforced	Reinforced (400 mm)	Reinforced (550 mm)
$E_m$ [MPa]	1500	3780	3200	1500	3665	3075
$G_m$ [MPa]	600	1512	1280	600	1466	1230
$\gamma_m$ [kN/m <sup>3</sup> ]	18.0	21.2	20.4	21.0	24.0	23.2
$f_{c,m}$ [MPa]	3.2	3.2	3.2	2.6	2.6	2.6
$f_{hc,m}$ [MPa]	1.6	1.6	1.6	1.3	1.3	1.3
$\tau_0$ [MPa]	0.076	0.181	0.154	0.056	0.156	0.129

Table 4.36 – Shear and bending resistances of piers and spandrels (being  $t$  the masonry thickness,  $b_S$  and  $b_P$  the spandrel and pier width,  $l_P$  the pier height,  $p$  the axial compressive stress,  $f_{c,m}$  and  $f_{hc,m}$  the masonry compressive resistances in the vertical and horizontal direction,  $H_p$  the tie beam tensile resistance at floor level, which has not to be greater than  $0.4 \cdot f_{hc,m} \cdot b_S \cdot t$ ).

	Piers	Spandrels
Shear	$V_P = b_P \cdot t \cdot \frac{1.5 \tau_0}{\alpha} \sqrt{1 + \frac{p}{1.5 \tau_0}}$ $\alpha = \begin{cases} 1.5 & 1.5 \leq l_P/b_P \\ l_P/b_P & 1 \leq l_P/b_P \leq 1.5 \\ 1.0 & l_P/b_P \leq 1.0 \end{cases}$	$V_S = b_S \cdot t \cdot \tau_0$
Bending	$M_P = \frac{p \cdot b_P^2 \cdot t}{2} \cdot \left( 1 - \frac{p}{0.85 \cdot f_{c,m}} \right)$	$M_S = \frac{H_p \cdot b_S}{2} \cdot \left( 1 - \frac{H_p}{0.85 \cdot f_{hc,m} \cdot b_S \cdot t} \right)$

For the characteristics of the plastic hinges of unreinforced elements, the elastic-plastic relationships suggested in “Circolare 2 febbraio 2009, n. 617” were adopted (Figure 4.53). The maximum spandrel bending drift was assumed very high (about 10%), provided that such a mechanism does not cause appreciable resistance reduction up to very large displacements (Magenes & Calvi, 1997).

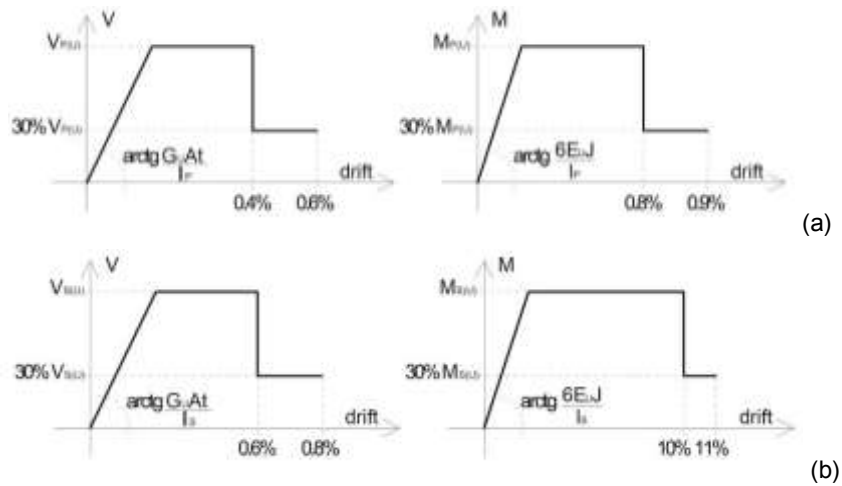


Figure 4.53 – Shear and bending behavior for the plastic hinges in (a) masonry piers and (b) spandrels (suffix “U” refers to unreinforced masonry)

The evaluation of the in-plane performances of reinforced masonry walls was based on the results of experimental investigations concerning diagonal compression tests (subsection 4.1) and cyclic shear-compression tests on masonry piers (Gattesco & al., 2015b). These tests evidenced that the GFRM intervenes in stiffening the masonry and increasing the shear strength; moreover the GFRP mesh permitted to improve ductility, opposing to the opening of cracks. The influence of tie beams at floor level on the performances of masonry spandrels was also investigated (Rinaldin & al., 2017; Gattesco & al., 2016a), evidencing that the collapse is governed by shear failure.

The curves plotted in Figure 4.54 were considered for the characteristics of the plastic hinges of reinforced elements. The shear capacity of both the piers and the spandrels was based on the results diagonal compression tests (subsection 4.1). The behavior of reinforced spandrels in bending was assumed equal to that of unreinforced ones, considering the strut-and-tie mechanism formed with the tensile element (tie beam) as the governing one for the flexural resistance.

An evaluation of the piers performances in bending was performed: the ultimate bending resistance ( $M_{P(R)}$ ) was estimated considering, in tension, only the contribution of the elastic-brittle behavior of GFRP wires. The bending moment associated to yielding ( $M_{P,0}$ ) was estimated by means of Equation ( 4.19 ) - CEB, 1985:

$$M_{P,0} = -N(x_I - x_{II}) \cdot \frac{1}{1 - \frac{E_{II}}{E_I}} \quad (4.19)$$

where  $N$  is the axial force,  $x_I$ ,  $x_{II}$ ,  $E_I$  and  $E_{II}$  are the position of the neutral axis and the flexural stiffness in pure bending for uncracked (I) and cracked (II) states. A parabolic-rectangle stress-strain diagram was considered for the masonry in compression, with strain  $\epsilon_{c2} = 0.35\%$  and

ultimate strain  $\epsilon_{cu} = 0.8\%$  (Figure 4.4). The second branch of the bilinear curve was assumed parallel to that of pure bending.

The maximum drift of the reinforced masonry piers in bending was estimated considering the pier rotation at the base due to the tensile strain of the reinforced mortar coating, neglecting the masonry contribution. The tensile behavior of the reinforcement was deduced from the results of the experimental tensile tests carried out GFRM layers (subsection 3.3.3) and depends, in general, from the pier dimensional characteristics. For the considered piers geometry, the calculated drift,  $\gamma_{P(R)}$ , ranged from 0.5% to 1.0%; prudentially, it was assumed not higher than 0.8%. After the reaching of  $\gamma_{P(R)}$ , the resistance then gradually dropped down to the same residual value of the unreinforced masonry one (that was 30%  $M_{P(U)}$ ), until reaching a 0.8% drift, as in case of unreinforced masonry.

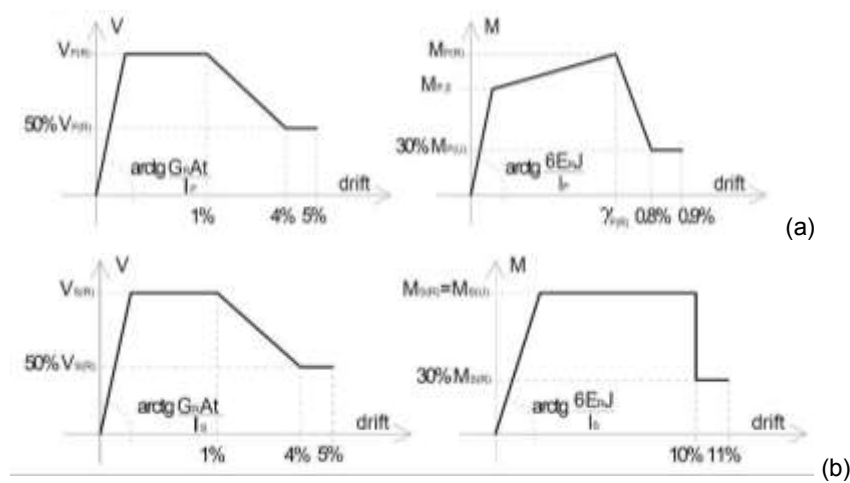


Figure 4.54 – Shear and bending behavior for the plastic hinges in (a) masonry piers and (b) spandrels (suffix “R” refers to unreinforced masonry)

It is evidenced that, in most of the available commercial structural programs allowing a pushover analysis of masonry buildings, the shear and bending resistances of the masonry elements ( $V_S$ ,  $V_P$ ,  $M_P$  and  $M_S$ ) are automatically calculated by the software through the equations reported in Table 4.36, once the shear ( $\tau_o$ ) and compressive strengths ( $f_{c,m}$ ,  $f_{hc,m}$ ) have been edited.

Some difficulties thus arise in the case of strengthened masonry, as the bending resistance of masonry piers differs from the value deduced through the Equation ( 4.17 ). Thus a special modification was introduced in the model, so to consider the actual resistance of reinforced piers in bending. In particular, the procedure consisted in the calculation of  $M_{P,0}$ , for each pier type, by means of Equation ( 4.19 ) and then in determine a fictitious compressive strength for the reinforced masonry in the vertical direction, imposing  $M_P = M_{P,0}$  in Equation ( 4.17 ) and solving for  $f_{c,m}$ . Moreover, the ratios  $M_{P(R)}/M_{P,0}$  were calculated so to define the slope of the hardening branch of the bending hinges.

#### 4.4.2 Method

Nonlinear static analyses (pushover) were performed on the considered numerical models, incrementing step-by-step the displacement at the centroid of the roof floor  $d_b$ ; the "capacity curves", representing the relation between the base shear force  $F_b$  and the displacement  $d_b$ , were obtained. The horizontal main directions of the seismic action (X and Y), both positive and negative, were considered; two loads distributions (a modal pattern, "S", and a uniform pattern, "M") were analyzed, according to EN 1998-1:2004.

To evaluate the maximum resisting ground acceleration  $a_{g,max}$  that the structure may support, the  $F_b-d_b$  capacity curve of the actual multi degree of freedom system (MDOF) was transformed to the  $F^*-d^*$  capacity curve of an equivalent single degree of freedom (SDOF) system, according to EN 1998-1:2004 and FEMA274:

$$F^* = \frac{F_b}{\Gamma} \quad d^* = \frac{d_b}{\Gamma} \quad (4.20)$$

being  $\Gamma$  the transformation factor, which depends on the mass  $m_i$  and the normalized displacement  $\phi_i$  of the i-th storey of the actual MDOF system:

$$\Gamma = \frac{\sum m_i \phi_i}{\sum m_i \phi_i^2} \quad (4.21)$$

Among the different procedures proposed in the literature for the evaluation of the seismic capacity of the buildings, as the N2 Method (Fajfar, 1999), the Coefficient and Secant Methods (FEMA274), etc., the modified Capacity Spectrum Method, based on equivalent viscous damping, was adopted (ATC 40; Freeman, 1998; Badoux, 1998; FEMA306; Freeman, 2004). This procedure was preferred to the N2-method suggested in Eurocode 8 (EN 1998-1:2004), as the hysteretic behavior of masonry structures is far away from that of reinforced concrete structures, from which Fajfar derived the N2-method.

The procedure is schematized in Figure 4.55, in a spectral pseudo-acceleration versus spectral displacement diagram. According to this approach, the maximum resistance ground acceleration  $a_{g,max}$  was thus determined searching for the design response spectrum, associated to the effective current period  $T_{eff}^*$  and damping  $\beta_{eff}$  of the structure, that is tangent to the capacity spectrum. It is evidenced that the intersection between the capacity spectrum and the design response spectrum defines the target displacement  $d_t^*$ . The value of  $d_t^*$  may be calculated by applying the equal displacement rule (4.22), as the effective period  $T_{eff}^*$  is normally greater than  $T_C$ :

$$d_t^* = S_D(T_{eff}^*; \beta_{eff}) = S_a(T_{eff}^*; \beta_{eff}) \left( \frac{T_{eff}^*}{2\pi} \right)^2 \quad (4.22)$$

where  $S_D$  and  $S_a$  represents the response spectrum in terms of displacement and acceleration, respectively. The effective period  $T_{eff}^*$  can be estimated through Equation ( 4.23 ), considering the secant stiffness of the idealized equivalent SDOF system,  $K_{eff}^*$ , defined as the slope of the line connecting the axis origin with the point of the capacity curve at target displacement  $d_t^*$ :

$$T_{eff}^* = 2\pi \sqrt{\frac{m^*}{K_{eff}^*}} \quad (4.23)$$

In case of  $T_C \leq T^* \leq T_D$ , the response spectrum acceleration  $S_a$  associated to the period  $T_{eff}^*$  and the damping  $\beta_{eff}$  is equal to:

$$S_a(T_{eff}^*; \beta_{eff}) = S a_g \eta_{eff} 2.5 \left( \frac{T_C}{T_{eff}^*} \right) \quad \text{with} \quad \eta_{eff} = \sqrt{\frac{10}{5 + \beta_{eff}}} \geq 0.55 \quad (4.24)$$

where  $a_g$  is the peak ground acceleration on type A ground,  $S$  the soil factor,  $T_D$  defines the beginning of the constant displacement response of the spectrum and  $\eta_{eff}$  is the effective damping correction factor, which depends on the effective equivalent viscous damping  $\beta_{eff}$ . Generally,  $\beta_{eff}$  is influenced by the structure global ductility at the considered target and by the shape of the hysteresis relation, at that ductility level, and is expressed by means of a sum of a viscous damping, inherent in the structure ( $\beta_{el}$ , commonly assumed equal to 5%), and the hysteretic damping  $\beta_{hys}$ :

$$\beta_{eff} = \beta_{el} + \beta_{hys} \quad (4.25)$$

The maximum ground acceleration  $a_{g,max}$  that may be supported by the structure is evaluated by substituting Equation ( 4.24 ) into Equation ( 4.22 ):

$$a_{g,max} = \frac{4\pi^2 d_t^*}{S \eta_{eff} 2.5 T_C T_{eff}^*} \quad (4.26)$$

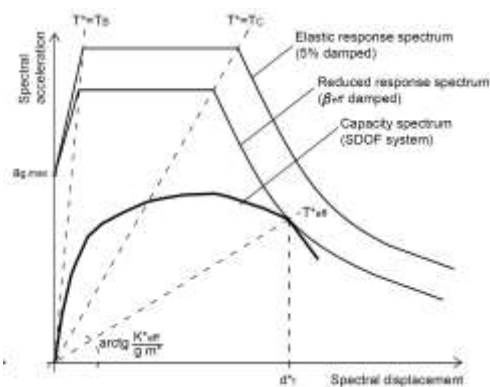


Figure 4.55 – Schematization of the procedure for the evaluation of the maximum ground acceleration  $a_{g,max}$

#### 4.4.3 Results and discussion

The unreinforced and reinforced cases were analysed. At first, a modal analysis was performed so to investigate on the fundamental vibration period and the effective modal masses. The vibration periods of the two storeys, unreinforced structures resulted of about 0.15 s and 0.26 s, in X and Y direction, respectively. Higher values emerged for the three storeys buildings (0.22 s and 0.41 s, on average). A 30% reduction of vibration periods emerged in reinforced models, in respect to those of unreinforced structures, due to the higher masonry stiffness determined by the strengthening intervention (Table 4.35). The first and the second vibration modes resulted of translational type, respectively in Y and X direction, and excited about 76% to 91% of the modal mass.

The nonlinear static analyses were then carried out and the capacity curves due to a distribution of the equivalent lateral loads proportional to the modal shape or to the storey masses, for both main directions of the seismic force were drawn. Figure 4.56 - Figure 4.57 show the capacity curves for solid brick and rubble stone masonry buildings, respectively. As resisting elements attained to ultimate displacement, a progressive drop of resistance in the global capacity curves occurred: the curves were cut when a 15% reduction of the peak load was reached. To make the figures easily readable, only the curves concerning the distribution of the equivalent lateral loads proportional to the modal shape ("S") were plotted, as always determined the lower values of  $a_{g,max}$ . The curves are related to a positive direction of the controlled displacement  $d_b$ . The curves related to a negative direction present identical trends for the regular buildings, due to symmetry; very similar trends emerged also for the non-regular in plan buildings.

The different structures were distinguished by an identifier (ID) which indicates the number of storeys (2 or 3), the in-plan regularity (R) or non-regularity (I), the type of masonry (S for solid brick, R for rubble stone) and the presence of the reinforcement (U for unreinforced, R for reinforced masonry).

The lower amount of masonry resisting elements in Y direction, in respect to X one, and the distribution on the vertical loads transmitted by floors resulted, in general, in a minor shear resistance for the buildings.

The capacity curves of the three-storey unreinforced structures showed an elastic-plastic path, with ultimate displacement attained at about 25-30 mm both for solid brick and rubble stone masonry. Differently, the capacity curves of the two-storey unreinforced buildings manifested a lower ultimate displacement (about 15-20 mm). The inelastic status of the plastic hinges in the numerical models evidenced that the failure occurred in consequence of the shear collapse of several spandrels and then the progressive bending failure of the piers of the external walls, at the

ground floor. This type of failure is typical of buildings classified as “weak spandrels” structures (Tomazevic, 1999), which actually resulted quite frequent configurations. This was due to the relatively high shear and bending resistances of the vertical elements, in respect to the poor shear strength of spandrels, due to the contribution provided by vertical axial loads. In fact, similar failure mechanism were obtained by many researchers, both adopting simplified macro-elements strategies and homogenised numerical modeling (Akhavessy & Milani, 2013).

The reinforced masonry buildings capacity curves evidenced, in general, considerably improved performances in respect to those of unreinforced masonry ones. In fact, the shear resistance increased from 81% to 123% in X direction and from 96 to 163% in Y direction. Moreover, the increments in terms of ultimate displacement capacity resulted of about 109% and 132%, respectively.

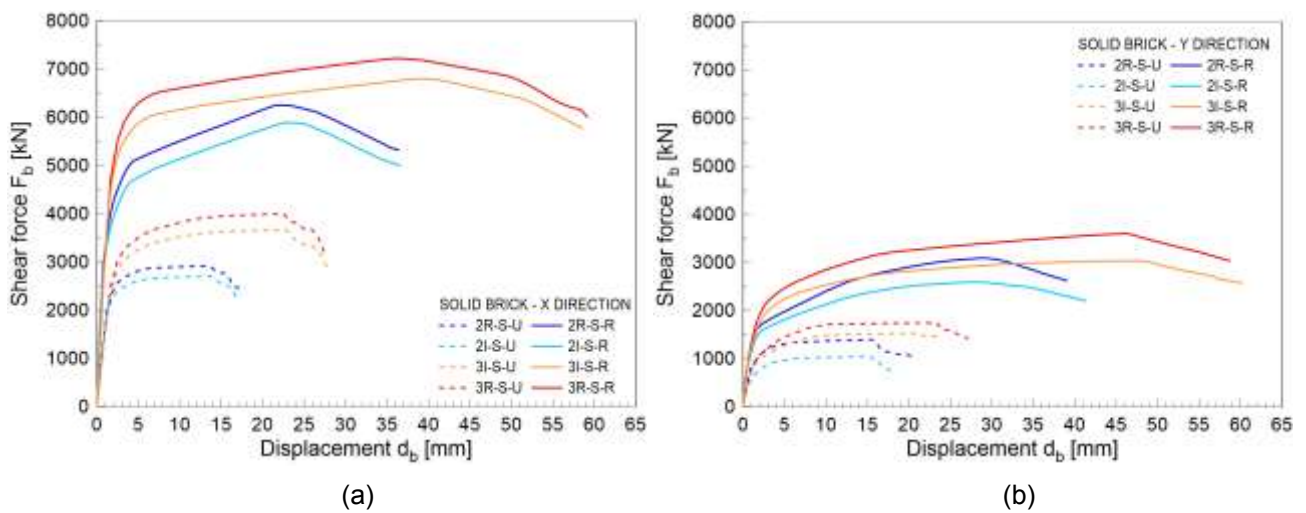


Figure 4.56 – Capacity curves of the solid brick unreinforced and reinforced masonry buildings in the X (a) and Y (b) direction - modal pattern “S”

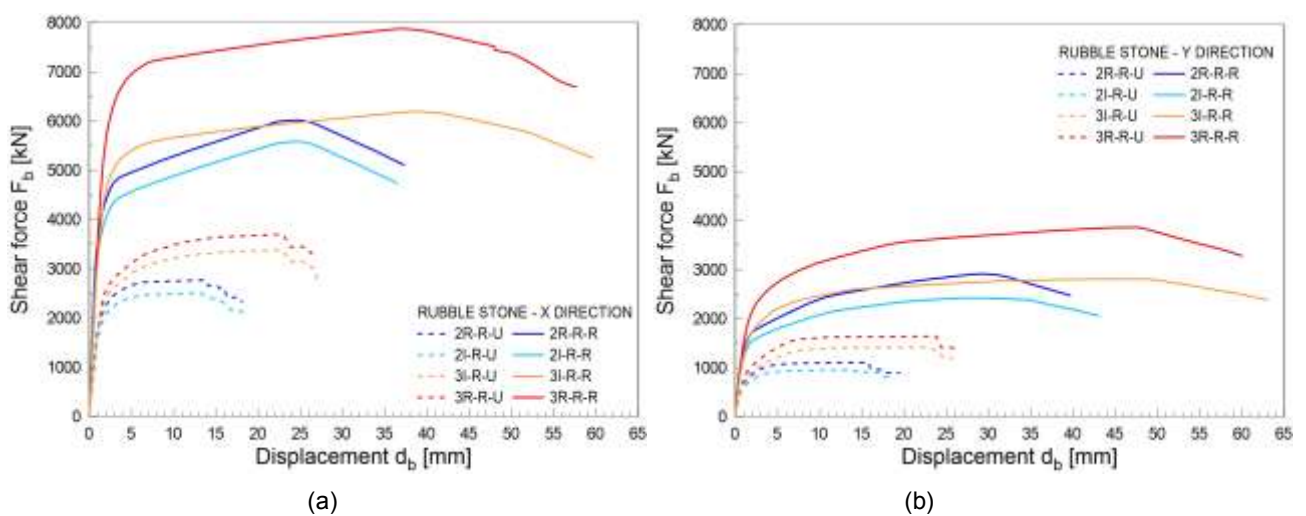


Figure 4.57 – Capacity curves of the rubble stone unreinforced and reinforced masonry buildings in the X (a) and Y (b) direction - modal pattern “S”.

The capacity curves of the reinforced masonry buildings in X direction evidenced an initial elastic branch followed by a second branch with decreasing stiffness, as the spandrels began to plasticise in shear and the piers both in bending and in shear. A gradual decrease of the global resistance capacity was then noted in consequence of the bending or the shear collapse of some piers of the external walls, at the ground floor. Also the capacity curves in Y direction evidenced an initial elastic branch; as the spandrels (in shear) and the piers (in bending and shear) exceeded the elastic range, the curves show a gradual stiffness reduction. Once the peak global resistance was reached, the shear force dropped down, as the bending failure of all the piers at the ground floor occurred almost simultaneously. The ultimate displacements attained by the reinforced masonry buildings were about 55-60 mm and 35-40 mm for the three-storey and two-storey structures, respectively.

The results showed that, in general, the in-plane bending action in reinforced masonry piers may be significant and sometimes may lead to the bending failure of the resisting element. This evidences the great importance of an appropriate application of the reinforcement, respecting the adequate anchorage and development lengths for the GFRP mesh. Diversely, the seismic performance of the building will be severely compromised, prejudicing the benefits of the reinforcement on the both in bending and shear.

According to the method described in 4.4.2, the capacity curves of the actual MDOF systems were transformed to those of equivalent SDOF ones and the values of peak load ( $F^*_{max}$ ), target displacement ( $d^*_t$ ), effective stiffness ( $K^*_{eff}$ ) and effective period ( $T^*_{eff}$ ) were calculated. The resisting ground accelerations  $a_{g,max}$  that may be supported by the structures were then derived. The main results are summarized in Table 4.37, referring to the distribution of the lateral loads proportional to the fundamental mode shape (S). In fact, as stated before, the values of resisting ground acceleration obtained from this load pattern were, in the analysed cases, always lower than those associated to the uniform pattern (M).

It is evidenced that the values of the resisting ground acceleration  $a_{g,max}$  were calculated according to Equation ( 4.26 ), assuming, for the evaluation of the effective damping correction factor  $\eta_{eff}$ , a value of effective equivalent viscous damping  $\beta_{eff}$  equal to 15%. This value was estimated considering the dissipative capacities of the different resisting elements deduced from the experimental results. In particular, in Gattesco & al. (2016) was evidenced that masonry spandrels with effective tie beams which exceed a 1% drift show a constant value for the hysteretic damping  $\beta_{hys}$  of about 15%. On the other hand, from the experimental shear-compression tests (Gattesco & al., 2015b)  $\beta_{hys}$  for drift up to 1% resulted on average equal to 15% for unreinforced masonry piers. A similar value was obtained also by Magenes & Calvi (1997) for unreinforced masonry piers failing in bending.

Thus, according to ( 4.25 ), an effective equivalent viscous damping  $\beta_{eff}$  equal to 20% may be considered for the unreinforced masonry buildings in case that all the resisting elements perform plastic deformations. However, as some spandrels and piers of the floor level remained in the elastic range,  $\beta_{eff}$  was reasonably reduced to 15%, according to the value of equivalent viscous damping for unreinforced masonry buildings suggested in NZSEE 2006. Similar values were also found by Magenes (2000) and Jahved (2009). Prudentially, the same value was assumed also for reinforced masonry buildings. However, a study to deepen this aspect is in progress.

Table 4.37 – Seismic performances of the analyzed buildings: peak load ( $F^*_{max}$ ), target displacement ( $d^*_t$ ), effective stiffness ( $K^*_{eff}$ ) and effective period ( $T^*_{eff}$ ) of the equivalent SDOF systems, resisting ground accelerations ( $a_{g,max}$ ) and ratio between  $a_{g,max}$  of reinforced (R) and unreinforced (U) structures

X DIRECTION							Y DIRECTION						
ID	$F^*_{max}$ [kN]	$d^*_t$ [mm]	$K^*_{eff}$ [kN/mm]	$T^*_{eff}$ [s]	$a_{g,max}$ [g]	$a_{g,max(R)}/a_{g,max(U)}$	ID	$F^*_{max}$ [kN]	$d^*_t$ [mm]	$K^*_{eff}$ [kN/mm]	$T^*_{eff}$ [s]	$a_{g,max}$ [g]	$a_{g,max(R)}/a_{g,max(U)}$
2R <sub>S</sub>	U 2312.1	15.12	123.04	0.625	0.137	1.98	2R <sub>S</sub>	U 1134.6	16.30	53.72	0.957	0.095	2.07
	R 4965.5	28.91	146.10	0.604	0.271			R 2518.3	31.84	67.12	0.902	0.197	
2R <sub>R</sub>	U 2200.4	14.38	136.71	0.634	0.126	2.01	2R <sub>R</sub>	U 905.5	14.25	70.13	0.896	0.080	2.28
	R 4787.5	29.63	137.22	0.662	0.253			R 2381.4	32.40	62.38	0.994	0.182	
2I <sub>S</sub>	U 2138.9	13.21	151.36	0.530	0.138	2.02	2I <sub>S</sub>	U 843.0	13.49	67.67	0.800	0.087	2.25
	R 4666.0	29.00	136.58	0.588	0.279			R 2091.9	33.39	53.25	0.952	0.196	
2I <sub>R</sub>	U 1988.9	14.61	113.10	0.656	0.121	2.11	2I <sub>R</sub>	U 773.0	14.38	48.57	1.012	0.079	2.25
	R 4433.3	28.95	130.04	0.642	0.255			R 1962.5	34.82	47.91	1.068	0.178	
3R <sub>S</sub>	U 3165.5	21.76	142.75	0.674	0.170	1.82	3R <sub>S</sub>	U 1396.7	21.72	74.48	0.949	0.109	1.96
	R 5716.5	46.83	101.51	0.848	0.309			R 2881.9	47.04	51.66	1.208	0.214	
3R <sub>R</sub>	U 2928.5	21.21	126.61	0.799	0.145	2.01	3R <sub>R</sub>	U 1317.3	20.20	69.06	1.100	0.095	2.15
	R 6234.3	45.60	116.16	0.875	0.291			R 2970.6	46.12	54.73	1.298	0.204	
3I <sub>S</sub>	U 2867.8	21.75	123.81	0.807	0.143	1.89	3I <sub>S</sub>	U 1203.3	19.18	57.53	1.199	0.087	2.03
	R 5316.9	45.77	98.68	0.944	0.270			R 2391.9	47.50	42.80	1.452	0.177	
3I <sub>R</sub>	U 2646.6	21.12	119.71	0.891	0.125	2.12	3I <sub>R</sub>	U 1118.6	19.35	60.06	1.275	0.078	2.32
	R 4841.7	46.55	88.19	0.998	0.265			R 2189.4	48.91	38.05	1.540	0.181	

A comparison between the values of  $a_{g,max}$  obtained from unreinforced and reinforced masonry buildings is illustrated in Figure 4.58, so to evidence the global seismic enhancement due to the application of the strengthening technique. As an example, the values of  $a_{g,max}$  were also compared with a ground acceleration local demand  $a_{g,req} = 0.17$  g, evaluated from a hypothetical reference ground acceleration of 0.14 g and assuming an amplification of 20% so to consider an importance factor for buildings whose seismic resistance is of importance in view of the consequences associated with a collapse (e.g. schools, assembly halls, cultural institutions - EN 1998-1:2004).

Considerably scarce values of resistance acceleration came out for all the unreinforced masonry cases, in respect to the seismic demand. Lower values were obtained in Y direction. In fact, the ratios  $a_{g,max}/a_{g,req}$  resulted of about 0.8 for X direction and 0.5 for Y direction.

In the reinforced masonry cases, the seismic capacity of the structures resulted always higher than the request, as the ratio  $a_{g,max}/a_{g,req}$  for both the main directions was about 1.4. The increments in terms of resisting ground acceleration due to the application of the reinforcement resulted on average 99% in X direction and 117% in Y direction.

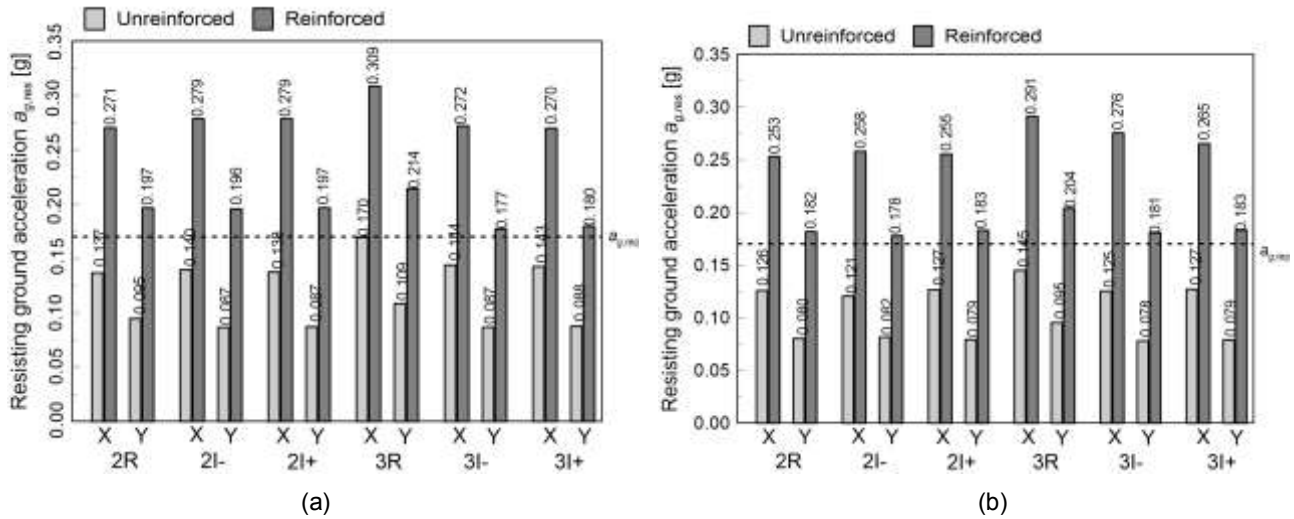


Figure 4.58 – Seismic performances of (a) solid brick and (b) rubble stone masonry structures, in terms of  $a_{g,max}$ , and comparison with a the seismic demand  $a_{g,req}$

These results are referred to the analysed building configurations so, to give more generality to the study, it is necessary to extend the analyses to other types of buildings (varying shape, geometry of elements, masonry type, etc.). Moreover, further experimental tests are needed to investigate the performances of reinforced masonry elements failing for in-plane bending. In fact, the study evidenced that the behavior of reinforced buildings is largely influenced by the type of collapse (bending or shear), so the actual behavior of flexural plastic hinges requests further investigations. Moreover, this first preliminary analysis evidenced the need of a deep study on the actual hysteretic behavior of reinforced structures at post yielding and ultimate limit states, so to more accurately calibrate the effective damping and guarantee a correct assessment of the reduced response spectrum.

## 4.5 Summary

The results of several diagonal compression test carried out on masonry specimens to check the in-plane effectiveness of the GFRM technique were reported. Different types of masonry were tested (solid brick, rubble stones and cobblestones) and variations in the masonry thickness, resistance, units characteristics and arrangement were considered. 74 diagonal compression tests on solid brick masonry and 34 on stone masonry (rubble stone and cobblestones), unreinforced and reinforced, were performed. The influence of the mortar coating at the varying of its mechanical characteristics and of that of the embedded GFRM meshes was evaluated experimentally.

In unreinforced masonry specimens a diagonal crack occurred along the force direction: in solid brick masonry, the crack spread rapidly, resulting in an abrupt decrease of masonry resistance while in samples made with rubble units or cobblestones a slower decrease of the resistance occurred after crack formation. In reinforced specimens, several parallel cracks generally formed in the mortar coating. The GFRP mesh intervened in the cracked areas of the plaster: the reinforcement contrasted the opening of cracks supporting tensile stresses, resulting in a gradual and moderate decrease of the resistance in the post-peak branch, up to the tensile failure of the mesh wires and the progressive damaging of the mortar among the cracks.

In regard to unreinforced masonry samples, it was observed that the greater was the masonry mortar resistance, the higher values of both shear modulus and resistance were attained. The reinforcement led to appreciable improvements in both resistance and dissipative capacities of samples. A comparison of the results with those of some specimens strengthened with steel weld fabric reinforced mortar coatings showed almost a similar behavior. The important role of an effective reinforcement embedded in the mortar plaster was clearly evidenced by comparing specimens with GFRP reinforced and plain mortar coating. Differently, diagonal compression tests did not permit to evidence the important role of the connectors in the exploitation of the reinforced mortar coating resistance contribution, which are, instead, fundamental in the presence of an axial compression.

The resistance increment ratios generally ranged from 1.5 to 2.1 for both in 250 mm and in 380 mm thick solid brick masonry. Lower values (about 1.2-1.7) emerged for 380 mm thick infill masonry. Peak loads resulted on average 1.7-1.9 times that of unreinforced masonry for rubble stone reinforced samples, but significantly higher values (3.2) were obtained in weaker masonry panels. Also in cobblestones samples the resistance increment ratios resulted very high: they ranged from 3.2 to 4.5, depending on the plain masonry strength characteristics.

The elastic deformability and the peak resistance of reinforced masonry samples resulted limitedly affected by the type of GFRP mesh used, because the tensile strength of the reinforced coating is very little influenced by the composite before cracking. However, a lower mesh grid dimension resulted in general in a higher diffusion of cracks, while lower reinforcement percentages determined a more pronounced resistance degradation. It was also evidenced that a too close mesh pitch dimension may induce a premature failure of the reinforcement, due to a progressive delamination of the plaster covering the GFRP mesh.

Some considerations on the influence of the mortar of the coating type were done. In general, it was observed that the mortar mechanical characteristics influenced the effectiveness of the technique. In particular, an increasing of the resistance increment ratios at the increasing of the mortar tensile strength was observed. However, the dependence from a single mechanical parameter (i.e. the mortar tensile strength, Young modulus or compressive strength) was not clear; so, it is likely a combined effect of the main parameters of the reinforced coating that affected the reinforced masonry performances. Moreover, by analysing post-peak behavior of reinforced samples curves, it was observed that the decrease of resistance (slope of the post-peak branch) occurred more rapidly in specimens which attained to higher peak loads and that the curves tended to converged at the increase of the deformations. However, the premature failure at the masonry-mortar interface level may prejudice the post-peak benefits of the reinforcement, leading to a more brittle collapse.

From the results of the experimental tests, the values of the equivalent principal tensile strength of the specimens associated to the peak load were derived and analytical formulations were then proposed to assess the stiffness, the resistance and, thus, the equivalent tensile strength and shear strength of reinforced masonry specimens. The resistance calculation was conducted by adding to the plain masonry resistance that of the coating and multiplying the result by a coefficient calibrated according to the characteristics of the coupled materials. The analytical predictions showed a good reliability and evidenced that the simple summation of the resistances of the masonry and the coating is not always on the safe side for brittle masonry types, such as solid brick ones. An interpretation of the resisting mechanism acting in reinforced masonry panels, based on experimental evidences and analytical considerations, was also provided.

The research proceeded with some numerical investigations on the actual equivalent stress state in the reinforced panels; it was thus possible to deduce some interesting considerations on the peak load of reinforced samples at the varying of mortar characteristics. Moreover, a preliminary, simplified modeling for the prediction of the post-peak behavior of reinforced samples was proposed. Even considering a single mortar coating type, the model resulted able to reproduce with good reliability the experimental performances at the varying of the masonry characteristics.

The global seismic response of some masonry buildings, before and after the application of the GFRM reinforcement, were compared by means of numerical simulations performed on an Equivalent Frame model, applying the nonlinear static analysis (pushover) and considering the in-plane nonlinearity of piers and spandrels by means of plastic hinges. In particular, four building configurations were considered and two different types of masonry were assumed: solid bricks and rubble stones. The force-displacement capacity curves were derived considering two horizontal forces distributions: proportional to the first mode and proportional to the masses. Moreover, the Capacity Spectrum Method was adopted for the evaluation of the maximum ground acceleration that the buildings may support, considering the effective current period and damping of the structures at collapse. It emerged that the shear resistance of the analysed reinforced masonry buildings ranged from 1.8 to 2.6 times that of unreinforced ones and that the ultimate displacement capacity was almost doubled. Low values of the maximum resisting ground acceleration were obtained for unreinforced buildings (ranging mostly from 0.08 g to 0.14 g), resulting in inadequate seismic performances when compared with the demand (0.17 g). The masonry strengthening permitted a considerable increase of the ground resistant acceleration, reaching values ranging from 0.18 g to 0.31 g.

## **5 OUT-OF-PLANE BEHAVIOUR**

As already evidenced in subsection 2.1.1, in most cases, the out-of-plane wall failure in existing masonry buildings may be inhibited providing an adequate in-plane stiffness to the floors and an effective connection among perpendicular walls and between the walls and the horizontal diaphragms. Once these structural deficiencies have been amended, attaining, thus, to the so called “box behavior”, the distribution of the seismic action among the vertical resisting elements depends on their stiffness and the building failure is generally due to the in-plane collapse of the masonry walls. However, in masonry structures with high interstorey distance (4-5 m), the out-of-plane bending actions may be relevant, constituting a great problem especially in upper storeys of tall buildings, where the out-of-plane forces are higher, the axial load is reduced and, frequently, walls are thinner than those at lower levels.

In this section, the out-of-plane performances of masonry walls reinforced with the GFRM technique are investigated and discussed in detail. In particular, some experimental results concerning four-point bending tests on full-scale unreinforced and reinforced masonry specimens are described. Then, analytical correlations for the evaluation of the out-of-plane bending resistance of reinforced masonry walls are presented. Moreover, a numerical model for the simulation of the out-of-plane behaviour of reinforced masonry is proposed. The model permitted to perform a parametric study to evaluate the influence of the material characteristics on the specimens global performances and to investigate on the actual behaviour of reinforced masonry walls.

Finally, by adopting a similar numerical model, a study was conducted on the behaviour of unreinforced and reinforced masonry barrel vaults subjected to vertical and horizontal loads acting in the direction perpendicular to the vault axis.

### **5.1 Experimental four-point bending tests**

The characteristics and the results of some experimental out-of-plane tests on masonry specimens are described and discussed in this subsection. Test were performed so to assess the effectiveness of the considered reinforcing technique in terms of resistance and displacement capacity, by comparing the results of four-point bending tests on unreinforced and reinforced full-scale masonry samples (Gattesco & Boem, 2014).

The characteristics of the specimens, the test setup, the loading procedure and measurements, the results and discussion are reported in the following.

### 5.1.1 Specimens characteristics

The out-of-plane experimental campaign concerned full-scale masonry specimen 3000 mm high and 1000 mm wide, of three different masonry types:

- solid brick, 250 mm thick (S) - Figure 5.1.a;
- rubble stones, 400 mm thick (R) - Figure 5.1.b;
- cobblestones, 400 mm thick (C) - Figure 5.1.c.

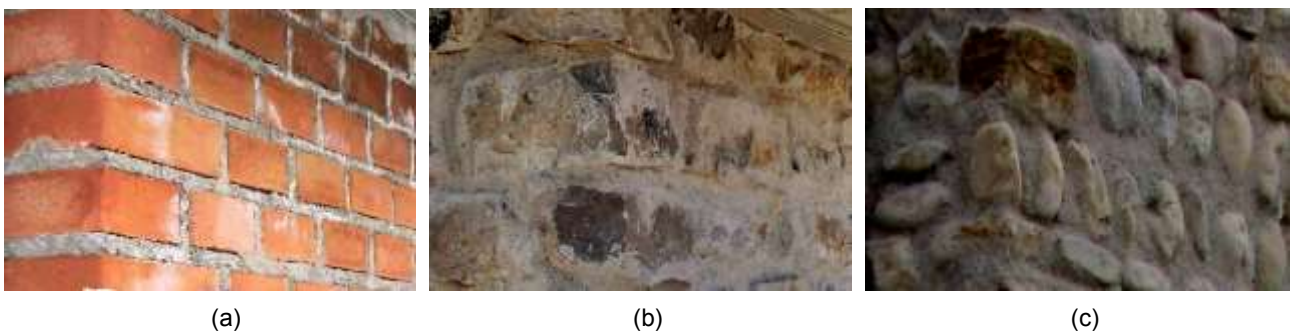


Figure 5.1 – Details of the masonry surface in (a) solid brick, (b) rubble stone and (c) cobblestones samples

In solid brick “S” masonry specimens (Figure 5.2.a), the bricks ( $55 \times 120 \times 250 \text{ mm}^3$ ) were all arranged according to the header bond pattern (single skin walls); 3/4 bat bricks were used at the lateral edges. The average resistance of solid bricks subjected to compression tests was 44.0 MPa (EN 772-1:2011+A1:2015). The mortar bed joints and vertical joints were 10 mm thick and had a flush profile. An hydraulic lime mortar made of 390 kg of binder per  $\text{m}^3$  of mortar was employed (type “B6” in Table 4.1,  $f_{c,m} = 5.26 \text{ MPa}$ ).

Stone elements were all sandstones and were arranged as close as possible so to limit the mortar joint dimensions. In rubble stone “R” masonry (Figure 5.2.b), the unit dimensions were roughly  $130 \times 230 \times 200 \text{ mm}^3$  (respectively height, width and depth) and the same hydraulic lime mortar used in solid brick samples (“B6”) was employed.

Cobblestones “C” masonry specimens (Figure 5.2.c) had elements with average dimensions  $90 \times 90 \times 130 \text{ mm}^3$ . An hydraulic lime mortar made of 320 kg of binder per  $\text{m}^3$  of mortar was utilized (type “B3” in Table 4.1,  $f_{c,m} = 2.93 \text{ MPa}$ ).

One unreinforced specimen and a reinforced one for each masonry type were subjected to four-point bending, so to compare the results and check the effectiveness of the reinforcement technique. To avoid local damage of the masonry at the base, the samples were built on a 50 mm

thick concrete basement, casted on a timber bench. The bench was removed before testing (subsection 5.1.2).

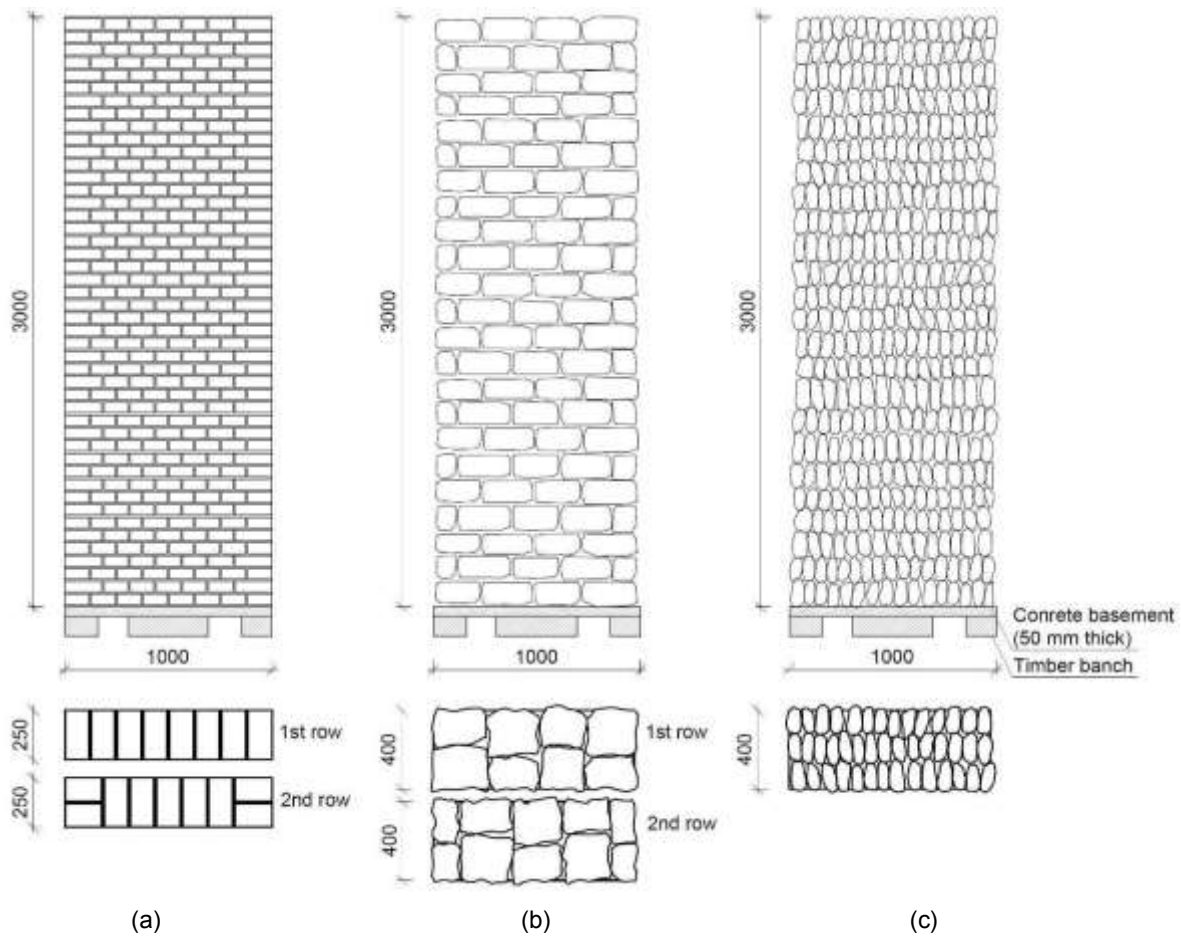


Figure 5.2 - Units arrangement in out-of-plane bending samples made of (a) solid brick, (b) rubble stone and (c) cobblestones masonry

The samples were designed by using preliminarily the analytical relationships presented in subsection 5.2.2 – Equation ( 5.7 ), so that the reinforced masonry flexural resistance ranged between 4 to 5 times that of the unreinforced walls and verifying that other types of failures (due to shear in masonry or to FRM delamination from masonry) did not anticipate the collapse.

The reinforcement was applied after about 8 days from the building of the masonry panel: at first, the masonry surfaces were wetted, so to avoid the absorption of the water of the mortar, then a cement based scratch coat (dosage 600 kg of cement per  $m^3$  of mortar) was applied. Passing through holes, 25 mm diameter, were drilled in the masonry and the GFRP mesh was positioned, leaving a gap from the substrate surface of about 15 mm. Couples of L-shaped GFRP connectors were inserted in the holes, assuring a lap splice of 120 mm; additional GFRP mesh devices ( $150 \times 150 \text{ mm}^2$  elements of a  $33 \times 33 \text{ mm}^2$  GFRP mesh) were introduced in correspondence of the

connectors, above the main mesh. The holes were then injected with a thixotropic cementitious mortar; then, the mortar layer was applied, assuring a minimum thickness of 30 mm. A lime and cement mortar was used for the plaster, with 66x66 mm<sup>2</sup>, type “S” GFRP mesh embedded (subsection 3.2). In particular, A “C4” lime and cement mortar (Table 4.3) was used for the plaster ( $f_{t,c} = 1.10$  MPa,  $f_{c,c} = 6.90$  MPa,  $E_c = 14.4$  GPa).

As evidenced in subsection 4.1.1, in solid brick masonry, the thickness of the mortar coating resulted approximately constant, due to the high planarity of the masonry surface (Figure 5.1.a); thus an average thickness about 30 mm can be assumed. Differently, in stone masonry, as the faces were more irregular, due to the blocks geometry, an average thickness higher than 30 mm resulted. In fact, the average thickness of the mortar coating in rubble stone (Figure 5.1.b) and cobblestones reinforced samples (Figure 5.1.c) was estimated equal to 35 and 45 mm, respectively.

The GFRP meshes were arranged so that the twisted fibers wires resulted oriented in the vertical direction of the masonry wall. 4 passing-through connections per square meter were applied; the connector disposition is illustrated in Figure 5.3.

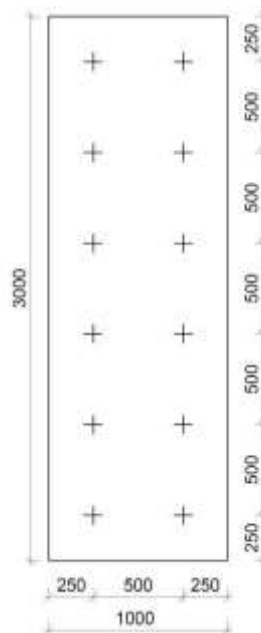


Figure 5.3 - Positioning of the connections in reinforced masonry samples.

The tested samples are summarised in Table 5.1. The specimens are distinguished by an identifier split in three parts: the first refers to the type of test (F for bending tests) and to the masonry group (S = solid bricks, R = rubble stones and C = cobblestones), the second indicates the type of masonry mortar (Table 4.1) and the latter distinguishes unreinforced masonry (U) and masonry strengthened with the GFRM technique (R).

Table 5.1 - Main characteristics of the out-of-plane bending samples

ID	Masonry mortar	Mortar coating	Reinforcement	Connections
FS-B6-U	B6	-	-	-
FS-B6-R	B6	C4	GFRP 66X66S	GRFP 4/m <sup>2</sup>
FR-B6-U	B6	-	-	-
FR-B6-R	B6	C4	GFRP 66X66S	GRFP 4/m <sup>2</sup>
FC-B3-U	B3	-	-	-
FC-B3-R	B3	C4	GFRP 66X66S	GRFP 4/m <sup>2</sup>

### 5.1.2 Tests apparatus

The out-of-plane behaviour of the masonry specimens was assessed through four-point bending tests, performed by applying two forces at the thirds of the height, with direction perpendicular to the wall surface. This type of test was chosen so to reproduce as close as possible the actual load pattern, by using a simple and easy to monitor setup. Three-point bending tests (ASTM C78/C78M-16) are not able to evidence the capacity of the GFRP reinforced mortar coating to distribute the cracks, as the stresses are concentrated in a small region, inducing the sample cracking at the loading height, rather than allowing to fail at its weakest point. Differently, four-point bending tests induce an approximately constant flexural stress in the central area, suitable to investigate on the flexural behavior of the reinforced masonry.

The reaction frame, illustrated in Figure 5.4, was composed by H-shaped steel profiles assembled together with bolts. In particular, two horizontal beams HEA 160, connected by two vertical struts HEA 200, were placed in contact with the top and the bottom ends of one sample face.

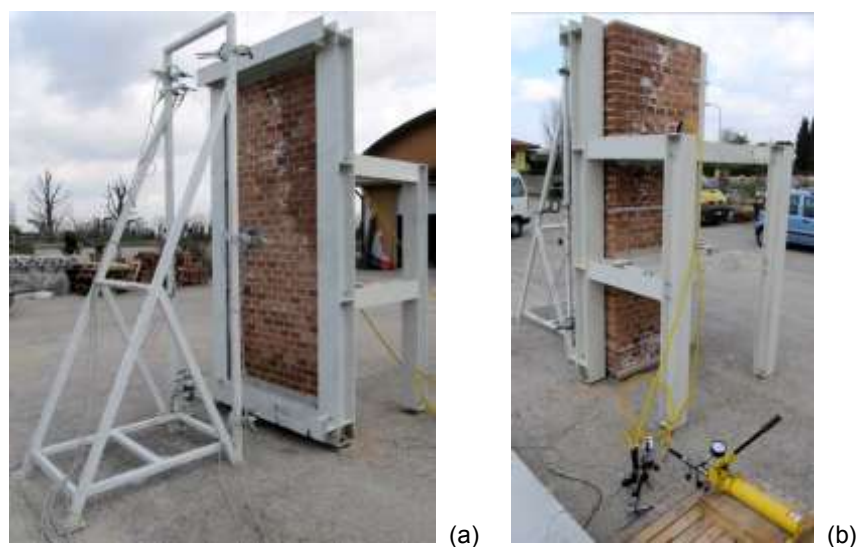


Figure 5.4 – Global views of the experimental apparatus for out-of-plane bending tests: (a) front and (b) back side

On the opposite side, the horizontal loads were applied by two hydraulic jacks associated in parallel (ENERPAC mod. RC-154, 142 kN each, stroke 101 mm) and governed by a hand pump (ENERPAC, mod. P84, 700 bar). The jacks were contrasted by a frame made of HEA 160 steel elements, which was bolted with the main vertical struts.

The jacks were located at the centre of the apparatus width, in correspondence of two horizontal beams of the contrast frame, positioned at the thirds of the specimen height. For the load application, an HEA 160 steel element was placed between each jack and the masonry sample, so to allow the distribution of the load to the whole masonry width. These elements were supported by the contrast frame, but their horizontal sliding was permitted (Figure 5.5.a).

All the contact areas between the specimens and the reaction frame were designed so to allow the samples rotation. In particular, steel smooth bars, 40 mm diameter, were welded to the two metallic profiles in the loading areas (Figure 5.5.a) and to the upper (Figure 5.5.b) and lower (Figure 5.5.c) contrast horizontal beams. Moreover, to permit a uniform application of the load along the whole width of the specimen, steel plates 10x150x1000 mm<sup>3</sup> were fixed on the masonry through screws and nylon dowels, in the four contact areas. Moreover, in unreinforced samples, a thin levelling layer of gypsum was applied between the plates and the masonry.

So to allow the specimen base rotation, the specimen base support was composed by a steel plate, placed on the ground, to which a metallic smooth bar, 40 mm diameter, was welded. The bar was oriented along the sample width, in correspondence of the half of the masonry thickness. A steel plate was interposed between the bar and the concrete basement of the sample, so to allow the stress distribution (Figure 5.5.d). Slots created in the timber basement on which the samples were built allowed the insertion of the mechanical lifting devices (plates, bolts and nuts), the removal of the timber elements and the positioning of the metallic base support.

The verticality of the apparatus and the correct height of the loads application were ensured by the adjustment of bolts couples fixed on steel plates placed on the ground in correspondence of the four feet of the metallic frame (Figure 5.5.e).

All metallic elements were made of steel S235 (EN10027-1:2005, 2005) and were jointed through M16 steel bolts (UNI EN14399:2015) with cl. 6.8 fasteners and cl. 6 nuts.

The main characteristics of the test apparatus are schematised in Figure 5.6. The elastic deformation was estimated through a pinned nodes frame schematization; it resulted a deformation of about 0.13 mm in correspondence of a global horizontal force of 1 kN.

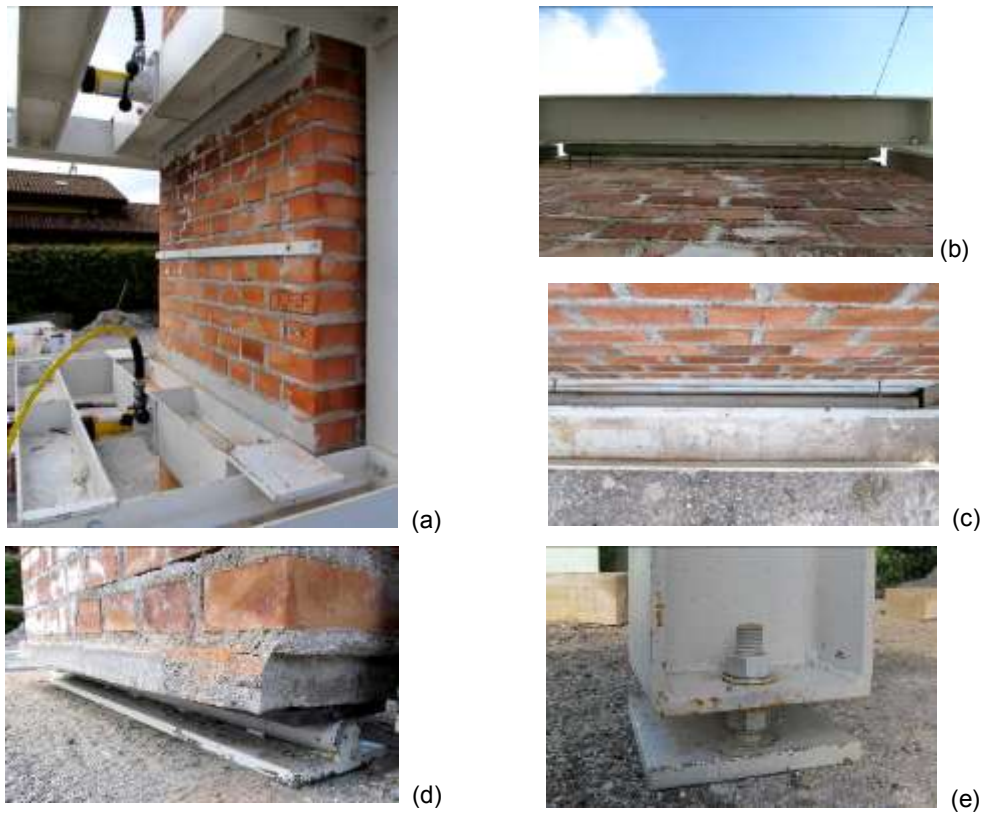


Figure 5.5 – Details of the apparatus for out-of-plane bending tests: (a) loading area, (b) upper and (c) lower steel contrasts (d) base support and (e) adjustable feet

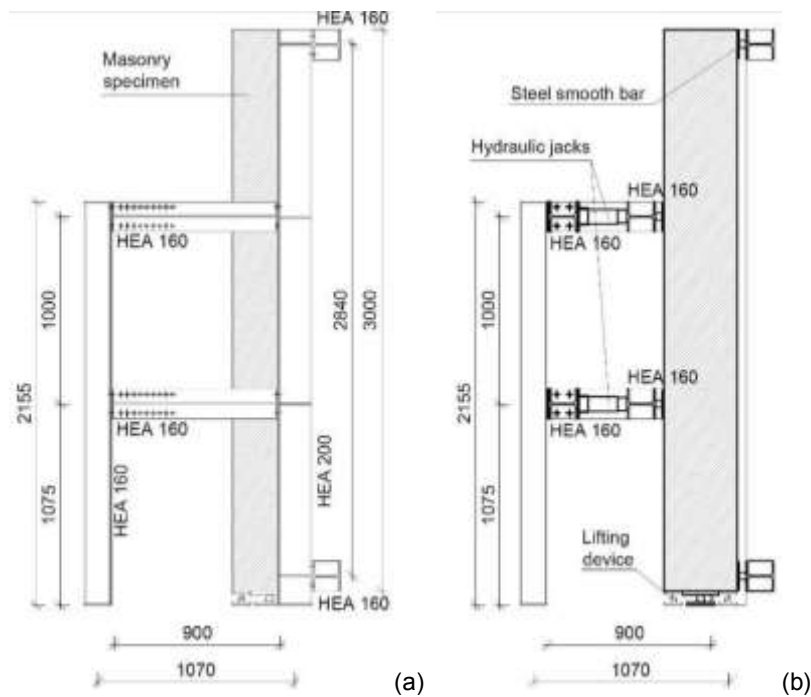


Figure 5.6 - Experimental apparatus for out-of-plane bending tests: (a) lateral view and (b) vertical section in the transversal direction

### 5.1.3 Loading procedure and measurements

Loading-unloading cycles were performed up to the occurrence of the first cracking; then the tests were prosecuted controlling the wall deflection. The applied force was measured with a pressure transducer (AEP Transducers, mod. LAB TP14, error 0.05%).

The loading steps were of about 1/3 of the estimated cracking load (3 kN for the solid brick unreinforced specimen, 5 kN for stones plain specimens and 10 kN for all the reinforced samples).

Linear and rotary potentiometer transducers were applied (Figure 5.4.a), so to evaluate the actual out-of-plane deflection performances. All the transducers were fixed to an external steel tripod and were connected to the specimen through thin metallic wires and hooks. In Figure 5.7 it is shown the position of the potentiometer transducers: 10 on the front face of the panel (Figure 5.7.a) and 4 on the back side (Figure 5.7.b). In particular, 6 linear transducers GEFTRAN LT, mod. PA1, 50 mm stroke (T3, T4, T7, T8), 6 linear transducers GEFTRAN LT, mod. PA1, 25 mm stroke (T1, T2, T9, T10, T11, T14), 2 rotary transducers VISHAY SPECTROL mod. 534-1, 180 mm stroke (T12, T13) and 2 rotary transducers UNIMEASURE mod. LX-PA-10, 250 mm stroke (T5, T6) were employed.

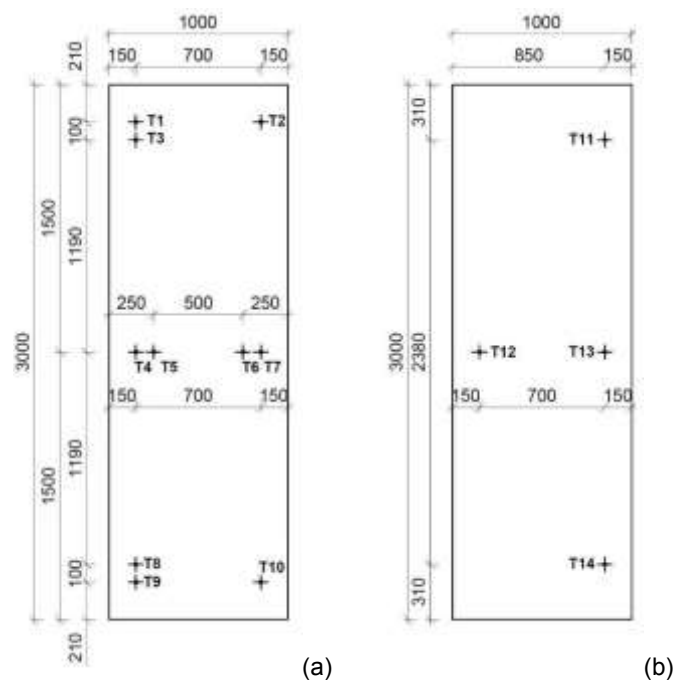


Figure 5.7 – Position of the displacement transducers (a) on the front and (b) on the back side of the samples

The horizontal displacement at the middle height of the specimen, on the front side, was monitored through transducers T4 and T7. Moreover, two additional potentiometers with higher stroke (T5 and T6) were installed, so to detect high displacements. Transducers T1, T2, T9, T10

detected the wall displacements close to the upper and lower steel contrasts, due to possible vertical or horizontal misalignment of the wall with the reaction frame. Additional measurements of T3 and T8 permitted an evaluation of the wall rotation at the top and at the base. Lastly, the displacements monitored through the transducers installed on the back side (T11, T12, T13 and T14) permitted to check transversal expansions of the wall, by comparison with displacements detected on the front side, at the same height.

The force and the displacements were real-time monitored by connecting the measure equipment to an electronic acquisition unit (PCMCi National Instruments, mod. DAQ Card-AI-16-XE-50) interfaced with a computer.

#### 5.1.4 Results and discussion

The samples were tested after about 4 months air curing. The results were expressed in terms of  $P$ - $\delta$  curves, representing the total horizontal load  $P$  against the out-of-plane average net deflection at half height of the wall.

To evaluate the two net deflections on the right and left side of the wall  $\delta_{net,i}$ , the horizontal displacement at mid height  $\delta_{mid,i}$  was reduced by the mean value of the horizontal displacements at the upper  $\delta_{up,i}$  and lower  $\delta_{low,i}$  steel contrasts:

$$\delta_{net,i} = \delta_{mid,i} - \frac{\delta_{up,i} + \delta_{low,i}}{2} \quad (5.1)$$

where the suffix  $i$  indicates the right or the left side. The out-of-plane average net deflection  $\delta$  was calculated as the mean value of the right and left side net deflections  $\delta_{net,right}$  and  $\delta_{net,left}$ .

Actually, at cracking, the curves presented an unreal constant force branch between the cracking and the drop of the resistance, due to the spring-back effect of the steel reaction frame. The deflection due to the spring-back effect (in mm) has been quantified in about  $0.13 P$  ( $P$  is the current global horizontal load, in kN). Thus, the experimental curves reported have been here corrected by removing this effect in correspondence of cracking.

#### – Behaviour of unreinforced masonry specimens

In the first part of the tests, the unreinforced specimens did not exhibit any damage. Then, suddenly, the formation and rapid opening of a single crack occurred. The crack started from the tensed face of the samples (the front side), at about the mid-height of the wall and followed an approximately horizontal trend involving, mostly, a single bed joint. The crack affected, for the most, the masonry-mortar interface and involved the whole masonry thickness.

Some global and detail illustrations of the unreinforced specimens at the end of the tests are reported in Figure 5.8, Figure 5.9 and Figure 5.10 for solid brick, rubble stone and cobblestones masonry, respectively.

The load – average net deflection  $P-\delta$  curves are plotted in Figure 5.11. The curves exhibited an initial linear elastic trend, as the specimens remained undamaged. The peak load was reached, then, at the occurrence of the masonry crack, an abrupt decrease of the resistance emerged. The load rapidly dropped down to a residual value, which was maintained approximately constant till a deflection of 30 mm for FS-B6-U and 50 mm for FR-B6-U and FC-B3-U. Then, the tests were stopped, so to prevent the walls overturning.

The initial slope of the  $P-\delta$  curves, in the linear elastic phase, resulted quite similar for stone masonry samples and lower for solid brick specimen. The peak load of the solid brick specimen was 9.55 kN, while rubble stone and cobblestones specimens reached values of 25.52 kN and 15.14 kN, respectively. The higher values obtained from stone masonry samples are reasonably related to the greater masonry thickness. Moreover, the lower resistance emerged in cobblestones sample, in respect to rubble stone one, is probably due to the weaker mortar (subsection 5.1.1) and to the different stone blocks roughness and porosity, which may have influenced the block-mortar interface resistance.

The residual resistance resulted of about 3.5 kN for solid brick sample, 9.0 kN for rubble stone one and 8.5 kN for cobblestones masonry.

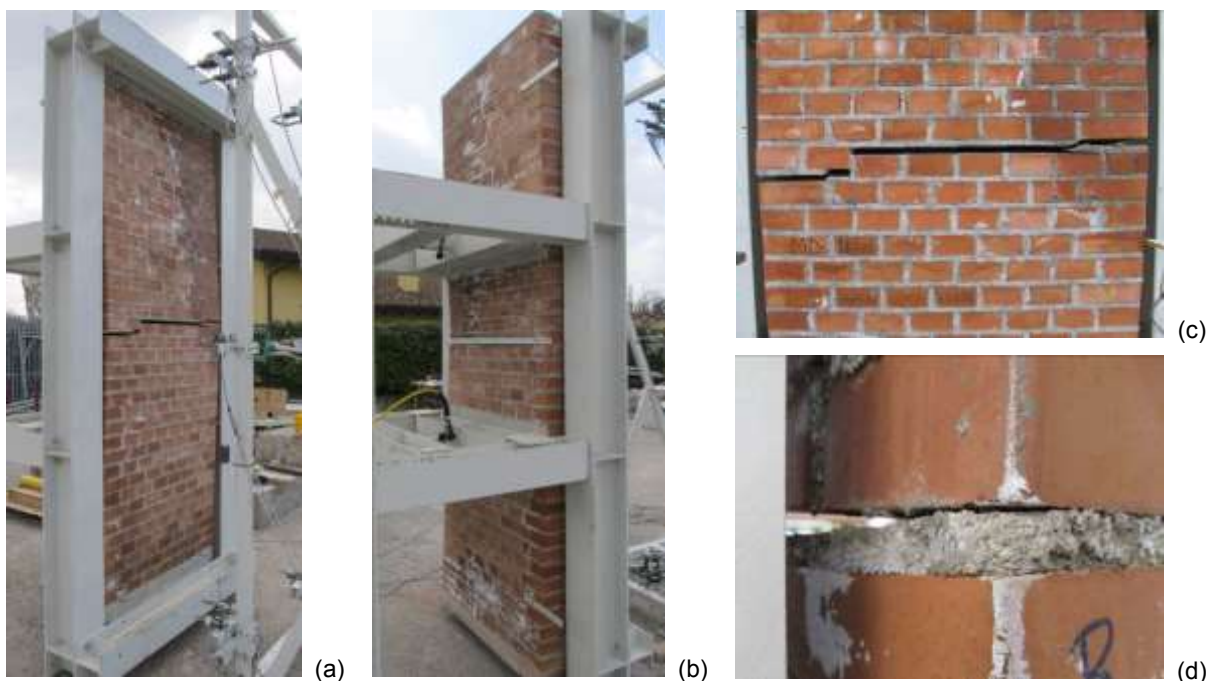


Figure 5.8 - Unreinforced solid brick masonry specimen (FS-B6-U) at the end of the experimental test: (a) frontal and (b) back side global views and detail of the crack opening (c) on the masonry tensed face and (d) on the masonry thickness and compressed face

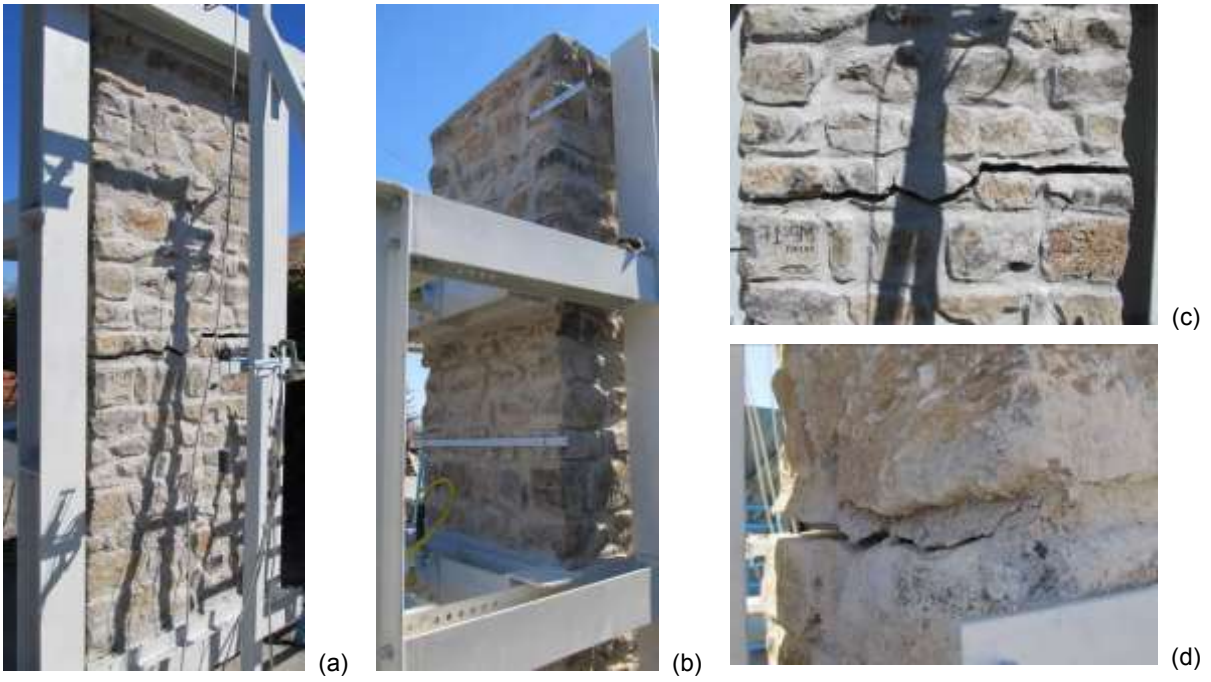


Figure 5.9 - Unreinforced rubble stone masonry specimen (FR-B6-U) at the end of the experimental test: (a) frontal and (b) back side global views and detail of the crack opening (c) on the masonry tensed face and (d) on the masonry thickness and compressed face

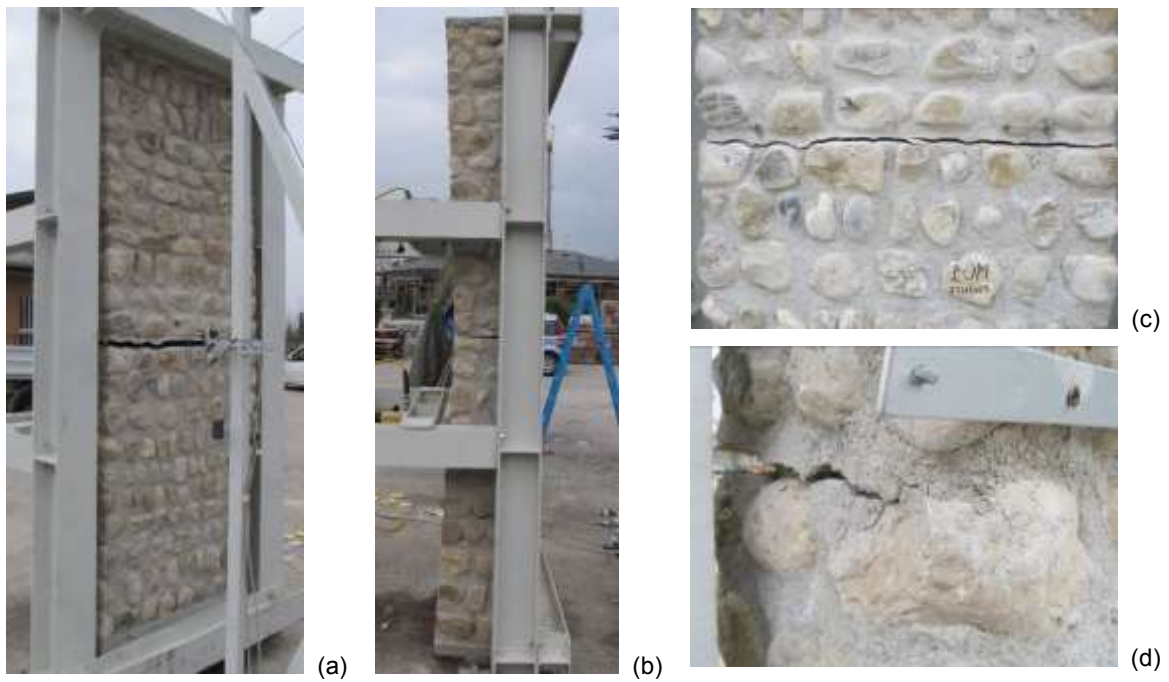


Figure 5.10 - Unreinforced cobblestones masonry specimen (FC-B3-U) at the end of the experimental test: (a) frontal and (b) lateral global views and detail of the crack opening (c) on the masonry tensed face and (d) on the masonry thickness and compressed face

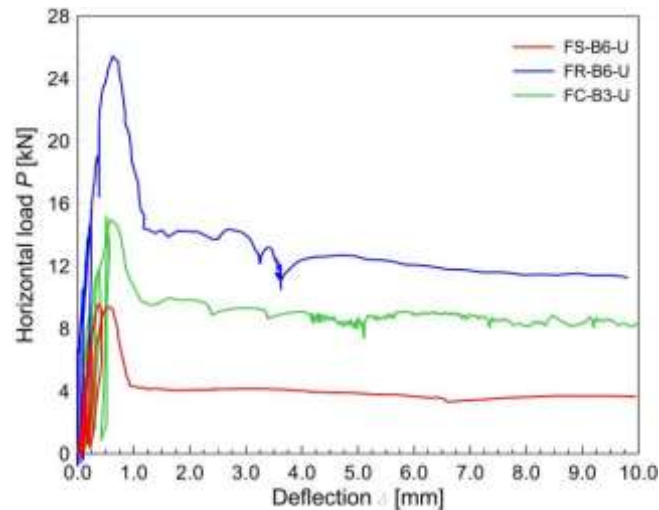


Figure 5.11 – Load  $P$  - deflection  $\delta$  curve of unreinforced masonry specimens

– Behaviour of reinforced masonry specimens

Reinforced masonry samples started to deflect remaining undamaged, until the opening of a first horizontal crack in the mortar coating, on the tensed wall face (front side). Other horizontal cracks, almost parallel to the first one, gradually appeared. All cracks were approximately concentrated in the middle third of the wall height and progressively affected the whole coating thickness and, then, sometimes, also the masonry. An illustration of the cracking evolution in the tensed mortar coating is reported, as an example, in Figure 5.12 (sample FR-B6-R).

The collapse occurred when, in correspondence of a crack, the vertical tensed wires of the GFRP mesh broke almost simultaneously (Figure 5.13.a). The tests were stopped in correspondence of a wall deflection of about 50 mm, so to prevent the walls overturning.

The main crack (where the GFRP wires failure occurred) involved the whole masonry thickness (Figure 5.13.b) and, in solid brick reinforced sample, also part of the compressed mortar coating (Figure 5.13.c). However, the external mortar surface on the back side resulted undamaged at the end of all tests.

The  $P$ - $\delta$  curves of reinforced samples are plotted in Figure 5.14 (also unreinforced specimens curves are illustrated, for comparison); the envelope curves are reported, for graphic readability. It can be distinguished a first, linear elastic branch (uncracked stage) and a cracking formation stage. To each crack formation was associated a drop of resistance, before to increase again. The sequence of crack formation is marked both on the  $P$ - $\delta$  curves and in Figure 5.15, which illustrates the front side of the reinforced specimens at the end of the tests. When the wires broke up, the load rapidly fall down to a residual value slightly greater than that obtained for unreinforced masonry samples.

The solid brick reinforced specimen cracked at 36.0 kN and reached a peak value of 45.5 kN in correspondence of a net deflection of 32.6 mm. The first cracking of the rubble stone sample occurred at 53.1 kN but then the load increased up to 86.2 kN, till a net deflection of 19.9 mm. In cobblestones specimen the first crack emerged at 66.42 kN and the maximum load was 101.28 kN (net deflection 13.8 mm). The higher resistance of cobblestone reinforced masonry, in respect to rubble stone one resulted a little anomalous, considering the similar material characteristics of the two specimens. This difference may be attributable to some accidental greater frictional effect at the base.

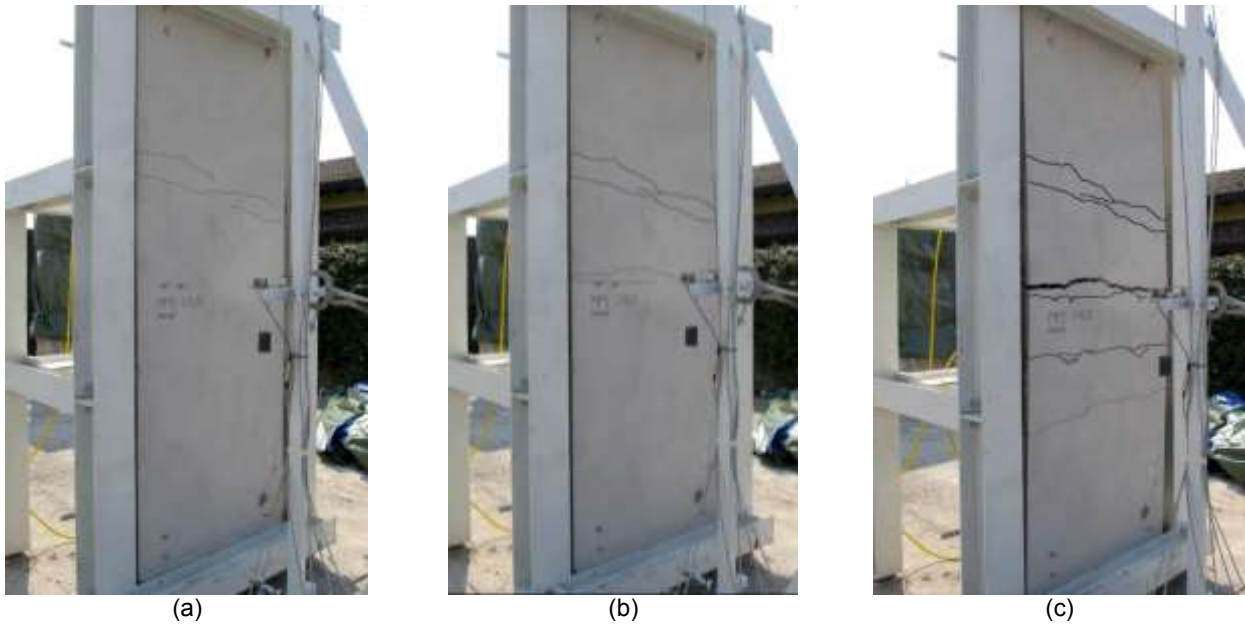


Figure 5.12 - Evolution of the crack pattern of the tensed mortar coating in sample FR-B6-R at the increasing of the wall deflection: (a)  $\delta = 0.5$  mm, (b)  $\delta = 4$  mm and (c)  $\delta = 20$  mm

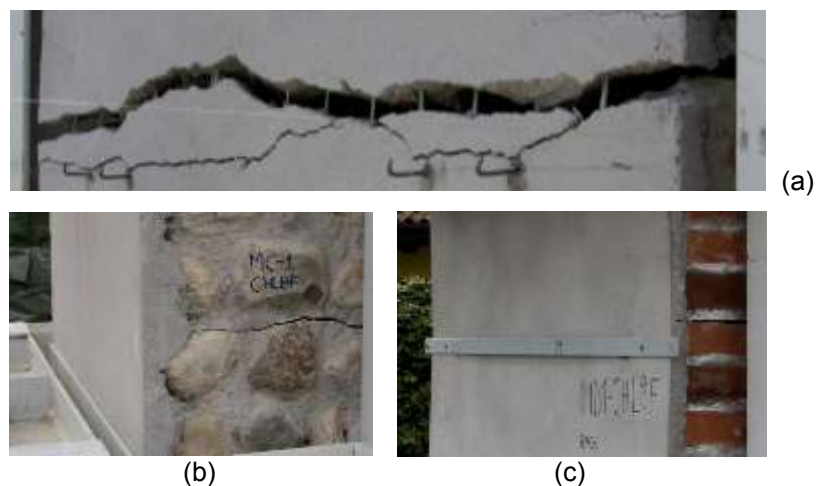


Figure 5.13 - Reinforced masonry samples at the end of the tests: details of the (a) vertical wire rupture in FR-B6-R and of the main crack opening (b) on the masonry thickness in FC-B2-R and (c) on the masonry back side in FS-B6-R

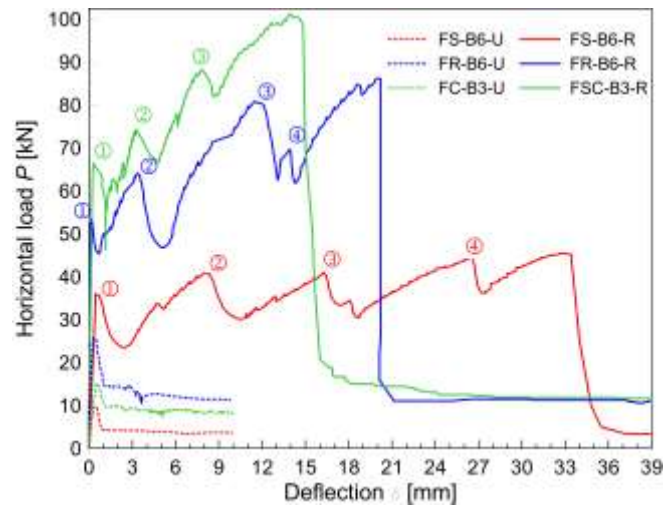


Figure 5.14 – Load  $P$  vs. deflection  $\delta$  curve of reinforced masonry specimens

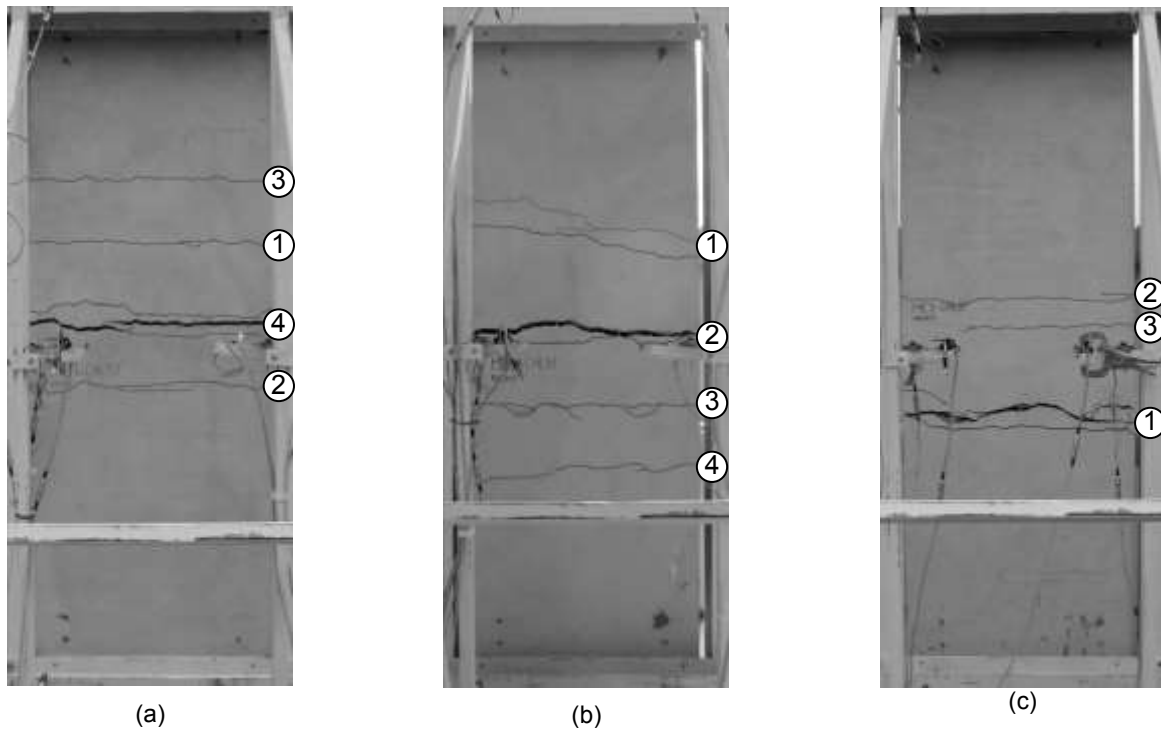


Figure 5.15 - Crack pattern of reinforced specimens at the end of the tests, with indication of cracks occurrence sequence: (a) FS-B6-R, (b) FR-B6-R and (c) FC-B2-R

### 5.1.5 Interpretation of the results

In Table 5.2 are reported the main results of the out-of-plane bending tests in terms of first cracking and maximum load ( $P_{cr}$  and  $P_u$ ) and deflection in correspondence of  $P_{cr}$  and  $P_u$  ( $\delta_{cr}$  and  $\delta_u$ ). Moreover, the bending moments associated to the first cracking  $M_{cr}$  and to the wall resistance

$M_u$  are evaluated and the ratios between the bending resistance of reinforced and unreinforced samples,  $M_{u(R)}/M_{u(U)}$ , are calculated.

The bending moment was derived through Equation ( 5.2 ) from the horizontal load  $P$  obtained from the experimental tests, assuming the simplified scheme reported in Figure 5.16, which accounts also for a base horizontal restraint due to steel-to-steel friction ( $F_\mu$  – subsection 5.1.2). For the evaluation of  $F_\mu = \mu W$ , the whole self-weight of the specimen  $W$  was considered (self-weights  $\gamma = 18 \text{ kN/m}^3$  for solid brick masonry,  $\gamma = 21 \text{ kN/m}^3$  for rubble stone,  $\gamma = 19 \text{ kN/m}^3$  for cobblestones, according to the values indicated in Circolare 2 febbraio 2009, n. 617 and  $\gamma = 20 \text{ kN/m}^3$  for the reinforced mortar coating) and a friction coefficient  $\mu = 0.74$  was applied.

$$M = P \frac{d_2}{2} - F_\mu \frac{d_2 \cdot d_3}{(d_1 + 2d_2)} \quad (5.2)$$

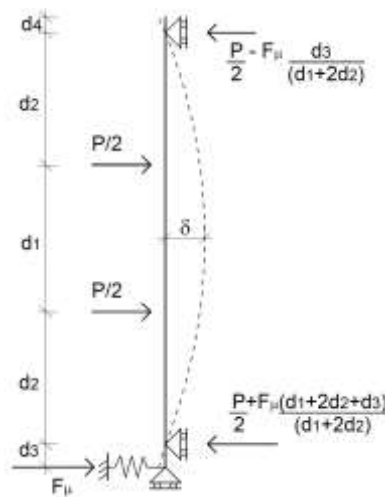


Figure 5.16 - Simplified scheme assumed for the experimental four-point bending tests

Table 5.2 - Main test results for out-of-plane bending tests in terms of horizontal load  $P$ , out-of-plane deflection  $\delta$  and bending moment  $M$  associated to first cracking (suffix “cr”) and collapse (suffix “u”) and ratios between the maximum bending resistance of reinforced and unreinforced samples  $M_{u(R)}/M_{u(U)}$

Specimen ID	$P_{cr}$ [kN]	$P_u$ [kN]	$\delta_{cr}$ [mm]	$\delta_u$ [mm]	$M_{cr}$ [kN*m]	$M_u$ [kN*m]	$M_{u(R)} / M_{u(U)}$
FS-B6-U	9.55	9.55	0.38	0.38	3.67	3.67	5.4
FS-B6-R	36.00	45.47	0.44	32.59	15.41	19.67	
FR-B6-U	25.52	25.52	0.46	0.46	10.75	10.75	3.5
FR-B6-R	53.08	86.19	0.41	19.93	22.99	37.89	
FC-B3-U	15.14	15.14	0.56	0.56	6.15	6.15	7.3
FC-B2-R	66.42	101.28	0.45	13.83	29.06	44.75	

The results were compared in terms of maximum bending moments  $M_u$  (Figure 5.17.a) and out-of-plane ultimate deflection  $\delta_u$  (Figure 5.17.b). It emerged that the masonry bending resistance increased 5.4 times in solid brick walls, 3.5 times in those made with rubble stones and reaches 7.3 times in cobblestones ones. The tests results also evidenced considerable increments in terms of deflection, due to the presence of the GFRP mesh, which is essential for the wall resistance once the mortar coating cracks. In fact, the deflection  $\delta_u$  did not exceed  $h/5000$  in unreinforced walls, while in reinforced specimens ranged approximately between  $h/200$  and  $h/100$ .

No evident detachment between the masonry and the mortar, neither in tension coating (ends of the wall or close to bending cracks) nor in compression coating at mid-height (maximum bending moment). were noted during the tests up to the specimen collapse. The measured transversal expansion of the wall was almost negligible in all the tested specimens.

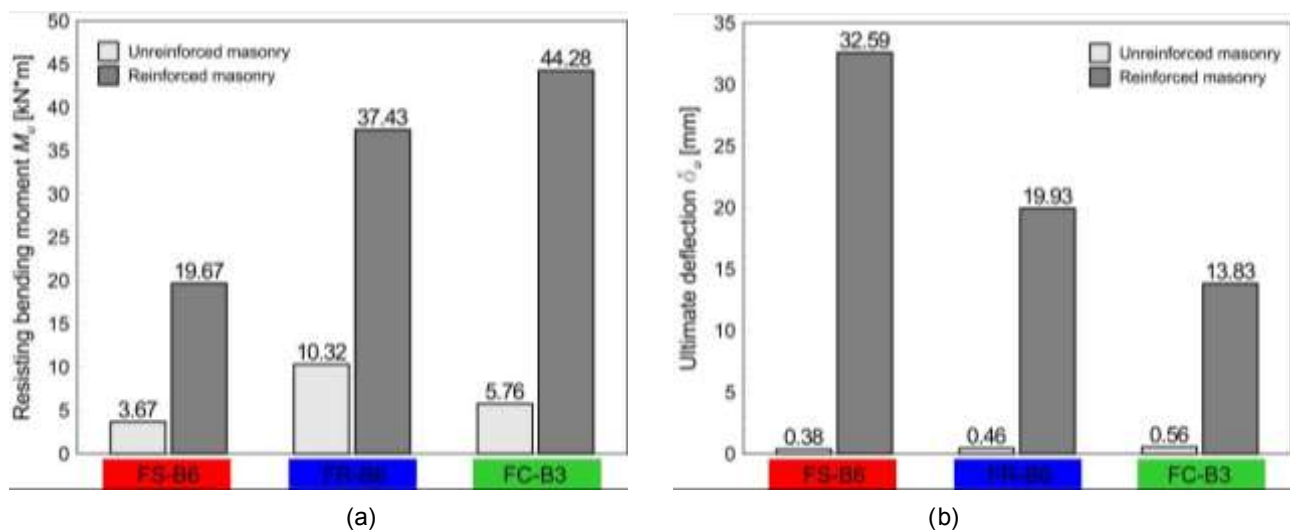


Figure 5.17 - Comparisons between unreinforced and reinforced masonry specimens in terms of (a) resisting bending moment and (b) out-of-plane ultimate deflection

## 5.2 Analytical estimations

The stress state in the generic cross section of a specimen subjected to four-point bending can be evaluated considering the combined effect of the axial force ( $N$ ), due to the masonry self-weight, and of the bending action ( $M$ ) induced by the two horizontal loads, as schematized in Figure 5.18, referring to the simplified static scheme illustrated in Figure 5.16.

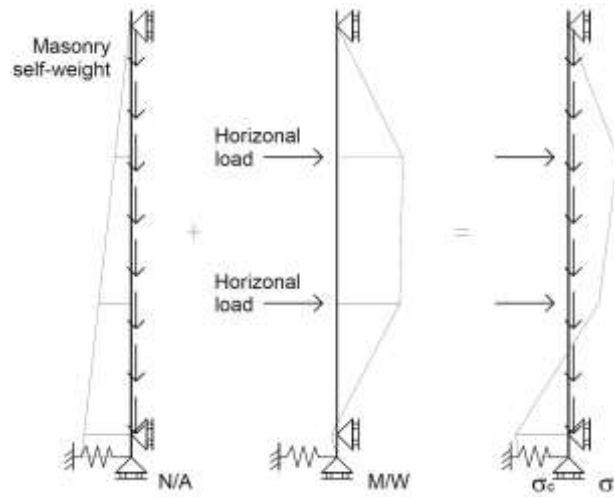


Figure 5.18 - Combined effect of axial force ( $N$ ) and bending action ( $M$ ) in specimens subjected to four-point bending ( $A$  is the cross section,  $W$  the resistance modulus)

### 5.2.1 Unreinforced specimens

In plain masonry specimens, the superposition principle can be applied to the fully reagent masonry cross section  $A_U$  subjected to the axial force  $N_U$  and to the bending action  $M_{cr,U}$  (Table 5.2) to evaluate the flexural tensile strength of unreinforced masonry  $f_{t(U)}$ , by means of equation ( 5.3 ).

$$f_{t(U)} = \frac{N_U}{A_U} - \frac{M_{cr,U}}{W_U} \quad ( 5.3 )$$

being  $W_U$  the masonry resistance modulus and considering, for the calculation of  $N_U$ , the weight of half wall, according to the experimental cracking pattern (Figure 5.8, Figure 5.9 and Figure 5.10). The considered self-weights are those indicated in 5.1.4. The results, reported in Table 5.3, evidenced an almost equal flexural tensile strength  $f_{t(U)}$  for solid brick and rubble stone masonry specimens and significantly lower value for the cobblestones specimen.

In 5.1.4 it has been evidenced that, due to the inhomogeneity of masonry, formed by blocks and mortar, the collapse of unreinforced specimens occurred in the weakness area, that is the interface between the materials. In general, many factors influence the bond strength between the mortar joints and masonry units, such as the surface roughness of the units, the binder dosage, the particle size distribution of sand, the unit rate of suction, the moisture content of mortar (Kamf, 1963; Lawrence & Cao, 1987).

It is observed that, for the tested specimens, the ratio between the masonry flexural tensile strength  $f_{f(U)}$  and the tensile strength of mortar  $f_{t,b}$  (subsection 5.1.1) assumed values of about 0.3.

Table 5.3 - Evaluation of the flexural tensile strength of unreinforced masonry  $f_{f(U)}$ : bending resistance of unreinforced sample  $M_{cr(U)}$ , half wall weight  $N_U$ , masonry cross section  $A_U$ , masonry resistance modulus  $W_U$ , mortar tensile strength  $f_{t,b}$  and ratio  $f_{f(U)}/f_{t,b}$

Specimen ID	$M_{cr(U)}$ [kN*m]	$N_U$ [kN]	$A_U$ [mm <sup>2</sup> ]	$W_U$ [mm <sup>3</sup> ]	$f_{f(U)}$ [MPa]	$f_{t,b}$ [MPa]	$f_{f(U)}/f_{t,b}$
FS-B6-U	3.67	6.75	250000	10416667	0.33	1.1	0.30
FR-B6-U	10.32	12.60	400000	26666667	0.36	1.1	0.32
FC-B3-U	5.76	11.40	400000	26666667	0.19	0.7	0.27

The residual load after the occurrence of cracking,  $M_{r(U)}$ , may be calculated by using the relation of bending resistance for cracked sections, assuming zero the tensile resistance:

$$M_{r(U)} = \frac{N_U t}{2} \left( 1 - \frac{N_U}{k f_{c,m} A_U} \right) \quad (5.4)$$

where  $t$  is the masonry thickness,  $k$  a coefficient that takes into account the effect of long term loads (assumed unitary, because the short loading of experimental test does not influence the strength) and  $f_{c,m}$  the masonry compressive strength (Table 4.2). It is evidenced that, actually, in unreinforced masonry walls, the bending resistance for cracked sections results generally higher than the first cracking bending, due to the greater axial load induced from the presence of overlaying storeys (subsection 5.3.4).

Table 5.4 - Evaluation of the residual load after the occurrence of cracking,  $M_{r(U),calc}$ : half wall weight  $N_U$ , masonry compressive strength  $f_{c,m}$ , masonry cross section  $A_U$ , experimental residual load  $M_{r(U),exp}$  and error percentage between calculated,  $M_{r(U),calc}$ , and experimental  $M_{r(U),exp}$  values

Specimen ID	$N_U$ [kN]	$f_{c,m}$ [MPa]	$A_U$ [mm <sup>2</sup> ]	$M_{r(U),calc}$ [kN*m]	$M_{r(U),exp}$ [kN*m]	$\Delta_{err}$ %
FS-B6-U	6.75	7.88	250000	0.84	0.91	-7
FR-B6-U	12.60	4.51	400000	2.50	3.15	-20
FC-B3-U	11.40	1.04	400000	2.22	2.59	-14

### 5.2.2 Reinforced specimens

In reinforced masonry walls, the superposition principle can be applied to estimate the value of the first cracking moment (Figure 5.19.a). Supposing no slip at materials interfaces (as emerged in experimental tests - 5.1), the Bernoulli's principle applies:

$$M_{cr(R)} = \left( \frac{N_R}{A_{id(R)}} + \frac{|f_{f,c}|}{\alpha_c} \right) \cdot W_{id(R)} \quad (5.5)$$

$N_R$  is the weight of half reinforced wall,  $A_{id(R)}$  and  $W_{id(R)}$  are the area and the resistance modulus of the uncracked section, idealized to masonry,  $f_{f,c}$  the flexural tensile strength of mortar coating and  $\alpha_c$  modular ratio  $E_d/E_m$  between the mortar of the coating and the masonry. The presence of the GFRP wires can be assumed negligible with quite accuracy up to the crack formation in the mortar coating, due to the low geometrical percentage and to the low modular ratio of the composite (subsection 3.2).

The flexural tensile strength of mortar coating,  $f_{f,c}$ , can be derived from its tensile strength  $f_{t,c}$  through Equation ( 5.6 ) in function of the global depth of the cross section  $h_{TOT}$  (in mm), according to Eurocode 2 (EN 1992-1-1:2004/A1:2014).

$$f_{f,c} = \max \left\{ (1.6 - h_{TOT} / 1000) f_{t,c} ; f_{t,c} \right\} \quad (5.6)$$

The maximum bending moment associated to the GFRP tensed wires rupture (Figure 5.19.b) can be calculated considering a cracked section composed by only compression reagent mortar and by the tensed GFRP wires:

$$M_{u(R)}(N_R) = 0.8x \cdot f_{c,c} \cdot b \left( \frac{h_{TOT}}{2} - 0.4x \right) + n_w T_w \left( \frac{h_{TOT}}{2} - c \right) \quad \text{with} \quad x = \frac{N_R + n_w T_w}{0.8 f_{c,c} \cdot b} \quad (5.7)$$

$n_w$  is the number of GFRP tensed wires in a cross section,  $T_w$  the tensile resistance of one wire,  $x$  the neutral axes depth,  $f_{c,c}$  the compressive stress of the mortar of the coating,  $h_{TOT}$  the global depth of the reinforced masonry cross section,  $b$  the width and  $c$  the wires cover.

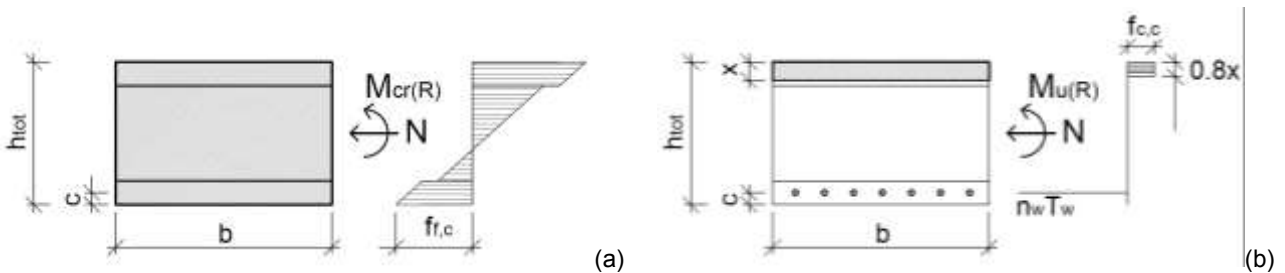


Figure 5.19 – Masonry cross section for the calculation of (a) first cracking and (b) maximum bending moment in reinforced panels

For residual load after the occurrence of cracking,  $M_{r(R)}$ , the same approach adopted for unreinforced walls can be applied ( 5.4 ). However, it is evidenced that in reinforced masonry walls the bending resistance for cracked sections is negligible in respect to the resistance associated to the GFRP mesh collapse.

A comparison between experimental results and analytical predictions is reported in Table 5.5 and Table 5.6: low error percentages can generally be observed in the calculations. It is evidenced that the specific weights assumed for the masonry and for the mortar of the coating are those indicated in subsection 5.1.4; the amount of GFRP tensed wires  $n_w$  is equal to 15. Two different tensile resistance values were considered for the GFRP mesh:  $T_{w,red} = 4.99$  kN and  $T_{w,inc} = 6.32$  kN, reducing (“red”) or increasing (“inc”) the average strength ( $T_{w,med} = 5.66$  kN) by the standard deviation emerged in the results of the tensile tests on GFRM layers described in subsection 3.3.3. According to the specimens characteristics (subsection 5.1.1), a 30 mm average thickness was assumed for the mortar in solid brick reinforced masonry, 35 mm in rubble stone and 45 mm in cobblestones reinforced specimens.

Table 5.5 - Comparison between experimental (suffix “exp.”) and analytical (suffix “calc.”) results in reinforced panels in terms of first cracking moments  $M_{cr(R)}$  ( $N_R$  weight of half reinforced wall,  $\alpha_c$  modular ratio,  $A_{id(R)}$  and  $W_{id(R)}$  cross section and the resistance modulus of the uncracked section, idealized to masonry,  $f_{f,c}$  mortar flexural tensile strength)

Specimen ID	$N_R$ [kN]	$\alpha_c$ -	$A_{id,R}$ [mm <sup>2</sup> ]	$f_{f,c}$ [MPa]	$W_{id,R}$ [mm <sup>3</sup> ]	$M_{cr(R)calc}$ [kN*m]	$M_{cr(R)exp}$ [kN*m]	$\Delta_{err}$ %
FS-B6-R	8.55	3.38	452954	1.42	34162549	14.98	15.41	-3
FR-B6-R	14.70	5.94	815679	1.24	106553117	24.22	22.53	7
FC-B2-R	14.10	11.49	1433997	1.22	231416837	26.87	28.59	-6

Table 5.6 - Comparison between experimental (suffix “exp.”) and analytical (suffix “calc.”) results in reinforced panels in terms of maximum bending moments  $M_{u(R)}$  ( $N_R$  weight of half reinforced wall)

Specimen ID	$N_R$ [kN]	$M_{u(R)calc,red}$ [kN*m]	$M_{u(R)calc,inc}$ [kN*m]	$M_{u(R)exp}$ [kN*m]	$\Delta_{err(red)}$ [%]	$\Delta_{err(inc)}$ [%]
FS-B6-R	8.55	22.93	28.58	19.67	17	45
FR-B6-R	14.70	36.15	44.78	37.43	-3	20
FC-B2-R	14.10	36.02	44.65	44.28	-19	1

It is important to note that the presented analytical equations are based on the assumption of bending cracking and failure of reinforced masonry wall. However, in general, the reinforced masonry shear resistance and the GFRM delamination need to be checked, so to prevent these premature failures, which could not permit to exploiting the whole GFRP mesh resistance in tension.

In particular, the shear resistance  $V_{Rd}$ , neglecting the reinforcement contribution, can be prudentially ensured by applying the Jourawski theory, checking that:

$$V_{Rd} = \frac{f_{v,Rd} \cdot b \cdot l}{S} = \frac{(f_{v,0} + \mu\sigma) \cdot b \cdot l}{S} \geq V_{Ed}(M_u) \quad (5.8)$$

$l$  is the second moment of area of the global cross section,  $S$  the first moment of area for half cross section and  $V_{Ed}(M_u)$  the maximum shear acting when the bending resistance  $M_u$  is attained. The masonry shear strength,  $f_{v,Rd}$ , can be evaluated by applying the Mohr-Coulomb failure criterion, considering the contribution of the masonry shear strength without axial loads ( $f_{v,0}$ , cohesion) and that due to friction related to the compressive stress  $\sigma$  acting in the cross section ( $\mu$  coefficient of internal friction of masonry, typically 0.4).

The delamination of the GFRM layer from the masonry surface can be avoided ensuring an adequate bond length at both wall ends. A prudential verification consists in assessing that, when the maximum bending resistance  $M_u$  is reached, the minimum distance  $l$  from the wall ends of the cross section in which the cracking bending moment  $M_{cr}$  is attained results higher of the minimum bond length  $l_{b,min}$ :

$$l(M_{cr}) \geq l_{b,min} \quad (5.9)$$

The main results of shear and delamination verifications for the three reinforced masonry tested samples are resumed in Table 5.7. It emerged that both masonry shear and GFRM delamination verifications resulted largely fulfilled.

Table 5.7 - Masonry shear and GFRM delamination checks for the three reinforced masonry samples: masonry shear strength,  $f_{v,Rd}$ , masonry shear resistance,  $V_{Rd}$ , maximum shear acting when  $M_{u(R)calc,inc}$  is attained,  $V_{Ed}(M_u)$ , calculated values of first cracking and maximum bending resistance,  $M_{cr(R)calc}$  and  $M_{u(R)calc,inc}$ , minimum distance from the wall end of the cross section where  $M_{cr(R)calc}$  is attained,  $l(M_{cr})$ , and minimum bond length,  $l_{b,min}$

Specimen ID	Masonry shear			GFRM delamination			
	$f_{v,Rd}$ [MPa]	$V_{Rd}(M_u)$ [kN]	$V_{Ed}(M_u)$ [kN*m]	$M_{cr(R)calc}$ [kN*m]	$M_{u(R)calc,inc}$ [kN*m]	$l(M_{cr})$ [mm]	$l_{b,min}$ [mm]
FS-B6-R	0.2	41.33	31.76	14.98	28.58	524	180
FR-B6-R	0.2	62.67	49.76	24.22	44.78	541	180
FC-B2-R	0.2	65.33	49.61	26.87	44.65	602	180

It is observed that, for the considered loading pattern (Figure 5.16), the verifications were conducted referring to the upper end of the walls, thus  $V_{Ed}(M_u) = M_u/d_2$  and  $l(M_{cr}) = (M_{cr}/M_u * d_2) + d_4$ .  $d_4$  is the distance from the upper wall end and the horizontal support; the calculated values of  $M_{cr(R),calc}$  and  $M_{u(R)calc,inc}$  (Table 5.5 and Table 5.6) were adopted. For the masonry shear strength, the values of cohesion  $f_{v,0}$  were derived from shove tests (Rinaldin & al., 2017).

The minimum bond length  $l_{b,min}$  was prudentially deduced from the results presented in subsection 3.3.4, from which emerged that a minimum bond length  $l_{b,min}$  of 180 mm has to be guaranteed in order to exploit the maximum resistance of the GFRP wires, avoiding both the premature detachment of the reinforced mortar coating from the masonry and the GFRP slippage from the mortar.

### 5.3 Numerical simulation of out-of-plane bending

A bi-dimensional finite element model was elaborated using the software Midas FEA (2015, v.1.1) so to simulate the out-of-plane behaviour of the unreinforced and reinforced specimens described in subsection 5.1 and investigate on the mechanisms which intervene in the resistance on the masonry walls. The characteristics of the FEM model and of the materials considered in the simulations are reported in the following.

Considering the geometry of the experimental samples and the load pattern of the four-point bending tests, a 2D model was at first preferred to a 3D one, for a preliminary study aimed to calibrate the different material parameters, so to reduce the time of analysis. However, a tri-dimensional model was also elaborated; the comparison on the results of the 2D and the 3D model proved that the bi-dimensional simplification is able to provide accurate results (Gattesco & Boem, 2015c; Gattesco & Boem, 2017c).

Furthermore, the 2D model was employed to investigate on the behavior of some typical, actual configurations of masonry walls, where the presence of intermediate storeys and roof was also considered in terms of loads and wall constraints (Gattesco & Boem, 2015d).

#### 5.3.1 Model characteristics

The bi-dimensional model for the specimens (Figure 5.20.a) was created using 4-node plane strain elements for the masonry and for the mortar of the coating. The height of the mesh elements was about 60 mm; the width was assumed 1/20 of the global element thickness for the masonry and 1/3 for the coating. A 66 thickness was considered for the plane strain element, so to represent the influence area of a single vertical GFRP wire (distance between two vertical wires). The presence of the concrete basement and also of the steel plates of the reaction frame in contact with the specimen was modelled; 4-node plane-strain elements were adopted for both. To guarantee the actual repartition of the horizontal load, a pinned nodes frame connecting the two loading areas was modelled and the horizontal displacement at the middle height of the frame was controlled.

According to the base asset (subsection 5.1.2), the vertical translation was contrasted in the middle of the basement width and the steel-to-steel friction was introduced by modeling a rigid-plastic extensional spring. Moreover, the horizontal displacement was constrained at the top and bottom plates.

The perfect adhesion between mortar and masonry was assumed, as no evident slips emerged in the experimental tests (subsection 5.1.4). The GFRP vertical wires and the connectors were modelled by means of truss elements; the presence of the horizontal wires was neglected.

Non-linear static analysis were performed by applying at first the whole self-weights and incrementing then step-by-step the imposed horizontal displacement. The Newton-Rapshon iterative method was considered (energy convergence criteria 0.001).

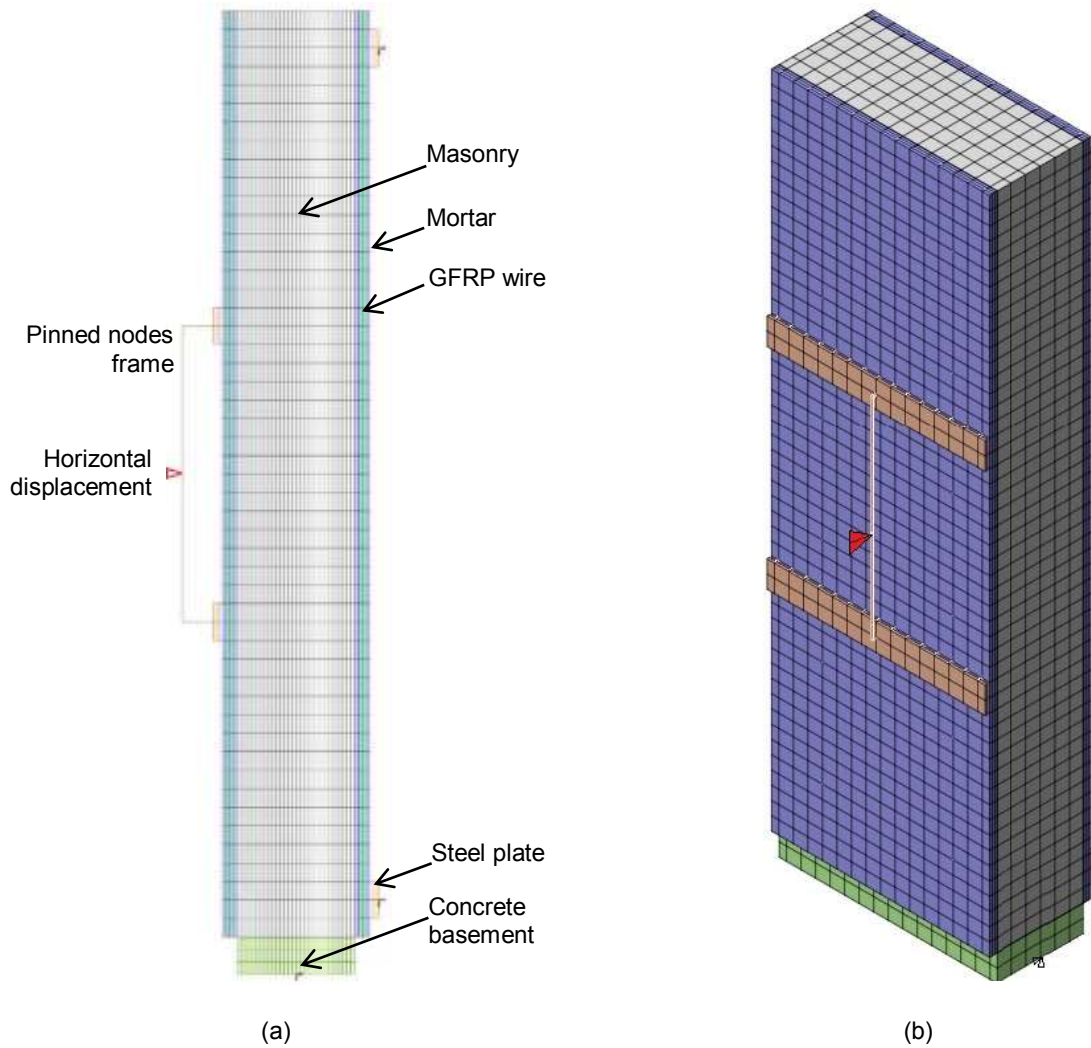


Figure 5.20 – Schematization of the numerical models adopted for the simulation of four-point bending tests:  
 (a) bidimensional and (b) tridimensional models

All the implemented materials were assumed being homogeneous and isotropic and a Smear Crack, fixed model was considered both for the masonry and the mortar coating. For the steel plates and the concrete basement an elastic behaviour was considered, with Young modulus equal to 21 GPa and 32 GPa, respectively, and Poisson modulus  $\nu = 0.3$  for both. The steel-to-steel static friction coefficient was  $\mu_s = 0.74$ .

The specific weights assumed are 18 kN/m<sup>3</sup> for solid brick masonry, 21 kN/m<sup>3</sup> for rubble stone and 19 kN/m<sup>3</sup> for cobblestones (Circolare 2 febbraio 2009, n. 617). The masonry Young modulus  $E_m$  were those deduced from the experimental compression tests (Table 4.2) and the Poisson modulus was equal to 0.2. A Total Strain Crack strength domain (TNO Building and Construction Research, 2002) was considered.

For the masonry compressive behaviour, a simplified elastic-plastic relationship was considered, with ultimate strain according to the results provided by experimental tests on masonry wallets (Table 4.2). The tensile strengths due to bending were derived from the results of the experimental bending tests on unreinforced specimens  $f_{t(U)}$  (Table 5.3). To calibrate the amount of the fracture energy of masonry in tension, a parametric study was conducted on the unreinforced specimens, so to fit as close as possible the experimental results. The main points of the tensile relationships adopted for the different masonry types are summarised in Table 5.8. It is evidenced that higher values of residual resistance resulted for stone masonry types; this is in accordance to the greater interlocking effect between blocks.

The comparison between the experimental and numerical behaviour of the unreinforced masonry specimens was reported in Figure 5.23.a, in a load against deflection graph.

Table 5.8 - Constitutive relationships adopted for the tensile behaviour of the masonry

Solid brick		Rubble stone		Cobblestones	
$\varepsilon_t$ [‰]	$\sigma_t$ [MPa]	$\varepsilon_t$ [‰]	$\sigma_t$ [MPa]	$\varepsilon_t$ [‰]	$\sigma_t$ [MPa]
0.000	0.000	0.000	0.000	0.000	0.000
0.057	0.320	0.117	0.360	0.138	0.190
0.090	0.055	0.160	0.100	0.250	0.050
0.150	0.009	0.290	0.022	0.350	0.025
0.500	0.009	0.500	0.022	0.500	0.025

The models were then completed with the GFRM layers. The weight assumed for the mortar of the reinforcement was 20 kN/m<sup>3</sup>; also for the coating, the Total Strain Crack strength domain (TNO Building and Construction Research, 2002) was adopted. The Young modulus  $E_c$  was 14.4 GPa (Table 4.3) and the Poisson ratio was equal to 0.2. For the compressive behaviour, a simplified elastic-plastic relationship was considered, with ultimate strain at 3.5 ‰.

The tensile behaviour of the mortar was derived from the tensile tests on GFRM layers (subsection 3.3.3), so to take into account for the tension stiffening effect of the mortar between two consecutive cracks. In particular, the mortar softening law, for a 30 mm thick mortar layer, was derived from the average stress – strain curve in Figure 3.22, by subtracting from the global GFRP reinforced mortar coating behavior that representing the longitudinal GFRP wires, as schematised

in Figure 5.21. The global tensile failure of the reinforced mortar coating was considered attained when a stress of 776 MPa ( $T_{w,med}/A_{w,tot} = 5.66 \text{ kN} / 7.29 \text{ mm}^2$ ) was reached.

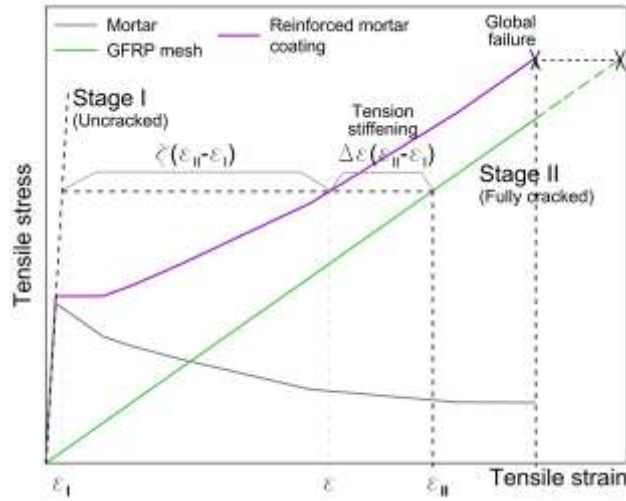


Figure 5.21 - Stress – strain behaviour of the GFRM layer, of the GFRP textile and of the mortar of the coating and indication of the main parameters considered in the tension stiffening model.

As evidenced in 5.1.1, the average mortar coating thickness was estimated equal to 30 mm in the solid brick reinforced specimens, 35 mm in rubble stone and 45 mm in cobblestones reinforced specimens. In these latter cases, the constitutive relationships of the mortar coating was adapted, applying the tension stiffening hyperbolic model proposed in Eurocode 2 (EN 1992-1-1:2004/A1:2014) for steel reinforced concrete sections

$$\varepsilon = \varepsilon_I + \xi \cdot (\varepsilon_{II} - \varepsilon_I), \quad (5.10)$$

$$\text{with } \begin{cases} \xi = 0 & \text{for uncracked sections} \\ \xi = 1 - \beta \left( \frac{N_{cr}}{N} \right)^2 \leq 1 & \text{for cracked sections} \end{cases}$$

$\varepsilon$  is the actual tensile strain,  $\varepsilon_I$  and  $\varepsilon_{II}$  are the values of strain calculated for the uncracked and fully cracked conditions, respectively,  $\beta$  is a constant accounting for the loading duration,  $N_{cr}$  represents the first cracking load and  $N$  the actual tensile force. According to such a model,  $\Delta\varepsilon$  represents the tension stiffening effect:

$$\Delta\varepsilon = \beta \left( \frac{N_{cr}}{N} \right)^2 (\varepsilon_{II} - \varepsilon_I), \quad (5.11)$$

It can be observed that, for thicker mortar coating,  $N_{cr}$  increases, thus a higher tension stiffening effect is expected. Comparing the tension stiffening effect of general mortar thickness ( $t_i$ ) with respect to that 30 mm thick ( $t_{30}$ ) through the relationship

$$\frac{\Delta\varepsilon_{t_i}}{\Delta\varepsilon_{t_{30}}} = \left[ \beta \left( \frac{f_{t,c} \cdot b \cdot t_i}{N} \right)^2 (\varepsilon_{II} - \varepsilon_I) \right] / \left[ \beta \left( \frac{f_{t,c} \cdot b \cdot t_{30}}{N} \right)^2 (\varepsilon_{II} - \varepsilon_I) \right] \quad (5.12)$$

it is observed that an increase of the tension stiffening effect of 1.36 and 2.25 times, respectively, for the 35 mm and the 45 mm thick mortar coating may be obtained. The main parameters considered in the tension stiffening model were indicated in Figure 5.21. In general, it is observed that the mortar softening relationship, which accounts for the tension stiffening effect, is dependent from the adopted mesh dimension. The main points of the tensile stress  $\sigma_t$  against strain  $\varepsilon_t$  curves assumed for the mortar coating in the numerical models are reported in Table 5.9 for the different coating thicknesses.

Table 5.9 - Constitutive relationships adopted for the tensile behaviour of the mortar of the coating, for the different coating thicknesses considered

30 mm thick (FS)		35 mm thick (FR)		45 mm thick (FC)	
$\varepsilon_t$ [‰]	$\sigma_t$ [MPa]	$\varepsilon_t$ [‰]	$\sigma_t$ [MPa]	$\varepsilon_t$ [‰]	$\sigma_t$ [MPa]
0.000	0.00	0.000	0.00	0.000	0.00
0.008	1.10	0.008	1.10	0.008	1.10
0.200	0.84	0.073	0.86	0.066	0.92
0.300	0.78	0.100	0.81	0.100	0.84
0.460	0.70	0.153	0.73	0.153	0.78
0.920	0.50	0.306	0.55	0.306	0.64
1.430	0.42	0.475	0.46	0.475	0.55
2.400	0.42	2.400	0.46	2.400	0.55

For the 3D-model (Figure 5.20.b), identical mechanical characteristics were used for the different materials. 8-node solid elements, instead of 4-node elements, were used for the masonry, for the mortar of the coating, for the concrete base element and for the steel plates of the reaction frame. A rotating crack model was adopted. The mesh elements were 60 mm height and 66 mm thick; the width was assumed 1/20 of the global element thickness for the masonry and 1/3 for the coating. Each single GFRP wire and each connector were modelled by means of truss elements.

### 5.3.2 Numerical results and discussion

In the numerical models of unreinforced masonry samples, the first crack of the masonry always occurred at the height of the upper horizontal force (Figure 5.22), due to the combined effect of the compressive and bending action on a homogeneous material. Differently, the horizontal crack position in the experimental specimens varied between this zone and the mid-height of the wall, localizing in correspondence of the weaker interface section (Figure 5.8, Figure 5.9 and Figure 5.10). However, the numerical curves resulted very similar to the experimental ones, both in terms of stiffness, peak load and residual load (Figure 5.23.a).

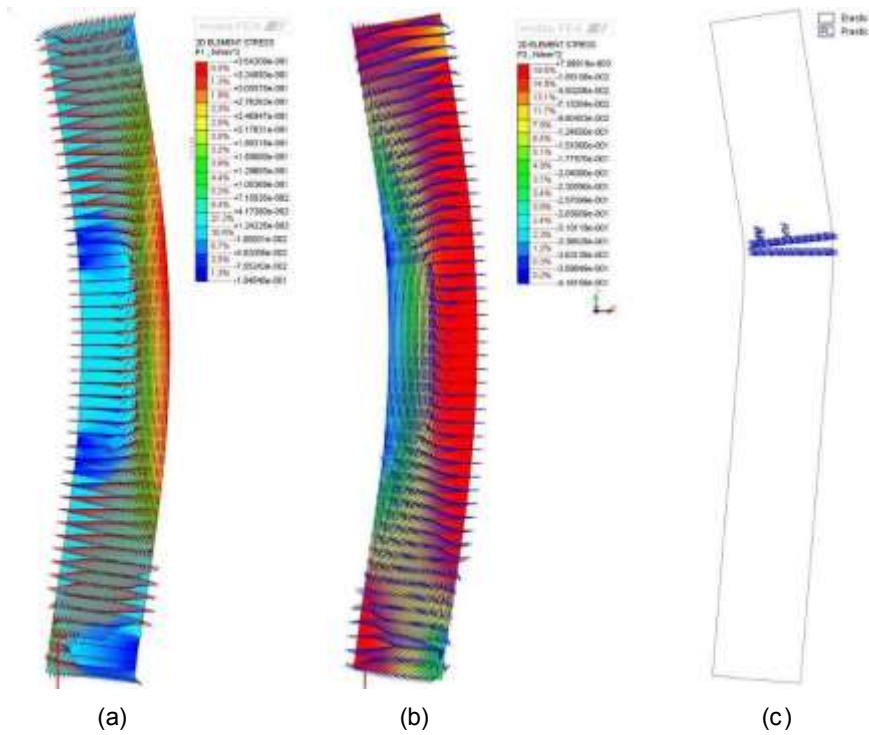


Figure 5.22 – Numerical results concerning unreinforced masonry: principal (a) tensile and (b) compressive stresses just before cracking and (c) plasticity status after cracking

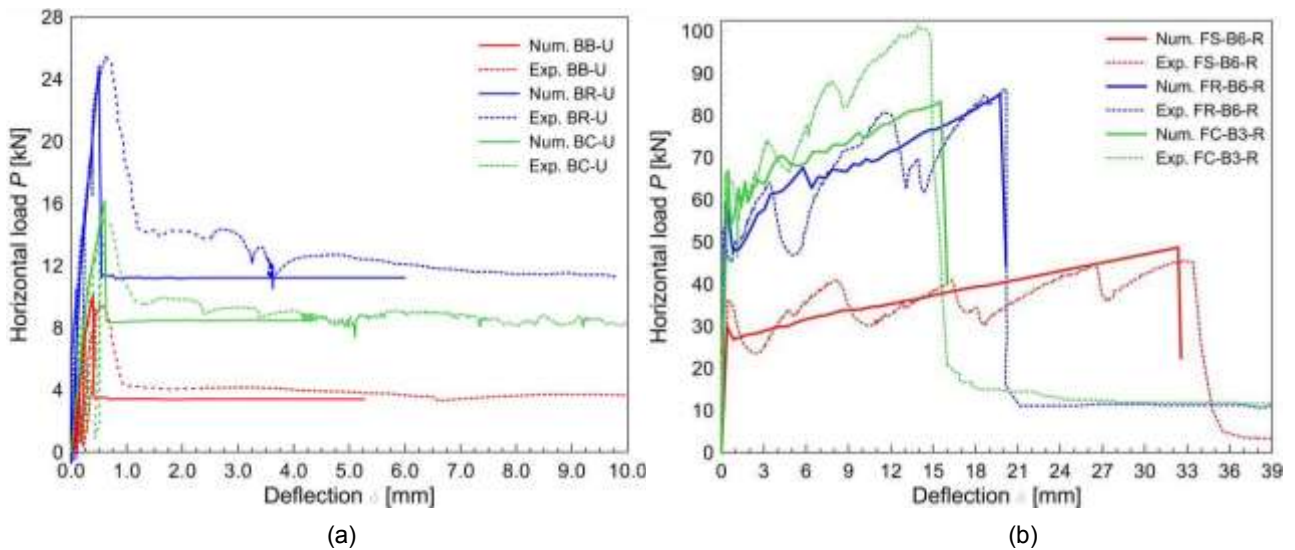


Figure 5.23 - Experimental (dotted lines) and numerical (solid lines) load  $P$  - deflection  $\delta$  curves of (a) unreinforced and (b) reinforced masonry specimens subjected to out-of-plane bending

The numerical results concerning reinforced masonry specimens were plotted in Figure 5.23.b, in comparisons with the experimental curves. Both the first cracking and the GFRP wires rupture occurred at the height of the upper horizontal force (Figure 5.24). It is evidenced that, in the numerical simulations, the plasticization of the masonry and mortar mesh elements extended wider in respect to the experimental cases, due to the Smear Crack model adopted. However, the actual

global behavior was attained with good accuracy. In particular, in solid brick and in rubble stone cases, good estimations emerged both for the cracking and the ultimate resistance points. Also the numerical behavior of the cobblestones specimen evidenced a trend similar to the experimental one up to the occurrence of the first crack, but then the numerical curve prosecuted with a lower slope and a lower value of maximum load was reached. This aspect is probably due to the marked irregularity of the coating thickness, as the cobblestones masonry surface was significantly uneven, due to the round and irregular shape of the stone units. This aspect may alternate the tension stiffening effect of the mortar between cracks. Moreover, it has been observed (subsection 5.1.4) that an anomalous, higher resistance in cobblestone reinforced masonry, in respect to rubble stone one, resulted from experimental results, despite the similar material characteristics; this difference has been attributed to some accidental greater frictional effect at the base.

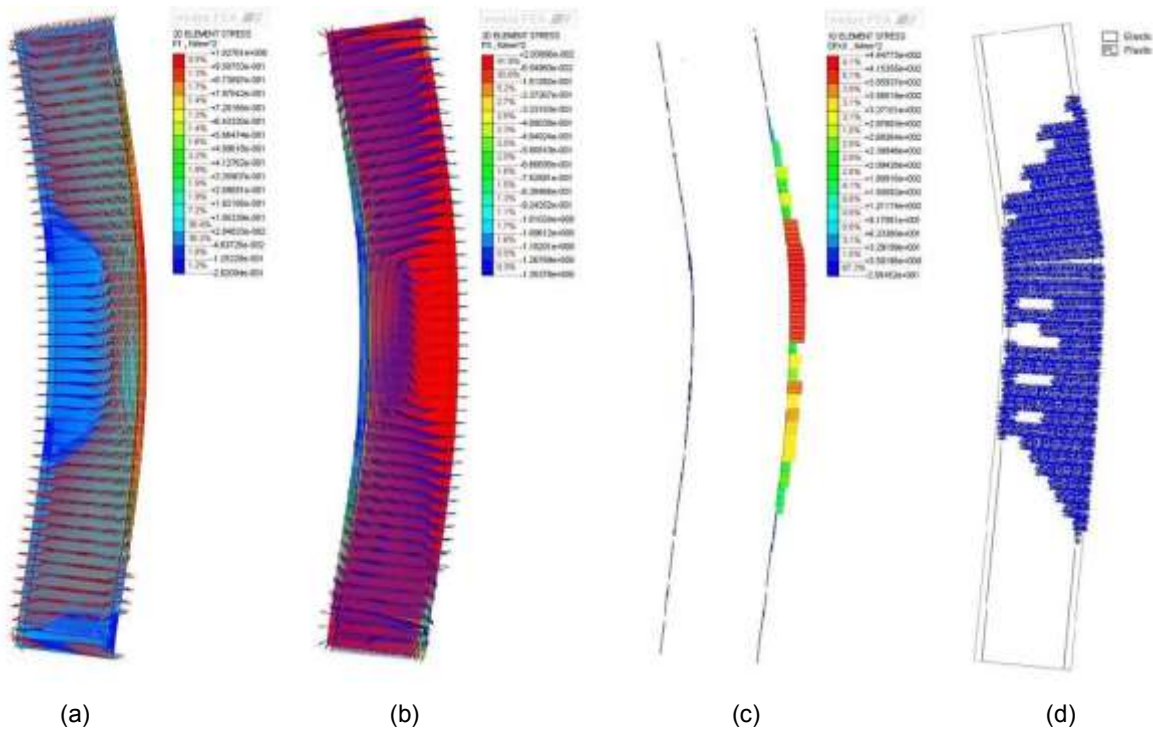


Figure 5.24 – Numerical results concerning reinforced masonry: principal (a) tensile and (b) compressive stresses in masonry and mortar just before the first cracking, (c) tensile stresses in GFRP mesh just before rupture and (d) mortar and masonry plasticity status after collapse

The results of the tridimensional numerical models are reported in Figure 5.25: it is observed that the load – deflection capacity curves are in agreement with the results of the bidimensional models (Figure 5.23). The 3D model will permit to investigate on the out-of-plane behavior of actual masonry walls with openings or having a more articulated geometry.

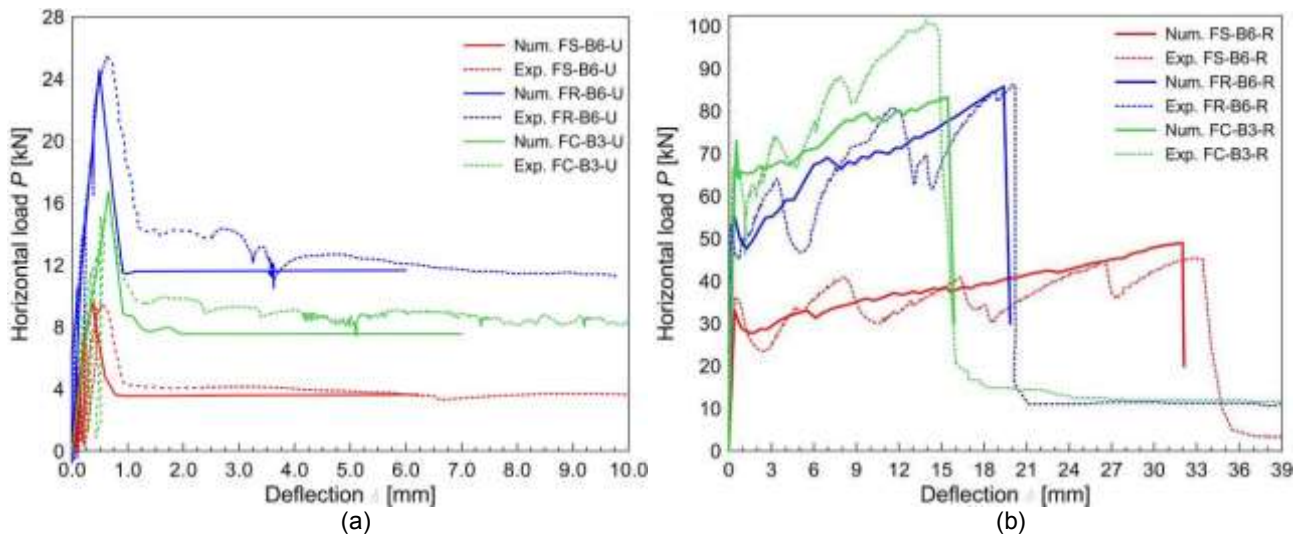


Figure 5.25 – Comparisons between experimental  $P$ - $\delta$  curves (dotted lines) and numerical behavior (solid lines) derived from the tridimensional models: (a) unreinforced and (b) reinforced masonry

### 5.3.3 Parametric study

By means of a numerical parametric study on the bidimensional model described in subsection 5.3.1, the influence of the main geometrical and mechanical characteristics of the masonry, the mortar coating and the GFRP mesh on the out-of-plane behavior of reinforced masonry was investigated.

At first (Figure 5.26.a), it is evidenced that the increase of the masonry stiffness reduces the wall ultimate load and deflection, while not significant modification in the cracking load occurs. Moreover, the variation of the wall thickness was considered (Figure 5.26.b): an increase of the effectiveness of the strengthening technique with the decreasing of the wall thickness was recorded. In fact, ratios  $P_{u(R)}/P_{u(U)}$  are 10.3 ( $=28.7/2.8$ ) and 3.4 ( $=70.5/20.6$ ), for a 125 mm and a 380 mm thick masonry, respectively.

The influence of a  $\pm 20\%$  variation of both the Young modulus and tensile resistance of the GFRP twisted wires on the reinforced masonry performances were also investigated. A decrease in the mesh rupture load resulted in an early breakdown of the  $P$ - $\delta$  curve (Figure 5.27.a). Moreover, a GFRP stiffness increase limited the wall deflection but did not influence the wall resistance capacity (Figure 5.27.b).

Moreover, it is observed (Figure 5.28.a) that a higher tensile resistance of the mortar (eg. 1.5 MPa) improves the first cracking load and limits the wall deflection, but does not affect appreciably the wall resistance. Differently, the modification of the mortar post cracking behavior (which accounts for the tension stiffening effect in the numerical model), induces in the  $P$ - $\delta$  curves a variation of the post cracking branch trend, while has no significant influence on ultimate loads.

This aspect can be observed in Figure 5.28.b where, for example, the effects of a brittle ( $\sigma_{res} = 0$ ) or an elastic-plastic ( $\sigma_{res} = f_{ct} = 1.1$  MPa) behavior of the mortar of the coating are compared. Thinner coating layers (e.g. 35 mm) induced a lower cracking load and a greater ultimate deflection.

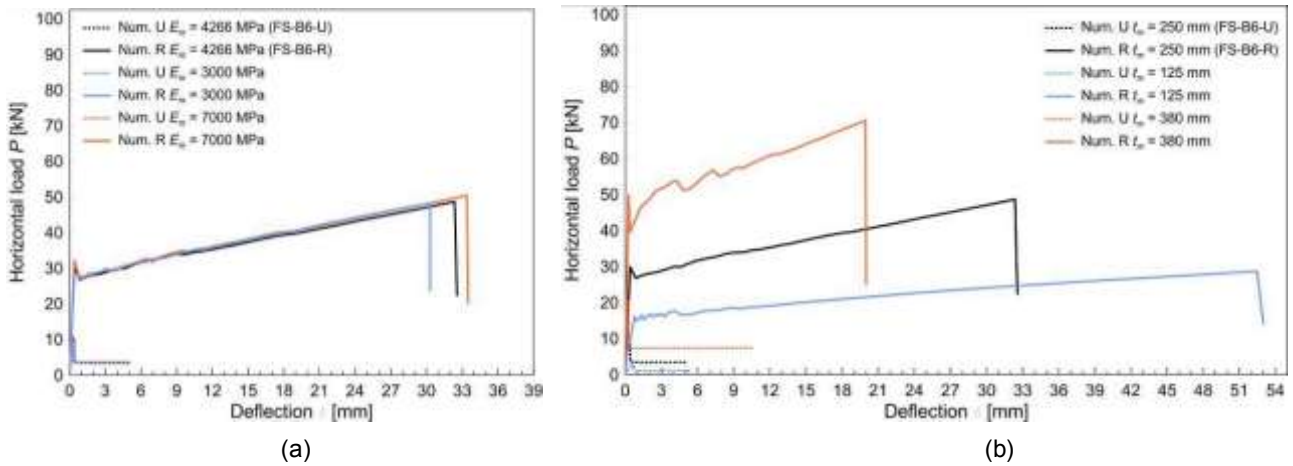


Figure 5.26 – Parametric study on solid brick reinforced masonry specimens: (a) influence of masonry stiffness  $E_m$  and (b) thickness  $t_m$

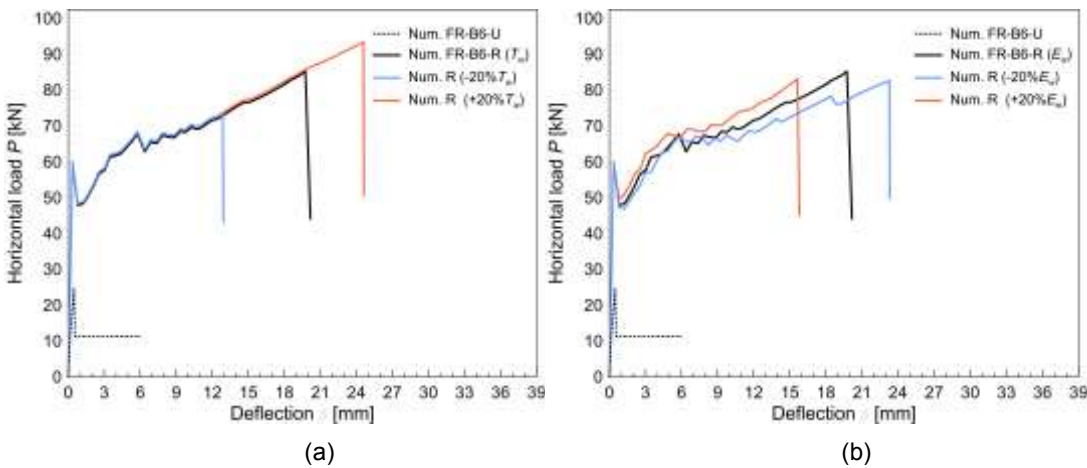
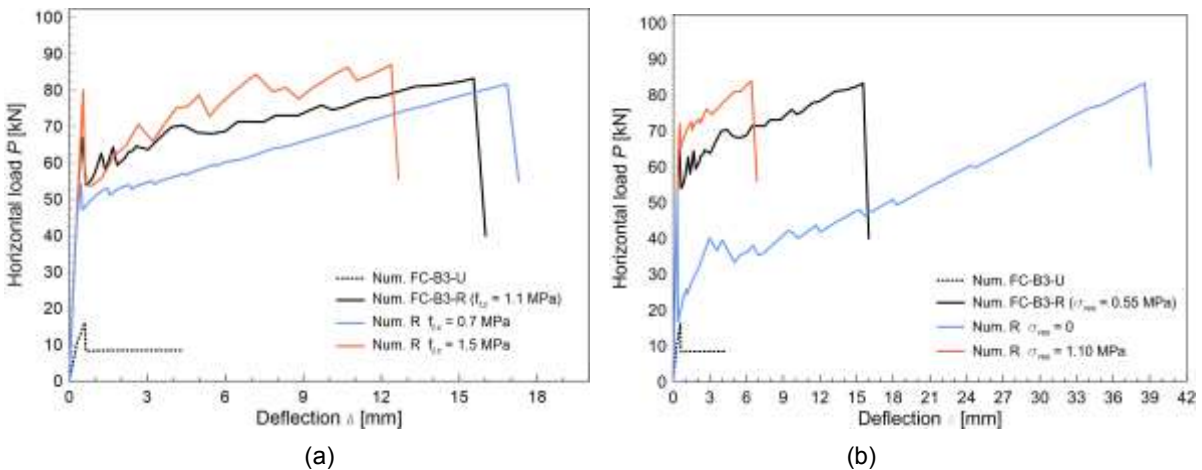


Figure 5.27 – Parametric study on rubble stone reinforced masonry specimens: (a) influence of GFRP mesh resistance  $T_w$  and (b) stiffness  $E_w$



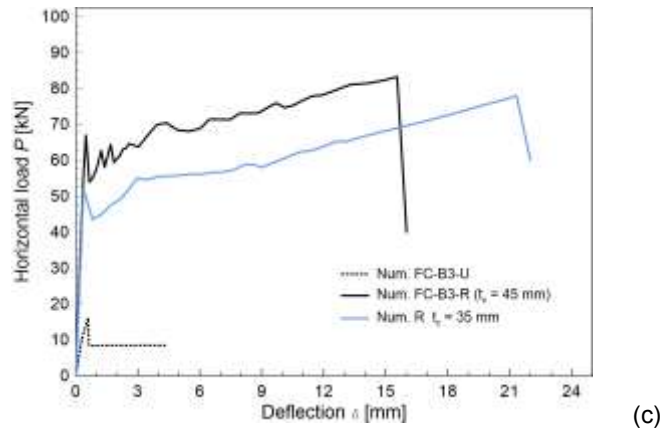


Figure 5.28 – Parametric study on cobblestones reinforced masonry specimens: (a) influence of the mortar tensile strength, (b) of the tension stiffening effect and (c) of the mortar thickness  $t_c$ .

#### 5.3.4 Actual out-of-plane performances of reinforced masonry walls

The bidimensional model described in subsection 5.3.1 was then adopted to simulate the actual out-of-plane performances of some typical configurations of unreinforced and reinforced masonry walls in existing buildings and assess the improvement of their performances induced by the application of the reinforcement. In particular, three different wall configurations were analyzed (Figure 5.29.a): “Case 1” consisted in a one storey building 7650 mm height; in “Case 2” a second storey, 3825 mm height, was added; in “Case 3” a three storey structure was considered, with a 3825 mm height for the ground floor and second floor and a first floor 7650 mm height.

The storey mass distribution related to the seismic combination was assumed to be equal to 480 kg/m<sup>2</sup> for the roof (dead load  $G_1 + G_2 = 4.8$  kN/m<sup>2</sup> and live load = 1.2 kN/m<sup>2</sup>, quasi-permanent factor equal to zero for live loads) and equal to 720 kg/m<sup>2</sup> for intermediate storeys (dead load =  $G_1 + G_2 = 4.8$  kN/m<sup>2</sup> and live load = 4.0 kN/m<sup>2</sup>, quasi permanent factor 0.3 for live loads).

For each case, both a solid brick masonry (thickness 380 mm, self-weight 18 kN/m<sup>3</sup>) and a rubble stone masonry (thickness 400 mm, self-weight 21 kN/m<sup>3</sup>) were investigated, comparing the performances of unreinforced and reinforced configurations.

In the numerical model, the mechanical characteristics of the reinforcement were those described in subsection 5.3.1. Differently, for the masonry, the lower limits of compressive strength and Young modulus indicated in Table C8A.2.1 of Circolare 2 febbraio 2009, n. 617, were adopted. In particular, the categories “bricks and lime mortar” and “uncoursed random rubble stone masonry” were considered. These values were then amplified by a correction factor of 1.5, assuming a mortar of good characteristics (Table C8A.2.2 of Circolare 2 febbraio 2009, n. 617).

Moreover, the compressive resistances were reduced by a safety factor for the material  $\gamma_M = 2$  (local analysis). The masonry mechanical parameters are summarized in Table 5.10. An elastic-plastic behavior in compression and elastic-brittle tension were considered for both the masonry types.

In the numerical model, the walls were considered fixed at the base, while horizontal displacements were avoided at floor levels, assuming an affective link between walls and floors (Figure 5.26.b). The horizontal load was uniformly distributed along the whole wall height; in addition, the gravitational loads of the floors (a 2500 mm width band was considered) and of the masonry spandrels (at floor level and at the upper edge of the openings) were applied.

Nonlinear static analysis were performed by applying at first the gravitational loads and then increasing step-by-step the horizontal displacement of a control point (that of maximum deflection in the elastic phase).

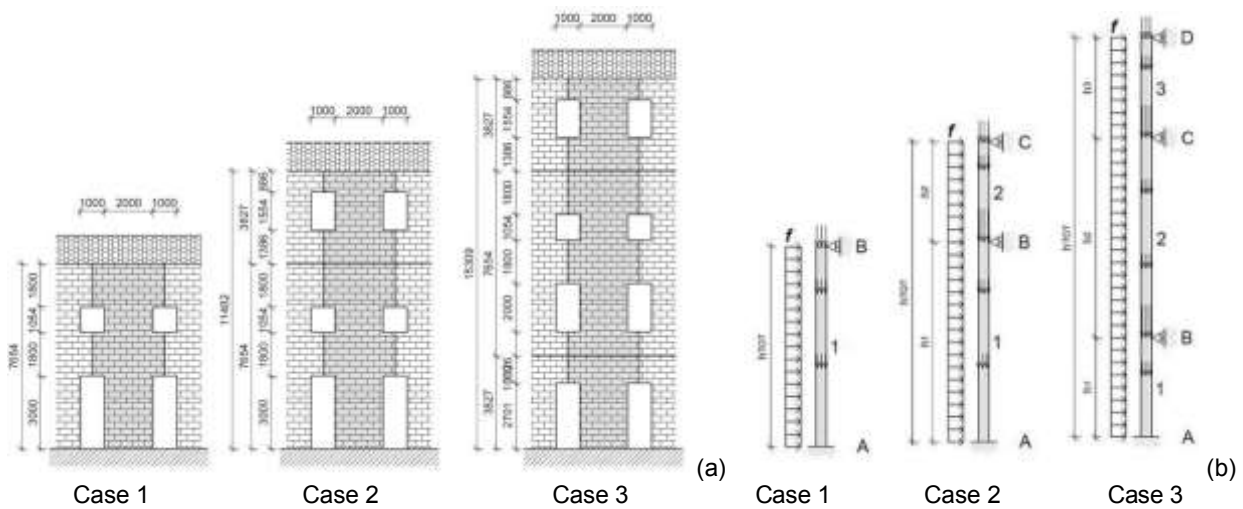


Figure 5.29 – Wall configurations analyzed: (a) frontal views and (b) static scheme assumed in the numerical simulation of the out-of-plane bending behavior

Table 5.10 – Masonry mechanical parameters: Young modulus ( $E_m$ ), compression ( $f_{c,m}$ ) and tensile ( $f_{t,m}$ ) strengths

Masonry type	$E_m$ [MPa]	$f_{c,m}$ [MPa]	$f_{t,m}$ [MPa]
Solid brick	1800	1.80	0.12
Rubble stone	1035	0.75	0.09

The load  $f$  - deflection  $\delta$  curves obtained from the numerical simulations are reported in Figure 5.30, Figure 5.31 and Figure 5.32 for the three different cases; the results are expressed referring to a wall portion 1000 mm width.

From the results of unreinforced masonry walls, a linear elastic behavior emerged until the formation of the first crack; then, a progressive stiffness degradation was noted. The opening of

new cracks occurred (the sequence is indicated on the curves) until the system became hypostatic. However, the wall resistance continued to increase till reaching a constant value: diversely from the result of the experimental tests (subsection 5.1.4), the unreinforced masonry walls exhibited an elastic plastic behavior. In fact, the formation of the kinematic mechanism, once the cracks opening occurred, does not induce the wall collapse, as its out-of-plane capacity is governed by the bending resistance of cracked sections (subsection 5.2.1), due to the great amount of gravitational loads transmitted by floors and spandrels.

Also the curves for the reinforced samples manifested a linear elastic trend until the formation of the first crack; then a stiffness reduction occurred. However, the out-of-plane deflection of the main wall (7650 mm height) remains very limited until the formation of a number of cracks equal to the number of redundant constraints. The GFRP mesh opposed to the cracks opening (the sequence of GFRP mesh failure is reported in the curves). The wall collapse was attained when the GFRP mesh broke in all the formed "plastic hinges".

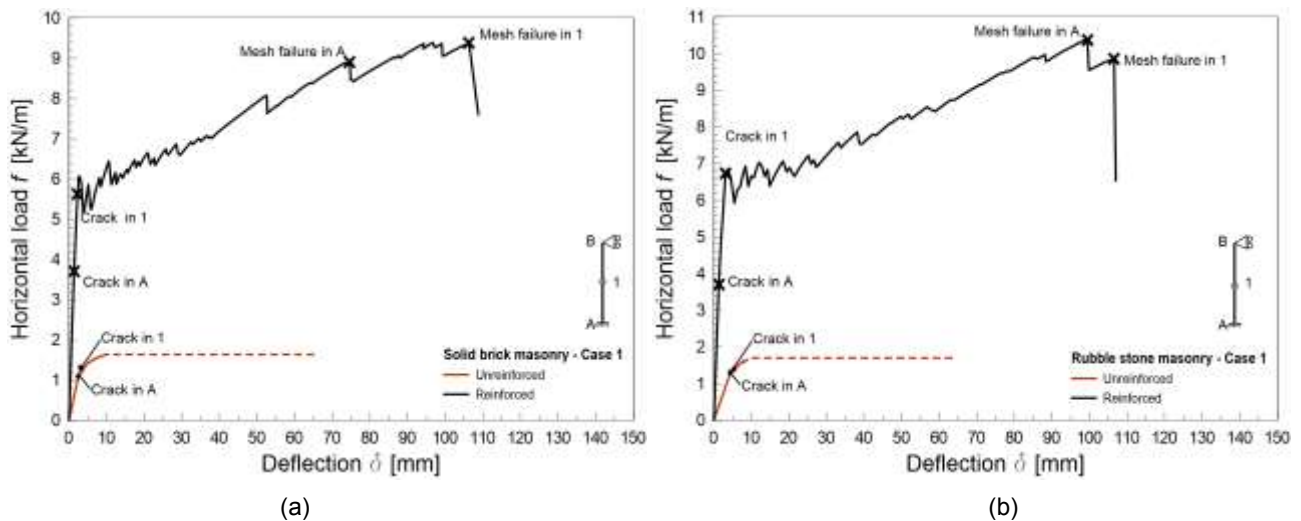


Figure 5.30 – Load deflection curves of Case 1: (a) solid brick and (b) rubble stone masonry

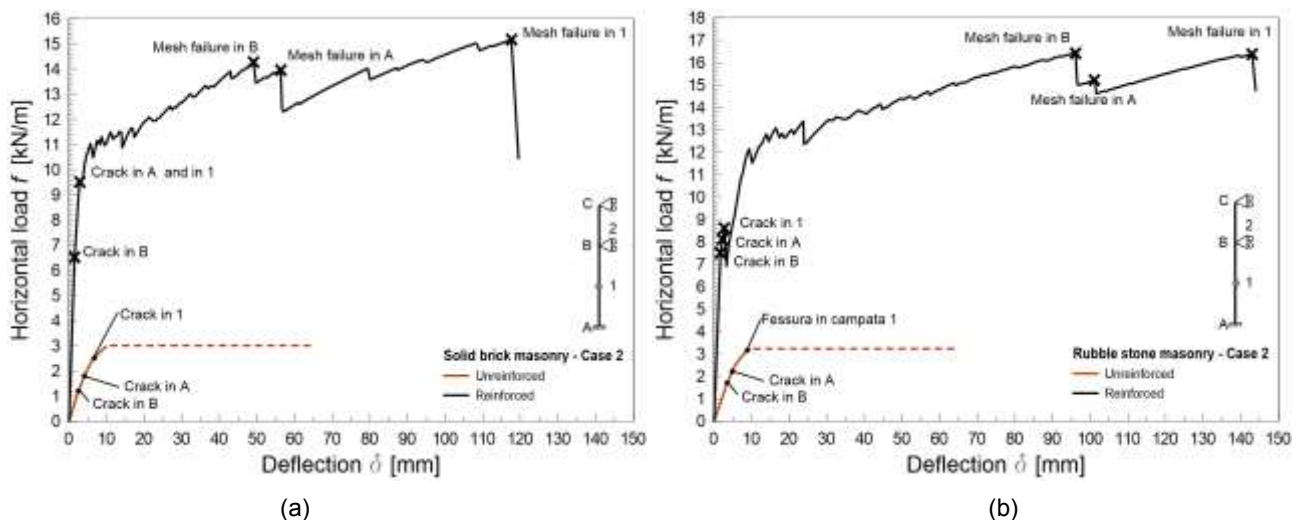


Figure 5.31 – Load deflection curves of Case 2: (a) solid brick and (b) rubble stone masonry

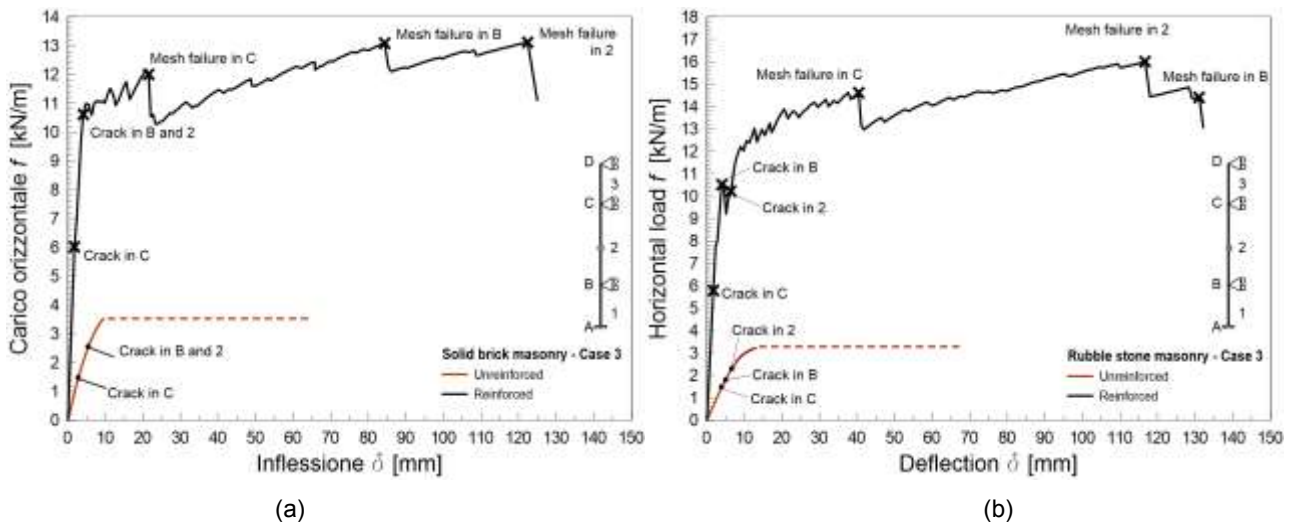


Figure 5.32 – Load deflection curves of Case 3: (a) solid brick and (b) rubble stone masonry

The results of the numerical simulations are illustrated in Figure 5.33 in terms of the maximum out-of-plane resistance  $f_{max}$ . Moreover, in Table 5.11, the ratio between the performances of reinforced and unreinforced walls are calculated; for the reinforced walls the ratio between the deflection at collapse and the height of the main wall is also reported.

The resistance increase ranged from 4 to 6 times, depending on the wall configuration. In addition to this improvement in terms of load-bearing capacity, the reinforced walls reached horizontal deflections of about 1/65 of the wall height before collapsing. As evidenced in the  $f$ - $\delta$  curves, these values were attained due to the presence of the GFRP mesh, which replaced the masonry and the mortar of the coating in tension, once they cracked: the significant reduction of stiffness of cracked sections permitted the achievement of high values of displacements.

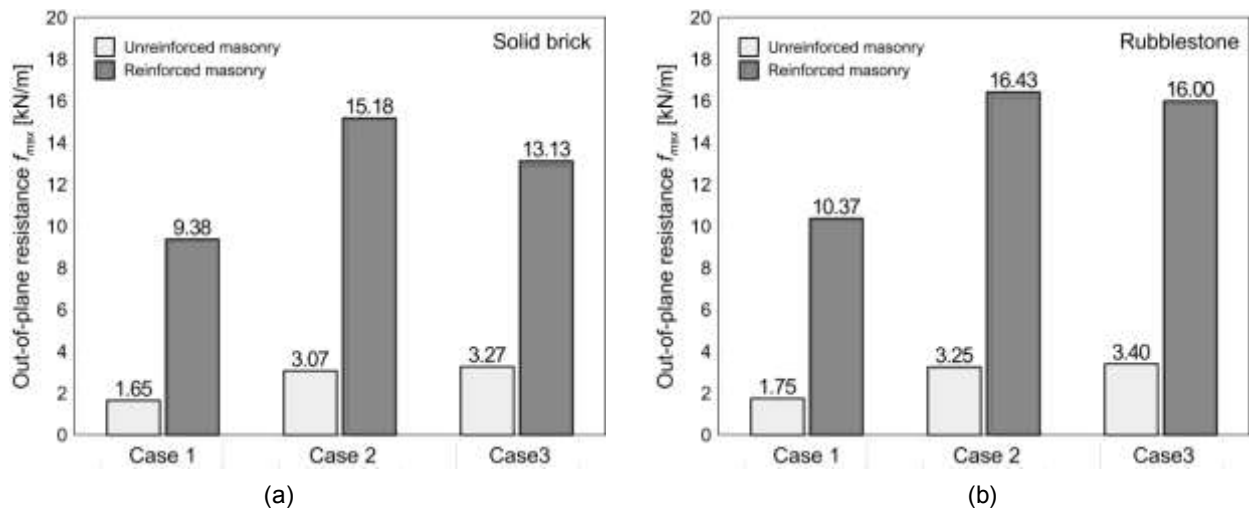


Figure 5.33 – Comparisons between unreinforced and reinforced masonry walls performances in terms of out-of-plane resistances: (a) solid brick and (b) rubble stone masonry

Table 5.11 – Numerical results: out-of-plane resistances of unreinforced ( $f_{max(U)}$ ) and reinforced ( $f_{max(R)}$ ) masonry, ratios ( $f_{max(R)}/f_{max(U)}$ ), and ratios between the maximum deflection of reinforced walls and the main wall height ( $\delta_{(R)}/h$ )

		Case 1	Case 2	Case 3
<b>Solid brick</b>	$f_{max(U)}$ [kN/m]	1.65	3.07	3.27
	$f_{max(R)}$ [kN/m]	9.38	15.18	13.13
	$f_{max(R)}/f_{max(U)}$	5.69	4.95	4.02
	$\delta_{(R)}/h$ [‰]	13.9	15.4	16.0
<b>Rubble stone</b>	$f_{max(U)}$ [kN/m]	1.75	3.25	3.40
	$f_{max(R)}$ [kN/m]	10.37	16.43	16.00
	$f_{max(R)}/f_{max(U)}$	5.93	5.06	4.71
	$\delta_{(R)}/h$ [‰]	14.1	18.7	17.22

## **5.4 Numerical investigation on the behaviour of reinforced masonry vaults**

In ancient masonry buildings of European cities, the presence of masonry arches and vaults is rather frequent. The necessity to prevent possible brittle failures of these structural elements, due, for example, to seismic actions, changes in their use or degradation of the materials, is often accompanied by the need to preserve the appearance of these elements, as parts of the architectural and cultural heritage. Thus, a particular attention to both the effectiveness and the compatibility of the reinforcement technique has to be considered in the design of the intervention.

The Finite Element Models developed in the literature for the study of reinforced masonry vaults (Elmalich and Rabinovitch, 2009) concern mostly nonlinear static analysis with smear crack in tension (Anania & al., 2013, Mahini, 2015; Szolomicki & al., 2015) or discrete crack models (Briccoli Bati and Rovero, 2001; Basilio I., 2007; Milani & al., 2014) for the masonry.

In this study, the Smear Crack numerical model developed for the out-of-plane behavior of masonry (subsection 5.3) was used to perform a preliminary numerical investigation on the performances of reinforced masonry vaults subjected to vertical and horizontal loads acting in the transversal direction in terms of load bearing capacity and displacement capacities (Gattesco & Boem, 2016b).

The main findings of the simulations are described and discussed. The extrados application of the GFRM was preferred in this first study, so to preserve the intrados (visible side), which aspect has often to be maintained for conservation needs. However, also the application at intrados represents a possible intervention solution.

### **5.4.1 Model characteristics**

Finite element models were elaborated using the software Midas FEA to simulate the behavior of unreinforced and reinforced solid brick masonry barrel vaults subjected to vertical loads and horizontal forces acting perpendicular to the vaults axis. Considering the stress state induced by these load patterns, governed by out-of-plane bending, the bi-dimensional model elaborated for the masonry walls (subsection 5.3) was adopted. Pinned nodes were provided in correspondence of the abutments. The influence of edge effect in the stress pattern was neglected in this preliminary approach. The check of the shear resistance in cracked sections and at each springer was performed evaluating the stresses derived from the numerical simulations.

The vaults span was assumed equal to 4000 mm and three different rise/radius ratios ( $f/r$ ) were considered: 1.00, 0.75 and 0.60 (Figure 5.34). The thickness of the vault was 120 mm, considering the 250 x 120 x 55 mm<sup>3</sup> solid units arranged in a running bond normal to the vault's surface (stretchers offset by 1/2 brick per course). A 1000 mm vault nominal width was considered.

The mechanical characteristics were those adopted in subsection 5.3.1 both for solid brick masonry and for the reinforcement.

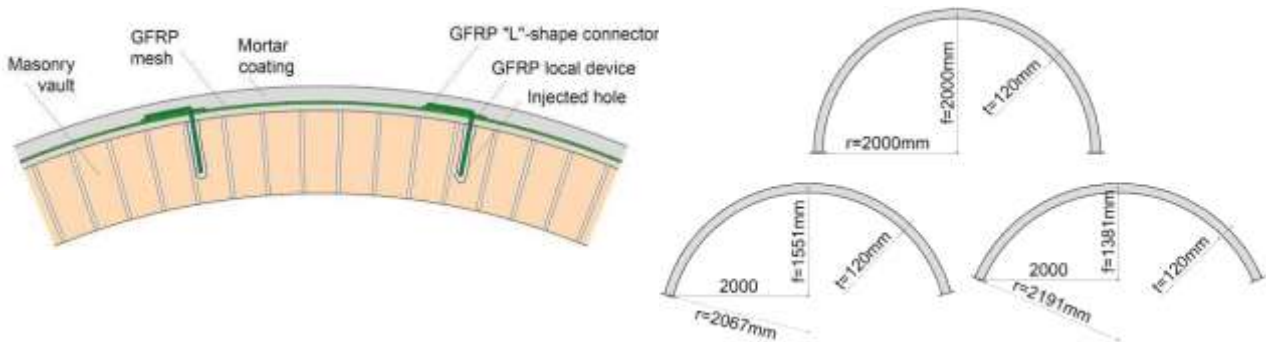


Figure 5.34 – Numerical study on masonry barrel vaults: (a) considered reinforcement technique and (b) cross section geometry of the analyzed cases

#### 5.4.2 Actual behavior of vaults

Two different load patterns were considered: vertical load (“Case V1”) and horizontal load (“Case V2”), both acting perpendicular to the vault axis (Figure 5.35). The considered vaults were assumed as elements supporting only their own weight (shelters), thus both the force distributions were considered proportional to the vault self-weight.

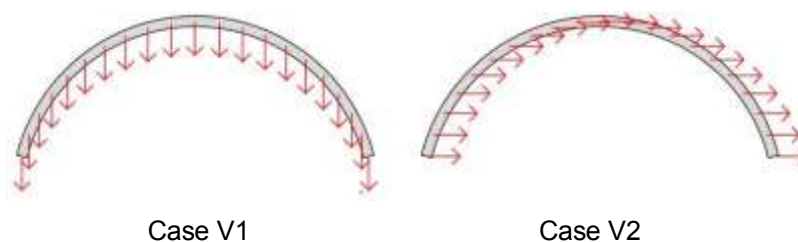


Figure 5.35 – Load patterns considered in the numerical simulations: vertical load (Case V1) and horizontal load (Case V2), acting perpendicular to vault axis, proportional to its self-weight

The nonlinear static analyses were carried out at displacement control, monitoring the vertical displacement of the crown section in Case V1 and the horizontal one in Case V2. It is evidenced that, in Case V2, the vault self-weight acting in the vertical direction was applied before incrementing the horizontal action.

The different numerical models analyzed were marked by an identifier with three parts: the former refers to the load pattern (V1 or V2), the second indicates the rise/radius ratio (1.00, 0.75 or 0.60) and the latter distinguish between unreinforced (U) and reinforced (R) masonry.

The vertical load  $F_v$  against the vertical displacement of the crown  $\delta_v$  curves of unreinforced vaults (Case V1) are displayed in Figure 5.36. The curves showed an initial linear elastic behavior; an example of the deformed shape and the stress pattern at the end of this first, elastic phase is reported in Figure 5.37.a. When the masonry tensile resistance is reached on the extrados side of two symmetrical sections (label “e” in Figure 5.36), two hinges suddenly formed and the load dropped rapidly down before increasing again till the cracking at the intrados of the crown section, with the formation of a third hinge (label “i”). The cracking mechanism is schematized in Figure 5.37.b. The system then offered a residual capacity due to the bending resistance of cracked sections. It is evidenced that, for the vaults with rise/radius ratios equal to 1.00 and 0.75, the maximum vertical load was attained in correspondence of the first cracking, at lateral sections (haunches); differently the capacity of the vault with rise/radius ratio equal to 0.60 was that associated to the bending resistance of cracked masonry without tensile strength.

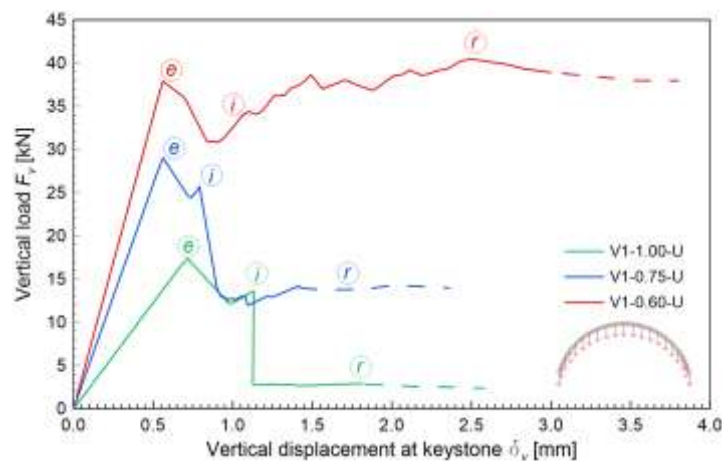


Figure 5.36 – Force-displacement numerical curves of unreinforced vaults subjected to vertical loads (Case V1)

The main numerical results are summarized in Table 5.12: the position of the lateral cracked sections, defined through the angle  $\theta_e$  (Figure 5.37.b) and the values of the related load ( $F_{v,e}$ ) and the crown section vertical displacements ( $\delta_{v,e}$ ) are indicated. Moreover, the load and the crown section displacements associated to the cracking at the crown section ( $F_{v,i}$  and  $\delta_{v,i}$ , respectively) and the amounts of the residual loads  $F_{v,r}$  due to bending of cracked sections,  $F_{v,r}$ , are also reported. Table 5.12 shows also the vault self-weight  $W$  and the amount of  $\alpha_v$ , that indicates the ratio between the overload and the self-weight ( 5.13 ). This coefficient gives an amount of the vertical component of the seismic action that the structure may support without collapse, in terms of ratio  $S_e(T)/g$  of the vertical elastic response spectrum to the acceleration of gravity.

$$\alpha_v = \frac{F_{v,\max} - W}{W} \quad (5.13)$$

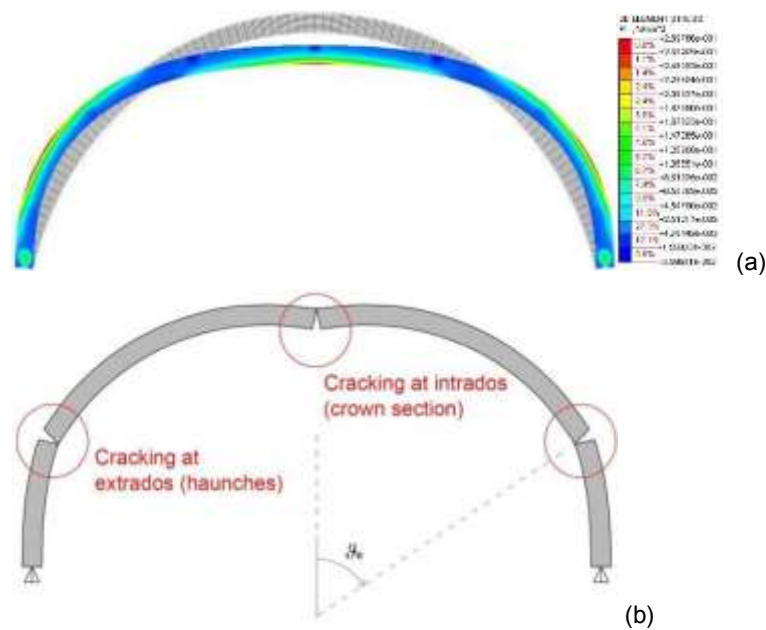


Figure 5.37 – Case V1: (a) principal tensile stresses distribution and deformed shape just before the reaching of the first cracking and (b) typical failure mechanism

Table 5.12 – Numerical results concerning unreinforced vaults - Case V1: position of the lateral cracked sections ( $\theta_e$ ), vertical loads ( $F_v$ ) and crown section vertical displacements ( $\delta_v$ ) associated to the crack formation at extrados (suffix e) and intrados (suffix i), residual load (suffix r), self-weight ( $W$ ) and ratio  $\alpha_v$ .

	V1-1.00-U	V1-0.75-U	V1-0.60-U
$\theta_e$ [°]	±67	±57	±48
$F_{v,e}$ [kN]	17.42	30.31	37.91
$\delta_{v,e}$ [mm]	0.72	0.61	0.56
$F_{v,i}$ [kN]	13.62	25.71	31.46
$\delta_{v,i}$ [mm]	1.13	0.79	0.95
$F_{v,r}$ [kN]	2.90	14.01	43.34
$W$ [kN]	14.65	12.93	12.04
$\alpha_v$ [-]	0.19	1.34	2.60

The  $F_v - \delta_v$  curves of reinforced vaults subjected to a vertical load (Case V1) are plotted in Figure 5.38: an initial linear elastic behavior was obtained, with a stiffness higher than that of the unreinforced vaults, due to the presence of the mortar coating. Then, when the masonry tensile strength was attained in correspondence of the intrados of the crown section, the vault cracked and a hinge formed; a temporary decrease of resistance was obtained and then grew up again. At the increasing of the displacement  $\delta_v$ , also the tensile resistance of the mortar of the coating was

attained at the extrados of two symmetrical lateral sections, but the presence of the GFRP wires permitted to maintain a significant bending resistance; the collapse occurred when the GFRP wires broke contemporary in these two sections.

In Table 5.13 the main results concerning reinforced vaults are summarized and, in particular, the values of the vertical load ( $F_v$ ) and of the crown section vertical displacements ( $\delta_v$ ) associated to the crack formation at the intrados of the crown section (suffix “ $i$ ”), at the extrados of the haunches (suffix “ $e$ ”) and to the GFRP wires rupture (suffix “ $w$ ”) are reported. Moreover, the angle  $\theta_w$  (in respect to the vault rise) at which this rupture occurred, the vault self-weights and the values of  $\alpha_v$  - equation ( 5.13 ) - are also reported.

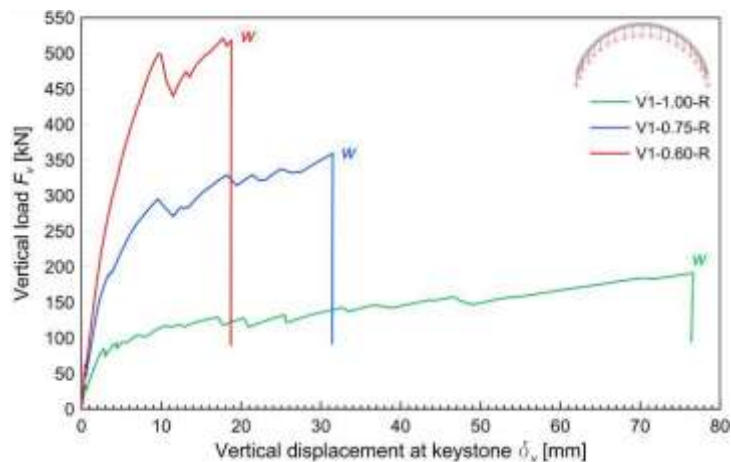


Figure 5.38 – Force-displacement numerical curves of reinforced vaults subjected to vertical loads (Case V1)

Table 5.13 – Numerical results concerning reinforced vaults - Case V1: vertical loads ( $F_v$ ) and crown section displacements ( $\delta_v$ ) associated to the crack formation at intrados (suffix  $i$ ) and extrados (suffix  $e$ ) and to the GFRP wire rupture (suffix  $w$ ), position of the cross section in which the wires rupture occurred ( $\theta_w$ ), self-weights ( $W$ ) and ratios  $\alpha_v$ .

	V1-1.00-R	V1-0.75-R	V1-0.60-R
$F_{v,i}$ [kN]	33.64	51.26	62.71
$\delta_{v,i}$ [mm]	0.54	0.44	0.45
$F_{v,e}$ [kN]	52.88	91.32	125.21
$\delta_{v,e}$ [mm]	1.43	1.23	1.31
$F_{v,w}$ [kN]	191.53	359.38	518.88
$\delta_{v,w}$ [mm]	76.64	31.50	18.77
$\theta_w$ [°]	±67	±57	±48
$W$ [kN]	19.17	16.93	15.23
$\alpha_v$ [-]	8.99	20.23	33.07

By comparing the tests results of reinforced and unreinforced masonry vaults subjected to vertical loads, considerable increments emerged both in terms of resistance and displacement

capacities, due to the presence of the GFRP mesh. The results, expressed in terms of ratio  $\alpha_v$ , evidence for the unreinforced rounded vault a value of 0.19, that is a resistance capacity very limited when compared to the typical amount of the spectral acceleration demand in seismic regions. Differently, the other two unreinforced configurations manifested greater values ( $\alpha_v = 1.34$  for  $f/r = 0.75$  and  $\alpha_v = 2.60$  for  $f/r = 0.60$ ), indicating a significant resistant capacity. In the reinforced configurations, the values of  $\alpha_v$  increased to 8.99 for the rounded vault, and to 20.23 or 33.07 for the segmental vaults with a ratio  $f/r$  of 0.75 or 0.60, respectively.

The horizontal load,  $F_h$ , at the varying of the horizontal displacement at the crown section,  $\delta_h$ , curves of unreinforced vaults subjected to Case V2 are plotted in Figure 5.39. It emerged a initial linear elastic behavior (Figure 5.40.a) up to reaching the masonry tensile resistance on the tensed extrados of one haunch. In correspondence of this section a hinge formed in the masonry and the load rapidly decreased before increasing again till the cracking at the intrados of the other haunch and the consequent opening of a second crack (Figure 5.40.b). It is evidenced that the maximum horizontal load was always attained in correspondence of the first cracking at the extrados.

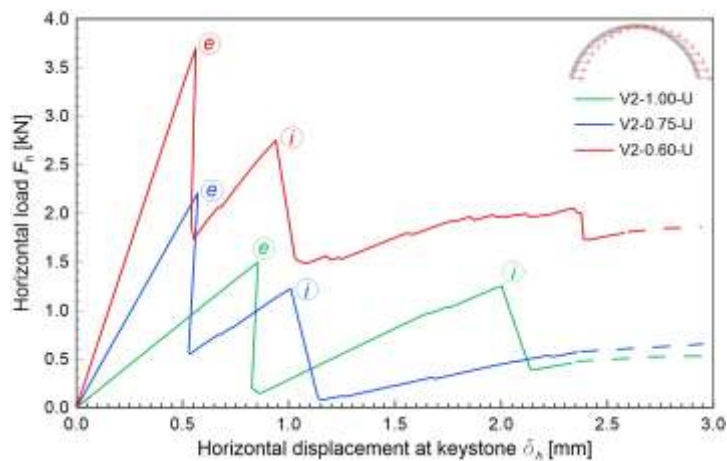


Figure 5.39 – Force-displacement numerical curves of unreinforced vaults subjected to horizontal loads (Case V2)

The main numerical results are summarized in Table 5.14: the inclination  $\theta$  of the cracking planes (in respect to the vault rise), the horizontal loads  $F_h$  and the crown section horizontal displacements  $\delta_h$  associated to the crack formation at extrados (suffix “e”) and intrados (suffix “i”) are indicated. Moreover the vaults self-weights and the amount of  $\alpha_h$  - ratio between the vault horizontal resistance and the self-weight ( 5.14 ) - are reported.

$$\alpha_h = \frac{F_{h, \max}}{W} \quad (5.14)$$

The coefficient  $\alpha_h$  represents the horizontal component of the seismic action that the structure may support without collapsing, in terms of ratio  $S_e(T)/g$  of the horizontal elastic response spectrum to the acceleration of gravity.

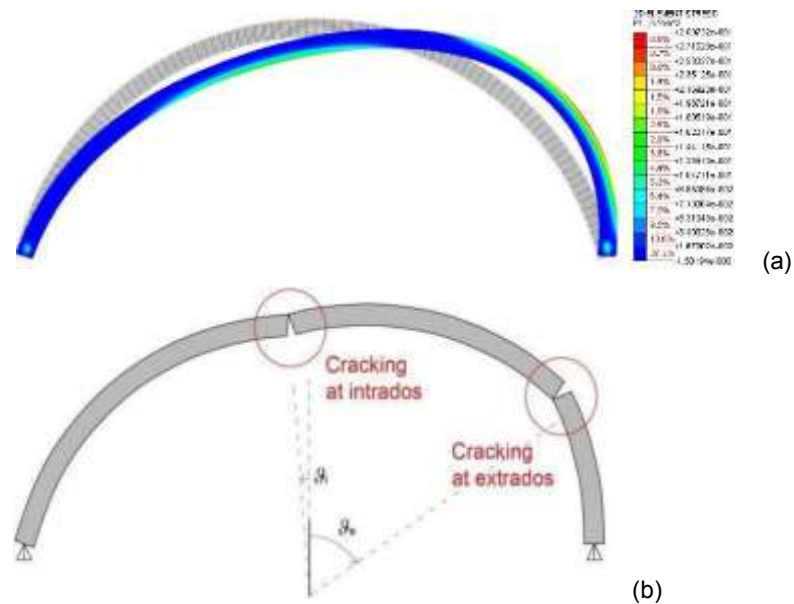


Figure 5.40 – Case V2: (a) principal tensile stresses distribution and deformed shape of unreinforced masonry vaults just before the reaching of the first cracking and (b) typical failure mechanism

Table 5.14 – Numerical results concerning unreinforced vaults - Case V2: inclination of the cracking planes ( $\theta$ ), loads ( $F_h$ ) and crown section displacements ( $\delta_h$ ) associated to the crack formation at extrados (suffix e) and intrados (suffix i), self-weights ( $W$ ) and ratios  $\alpha_h$

	V2-1.00-U	V2-0.75-U	V2-0.60-U
$\theta_e$ [°]	+57	+49	+43
$F_{h,e}$ [kN]	1.50	2.21	3.70
$\delta_{h,e}$ [mm]	0.86	0.57	0.56
$\theta_i$ [°]	-33	-7	-15
$F_{h,i}$ [kN]	1.26	1.22	2.00
$\delta_{h,i}$ [mm]	2.00	1.01	2.38
$W$ [kN]	14.65	12.93	12.04
$\alpha_h$ [-]	0.10	0.17	0.31

The  $F_h - \delta_h$  curves of reinforced vaults subjected to horizontal load (Case V2) - Figure 5.41 - manifested an initial linear elastic behavior with stiffness higher than that of the unreinforced ones, due to a thicker cross section and a higher Young modulus of the mortar of the coating. The first crack occurred at the tensed intrados of a haunch, when the masonry tensile strength was attained, and induced the formation of a hinge (Figure 5.42.a). A temporary decrease of resistance was noted; then, as the load increased, the tensile resistance of the mortar was attained at the

tensed extrados of the other haunch but the GFRP wires prevented the crack opening and the formation of another hinge. Then, as the displacement  $\delta_h$  increased, the formation of a new hinge occurred in masonry at intrados, below the first one (Figure 5.42.b). The collapse of the vault occurred in consequence of the tensile rupture of the GFRP wires at the opposite haunch.

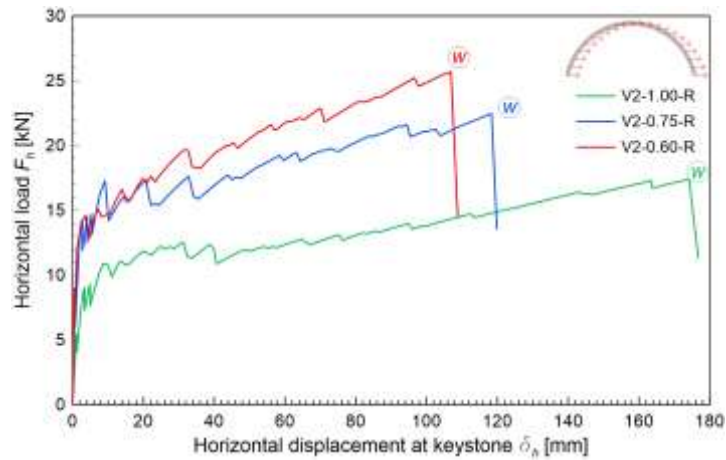


Figure 5.41 – Force-displacement numerical curves of reinforced vaults subjected to horizontal loads (Case V2)

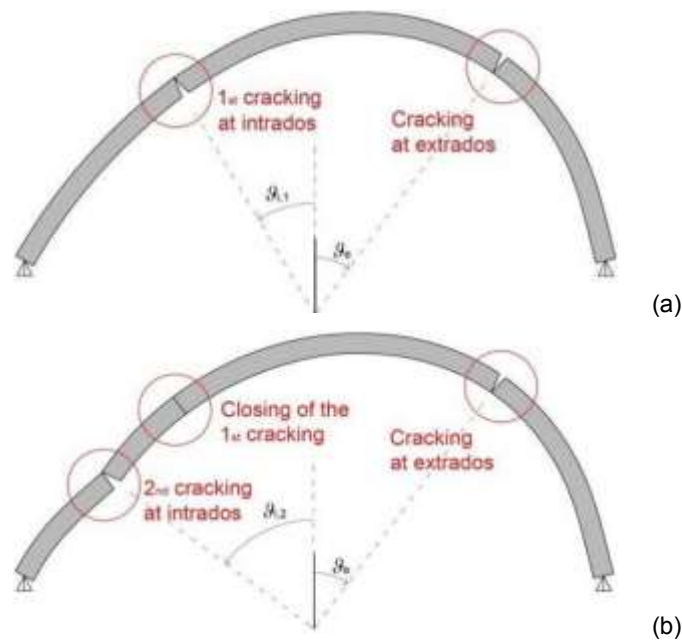


Figure 5.42 – Typical failure mechanism of reinforced vaults subjected to “Case V2” load pattern: (a) up to cracking at the extrados, (b) due to bending resistance of right haunch section provided by the GFRP mesh

Table 5.15 contains the main results obtained from the numerical simulations of reinforced vaults, indicating the inclination of the cracking planes (in respect to the vertical), the horizontal loads  $F_h$  and the crown section displacements  $\delta_h$  associated to each crack formation and to the

GFRP wires rupture. The vaults self-weights and the amount of  $\alpha_h$  - equation ( 5.14 ) - are also indicated.

Appreciable increments emerged by comparison of the results of reinforced and unreinforced vaults subjected to horizontal loads, both in terms of resistance and displacement capacity. As in Case V1, also in Case V2 the GFRP mesh provided a primary role in the load carrying capacity of the structural element once the mortar coating cracks. The values of the ratio  $\alpha_h$  obtained for the unreinforced vaults, compared to the typical range of the spectral acceleration demand in seismic regions, evidenced very low resistance capacities:  $\alpha_h$  resulted equal to 0.10 for the rounded barrel vault, 0.17 for the vault with  $f/r = 0.75$  and 0.31 for that with  $f/r = 0.75$ . Differently, in the reinforced configurations, the ratios  $\alpha_h$  attained to considerably higher values: 0.91 for the rounded vault and 1.33 or 1.69 for the segmented vaults with a ratio  $f/r$  of 0.75 or 0.60, respectively.

In general, the numerical simulations of the actual behavior of masonry vaults evidenced that the GFRM technique enhances of about 11-12 times the vertical load carrying capacity of the vaults, with slightly higher values at the reducing of the  $f/r$  ratio (Figure 5.43.a). Increments ranging from 7 to 11 times result for the horizontal load carrying capacity, with a higher effectiveness as the  $f/r$  ratio increased (Figure 5.43.b).

Table 5.15 – Numerical results concerning reinforced vaults - Case V2: inclination of the cracking planes ( $\theta$ ), loads ( $F_h$ ) and crown section displacements ( $\delta_h$ ) associated to the crack formation at intrados (suffixes  $i1$  and  $i2$ ) at extrados (suffix  $e$ ) and to the GFRP wire rupture (suffix  $w$ ), self-weights ( $W$ ) and ratios  $\alpha_h$

	V2-1.00-R	V2-0.75-R	V2-0.60-R
$\theta_{i1}$ [°]	-29	-33	-28
$F_{h,i1}$ [kN]	5.48	8.04	8.93
$\delta_{h,i1}$ [mm]	1.09	0.69	0.52
$\theta_e$ [°]	+56	+48	+38
$F_{h,e}$ [kN]	5.56	9.83	11.27
$\delta_{h,e}$ [mm]	1.71	1.42	1.17
$\theta_{i2}$ [°]	-59	-52	-44
$F_{h,i2}$ [kN]	12.09	17.26	14.57
$\delta_{h,i2}$ [mm]	39.84	9.17	3.62
$\theta_w$ [°]	+47	+33	+26
$F_{h,w}$ [kN]	17.39	22.46	25.69
$\delta_{h,w}$ [mm]	174.12	118.37	106.89
$W$ [kN]	19.17	16.93	15.23
$\alpha_h$ [-]	0.91	1.33	1.69

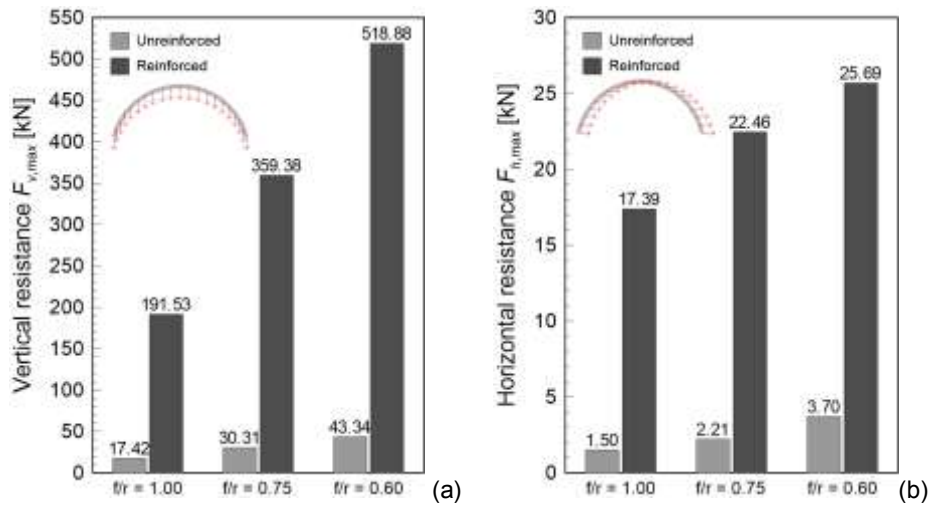


Figure 5.43 – Comparisons between the load carrying capacity of unreinforced reinforced vaults for (a) Case V1 and (b) Case V2

#### 5.4.3 Incidence of load pattern on the vault behavior

As evidenced in 2.2.1, several experimental campaigns concerning comparisons between the performances of unreinforced and reinforced arches and vaults are nowadays available in the literature. The most of these results consists in quasi-static tests and commonly refers to two loading patterns (Figure 5.44): in the former (named “Case V3”) a concentrated vertical load is applied symmetrically, at the crown section; in the latter (“Case V4”) the vertical load acts asymmetrically, at 1/4 of the span. These schemes are in agreement with the typical test setups used in the past for the experimental investigation on unreinforced vaults and derived from the need to simplify the experimental loading procedure while reproducing the typical failure mechanisms of actual vaults. These setups were then extended also to reinforced vaults by several researches.

To assess the reliability of these simplified loading schemes, the vaults described in subsection 5.4.1 were subjected to the two load patterns V3 and V4 and the results were then compared with those obtained from cases V1 and V2 (subsection 5.4.2).

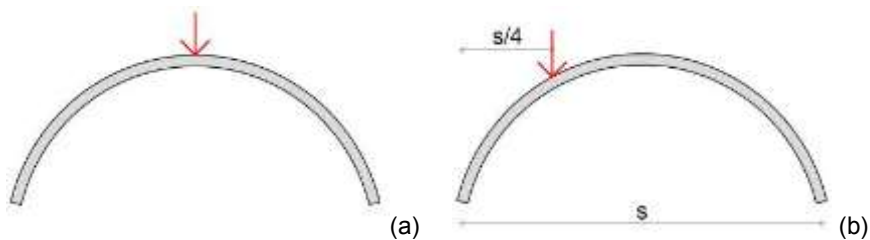


Figure 5.44 – Simplified load patterns usually considered in quasi-static experimental tests on masonry vaults: (a) vertical load at crown - Case V3 - and (b) at 1/4 of the span - Case V4

In Case V3, the unreinforced vaults exhibited, at first, a crack at the crown section (intrados) and, then, two symmetric cracks at the haunches (extrados). For the vaults with rise/radius ratios equal to 0.75 and 0.60, the maximum vertical load was attained in correspondence of the cracking at the haunches; differently the capacity of the rounded vault was that associated to the first cracking, at the crown section. The behavior of reinforced vaults (Figure 5.45.a) qualitatively is in agreement with that described for Case V1.

A comparisons between the results of Case V1 and Case V3 is summarized in Table 5.16, in terms of position of the cracked haunch section in respect to the arch rise  $\theta_e$ , maximum overload  $Q_{v,max}$ , evaluated as difference between the vault vertical load-carrying capacity and the self-weight. Both for unreinforced and reinforced vaults, significantly lower values of  $Q_{v,max}$  emerged for case V3. In fact, as the load is concentrated in the central part of the vault, the masonry tensile strength was attained more rapidly. Moreover, due to the lower stabilizing contribute of the compression among blocks in the lateral parts of the vault, the hinges opening at the haunches was anticipated. It is also evidenced that in Case V3 the formation of these hinges occurred at a higher inclination in respect to that occurred in Case V1.

The ratio between the maximum overloads in Case V1 and Case V3 ( $Q_{max,V1}/Q_{max,V3}$ ) are also reported in Table 5.16: this value is not constant but increases with the decrease of  $f/r$  and is influenced by the presence of the reinforcement. Thus, in general, even if the collapse mechanism is qualitatively the same, there is not a unique correlation between the vertical load-bearing capacity of masonry vaults subjected to V1 and V3 load patterns, but it depends on the geometrical and mechanical characteristic of the vault.

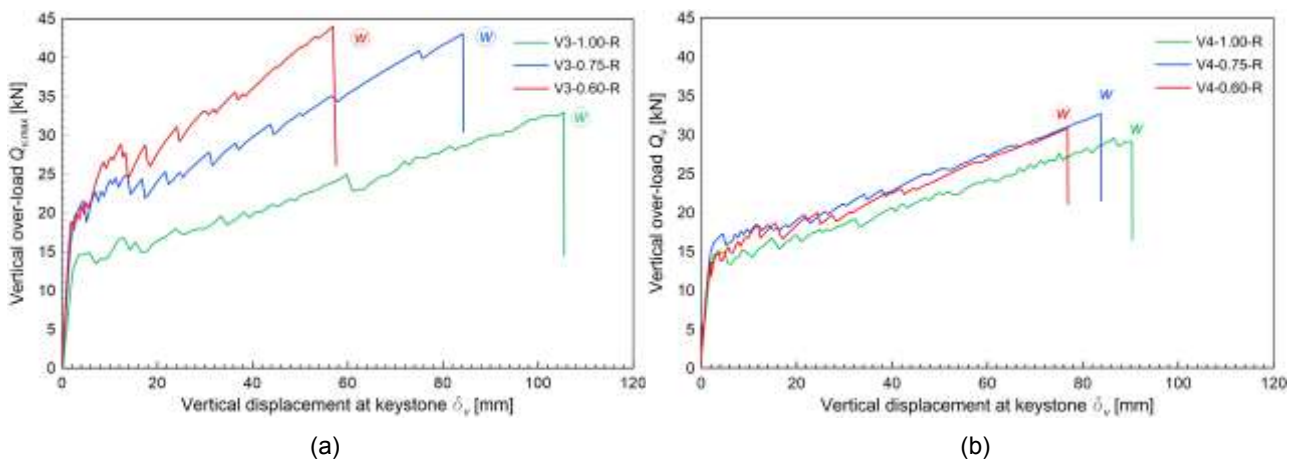


Figure 5.45 – Numerical results of in terms of vertical force-displacement curves for (a) Case V3 and (b) Case V4

Table 5.16 – Numerical results of unreinforced and reinforced vaults: comparisons between Case V1 and Case V3 in terms of position of the haunch cracked section ( $\theta_{v,e}$ ), maximum over-loads ( $Q_{max}$ ) and the ratio between maximum over-loads in case V1 and V3 ( $Q_{max,V1} / Q_{max,V3}$ ).

		<b>f/r = 1.00</b>		<b>f/r = 0.75</b>		<b>f/r = 0.60</b>	
		<b>V1</b>	<b>V3</b>	<b>V1</b>	<b>V3</b>	<b>V1</b>	<b>V3</b>
<b>URM</b>	$\theta_{v,e}$ [°]	±67	±61	±57	±51	±48	±42
	$Q_{v,max}$ [kN]	2.77	0.78	17.38	2.05	31.20	3.15
	$Q_{maxV1}/Q_{maxV3}$	3.55		8.48		9.90	
<b>RM</b>	$\theta_{v,e}$ [°]	±67	±51	±57	±37	±48	±35
	$Q_{v,max}$ [kN]	172.36	32.97	342.45	43.06	503.65	44.03
	$Q_{maxV1}/Q_{maxV3}$	5.23		7.95		11.44	

In unreinforced vaults subjected to the load pattern V4, the formation of the first crack occurred at the intrados of one haunch, in correspondence of the loaded cross section; then, a second crack appeared at the extrados of the other haunch; the maximum horizontal load was always attained in correspondence of the first cracking. The failure mechanism is qualitatively in agreement with that described for Case V2 (Figure 5.40.b), even though a quite different position of these sections was obtained. However, it is not possible to compare the results in terms of load carrying capacity, due to the different direction of the load.

Also in reinforced vaults (Figure 5.45.b) the first hinge occurred in correspondence of the loaded cross section, at intrados; then, as the load increased, the tensile resistance of the mortar was attained on the tensed extrados of the other haunch. The GFRP wires contrasted the crack opening, thus the formation of the second hinge occurred only at the reaching of the wires rupture. It is evidenced that, in this case, the failure mechanism differed to that of Case V2 (Figure 5.42), characterized by two cracks at the intrados of one haunch.

In Table 5.17 the results of Case V2 and Case V4 are compared: the ratio between the reinforced and unreinforced maximum overloads are indicated for Case V2 and Case V4. It is evidenced that the resistance increments are almost the same for the rounded vault and then tended to diverge at the decrease of ratio  $f/r$ .

Numerical results evidenced that the analysed simplified configurations are not able, in general, neither to reproduce the actual vaults behavior (both of unreinforced and reinforced cases) nor to predict the actual effectiveness of the reinforcement, providing only a qualitative indication of the possible reinforcement benefits.

Table 5.17 – Numerical results of unreinforced and reinforced vaults: comparisons between Case V2 and V4 in terms of position of the haunch cracked section ( $\theta$ ), maximum over-loads in the horizontal ( $H_{max}$ ) and in the vertical ( $Q_{max}$ ) direction and ratio between the reinforced and unreinforced masonry resistances.

		<b>f/r = 1.00</b>		<b>f/r = 0.75</b>		<b>f/r = 0.60</b>	
		V2	V4	V2	V4	V2	V4
<b>U</b>	$\theta_e$ [°]	+57	+40	+49	+39	+43	+38
	$H_{max}$ ; $Q_{max}$ [kN]	1.50	2.41	2.21	2.86	3.70	3.05
<b>R</b>	$\theta_w$ [°]	+49	+37	+33	+30	+26	+29
	$H_{max}$ ; $Q_{max}$ [kN]	17.39	29.58	22.46	32.70	25.69	30.85
$H_{max,R} / H_{max,U}$		11.59	12.27	10.16	11.43	6.94	10.11
$Q_{max,R} / Q_{max,U}$							

## 5.5 Summary

The GFRM effectiveness against the out-of-plane masonry failure was investigated experimentally and numerically comparing the load carrying and displacement capacities of plain and reinforced masonry full-scale samples.

Four point bending tests were performed considering three types of masonry (solid brick, rubble stone and cobblestones) and the failure modes of the specimens were analysed. It emerged that, in unreinforced masonry, the collapse occurred abruptly, due to the opening of a single horizontal crack, almost at mid-height of the specimen, at the interface between mortar joint and masonry units. In reinforced masonry, it can be distinguished a first phase, until the first cracking in the mortar coating, in which the wall is almost intact, and a second phase, in which more horizontal cracks sequentially formed, in the middle third of the height. The collapse occurs when, in correspondence of a crack, the GFRP wires fail in tension.

By comparing the resistances of reinforced and unreinforced samples, emerged that strengthened specimens are able to resist to out-of-plane bending moments almost 5 times greater than that of plain specimens and can overcome to deflections ranging from 1/200 to 1/100 the wall height before collapse (while unreinforced samples collapsed for very little deflections, up to 1/5000 of the wall height).

An analytical study on reinforced walls showed that the cracking and the ultimate bending moments can be easily predicted by applying the well-known relationships used in the design of reinforced concrete beams subjected to combined axial and bending actions for uncracked and cracked sections, respectively.

A 2D numerical model was then developed so to comprehend the mechanical behaviour of reinforced masonry walls. Four-node plane strain elements were utilized for the masonry and for the mortar of the coating, while the GFRP wires were modelled by means of truss elements. Nonlinear static analyses were performed by applying firstly the whole self-weights and incrementing then step-by-step the imposed out-of-plane displacement. The mechanical characteristics of the adopted materials were deduced from experimental characterization tests and the numerical simulation on unreinforced specimens permitted to calibrate the dissipative capacity of the different masonry types.

The numerical results concerning reinforced samples resulted in agreement with the experimental ones, proving the reliability of the simulations. The possibility to extend the 2D model to a 3D model, based on the same material characteristics and on eight node solid elements instead of four-node plane strain elements, was also proved.

The numerical simulations allowed evaluating the influence on the cracking and on the collapse point of different masonry and reinforcement parameters. In particular, an increase of the stiffness of either the masonry or the GFRP mesh limited the wall deflection but did not influence the wall resistance capacity, whereas a premature rupture of the mesh resulted in an early wall collapse both in terms of load and displacement. The effectiveness of the reinforcement technique decreased with the wall thickness. The increase of the tensile resistance of the mortar affected the first cracking load and limited the wall ultimate deflection, while the increase of the mortar residual resistance (accounting for a higher tension stiffening effect) induced in the load-displacement curves a modification of the trend of the post cracking branch. An amplification of the coating thickness resulted in both of these effects.

The 2D finite element numerical model was then employed to simulate and compare, in terms of both resistance to out-of-plane deflection, the structural performances of some actual wall configurations before and after the execution of the reinforcement. In particular, three different configurations (one, two and three storey levels) and two types of masonry (solid brick, 380 mm thick and rubble stone masonry, 400 mm thick) were analysed. In addition to the wall self-weight, also the stabilizing contribution of gravity loads transmitted by the floors and by adjacent masonry spandrels was considered. According to the experimental findings, unreinforced walls manifested limited resistance and displacement performances, governed by the bending resistance of cracked sections. Differently, in reinforced cases the contribution of the GFRP mesh allowed the reinforced walls to provide excellent characteristics of load-bearing capacity. In the analyzed cases, the out-of-plane resistances ranging from 4 to 6 times those of the respective unreinforced configurations were attained and wall deflections of about 1/65 of the height of the wall were reached.

Based on the 2D finite element model created for reinforced masonry walls subjected to out-of-plane bending, a numerical study aimed to assess the effectiveness of the GFRM strengthening technique applied at the extrados of existing masonry vaults was also conducted. The investigated vaults had a 120 mm thickness and a span of 4000 mm; three different rise/radius ratios ( $f/r$ ) were considered: 1.00, 0.75 and 0.60. The performances were compared in terms of capacity curves representing the vertical or horizontal load against the vertical or horizontal displacement at the crown section. The different failure mechanisms were also discussed.

Very limited capacities emerged for the unreinforced vaults subjected to horizontal load and also for the rounded vault excited by vertical forces. A significant improvement was evidenced by analysing of reinforced masonry cases. In fact, the GFRP mesh at the extrados prevents the crack opening once the mortar of the coating failed in tension. The numerical simulations of the actual behavior of masonry vaults evidenced that the reinforcement technique proposed enhances of about 11-12 times the vertical load carrying capacity of the vaults, with slightly higher values at the

reducing of the  $f/r$  ratio. Increments ranging from 7 to 11 times were obtained for the horizontal load carrying capacity, with a higher effectiveness as the  $f/r$  ratio increased.

The performances were then compared to those of vaults subjected to concentrated vertical loads at the crown section or at  $1/4$  of the span, which represents the typical test setups used in the literature. Numerical results evidenced that these simplified configurations are not able, in general, neither to reproduce the actual vaults behavior nor to predict the actual effectiveness of the reinforcement, providing qualitative information of the reinforcement behavior, and evidencing the necessity to individuate more appropriate and representative testing methods.

## 6 CONCLUSIONS

Though summarised in detail at the end of each section, a brief collection on the contents and main results of the present work is necessary to present conclusion remarks and future developments of the research.

The aim was to investigate on the effectiveness of a reinforcing system for improving the seismic performances of existing, unreinforced masonry walls and buildings in terms of load bearing and displacement capacity.

The considered technique (called Glass Fiber Reinforced Mortar - GFRM) consisted in the application, on both the masonry surfaces, of a mortar coating (at least 30 mm thick) with GFRP meshes embedded. Different types of mortar may be utilized for the coating, made with calcareous or siliceous sand and using natural binders, cement and pozzolanic additives. GFRP meshes of different grid dimensions and fiber percentages can be applied.

The research comprehended, at first, the characterization of the GFRM composite material and, then, a study of its influence on the in-plane and out-of plane behavior of masonry walls. The adopted method consisted in performing experimental investigations on elemental specimens aimed to assess, from the empirical point of view, the reinforced masonry performances in comparison with that of plain masonry. The analysis and discussion of the experimental results permitted to understand the mechanisms, which intervene in the development of the resisting system. It was thus possible to provide some analytical correlation to estimate the reinforced masonry performances. Moreover, finite element models were elaborated, allowing numerical investigations, which permitted to extend the reinforced masonry study on actual and more complex configurations.

In particular, the results of several characterization tests (pull-out, lap-splice, bond and tensile tests) performed so to investigate on the tensile properties and bond performances of the strengthening system were presented and discussed. Proper characterization tests permitted the estimation of the anchorage length to make effective the reinforcement and the definition of the stress-strain curve of the composite material subjected to tensile force. The influence of some fundamental parameters, such as the clamping system, the anchorage length, the boundary conditions and the sample dimensions, were discussed. Though not exhaustive of the wide background of different assets available for the reinforcement technique, the test results pointed out on the main aspects to consider for the definition of correct testing procedures for the GFRM characterization and obtaining useful information for correct design procedures and numerical modeling purposes.

The in-plane performances of GFRM reinforced masonry walls were then investigated. A broad collection of results of diagonal compression tests were presented. Experimental tests concerned square wallets of different masonry types and thicknesses and the influence of the mortar coating and GFRM meshes mechanical characteristics were investigated.

The different performances were analysed, discussed and compared in terms of stiffness, resistance and deformation capacities. Significant increasing, both in resistance and ductility, emerged in reinforced masonry, proving the in-plane effectiveness of the reinforcement technique.

In particular, though it generally did not affect significantly the elastic deformability and the peak strength, the GFRP mesh played a fundamental role in the post-elastic phase, contrasting the opening of cracks and supporting tensile stresses. Thus, lower reinforcement percentages determined a more pronounced resistance degradation. Moreover, lower mesh grid dimensions led to a higher diffusion of cracks but in some cases induced a premature failure of the reinforcement, due to the plaster delamination. In regard to the influence of the mortar of the coating type, the dependence from a single mechanical parameter (i.e. the mortar tensile strength, Young modulus or compressive strength) was not clear. However, an increasing of the resistance increment ratios at the increasing of the mortar tensile strength was observed and the decrease of resistance resulted more rapid in stronger samples. Future insights regarding the interaction at the masonry-mortar interface should investigate deeper on this aspect, as premature slippages and detachments can occur.

The equivalent principal tensile strengths of masonry were derived from experimental results and analytical formulations were proposed for the reinforced masonry stiffness and resistance predictions. It emerged that the contribution of the reinforced mortar coating on the reinforced masonry resistance is influenced by the characteristics of both the masonry and the reinforcement (i.e., stiffness, thicknesses, tensile strengths, post cracking behavior etc.) and that the simple summation of the unreinforced masonry and plain mortar coating contributions is not always on the safe side, for brittle masonry (such as solid brick). An interpretation of the resisting mechanism responsible of the reinforced samples diagonal peak load was provided, supported also by some numerical simulations on a simplified model based on continuum. A preliminary numerical investigation on the post-peak behavior of GFRM reinforced masonry was then presented: it permitted to investigate on the reinforced masonry performances at the varying of the masonry characteristics, evidencing, in particular, a not negligible interlocking effect of the mortar between cracks. Further experimental and numerical study can be performed to refine the model, so to account also for the non-linearities in the both the masonry-mortar and mortar-GFRP meshes interaction.

However, as the experimental results proved the in-plane effectiveness of the GFRM technique, a numerical study on the global seismic performances of GFRM reinforced masonry buildings was performed. The Equivalent Frame method was adopted to model four different building configurations; both solid brick and rubble stone masonry were considered, with concentration of the nonlinear response in shear and bending “plastic hinges”. Nonlinear static analysis were executed and the modified Capacity Spectrum Method was applied. The performances of reinforced and unreinforced buildings were compared in terms of capacity curves and maximum resisting ground acceleration: the results evidenced for reinforced buildings increases ranging from 1.8 to 2.6 times that of unreinforced ones. The analyses evidenced also the importance of deeper investigations on the actual resistance and displacement performances concerning the in-plane bending behavior of reinforced masonry, to a proper quantification and modeling to this failure mechanism.

The study then focused on the out-of-plane behavior of reinforced masonry. Experimental results of some full scale four point bending tests evidenced significant improvements of the masonry performances both in resistance and displacement capacities. In fact, once the mortar and the masonry cracked, the GFRM mesh on the tensed wall face opposed to the abrupt collapse, permitting a stress redistribution and the achievement of high resistance and deflection values.

Moreover, it was observed that that the cracking and the ultimate bending moment of reinforced masonry panels can be evaluated analytically, by adopting the well-known relationships used in the design of reinforced concrete beams subjected to combined axial and bending actions.

A 2D numerical model, based on four-node, plane strain elements and truss elements, was then developed. It was thus possible to perform, through non-linear static analyses, a parametric study, evidencing how variations in the main masonry, mortar and GFRP reinforcement mechanical and geometrical characteristics may affect the reinforced masonry out-of-plane bending performances. This permits, in general, to design a suitable reinforcement intervention, calibrated of the basis of the masonry characteristics and of the required performances.

A first approach to the study of the out-of-plane behavior of actual wall configurations was presented, confirming the excellent performances increases attributable to the GFRM application obtained in laboratory tests. Moreover, the possibility to extend the 2D model to a 3D model, based on the same material characteristics and on eight node solid elements instead of four-node plane strain elements, was also proved: in fact, the 3D model will be useful to permit, in the near future, to prosecute the numerical study, extending the investigations on masonry walls with openings or with a more articulated geometry.

The 2D smear crack model, based on nonlinear static analysis, resulted also useful to perform a numerical study on the effectiveness of the GFRM technique in strengthening existing masonry vaults. In particular, solid brick barrel vaults with different aspect ratio between the arch rise and the curvature radius were considered (1, 0.75 and 0.6) and two different load patterns are analyzed: vertical and horizontal load, acting in the transversal direction, with distributions proportional to the self-weight. The application of the reinforcement at the vaults extrados was considered. The simulations permitted to evaluate the collapse mechanisms of the vaults, governed by the flexural behavior. The great effectiveness of the reinforcement technique was evidenced by comparing both the resistance and the displacement capacities of reinforced and unreinforced vaults. Furthermore, a comparison with the numerical results derived by simplified load patterns permitted to individuate some critical issues in the typical, adopted test methods based on the application of concentrated loads, which alter the vaults behavior.

The proceed of the research aims to extend the numerical model to the simulation of different geometries of the barrel vault, by performing a parametric study for evaluating the influence of the masonry thickness, the span dimension, the masonry and the reinforcement mechanical characteristics. Also the reinforcement application it intrados could be considered. Moreover, experimental tests are in progress so to prove the actual effectiveness of the technique, paying a particular attention in reproducing as close as possible the actual load patterns (cyclic loading with uniform distribution instead of concentrated actions, increased monotonically).

## 7 REFERENCES

- Abrams D., Smith T., Lynch J., Franklin S. (2007). Effectiveness of Rehabilitation on Seismic Behavior of Masonry Piers. *Journal of Structural Engineering*, 133(1), 32-43.
- AC434. (2013). Acceptance criteria for masonry and concrete strengthening using fabric-reinforced cementitious matrix (FRCM) composite systems. Whittier, California (US): ICC Evaluation Service.
- Accardi M., Cucchiara C., Failla A., La Mendola L. (2007). CFRP flexural strengthening of masonry walls: experimental and analytical approach. In: *Proceedings of FraMCoS-6 Conference*. Catania (I).
- ACI 440. (2002). State-of-the-Art Report on Fiber Reinforced Plastic (FRP). ACI Committee .
- ACI 440.7R-10. (2010). Guide for Design and Construction of Externally Bonded FRP Systems for Strengthening Unreinforced Masonry Structures. ACI Committee 440.
- ACI 530-05. (2005). Building Code Requirements for Masonry Structures and Commentary. Farmington Hills (US): American Concrete Institute.
- ACI 549.4R-13. (2013). Guide to Design and Construction of Externally Bonded Fabric-Reinforced Cementitious Matrix (FRCM) Systems for Repair and Strengthening Concrete and Masonry Structures. ACI Committee 549.
- Akhaveissy A.H., Milani, G. (2013). Pushover analysis of large scale unreinforced masonry structures by means of a fully 2D non-linear model. *Construction and Building Materials*, 41, 276-295.
- Aldea M.C., Mobasher B., Jain N. (2007). Cement-Based Matrix-Grid System for Masonry Rehabilitation. *SP-244: Thin Fiber and Textile Reinforced Cementitious Systems*, 141-156.
- Alecci V., Misseri G., Rovero L., Stipo G., De Stefano M., Feo L., Luciano R. (2016). Experimental investigation on masonry arches strengthened with PBO-FRCM composite. *Composites Part B*, 100, 228-239.
- Alecci V., Fagone M., Rotunno T., De Stefano M. (2013). Shear strength of brick masonry walls assembled with different types of mortar. *Construction and Building Materials*, 40, 1038–1045.
- Al-Salloum Y.A., Almusallam T.H. (2004). Load Capacity of Concrete Masonry Block Walls Strengthened with Epoxy-bonded GFRP Sheets. *Journal of Composite Material*, 39(19), 1719-1774.
- Amadio C., Gattesco N., Dudine A., Franceschinis R. (2012). Structural performance of spandrels in stone masonry buildings. In: *Proceedings of the 15th World Conference on Earthquake Engineering*. Lisbon (PT).
- Anania L., Badalà A., D'Agata G. (2013). The post strengthen-ing of the masonry vaults by the X-Wrap technique based on the use of C-FRP. *Construction and Building Materials*, 47, 1053–1068.
- Anil O., Tatayoglu M., Demirhan M. (2012). Out-of-plane behavior of unreinforced masonry brick walls strengthened with CFRP strips. *Construction and Building Materials*, 35, 614-624.
- Anthoine A., Magonette G., Magenes G. (1995). Shear-Compression Testing and Analysis of Brick Masonry Walls. In: *Proceedings of the 10th European Conference on Earthquake Engineering*. Duma (NL).
- Arboleda D., Carozzi F.G., Nanni A., Poggi C. (2016). Testing Procedures for the Uniaxial Tensile Characterization of Fabric-Reinforced Cementitious Matrix Composites. *Journal of Composite Constructions*, 20(3).
- Arifuzzaman S., Saatcioglu M. (2012). Seismic Retrofit of Load Bearing Masonry Walls by FRP sheets and Anchors Sheets and Anchors. In: *Proceedings of the 15th World Conference on Earthquake Engineering*. Lisbon (PT).
- Ascione L., D'Aponte A., Mancusi G. (2015). Fabric-Reinforced Cementitious Matrix (FRCM): A New Italian Guideline under development. *Key Engineering Materials*, 624, 3-10.
- Ashraf M., Khan A.N., Ali Q., Shahzada K., Naseer A. (2011). Experimental behavior of full-scale URM building retrofitted with ferrocement overlay. *Advanced Materials Research*, 255-260, 319-323.
- ASTM C1531-03. (2007). Standard Test Methods for in Situ Measurement of Masonry Mortar Joint Shear Strength Index. International.
- ASTM C1583/C1583M-13. (2013). Standard Test Method for Tensile Strength of Concrete Surfaces and the Bond Strength or Tensile Strength of Concrete Repair and Overlay Materials by Direct Tension (Pull-off Method). ASTM International.
- ASTM C1666/C1666M-07. (2007). Standard Specification for Alkali Resistant (AR) Glass Fiber for GFRC and Fiber-Reinforced Concrete and Cement. ASTM International.
- ASTM C78/C78M-16. (2016). Standard Test Method for Flexural Strength of Concrete (Using Simple Beam with Third-Point Loading). ASTM International.
- ASTM E518/E518M-15. (2015). Standard Test Methods for Flexural Bond Strength of Masonry. ASTM International.

- ASTM E519-2010. (2010). Standard test method for diagonal tension (shear) in masonry assemblages. American Society for Testing Material. ASTM International.
- ASTM E72-02. (2002). Standard Test Method for Conducting Strength Tests of Panels for Building Constructions. ASTM International.
- ATC 40. (1996). Seismic evaluation and retrofit of concrete buildings. 1. Redwood City, California (US): ATC Applied Technology Council.
- Augenti N., Parisi F. (2010). Learning from Construction Failures due to the 2009 L'Aquila, Italy, Earthquake. *Journal of Performance of Constructed Facilities*. ASCE, 24(6), 536-555.
- Babaeidarabad S. (2013). Masonry Walls Strengthened with Fabric-Reinforced Cementitious Matrix Composite Subjected to In-Plane and Out-of-Plane Load. *PhD Thesis*. Miami (US): University of Miami.
- Babatunde S.A. (2017). Review of strengthening techniques for masonry using fiber reinforced polymers. *Composite Structures*, 161, 246–255.
- Badoux M. (1998). Comparison of Seismic Retrofitting Strategies with the Capacity Spectrum Method. In: *Proceedings of the 11th European Conference on Earthquake Engineering*. Paris (F).
- Baker L.R. (1979). Measurement of the flexural bond strength of masonry. In: *Proceedings of the 5th International Brick Masonry Conference*, 79-83. Washington D.C. (US).
- Bakis C.E., Bank L.C., Brown V.L., Cosenza V., Davalos E., Lesko J., Machida J. (2002). Fiber-reinforced polymer composites for construction, state-of-the-art review. *Journal of Composites for Constructions*, 6(2), 73-87.
- Barbieri G., Biolzi L., Bocciarelli M., Fregonese L., Frigeri A. (2013). Assessing the seismic vulnerability of a historical building. *Engineering Structures*, 57, 523-535.
- Basili M., Marcari G., Vestroni F. (2016). Nonlinear analysis of masonry panels strengthened with textile reinforced mortar. *Engineering Structures*, 113, 245–258.
- Basilio I. (2007). Strengthening of arched masonry structures with composite materials. *PhD Thesis*. Department of Civil Engineering, Guimaraes.
- Bednarz L., Gorski A., Jasienko J., Rusinsk E. (2011). Simulations and analyses of arched brick structures. *Automation in Construction*, 20, 741–754.
- Bertolesi E., Carozzi F.G., Milani G., Poggi C. (2014). Numerical modeling of Fabric Reinforce Cementitious Matrix composites (FRCM) in tension. *Construction and Building Materials*, 70, 531–548.
- Betti M., Galano L., Vignoli A. (2014). Comparative analysis on the seismic behaviour of unreinforced masonry buildings with flexible diaphragms. *Engineering Structures*, 61, 195-208.
- Beyer C., Dazio A. (2012). Developing force-deformation characteristics of brick masonry spandrels in historic buildings. In: *Proceedings of the 15th World Conference on Earthquake Engineering*. Lisbon (PT).
- Binda L., S. A. (2002). State of the art of research on historic structures in Italy . In: *Workshop Ariadne 11, Historic structures - programme of the EC 5th framework activities*. Praha (CZ).
- Binda L., Modena C., Baronio G., Abbaneo S. (1997). Repair and investigation techniques for stone masonry walls. *Construction and Building Materials*, 11(3), 133-142.
- Binda L., Modena C., Baronio L., Gelmi A. (1994). Experimental qualification of injection admixtures used for repair and strengthening of stone masonry walls. In: *Proceedings of Tenth International Brick and Block Masonry Conference*. Calgary (CA).
- Binda L., Baronio G., Tiraboschi C. (1993). Repair of brick masonries by injection of grouts: experimental research. *Journal of Structural Engineering*, 20(1), 29-44.
- Bisby L.A., Stratford T., Hart C., Farren S. (2013). Fire performance of well-anchored TRM, FRCM and FRP flexural strengthening systems. In: *Proceedings of Advanced Composites in Construction Conference* . Belfast (UK).
- Borri A., Corradi M., Castori G., De Maria A. (2015a). A method for the analysis and classification of historic masonry. *Bulletin of Earthquake Engineering*, 13, 2647–2665.
- Borri A., Castori G., Corradi M. (2015b). Determination of Shear Strength of Masonry Panels Through Different Tests. *International Journal of Architectural Heritage*, 9(8), 913-927.
- Borri A., Corradi M., Sisti R., Buratti C., Belloni E., Moretti E. (2015c). Masonry wall panels retrofitted with thermal-insulating GFRP-reinforced jacketing. *Materials and Structures*, 49, 3957.
- Borri A., Castori G., Corradi M., Sisti R. (2014). Masonry wall panels with GFRP and steel-cord strengthening subjected to cyclic shear: An experimental study. *Construction and Building Materials*, 56, 63-73.
- Borri A., Castori G., Corradi M. (2011). Intrados strengthening of brick masonry arches with composite materials. *Composites: Part B*, 42, 1164–1172.

- Borri A., Casadei P., Castori G., Hammond J. (2009). Strengthening of Brick Masonry Arches with Externally Bonded Steel Reinforced Composites. *Journal of Composites for Construction*, 13(6), 468-475.
- Brasile S., Casciaro R., Formica G. (2007). Multilevel approach for brick masonry walls – Part I: A numerical strategy for the nonlinear analysis. *Computer Methods in Applied Mechanics and Engineering*, 196(49-52), 4934-4951.
- Briccoli Bati S., Rovero L. (2001). Experimental validation of a proposed numerical model for the FRP consolidation of masonry arches. In: Lourenço P.B., Roca P. (eds.) *Historical Constructions*, 1057-1066. Guimarães: University of Minho.
- Briccoli Bati S., Rovero L., Tonietti U. (2007). Strengthening masonry arches with composite materials. *Journal of Composites for Construction*, 1(33), 33-41.
- Brignola A., Frumento S., Lagomarsino S., Podesta S. (2009). Identification of shear parameters of masonry panels through the in-situ diagonal compression test. *International Journal of Architectural Heritage*, 3(1), 52-73.
- Bui T.L., Si Larbi A., Reboul N., Ferrier E. (2015). Shear behaviour of masonry walls strengthened by external bonded FRP and TRC. *Composite Structures*, 132, 923-932.
- Calderini C., Cattari S., Lagomarsino S. (2010). The use of the diagonal compression test to identify the shear mechanical parameters of masonry. *Construction and Building Materials*, 24, 677-685.
- Calderini C., Cattari S., Lagomarsino S. (2009). In-plane strength of unreinforced masonry piers. *Earthquake Engineering and Structural Dynamics*, 38, 243-267.
- Calderini C., Lagomarsino S. (2008). Continuum model for in-plane anisotropic inelastic behavior of masonry. *Journal of Structural Engineering*, 134, 209-220. ASCE.
- Calderoni B., Cordasco E.A., Pacella G. (2016). The improvement of spandrels in existing masonry buildings in order to avoid brittle failure: ExExperimental campaign on reinforced specimens. In: *Proceedings of the 16th International Brick and Block Masonry Conference*. Padua (I).
- Calderoni B. (1996). Valutazione sperimentale delle caratteristiche meccaniche di muratura di tufo per modelli in scala intermedia. In: *Atti del Convegno Nazionale La Meccanica delle Murature tra Teoria e Progetto*, 95-104. Messina (I), (in Italian).
- Calderoni B., Marone P., Pagano M. (1987). Modelli per la verifica statica degli edifici in muratura in zona sismica. *Ingegneria sismica*, 3, 19-27, (in Italian).
- Caliò I., Marletta M., Pantò B. (2005). A Simplified Model for the Evaluation of the Seismic Behaviour of Masonry Buildings. In: *Proceedings of the 10th International Conference on Civil, Structural and Environmental Engineering Computing (Paper 195)*. Civil Comp Press.
- Calliari R., Manzini C.F., Morandi P., Magenes G., Remino M. (2010). User manual of ANDILWall, version 2.5. *ANDIL Assolaterizi*. Roma (I).
- Calvi G.M., Magenes G. (1994). Experimental results on unreinforced masonry shear walls damaged and repaired. In: *Proceedings of Tenth International Brick and Block Masonry Conference*. Calgary (CA).
- Cancelliere I., Imbimbo M., Sacco E. (2010). Experimental tests and numerical modeling of reinforced masonry arches. *Engineering Structures*, 32, 776-792.
- Capozucca R. (2011). Shear Behaviour of Historic Masonry Made of Clay Bricks. *The Open Construction and Building Technology Journal*, 5(1-M6), 89-96.
- Capozucca R. (2013). Effects of mortar layers in the delamination of GFRP bonded to historic masonry. *Composites Part B: Engineering*, 44, 639-649.
- Carbonara G. (1996). *Restauro Architettonico. II(E2)*. Torino (I): UTET, (in Italian).
- Carbone I. (2010). Delaminazione di compositi a matrice cementizia su supporti murari. *PhD Thesis*. Rome (I): Università degli studi Roma TRE, (in Italian).
- Carozzi F.G., Milani G., Poggi C. (2014). Mechanical properties and numerical modeling of Fabric Reinforced Cementitious Matrix (FRCM) systems for strengthening of masonry structures. *Construction and Building Materials*, 107, 711-725.
- Carrara P., Ferretti D., Freddi F. (2013). Debonding behavior of ancient masonry elements strengthened with CFRP sheets. *Composites Part B: Engineering*, 45, 800-810.
- Cattari S. (2007). Modellazione a telaio equivalente di strutture esistenti in muratura e miste muratura-c.a.: formulazione di modelli sintetici. University of Genoa (I), (in Italian).
- CEB - Comité Euro-International du Béton. (1985). Manual on Cracking and Deformations. Bulletin d'Information 158.
- Chaimoon K., Attard M.M. (2007). Modeling of unreinforced masonry walls under shear and compression. *Engineering Structures*, 29(9), 2056-2068.
- Chen S.P. (2011). Out-of-Plane Behavior of Masonry Walls Strengthened with Ferrocement. *Advanced Materials Research*, 163-167, 3545-3550.

- Chiostrini S., Galano L., Vignoli A. (2000). On the determination of strength of ancient masonry walls via experimental tests. *In: Proceedings of the 12th World Conference of Earthquake Engineering*. Auckland (NZ).
- Chiostrini S., Vignoli A. (1994). In-situ determination of the strength properties of masonry walls by destructive shear and compression tests. *Masonry International*, 7(3), 87-96.
- Chuang S.W., Zhuge Y., Wong T.Y., Peters L., Mc Bean P.C. (2003). Seismic retrofitting of unreinforced masonry walls by FRP strips. *In: Proceedings of the 2003 Pacific Conference on Earthquake Engineering*. Christchurch (NZ).
- Churilov S., Dumova-Jovanoska E. (2012). Analysis of masonry walls strengthened with RC jackets. *In: Proceedings of the 15th World Conference on Earthquake Engineering*. Lisboa (P).
- Circolare 2 febbraio 2009, n. 617. (2009). Istruzioni per l'applicazione delle "Nuove norme tecniche per le costruzioni" di cui al decreto ministeriale 14 gennaio 2008. Italian Ministry of Infrastructures, Rome, (*in Italian*).
- CNR DT 203/2006. (2006). Istruzioni per la progettazione, l'esecuzione ed il controllo di strutture di calcestruzzo armato con barre di materiale composito fibrorinforzato, (*in Italian*).
- CNR-DT 200/R1 2013. (2013). Istruzioni per la Progettazione, l'Esecuzione ed il Controllo di Interventi di Consolidamento Statico mediante l'utilizzo di Compositi Fibrorinforzati. Materiali, strutture di c.a. e di c.a.p., strutture murarie. Rome (I): CNR, (*in Italian*).
- Codispoti R., Oliveira D.V., Olivito R.S., Lourenco P.B., Figueiro R. (2015). Mechanical performance of natural fiber-reinforced composites for the strengthening of masonry. *Composites Part B: Engineering*, 77, 74-83.
- Corradi M., Borri A., Castori G., Osofero A.I. (2016). Durability of GFRP grids for masonry structures. *International Journal of Forensic Engineering*, 3(1/2).
- Corradi M., Borri A., Castori G., Sisti R. (2014). Shear strengthening of wall panels through jacketing with cement mortar reinforced by GFRP grids. *Composites: Part B*, 64, 33-42.
- Corradi M., Tedeschi C., Binda L., Borri A. (2008a). Experimental evaluation of shear and compression strength of masonry wall before and after reinforcement: Deep repointing. *Construction and Building Materials*, 22(4), 463-472.
- Corradi M., Borri A., Vilgnoli A. (2008b). Experimental evaluation of the in-plane shear behaviour of masonry walls retrofitted using and innovative methods. *Masonry International*, 21(1).
- Corradi M., Borri A., Vignoli A. (2003). Experimental study on the determination of strength of masonry walls. *Construction and Building Materials*, 17, 325-337.
- Csikai B., Ramos C.F., Basto P., Moreira S., Lourenco P.B. (2014). Flexural out-of-plane retrofitting technique for masonry walls in historical constructions. *In: Proceedings of the 9th International Conference on Structural Analysis of Historical Constructions SAHC*. Mexico City (MX).
- D.M.14.01.2008. (2008). Nuove norme tecniche per le costruzioni. Italian Ministry of Infrastructures, Rome (I) , (*in Italian*).
- D'Ambrisi A., Mezzi M., Caporale A. (2013). Experimental investigation on polymeric net-FRCM reinforced masonry panels. *Composite Structures*, 105, 207-215.
- D'Asdia P., Viskovic A. (1994). L'analisi sismica degli edifici in muratura. *Ingegneria Sismica*, 1, 32-42, (*in Italian*).
- D'Ayala D., Speranza E. (2002). An integrated procedure for the assessment of the seismic vulnerability of historic buildings. *In: Proceedings of the 12th European conference on earthquake engineering*, Paper 561. London (UK).
- De Felice G., De Santis S., Garmendia L., Ghiassi B., Larrinaga P., Lourenco P.B., Oliveira D.V., Paolacci F., Papanicolaou C.G. (2014). Mortar-based systems for externally bonded strengthening of masonry. *Materials and Structures*, 4(2), 16.
- De Santis S., Casadei P., De Canio G., De Felice G., Malena M., Mongelli M., Roselli I. (2016). Seismic performance of masonry walls retrofitted with steel reinforced grout. *Earthquake Engineering and Structural Dynamics*, 45, 229-251.
- De Santis S., De Felice G. (2015a). Tensile behavior of mortar-based composites for externally bonded reinforcement systems. *Composites: Part B*, 68, 401-413.
- De Santis S., De Felice G. (2015b). Tensile Behaviour and Durability of Mortar-Based Strengthening systems with Glass-Aramid Textiles. *Key Engineering Materials*, 624, 346-353.
- Derakhshan H., Griffith M.C., Ingham J.M. (2013). Airbag testing of multi-leaf unreinforced masonry walls subjected to one-way bending. *Engineering Structures*, 57, 512-522.
- Dhanasekar M., Kleeman P.W., Page A.W. (1985). Biaxial stress-strain relations for brick masonry. *Journal of structural Engineering*, 111(5), 1085-1100.
- DIN 1053-100. (2004). Masonry: Design on the Basis of Semi-Probabilistic Safety Concept. Berlin (D): NABau.

- Dizhur D., Griffith M., Ingham J. (2013). In-Plane Shear Improvement of Unreinforced Masonry Wall Panels Using NSM CFRP Strips. *Journal of Composite Constructions*, 17(6).
- Dolce M. (1989). Schematizzazione e modellazione per azioni nel piano delle pareti, Corso sul consolidamento degli edifici in muratura in zona sismica. Ordine degli Ingegneri, Potenza (I) , (in Italian).
- Donnini J., De Caso y Basalo F., Corinaldesi V., Lancioni G., Nanni A. (2017). Fabric-reinforced cementitious matrix behavior at high-temperature: Experimental and numerical results. *Composites Part B: Engineering*, 108, 108-121.
- Drysdale R.G., Hamid A.A., Baker L.R. (1994). *Masonry structures, behaviour and design*. Englewood Cliffs, New Jersey (US): Prentice Hall.
- Ehsani M., Saasatmanesh H. (1996). Seismic retrofit of URM Walls with Fiber Composites. *TMS Journal*, 63-72.
- ElGawady M., Lestuzzi P., Badoux M. (2006). Seismic behavior of URM walls retrofitted using Shotcrete. In: *Proceedings of the New Zealand Society of Earthquake Engineering Annual Conference*. At Napier (NZ).
- ElGawady M., Lestuzzi P., Badoux M. (2004a). A review of conventional seismic retrofitting techniques for URM. In: *Proceedings of the 13th International Brick and Block Masonry Conference*, 4-7 July. Amsterdam (NL).
- ElGawady M., Lestuzzi P., Badoux M. (2004b). A review of retrofitting unreinforced masonry walls using composites. In: *4th International Conference on Advanced Composite Materials in Bridges and Structures*. Calgary (CA).
- ElGawady M.A. (2004). Seismic in-plane behavior of URM walls upgraded with composites. *PhD Thesis*. Lausanne (CH): Ecole Polytechnique Federale de Lausanne.
- Elmalich D., Rabinovitch O. (2009). Masonry and monolithic circular arches strengthened with composite materials – A finite element model. *Computers and Structures*, 87, 521–533.
- EN 1015-12:2016. (2016). Methods of test for mortar for masonry - Part 12: Determination of adhesive strength of hardened rendering and plastering mortars on substrates. Brussels (BE): CEN.
- EN 1998-1:2004. (2004). Eurocode 8: Design of structures for earthquake resistance - Part 1: General rules, seismic actions and rules for buildings . Brussels (BE): CEN.
- EN10027-1:2005. (2005). Designation systems for steels. *Part 1: steel names*. Brussels: CEN.
- EN1052-3:2002/A1:2007. (2007). Methods of test for masonry. Part 3: Determination of initial shear strength. Brussels (BE): CEN.
- EN12390-13:2013. (2013). Testing hardened concrete. *Part 13: Determination of secant modulus of elasticity in compression*. Brussels (BE): CEN.
- EN12390-3:2009/AC:2011. (2011). Testing hardened concrete. *Part 3: Compressive strength of test specimens*. (BE): CEN.
- EN12390-6:2009. (2009). Testing hardened concrete. *Part 6: Tensile splitting strength of test specimens*. Brussels (BE): CEN.
- EN196-1:2005. (2005). Methods of testing cement. - *Part 1: Determination of strength*. Brussels (BE): CEN.
- EN1992-1-1:2004/A1:2014. (2014). Eurocode 2 - Design of concrete structures. *Part 1-1: General rules and rules for buildings*. Brussels (BE): CEN.
- EN1996-1-1. (2005). Eurocode 6: Design of masonry structures - Part 1-1: General rules for reinforced and unreinforced masonry structures. Brussels (BE): CEN.
- EN772-1:2011+A1:2015. (2015). Methods of test for masonry units. *Part 1: Determination of compressive strength*. Brussels (BE): CEN.
- Faella C., Camorani P., Martinelli E., Paciello S.O., Perri F. (2012). Bond behaviour of FRP strips glued on masonry: Experimental investigation and empirical formulation. *Construction and Building Materials*, 31, 353–363.
- Faella C., Martinelli E., Nigro E., Paciello S. (2010). Shear capacity of masonry walls externally strengthened by a cement-based composite material: An experimental campaign. *Construction and Building Materials*, 24, 84–93.
- Faella C., Martinelli E., Nigro E., Paciello S. (2004). Tuff masonry walls strengthened with a new kind of C-FRP sheet: experimental tests and analysis. In: *Proceedings of the 13th world conference on earthquake engineering*. Vancouver (CA).
- Fajfar P. (1999). Capacity spectrum method based on inelastic demand spectra. *Earthquake Engineering and Structural Dynamics*, 28, 979-993.
- FEMA 274. (1997). NEHRP Commentary on the Guidelines for the Seismic rehabilitation of buildings. Washington D.C. (US): Building Seismic Safety Council.
- FEMA 306. (1999). Evaluation of earthquake damaged concrete and masonry wall buildings – basic procedures manual. Washington D.C. (US): ATC.

- Ferreira T.M., Costa A.A., Costa A. (2015). Analysis of the Out-Of-Plane Seismic Behavior of Unreinforced Masonry: A Literature Review. *International Journal of Architectural Heritage Conservation, Analysis, and Restoration*, 9(8), 949-972.
- Foraboschi P. (2001). Strength assessment of masonry arch ret-rofitted using composite reinforcements. *Masonry International*, 15(1), 17–25.
- Franklin S., Lynch J., Abrams D.P. (2001). Performance of Rehabilitated URM shear walls: flexural behavior of piers. *Mid-America Earthquake Center*.
- Freeman S.A. (2004). Review of the development of the Capacity Spectrum Method. *ISET Journal of Earthquake Technology*, 41(1), 1-13.
- Freeman S.A. (1998). The Capacity Spectrum Method as a Tool for Seismic Design. In: *Proceedings of the 11th European Conference on Earthquake Engineering*. Paris (F).
- Frigione M., Lettieri M., Mecchi A.M. (2006). Environmental Effects on Epoxy Adhesives Employed for Restoration of Historical Buildings. *Journal of Materials in Civil Engineering*, 18(5).
- Frocht M.M. (1931). Recent Advances in Photoelasticity: an Investigation of the Stress Distribution in Square Blocks Subjected to Diagonal Compression. 53, 135–153. American Society of Mechanical Engineers.
- Gabor A., Bennani A., Jacquelin E., Lebon F. (2006). Modelling approaches of the in-plane shear behaviour of unreinforced and FRP strengthened masonry panels. *Composite Structures*, 74, 277–288 .
- Galasco A., Lagomarsino S., Penna A. (2006). On the use of pushover analysis for existing masonry buildings. In: *Proceedings of the 1st European conference on earthquake engineering and seismology* . Geneva (CH).
- Gambarotta L., Lagomarsino S. (1997a). Damage models for the seismic response of brick masonry shear walls. Part I: The mortar joint model and its applications. *Earthquake Engineering & Structural Dynamics*, 26(4), 423-439.
- Gambrotta L., Lagomarsino S. (1997b). Damage models for the seismic response of brick masonry shear walls. Part II: The continuum model and its applications. *Earthquake Engineering & Structural Dynamics*, 26(4), 441-462.
- Gams M., Tomazevic M. (2012). Experimental simulation of seismic response of masonry. In: *Proceedings of the 15th World Conference on Earthquake Engineering*. Lisbon (PT).
- Gams M., Tomazevic M., Kwiecien A. (2015). Strengthening Brick Masonry by Repointing – An Experimental Study. *Key Engineering Materials*, 624, 444-452.
- Garmendia L., Larrinaga P., Garcia D., Marcos I. (2014). Textile-reinforced mortar as strengthening material for masonry arches. *International Journal of Architectural Heritage*, 8, 627–648.
- Garmendia L., Larrinaga P., San-Mateos R., San-José J.T. (2015). Strengthening masonry vaults with organic and inorganic composites: an experimental approach. *Materials and Design*, 85, 102–114.
- Garofano A., Ceroni F., Pecce M. (2016). Modelling of the in-plane behaviour of masonry walls strengthened with polymeric grids embedded in cementitious mortar layers. *Composites Part B*, 85, 243-258.
- Gattesco N., Boem I. (2017a). Characterization tests of GFRM coating as a strengthening technique for masonry buildings. *Composite Structures*, 165, 209-222.
- Gattesco N., Boem I. (2017b). Assessment of the seismic capacity increase of masonry buildings strengthened through the application of GFRM coatings on the walls. *International Journal of Masonry Research and Innovation*. Peer review.
- Gattesco N., Boem I. (2017c). Out-of-plane behavior of reinforced masonry walls: experimental and numerical study. *Composites Part B: Engineering*, peer review.
- Gattesco N., Boem I. (2016a). Influence of mortar coating type on the shear resistance of a GFRP based strengthening technique for brick masonry walls. In: *Proceedings of the 16th International Brick and Block Masonry Conference*. Padua (I).
- Gattesco N., Boem I. (2016b). Strengthening of masonry vaults through a thin extradosal layer of fiber reinforced lime mortar. In: *Proceedings of the 10th International Conference on Structural Analysis of Historical Constructions – SAHC*. Leuven (BE).
- Gattesco N., Boem I. (2015a). Experimental and analytical study to evaluate the effectiveness of an in-plane reinforcement for masonry walls using GFRP meshes. *Construction and Building Materials*, 88, 94-104.
- Gattesco N., Boem I. (2015b). Seismic enhancement of masonry buildings strengthened through GFRP reinforced mortar coating. *Applied Mechanics and Materials*, 796, 53-67.
- Gattesco N., Boem I. (2015c). Numerical Simulation of the Out-of-plane Performance of Masonry Walls Strengthened with a GFRP Reinforced Mortar. In: *Proceedings of the 15th International Conference on Civil, Structural and Environmental Engineering Computing*. Prague (CZ).

- Gattesco N., Boem I. (2015d). Studio numerico sulla resistenza a flessione fuori piano di murature rinforzate mediante intonaco armato con rete in GFRP. In: *Proceedings of the XVI conference ANIDIS, L'Ingegneria Sismica in Italia*. L'Aquila (I), (in Italian).
- Gattesco N., Boem I. (2014). Out-of-plane behaviour of masonry walls strengthened with a GFRP reinforced mortar coating. In: *Proceedings of the 9th International Masonry Conference*. Guimarães (PT).
- Gattesco N., Macorini L., Dudine A. (2016a). Experimental Response of Brick-Masonry Spandrels under In-Plane Cyclic Loading. *Journal of Structural Engineering*, 142(2).
- Gattesco N., Gubana A., Melotto M. (2016b). GFRP to strengthen masonry walls: Numerical analysis and evaluation of the different mechanical parameters role. In: *Proceedings of the 10th International Conference on Structural Analysis of Historical Constructions – SAHC*. Leuven (BE).
- Gattesco N., Boem I., Dudine A. (2015a). Diagonal compression tests on masonry walls strengthened with a GFRP mesh reinforced mortar coating. *Bulletin of Earthquake Engineering*, 13(6), 1703-1726.
- Gattesco N., Amadio C., Bedon C. (2015b). Experimental and numerical study on the shear behavior of stone masonry walls strengthened with GFRP reinforced mortar coating and steel-cord reinforced repointing. *Engineering Structures*, 90, 143-157.
- Gattesco N., Macorini L. (2014). In-plane stiffening techniques with nail plates or CFRP strips for timber floors in historical masonry buildings. *Construction and Building Materials*, 58, 64-76.
- Gattesco N.; Amadio C.; Barelli S.; Bedon C.; Rinaldin G.; Zorzini F. (2013). Analisi ciclica di pareti murarie in pietrame rinforzate mediante intonaco armato con rete in GFRP. In: *XV Convegno ANIDIS L'Ingegneria Sismica in Italia*. 30 June - 4 July. Padova (I), (in Italian).
- Ghanem G., Sheirf A., Honsy H. (1994). Suggested modifications to the diagonal tension test calculation for masonry assemblages. In: *Proceedings of 10th International Brick and Block Masonry Conference*. Calgary (PT).
- Ghiassi B., Marcarì G., Oliveira D.V., Lourenco P.B. (2013). Water degrading effects on the bond behavior in FRP-strengthened masonry. *Composites Part B: Engineering*, 54, 11-19.
- Ghiassi B., Razavizadeh A., Oliveira D.V., Marques V., Lourenco P.B. (2015). Tensile and bond characterization of natural fibers. In: *Proceedings of the 2nd International Conference on Natural Fibers*. Azores (PT).
- Gilstrap J.M., Dolan C.W. (1998). Out-of-plane bending of FRP-reinforced masonry walls. *Composites Science and Technology*, 58(8), 1277-1284.
- Girardello P., Da Porto F., Modena C., Valluzzi M.R. (2013). Comportamento sperimentale di volte in muratura rinforzate con materiali compositi a matrice inorganica. In: *Proceedings of the XV Conference "ANIDIS, L'Ingegneria sismica in Italia"*. Padua (I), (in Italian).
- Giuffrè A. (1990). Letture sulla meccanica delle murature storiche. Kappa, (in Italian).
- Giuffrè A. (1993). Sicurezza e Conservazione dei Centri Storici: il caso Ortigia. Bari (I): Laterza, (in Italian).
- Gostic S., Dolinsek B. (2008). Lessons learned after 1998 and 2004 earthquake in Posocje region. In: *Proceedings of the 4th International i-Rec Conference Building Resilience*. Christchurch (NZ).
- Graziotti F., Magenes G., Penna A. (2012). Experimental cyclic behaviour of stone masonry spandrels. In: *Proceedings of the 15th World Conference on Earthquake Engineering*. Lisbon (PT).
- Hamed E., Rabinovitch O. (2010). Failure characteristics of FRP-strengthened masonry walls under out-of-plane loads. *Engineering Structures*, 32(8), 2134-2145.
- Hamid A.A., Mohmoud A.D.S., El Magd S.A. (1994). Strengthening and repair of unreinforced masonry structures: state of the art. In: *Proceedings of the 10th International Brick and Block Masonry Conference*, 5-7 July, 485-497. Calgary (CA).
- Hendry A.W. (1981). *Structural Brickwork*. London (UK): Macmillan.
- Hojdys L., Krajewski P. (2012). Experimental tests on strengthened and unstrengthened masonry vault with backfill. *Journal of Heritage Conservation*, 32, 105-108.
- Hordijk D.A. (1991). Local approach to fatigue of concrete, PhD thesis. Delft (NL): Delft University of Technology.
- Hracov S., Pospisil S., Garofano A., Urushadze S. (2016). In-plane cyclic behaviour of unfired clay and earth brick walls in both unstrengthened and strengthened conditions. *Materials and Structures*, 45, 3293-3308.
- Hutchinson D.L., Yong P.M.F., McKenzie G.H.F. (1984). Laboratory Testing of a Variety of Strengthening Solutions for Brick Masonry Wall Panels. In: *Proceedings of the 8th World Conference on Earthquake Engineering*, 1, 575-582. San Francisco, California (US).
- Ismail N., Ingham J.M. (2016). In-plane and out-of-plane testing of unreinforced masonry walls strengthened using polymer textile reinforced mortar. *Engineering Structures*, 118, 167-177.
- Ismail N., Petersen R.B., Masia M.J., Ingham J.M. (2011). Diagonal shear behaviour of unreinforced masonry walls strengthened using twisted steel bars. *Construction and Building Materials*, 25(12), 4386-4393.

- ISO 1144:2016. (2016). Textiles - Universal system for designating linear density (Tex System).
- Jabarov M., Kozharinov S., Lunyov A. (1980). Strengthening of damaged masonry by reinforced mortar layers. *In: Proceedings of the 7th World Conference on Earthquake Engineering*, 6, 73-80. Istanbul (TR).
- Jahved M. (2009). Seismic Risk Assessment of Unreinforced Brick Masonry Buildings System of Northern Pakistan. *PhD Thesis*. Peshawar (PK): Department of Civil Engineering, University of Engineering and Technology.
- Kadam S.B., Singh Y. (2012). Mechanical properties of externally strengthened masonry. *In: Proceedings of the 15th World Conference on Earthquake Engineering*. Lisbon (PT).
- Kadam S.B., Singh Y., Li B. (2014). Strengthening of unreinforced masonry using welded wire mesh and micro-concrete - Behaviour under in-plane action. *Construction and Building Materials*, 54, 247-257.
- Kahn L. (1984). Shotcrete retrofit for unreinforced brick masonry. *In: Proceedings of the 8th World Conference on Earthquake Engineering*, 583-590. San Francisco, California (US).
- Kamf, L. (1963). Factors affecting bond between bricks and mortar. *In: Proceedings of the Symposium on Masonry Testing*, 127-141. ASTM, West Conshohocken (US).
- Karantoni F.V., Fardis M.N. (1992). Effectiveness of Seismic Strengthening Techniques for Masonry Buildings. *Journal of Structural Engineering*, 118(7), 1884-1902. ASCE.
- Karbhari V.M. (2007). Durability of Composites for Civil Structural Applications. Woodhead Publishing.
- Karbhari V.M., Chin J.W., Hunston D., Benmokrane B., Juska T., Morgan R. (2007). Durability gap analysis for fiber-reinforced polymer composites in civil infrastructure. *Journal of Composite Constructions*, 7, 238-247.
- Kashyap J., Willis C.R., Griffith M.C., Ingham J.M., Masia M.J. (2012). Debonding resistance of FRP-to-clay brick masonry joints. *Engineering Structures*, 41, 186-198.
- Khalifa A., Gold W.J., Nanni A., Mi A.A. (1998). Contribution of externally bonded FRP to shear capacity of RC flexural members. *Journal of Composite Constructions*, 2(4), 195-202.
- Kolsch H. (1998). Carbon Fiber Cement Matrix (CFCM) Overlay System for Masonry Strengthening. *Journal of Composite for Constructions*, 2(2).
- Ku H., Wang H., Pattarachaiyakooop N., Trada M. (2011). A review on the tensile properties of natural fiber reinforced polymer composites. *Composites Part B: Engineering*, 42(4), 856-873.
- Lagomarsino S., Penna A., Galasco A., Cattari S. (2013). TREMURI program: An equivalent frame model for the nonlinear seismic analysis of masonry buildings. *Engineering Structures*, 56, 1787-1799.
- Lawrence S.; Cao H. T. (1987). An experimental study of the interface between brick and mortar. *In: Proceedings of the 4th North American Masonry Conference*, 1-14. Masonry Society. Boulder (US).
- Leone M., Aiello M.A., Balsamo A., Carrozzi F.G., Ceroni F., Corradi M., Gams M., Garbin E., Gattesco N., Krajewski P., Mazzotti C., Oliveira D., Papanicolaou C., Ranocchiali G., Roscini F., Saenger D. (2016). Glass Fabric Reinforced Cementitious Matrix: tensile properties and bond performance on masonry sub-strate. *Technical Report of the Rilem Committee 250-CSM "Composites for Sustainable Strengthening of Masonry"*.
- Lignola G.P., Prota A., Manfredi G. (2009). Nonlinear Analyses of Tuff Masonry Walls Strengthened with Cementitious Matrix-Grid Composites. *Journal of Composite Constructions*, 13(4), 243-251.
- Lourenco P.B. (2013). Computational strategies for masonry structures: multi-scale modeling, dynamics, engineering applications and other challenges. *Congreso de Métodos Numéricos en Ingeniería*, . Bilbao (ES).
- Lourenco P.B., Rots J.G., Blaauwendraad J. (1998). Continuum Model for Masonry: Parameter Estimation and Validation. *Journal of Structural Engineering*, 124(6), 642-652.
- Lourenco P.B., Rots J.G. (1997). Multisurface Interface Model for Analysis of Masonry Structures. *Journal of Engineering Mechanics*, 123(7), 660-668.
- Lourenco P.B. (1996). Computational strategies for masonry structures. *PhD Thesis*. University of Porto (PT).
- Lucciconi B, Rougier V.C. (2011). In-plane retrofitting of masonry panels with fibre reinforced composite materials. *Construction and Building Materials*, 25, 1772-1788.
- Magenes G., Penna A., Rota M., Galasco A., Senaldi I. (2012). Shaking table test of a full scale stone masonry. *In: Proceedings of the 15th World Conference on Earthquake Engineering*. Lisbon (PT).
- Magenes G. (2000). A method for pushover analysis in seismic assessment of masonry buildings. *in: Proceedings of the 12th World Conference on Earthquake Engineering*, Paper 423. Auckland (NZ).
- Magenes G., Bolognini D., Braggio C. (2000). Metodi semplificati per l'analisi sismica non lineare di edifici in muratura. *CNR-Gruppo Nazionale per la Difesa dai Terremoti Roma*. Roma (I), (in Italian).
- Magenes G., Calvi G.M. (1997). In-plane seismic response of brick masonry walls. *Earthquake Engineering and Structural Dynamics*, 26, 1091-1112.

- Mahini S.S. (2015). Smearred crack material modelling for the nonlinear analysis of CFRP-strengthened historical brick vaults with adobe piers. *Construction and Building Materials*, 74, 201–218.
- Mahmood H., Ingham J.M. (2011). Diagonal compression testing of FRP retrofitted unreinforced clay brick masonry wallets. *Journal of Composite Construction*, 15(5), 810–820.
- Mann W., Muller H. (1973). Failure criteria for laterally loaded masonry and their application to shear walls. *Die Bautechnik* 50(12), 421–425, (in German).
- Mannoni T. (2005). Archeologia della produzione architettonica. Le tecniche costruttive. *Arqueologia de la Arquitectura*, 4, 11-19, (in Italian).
- Manzoni E., Dusi A., Mezzi M. (2008). Polypmeric grid for a cost effective enhancement of the seismic performance of masonry buildings. In: *Proceedings of the 14th World Conference on Earthquake Engineering*. Beijing (CN).
- Marcari G., Basili M., Vestroni F. (2017). Experimental investigation of tuff masonry panels reinforced with surface bonded basalt textile-reinforced mortar. *Composites Part B*, 108, 131-142.
- Marques L., Lourenco P.B. (2014). Unreinforced and confined masonry buildings in seismic regions: validation of macro-element models and cost analysis. *Engineering Structures*, 64, 52–67.
- Marques R., Lourenco P.B. (2011). Possibilities and comparison of structural component models for the seismic assessment of modern unreinforced masonry buildings. *Computers & Structures*, 89(21-22), 2079-2091.
- Martellotta L., Martens D.R.W., Teuffel P.M. (2015). Review of Seismic Retrofitting Strategies for Residential Buildings in an International Context. In: *Proceedings of the International Association for Shell and Spatial Structures Symposium*. Amsterdam (NL).
- Maruccio C. (2010). Numerical Analysis of FRP Strengthened Masonry Structures. *PhD Thesis*. Università di Roma “La Sapienza” (I) e Università del Minho (PT).
- Mastrodicasa S. (2012). Dissesti statici delle strutture edilizie. Hoepli, (in Italian).
- Mazzon N., Chavez C.M., Valluzzi M.R., Casarin F., Modena C. (2010). Shaking Table Tests on Multi-leaf Stone Masonry Structures: Analysis of Stiffness Decay. *Advanced Materials Research*, 133-134, 647-652.
- Mazzotti C., Ferracuti B., Bellini A. (2015). Experimental study on masonry panels strengthened by GFRP: the role of inclination between mortar joints and GFRP sheets. *Key Engineering Materials*, 624, 559-566.
- Mazzotti C., Murgo F.S. (2015). Numerical and experimental study of GFRP-masonry interface behavior: Bond evolution and role of the mortar layers. *Composites Part B: Engineering*, 75, 212-225.
- McCann D.M., Forde M.C. (2001). Review of NDT methods in the assessment of concrete and masonry structures. *NDT & E International*, 34(2), 71-84.
- Melotto M. (2013). Analisi sperimentali e numeriche di pannelli in muratura senza a con rinforzi in rete in fibre di vetro. *Thesis*. Udine (I): Università degli Studi di Udine, (in Italian).
- Milani G., Bruggi M. (2016). Simple homogenization-topology optimization approach for the pushover analysis of masonry walls. In: *Proceedings of SAHC 2016, Structural Analysis of Historical Constructions*.
- Milani G., Fedele R., Lourenço P., Basilio I. (2014, 14–17 October). Experimental and numerical FE analyses of curved masonry prisms and arches reinforced with FRP materials. In: *Proceedings of the 9th International Conference on Structural Analysis of Historical Constructions "SAHC2014"*. Mexico.
- Mirmiran A., Bank L.C., Neale K.W., Mottram T. (2003). World Survey of Civil Engineering Programs on Fiber Reinforced Polymer Composites for Construction. *Journal of Professional Issues in Engineering Education and Practice*, 129(3).
- Modena C. (1994). Repair and upgrading techniques of unreinforced masonry structures utilized after the Friuli and Campania/Basilicata earthquakes. *Earthquake Spectra*, 10(2), 171-185 .
- Monaco A., Minafò G., Cucchiara C., D'Anna J., La Mendola L. (2016). Finite element analysis of the out-of-plane behavior of FRP strengthened masonry panels. *Composites Part B: Engineering*, ISSN 1359-8368.
- Nanni A. (1993). Fiber-Reinforced-Plastic (FRP) Reinforcement for Concrete Structures. Oxford (UK): Elsevier.
- Napoli A.; De Felice G.; De Santis S.; Realfonzo R. (2016). Bond behaviour of Steel Reinforced Polymer. *Composite Structures*(152), 499-515.
- NZSEE 2006. (2014). Assessment and improvement of the structural performance of buildings in Earthquakes (including Corrigendum N°s 1, 2 & 3, 2014). New Zealand Society of Earthquake Engineering.
- Oliveira D.V., Ghiassi B., Lourenco P.B. (2014). Bond behaviour and durability of FRP composites applied externally to masonry structures. In: *Proceedings of the 9th International Masonry Conference*. Guimaraes (PT).
- Oliveira D., Basilio I., Lourenço P. (2010). Experimental behavior of FRP strengthened masonry arches. *Journal of Composites for Construction*, 14(3), 312-322.

- Panizza M. (2010). FRP strengthening of masonry arches: analysis of local mechanisms and global behaviour. *PhD Thesis*. Padua (I): Università degli studi di Padova.
- Papanicolaou C., Triantafillou T., Lekka M. (2011). Externally bonded grids as strengthening and seismic retrofitting materials of masonry panels. *Construction and Building Materials*, 25, 504–514.
- Papanicolaou C.G., Triantafillou T.C., Papathanasiou M., Karlos K. (2008). Textile reinforced mortar (TRM) versus FRP as strengthening material of URM walls: out-of-plane cyclic loading. *Materials And Structures*, 41, 153-157.
- Papanicolaou C.G., Triantafillou T.C., Karlos K., Papathanasiou M. (2007). Textile-reinforced mortar (TRM) versus FRP as strengthening material of URM walls: in-plane cyclic loading. *Material and Structures*, 40(10), 1081-1097.
- Parisi F., De Luca F., Petruzzelli F., De Risi R., Chioccarelli E., Iervolino I. (2012a). Field inspection after the May 20th and 29th 2012 Emilia-Romagna earthquakes. RELUIS.
- Parisi F., Augenti N., Prota A., Manfredi G. (2012b). Full scale testing of unreinforced masonry walls. *In: Proceedings of the 15th World Conference on Earthquake Engineering*. Lisbon (PT).
- Parisi F. (2010). Non-Linear Seismic Analysis of Masonry Buildings. *PhD Thesis*. University of Naples Federico II (I).
- Park R. (1989). Bulletin of the New Zealand National Society for Earthquake Engineering. 22(3), 155-166.
- Parvin A., Shah T.S. (2016). Fiber Reinforced Polymer Strengthening of Structures by Near-Surface Mounting Method. *Polymers*, 8(8), n. 298.
- Pasticier L.A., Amadio C., Fragiaco M. (2008). Non-linear seismic analysis and vulnerability evaluation of a masonry building by means of the SAP2000 V.10 code. *Earthquake Engineering and Structural Dynamics*, 37(3), 467-485.
- Paulay T., Priestley M.J.N. (1992). Seismic design of reinforced concrete and masonry buildings. John Wiley & Sons, inc.
- Penna A., Morandi P., Rota M, Manzini C.F., Da Porto F., Magenes G. (2014). Performance of masonry buildings during the Emilia 2012 earthquake. *Bulletin of Earthquake Engineering*, 12(5), 2255–2273.
- Petersen R.B., Masia M., Seracino R. (2010a). In-Plane Shear Behavior of Masonry Panels Strengthened with NSM CFRP Strips. I: Experimental Investigation. *Journal of Composite for Construction*, 14(6), 754–763.
- Petersen R.B., Masia M.J., Seracino R. (2010b). In-Plane Shear Behavior of Masonry Panels Strengthened with NSM CFRP Strips. II: Finite-Element Model. *Journal of Composites for Construction*, 14(6), 764-774.
- Petrovic S., Kilar V. (2013). Seismic failure mode interaction for the equivalent frame modeling of unreinforced masonry structures. *Engineering Structures*, 54, 9–22.
- Petry S., Beyer K. (2014). Influence of boundary conditions and size effect on the drift capacity of URM walls. *Engineering structures*, 65, 76-68.
- Portoghesi P. (2011). Dizionario enciclopedico di architettura e urbanistica. Gangemi, (in Italian).
- Prawel S.P., Reinhorn S.P., Qazi S. (1988). Upgrading the seismic resistance of unreinforced brick masonry using ferrocement coating. *In: Proceedings of the 8th International Brick and Block Masonry Conference*, 785-791. London (UK).
- Prota A., Marcari G., Fabbrocino G., Manfredi G. (2006). Experimental In-Plane Behavior of Tuff Masonry Strengthened with Cementitious Matrix–Grid Composites. *Journal of Composites for Constructions*, 10(3).
- Reinhorn A.M., Prawel S.P. (1985). Experimental Study of Ferrocement as a Seismic Retrofit Material for Masonry Walls. *Journal of Ferrocement*, 15(3), 247–260.
- RILEM TC127-MS. (1996). Tests for masonry materials and structures. *Materials and Structures*, 29, 459-475.
- RILEM TC76-LUM. (1994). Diagonal tensile strength tests of small wall specimens. *In: RILEM recommendations for the testing and use of constructions materials*, 488–9. London (UK): E&EN SPON.
- Rinaldin G., Amadio C., Gattesco N. (2017). Review of experimental cyclic tests on unreinforced and strengthened masonry spandrels and numerical modelling of their cyclic behaviour. *Engineering Structures*, 132, 609–623.
- Rinaldin G., Amadio C. (2016). Static and dynamic analysis of masonry buildings using a new macroelement within the equivalent frame method. *In: Proceedings of the 16th International Brick and Block Masonry Conference*. Padua (I).
- Roca P., Cervera M., Gariup G., Pela L. (2010). Structural Analysis of Masonry Historical Constructions. Classical and Advanced Approaches. *Archives of Computational Methods in Engineering*, 17(3), 299–325.
- Roca P., Molins C., Mari A.R. (2005). Strength capacity of masonry wall structures by the equivalent frame method. *Journal of Structural Engineering*, 10, 1601–1610.
- Rovero L., Focacci F., Stipo G. (2013). Structural behavior of arch models strengthened using fiber-reinforced polymer strips of different lengths. *Journal of Composites for Construction*, 7(12), 249-258.
- Sacco E., Grande E., Imbimbo M. (2009). Rinforzo di murature con FRP: modellazione strutturale. *In: Atti del III Convegno Nazionale sulla meccanica delle strutture in muratura rinforzate con compositi*. Venice (I).

- Samarasinghe W. (1980). The in-plane failure of brickwork. *PhD thesis*. University of Edinburgh.
- Schuller M., Atkinson R., Borgsmiller J. (1994). Injection grouting for repair and retrofit of unreinforced masonry. *In: Proceedings of Tenth International Brick and Block Masonry Conference*. Calgary (CA).
- Schwegler G. (1994). Masonry Construction Strengthened with Fiber Composites in Seismically Endangered Zones. *In: Proceedings of the 10th European Conference on Earthquake Engineering*. Wien (A).
- Sciolti M.S., Aiello M.A., Frigione M. (2015). Effect of thermo-hygrometric exposure on FRM, natural stone and their adhesive interface. *Composites Part B: Engineering*, 80, 162-176.
- Sheppard P., Tercej S. (1980). The effect of repair and strengthening methods for masonry walls. *In: Proceedings of the 7th World Conference on Earthquake Engineering*, 6, 255-262. Istanbul (TR).
- Shrive N.G., Masia M.J., Lissel S.L. (2001). Strengthening and Rehabilitation of Masonry Using Fiber Reinforced Polymers. *In: Historical Constructions*, 1047-1056. Guimaraes (P): Lourenco P.B., Roca P.
- Singer C., Holmyard E.J., Hall A.R., Williams T.J. (1954-1978). A history of technology. Oxford (UK): Clarendon Press.
- Sorrentino L., D'Ayala D., De Felice G., Griffith M.C., Lagomarsino S., Magenes G. (2017). Review Of Out-Of-Plane Seismic Assessment Techniques Applied To Existing Masonry Buildings. *International Journal of Architectural Heritage*, 11(1).
- Spada A., Giambanco G., Rizzo P. (2009). Damage and plasticity at the interfaces in composite materials and structures. *Computer Methods in Applied Mechanics and Engineering*, 198(49-52), 3884-3901.
- Spyrakos C., Francioso A. (2012). Shaking Table Test and Pushover Analysis on a Scaled Masonry Building. *In: Proceedings of the 15th World Conference on Earthquake Engineering*. Lisbon (PT).
- Stratford T., Pascale G., Manfroni O., Bonfiglioli B. (2004). Shear Strengthening Masonry Panels with Sheet Glass-Fiber Reinforced Polymer. *Journal of Composite Constructions*, 8(5), 434-443.
- Szolomicki J., Berkowski P., Baranski J. (2015). Computer modelling of masonry cross vaults strengthened with fiber reinforced polymer strips. *Archives of Civil and Mechanical Engineering*, 15, 751-766.
- Theodossopoulos D., Sinha B. (2013). A review of analytical methods in the current design processes and assessment of performance of masonry structures. *Construction and Building Materials*, 41, 990-1001.
- Tinazzi D., Modena C., Nanni A. (2000). Strengthening of Masonry Assemblages with FRP Rods and Laminates. *In: Proceedings of the International Meeting on Composite Materials - Ed. 1*, 411-418. Milan (I).
- TNO Building and Construction Research. (2002, September). DIANA – Finite Element Analysis User's Manual. Release 8.1 .
- Tomazevic M., Gams M., Berset T. (2011). Seismic strengthening of brick masonry walls with composites: an experimental study. *In: Proceedings of the Structural Engineering World Congress*. Como (I).
- Tomazevic M. (1999). Earthquake-resistant design of masonry buildings. Imperial College Press.
- Tomazevic M., Eeri M., Lutman M., Weiss P. (1996). Seismic upgrading of old brick masonry urban houses: Tying of walls with steel ties. *Earthquake Spectra*, 12(3).
- Tomazevic M., Lutman M. (1996). Seismic behavior of masonry walls: Modeling of hysteretic rules. *Journal of Structural Engineering*, 122(9), 1048-1054.
- Tomazevic M., Apih V. (1993). The strengthening of stone-masonry walls by injecting the masonry-friendly grouts. *European earthquake engineering*, 7(2), 10-20. Bologna (I).
- Tomazevic M., Eeri M., Lutman M., Weiss P. (1993). The seismic resistance of historical urban buildings and the interventions in their floor systems: an experimental study. *The Masonry Society Journal*, 12(1).
- Tomazevic M. (1978). The computer program POR. *Report ZRMK (in Slovene)*.
- Touliatos P.G. (1996). Seismic behaviour of traditionally-built constructions: repair and strengthening. *In: Courses and lectures-international centre for mechanical sciences*, 57-70. New York (US): Springer.
- Triantafillou T.C. (2011). Textile-Reinforced Mortars (TRM) - A new generation of composite materials as alternative to fiber reinforced polymers for strengthening and seismic retrofitting of structures. *Composite Materials - A Vision for the Future*, 113-127.
- Triantafillou T.C. (1998a). Strengthening of masonry structures using epoxy-bonded FRP laminates. *Journal of Composite for Construction*, 2(2), 96-104.
- Triantafillou T.C. (1998b). Shear strengthening of reinforced concrete beams using epoxy-bonded FRP composites. *ACI Structural Journal*, 95(2), 107-115.
- Triantafillou T.C., Fardis M.N. (1997). Strengthening of historic masonry structures with composite materials. *Materials and Structures*, 30(8), 486-496 .
- Tubi N. (1993). La realizzazione di murature in laterizio. *Andil, Sezione Murature*. Ed. Laterconsult, (in Italian).

- Tumialan J.C., Micelli F., Nanni A. (2001a). Strengthening of Masonry Structures with FRP composites. *In: Proceedings of Structures Congress 2001*. Washington D.C. (US)
- Tumialan J.G., Huang P.C., Nanni A., Silva P. (2001b). Strengthening of masonry walls by FRP structural repointing. Non-metallic reinforcement for concrete structures. *In: Proceedings of the 5th International Research Symposium on Fiber Reinforced Polymer for Reinforced Concrete Structures*. Cambridge (UK).
- Turco V., Secondin S., Morbin A., Valluzzi M.R., Modena C. (2006). Flexural and shear strengthening of un-reinforced masonry with FRP bars. *Composites Science and Technology*, 66(2), 289-296.
- Turnsek V., Cacovic A. (1971). Some experimental results on the strength of brick masonry walls. *In: Proceedings of the 2nd International Brick Masonry Conference*, 149-156. Stoke on Trent (UK).
- Umair S.M., Numada M., Amin M.N., Meguro K. (2015). Fiber Reinforced Polymer and Polypropylene Composite Retrofitting Technique for Masonry Structures. *Polymers*, 7(5), 963-984.
- Umair S.M., Numada M., Meguro K. (2012). In-plane Behavior of Polypropylene and FRP Retrofitted Brick Masonry Wallets under Diagonal Compression Test. *In: Proceedings of the 15th World Conference on Earthquake Engineering*. Lisbon (PT).
- UNI EN14399:2015. (2015). Assiemi di bulloneria strutturale ad alta resistenza da precarico, (in Italian).
- Urban M., Stempniewski L. (2012). Comparison of different earthquake strengthening methods for masonry buildings. *In: Proceedings of the 15th World Conference on Earthquake Engineering*. Lisboa (PT).
- Valluzzi M.R., Oliveira D.V., Caratelli A., Castori G., Corradi M., De Felice G., Garbin E., Garcia D., Garmendia L., Grande E., Ianniruberto U., Kwecien A., Leone M., Lignola G.P., Lourenco P.B., Malena M., Micelli F., Panizza M. & al. (2012). Round Robin Test for composite-to-brick shear bond. *Materials and Structures*, 45, 1761–1791.
- Valluzzi M.R., Binda L., Modena C. (2005). Mechanical behaviour of historic masonry structures strengthened by bed joints structural repointing. *Construction and Building Materials*, 19(11), 63-73.
- Valluzzi M.R., Tinazzi D., Modena C. (2002). Shear behavior of masonry panels strengthened by FRP laminates. *Construction and Building Materials*, 16, 409–416.
- Valluzzi M.R., Valdemarca M., Modena C. (2001). Behavior of brick masonry vaults strengthened by FRP laminates. *Journal of Composites for Construction*, 5(3), 163-169.
- Van Der Pluijm R. (1999). Out-of-plane bending of masonry: behaviour and strength. Eindhoven: Technische Universiteit Eindhoven.
- Vecchio F.J., Collins M.P. (1986). The moed compression-field theory for reinforced concrete elements subjected to shear. *ACI journal*, 83(22), 219-231.
- Vecco M. (2010). Definition of cultural heritage: from the tangible to the intangible. *Journal of Cultural Heritage*, 11(3), 321-324.
- Velazquez-Dimas J.I., Ehsani M.R., Saadatmanesh H. (2000). Seismic retrofit of URM walls with fiber composites. *In: Proceedings of the 12th World Conference on Earthquake Engineering*. Auckland (NZ).
- Vintzielou E., Tassios T.P. (1995). Three-Leaf Stone Masonry Strengthened by Injecting Cement Grouts. *Journal of Structural Engineering*, 121(5). ASCE.
- Willis C.R., Seracino R., Griffith M.C. (2010). Out-of-plane strength of brick masonry retrofitted with horizontal NSM CFRP strips. *Engineering Structures*, 32, 547-555.
- Xu L., Zhang S., Hu X., Zhang M. (2012). Seismic Responses of Masonry Structures Strengthened with FRP Laminates: a Shaking-table Study. *In: Proceedings of the 15th World Conference on Earthquake Engineering*. Lisboa (PT).
- Yan L., Kasal B., Huang L. (2016). A review of recent research on the use of cellulosic fibres, their fibre fabric reinforced cementitious, geo-polymer and polymer composites in civil engineering. *Composites Part B: Engineering*, 92, 94-132.
- Yardim Y., Lalaj O. (2016). Shear strengthening of unreinforced masonry wall with different fiber reinforced mortar jacketing. *Construction and Building Materials*, 102, 149–154.
- Yokel F.Y., Fattal S.G. (1975). A failure hypothesis for masonry shearwalls. *NBSIR 75-703*. Washington D.C. (US): Center for Building Technology Institute for Applied Technology, National Bureau of Standards.
- Zlamal M., Stepanek P. (2009). Additional strengthening of masonry vaulted structures by nonprestressed reinforcement. *Architecture Civil Engineering Environment*, 2(3), 85-90.
- Zoghi M. (2013). The International handbook of FRP composites in civil engineering. CRC Press.
- Zorzi T. (2014). Valutazione sperimentale in situ delle efficacia di connettori trasversali per il rinforzo di murature con materiali compositi. *PhD Thesis*. Padua (I): Università degli Studi di Padova.

## 8 FIGURE INDEX

- Figure 2.1 – Structural behavior of masonry buildings: (a) schematization of “box behavior”, which leads to the desirable activation of (b) in-plane response of masonry walls, avoiding the activation of (c) out-of-plane, poor resistance reserves
- Figure 2.2 – Subdivision of a masonry façade in piers and spandrels
- Figure 2.3 – Typical failure mechanisms of masonry piers: (a) shear, (b) sliding and (c) bending/rocking
- Figure 2.4 – Typical failure mechanisms of masonry spandrels: (a) shear and (b) rocking. Rocking can be effectively prevented through lintels or tie beams (c)
- Figure 2.5 – In-situ characterization tests: (a) direct shear test and (b) diagonal compression destructive test on masonry panels and (c) semi-destructive shove test
- Figure 2.6 – Laboratory characterization tests: (a) shear-compression test and (b) diagonal compression test on masonry panels and (c) shear tests on masonry triplet
- Figure 2.7 – Typical setup for laboratory characterization test on masonry spandrels
- Figure 2.8 – Mohr’s circle representation of different interpretations on the stress state in the centre of a panel subjected to diagonal compression
- Figure 2.9 – Modeling strategies for masonry: (a) discrete micro-modeling, (b) simplified discrete micro-modeling and (c) based on continuum
- Figure 2.10 – Examples of macro-element models based on (a) monodimensional (Magenes & al., 2000) or (b) bidimensional elements (Caliò, 2005)
- Figure 2.11 – Out-of-plane mechanisms typically considered in the limit equilibrium analysis of masonry walls (D’Ayala & Speranza, 2002)
- Figure 2.12 – Example of (a) typical tensile stress-strain behavior of various reinforcing fibers (ACI 440) and (b) behavior of FRP composites in respect to that of reinforcing fibers and matrix (CNR DT 200 R1/2013) and (c) typical fiber arrangements (CNR DT 200 R1/2013)
- Figure 2.13 – Typical three-stages behavior of a FRM sample subjected to tensile test
- Figure 3.1 – GFRM reinforcement technique (a) schematization and (b) illustration during installation on a stone masonry wall, before the application of the mortar coating
- Figure 3.2 – Production of the GFRP meshes: (a) spools of dry Alkali-Resistant glass fibers wires, (b) soaking of dry fibers wires in the thermosetting resin, (c) storage of the GFRP mesh in rolls and (d) production of the angle brackets for corner devices
- Figure 3.3 – Details of typical 66x66 mm<sup>2</sup> type “S” GFRP mesh used in practice: the warp (twisted fibers wires) is vertical and the weft (parallel fibers wires) is horizontal
- Figure 3.4 – Characterization of GFRP wires: (a) equivalent cross section evaluation and (b) tensile tests
- Figure 3.5 – A GFRP L-shaped connector
- Figure 3.6 – Tests on GFRP angle brackets: (a) test setup and detail of wire failure at corner in (b) 66x33S and (c) 66x66D samples
- Figure 3.7 – Mortar characterization tests: (a) flexural tensile and (b) compressive strength tests on prisms and (c) indirect tensile and (d) Young modulus and compressive strength tests on cylinders
- Figure 3.8 - Test setup for pull-out tests on plate samples: (a) picture before the beginning of a test and (b) main geometrical characteristics in frontal and lateral vertical sections
- Figure 3.9 - Load vs. displacement curves of the pull-out tests performed of GFRM plate samples with twisted fibers wires oriented in the longitudinal direction
- Figure 3.10 - Pull-out tests performed of GFRM plate samples with twisted fibers wires oriented in the longitudinal direction: (a) failure of the GFRP central wire in PO-PT3 and (b) vertical cracking of the mortar and (c) failure of the mesh nodes at the end of the test in PO-PT4
- Figure 3.11 - Pull-out tests performed of GFRM cylindric samples with twisted fibers wires oriented in the longitudinal direction: (a) test setup and (b) failure of the GFRP wire in PO-CT5
- Figure 3.12 – Pull-out tests: comparison between PO-CT and PO-PT samples (load vs. displacement curves)
- Figure 3.13 - Pull-out tests performed of GFRM plate samples with parallel fibers wires oriented in the longitudinal direction: (a) comparison between PO-PP and PO-PT samples ( load vs. displacement curves) and (b) detail of the slippage of the central wire from the transversal ones at the end of the test PO-PP2

Figure 3.14 – Lap-splice tests on plate samples: main geometrical characteristics in frontal and lateral vertical section and (b) load vs. average displacement curves

Figure 3.15 – Lap-splice tests on plate samples: (a) failure of the GFRP central wire in LS-PT5 and (b) failure mode of the mesh nodes at the end of the test in LS-PT3,

Figure 3.16 – Lap-splice tests performed of GFRM cylindrical samples with twisted fibers wires oriented in the longitudinal direction: (a) comparison between LS-CT and LS-PT samples in terms of load vs. displacement curves and (b) failure of the GFRP central wire in LS-CT1

Figure 3.17 – Lap-splice tests performed of GFRM plate samples with parallel fibers wires oriented in the longitudinal direction: (a) comparison between LS-PP and LS-PT samples in terms of load vs. displacement curves and (b) failure of the GFRP central wire in LS-PP2

Figure 3.18 – Tensile tests: main geometrical characteristics of the GFRM samples TA66, in frontal and lateral vertical sections

Figure 3.19 – Tensile tests on GFRM: (a) global and (b) detail views and (c) schematization of the test setup

Figure 3.20 – Tensile tests on GFRM samples: (a) stress  $\sigma$  against strain  $\varepsilon$  curves and (b) crack pattern at the end of test TA66-4

Figure 3.21 – Tensile tests on GFRM samples: (a) main characteristics of TB66 samples and (b) crack pattern at the end of test TB66-4

Figure 3.22 – Tensile tests on GFRM layers: comparison between TB66 and TA66 samples in terms of stress  $\sigma$  - strain  $\varepsilon$  curves

Figure 3.23 - Tensile tests TA99: (a) samples characteristics, (b) view at the end of the tests and (c) example of  $\sigma$ - $\varepsilon$  curve

Figure 3.24 – Illustration of (a) the construction of a masonry wallet for bond tests and (b) compressive strength test on a solid brick unit

Figure 3.25 - Characteristics of the samples for bond tests: (a) type A66-1, (b) A66-2, (c) A66-3 and (d) type A33-1

Figure 3.26 – Shear bond tests: (a) global and (b) detail views and (c) schematization of the test setup

Figure 3.27 - Load  $P$  against displacement  $\delta_{t-m}$  of samples subjected to bond tests

Figure 3.28 - Examples of failure mechanism emerged in bond tests: (a) mesh-mortar slip with cracking of the mortar in a A66-1 sample, (b) debonding at mortar-masonry interface and (c) GFRP wire rupture in A66-2 samples, (d) GFRP wire rupture in a A66-3 sample and (e) debonding of the mortar covering the mesh in a A33-3 sample

Figure 4.1 – Specimens of different masonry types subjected to diagonal compression tests: solid brick 250 mm thick (S), solid brick 380 mm thick (S2), two-leaf solid brick with small rubble conglomerate infill 120 + 140 + 120 mm thick (I), rubble stones 400mm thick (R and R2), rubble stones 700 mm thick (R3) and cobblestones 400 mm thick (C)

Figure 4.2 – Texture details of the masonry in specimens subjected to diagonal compression tests: (a) solid brick masonry S and S2, (b) solid brick infill masonry I, (c) R-R3 and (d) R2 rubble stone masonry and (e) cobblestones masonry C

Figure 4.3 - Compression tests on masonry specimens: (a) test setup and failure mode of (b) solid brick S, (b) rubble stone R and (c) cobblestones C specimens

Figure 4.4 - Compression tests on masonry specimens: compressive stress  $\sigma_c$  vs. strain  $\varepsilon_c$  curves

Figure 4.5 – Main realization stages of a sample for diagonal compression test (DS-B3-R19): (a) building of the masonry panel, (b) installation of the GFRP mesh and connectors and (c) application of the mortar coating

Figure 4.6 – Correlation between mortar coating characteristics: (a) compressive against tensile strengths and (b) compressive strength against Young modulus

Figure 4.7 - Connectors arrangement in reinforced samples: (a) 6 and (b) 4 connectors / m<sup>2</sup>.

Figure 4.8 - Test setup for diagonal loading: (a) illustration of the apparatus, set on a reinforced sample and (b) schematization of frontal and lateral views

Figure 4.9 – Details of the steel contrast devices used for diagonal compression tests: frontal and lateral views

Figure 4.10 - Example of a loading-unloading sequence applied to samples subjected to diagonal compression tests

Figure 4.11 – Displacement transducers arrangement on the (a) front and (b) back side of the specimens

Figure 4.12 – Example of  $P$ - $\varepsilon_c$  and  $P$ - $\varepsilon_t$  curves complete of the loading and unloading branches obtained from experimental diagonal compression tests

Figure 4.13 – Illustration of the shear strains  $\gamma_s$ ,  $\gamma_{0.8}$  and  $\gamma_{0.6}$

Figure 4.14 –  $P$ - $\varepsilon_c$  and  $P$ - $\varepsilon_t$  envelope curves of unreinforced solid brick masonry samples: (a) DS, (b) DS2 and (c) DI

Figure 4.15 – Examples of typical crack patterns in unreinforced solid brick masonry samples at the end of the diagonal compression test: (a) DS-B3-U05, (b) DS2-B2-U02 and (c) DI-B2-U01

Figure 4.16 – Comparison between  $P-\varepsilon_c$  and  $P-\varepsilon_t$  envelope curves concerning samples made of 250 mm thick solid brick masonry DS

Figure 4.17 – Comparison between  $P-\varepsilon_c$  and  $P-\varepsilon_t$  envelope curves concerning samples made of 380 mm thick solid brick masonry DS2

Figure 4.18 – Comparison between  $P-\varepsilon_c$  and  $P-\varepsilon_t$  envelope curves concerning samples made of two-leaf solid brick with conglomerate infill masonry DI.

Figure 4.19 – Example of typical crack pattern evolution in a reinforced solid brick masonry specimen: sample DS-B3-R14 at (a)  $\varepsilon_c = 0.18\%$ , (b)  $\varepsilon_c = 0.43\%$ , (c)  $\varepsilon_c = 0.65\%$  and (a) at the end of the test, after removing some damaged mortar portions

Figure 4.20 – Comparison among solid brick masonry specimens enhanced by means of (a) 99x99S, (b) 66x66S (c) 33x33S, (d) 66x66D and (e) 99x99D GFRP meshes at the end of the tests and (f) sample without any reinforcement embedded in the plaster

Figure 4.21 – Typical crack patterns at the end of the test in samples of group 1: coatings made of (a) C2, (b) C4 and (c) C8 mortars

Figure 4.22 – Typical crack pattern at the end of the test in samples of group 2 (coating made of C5 mortar)

Figure 4.23 – Typical crack patterns at the end of the test in samples of group 3: coatings made of (a) C6, (b) C7 and (c) C8 mortars

Figure 4.24 – Typical crack patterns at the end of the test in samples of group 4 and 5: coatings made of (a) C10, (b) C11 and (c) C12 mortars

Figure 4.25 – Ratios  $P_{m(R)}/P_{m(R)}$  against the mortar coating tensile strength in solid brick DS-B3 samples.

Figure 4.26 –  $P-\varepsilon_c$  and  $P-\varepsilon_t$  envelope curves of unreinforced stone masonry samples: (a) DR and DR2, (b) DR3 and (c) DC

Figure 4.27 – Examples of typical crack patterns in unreinforced stone masonry samples at the end of the diagonal compression test: (a) DR-B5-U02, (b) DR2-B3-U02, (c) DR3-B4-U01 and (D) DC-B2-U02

Figure 4.28 – Comparison between  $P-\varepsilon_c$  and  $P-\varepsilon_t$  envelope curves concerning rubble stones samples

Figure 4.29 – Comparison between  $P-\varepsilon_c$  and  $P-\varepsilon_t$  envelope curves concerning cobblestones samples DC

Figure 4.30 – Example of typical crack pattern evolution in a reinforced stone masonry specimen (sample DR-B5-R06): (a) at  $\varepsilon_c = 0.3\%$ , (b)  $\varepsilon_c = 0.5\%$ , and (c)  $\varepsilon_c = 1.1\%$  and (d) detail of the GFRP mesh rupture at the end of the test, after removing some pieces of the cracking mortar

Figure 4.31 – Comparison among stone masonry specimens enhanced by means of (a) 33x33S and (b) 66x66D GFRP meshes, for 400 mm thick masonry, and by means of (c) 66x66D and (d) 66x66S GFRP meshes, for 700 mm thick samples

Figure 4.32 – Elastic stress on a square plate loaded by diagonal load: comparison between the Frocht's solution and numerical results (Yokel & Fattal, 1975)

Figure 4.33 - Representation of the stress state at the centre of the panel in the Mohr's circle

Figure 4.34 – Curves representing the equivalent principal tensile stress at the varying of the diagonal strains  $\varepsilon_c-\varepsilon_t$ : comparison between some reinforced samples made of (a) 250 and 380 mm thick solid brick and (b) 400 and 700 mm rubble stone masonry

Figure 4.35 – Comparisons between experimental values (light grey) and analytical estimations (dark grey) of shear modulus  $G_{(R)}$  of reinforced masonry panels subjected to diagonal compression tests: (a) DS-B3, (b) DS-B6, DS and DI and (c) DR, DR2, DR3 and DC

Figure 4.36 – Coefficient  $\beta$  in solid brick masonry samples enhanced with C3 mortar; mean values are also reported for each category

Figure 4.37 – Coefficient  $\beta$  at the varying of the mortar coating tensile resistance  $f_{t,c}$  in solid brick DS-B3 masonry

Figure 4.38 – Coefficient  $\beta$  in stone masonry samples; mean values are also reported for each category

Figure 4.39 – Coefficient  $\beta$  at the varying of the mortar coating tensile resistance  $f_{t,c}$  in rubble stone DR-B5 and DR3-B4 reinforced masonry samples

Figure 4.40 – Schematization of different collapse cases in solid brick reinforced specimens DS-B3: (a) simultaneous cracking of masonry and reinforced coating, (b) cracking occurs first in the masonry, (c) cracking occurs first in the mortar coating and (d) simultaneous cracking with higher stiffness mortar

Figure 4.41 – Schematization of possible collapse mechanism in stone masonry specimens

Figure 4.42 – Comparisons between experimental values (light grey) and analytical estimations (dark grey) of equivalent diagonal tensile strength  $f_{t(R)}$  of reinforced masonry panels subjected to diagonal compression tests: (a) DS-B3, (b) DS-B6, DS and DI and (c) DR, DR2, DR3 and DC

Figure 4.43 – Schematization of the numerical model adopted for the preliminary simulations of diagonal compression tests

Figure 4.44 – Schematization of the parabolic softening law adopted for masonry in compression (TNO Building and Construction Research, 2002)

Figure 4.45 –  $P-\alpha$  numeric curves concerning unreinforced masonry and unreinforced mortar layers

Figure 4.46 - Finite element numerical simulations on a square panel type DS-B3 subject to diagonal compression: principal stresses (a) in tension  $\sigma_I$  and (b) in compression  $\sigma_{III}$  (b) at peak load

Figure 4.47 –  $P-\alpha$  numeric curves concerning a solid brick masonry panel DS-B3-U with unreinforced mortar layers at both faces, at the varying of the mortar type: (a) DS+C2, (b) DS+C4, (c) DS+C8 and (d) DS+C12

Figure 4.48 – DS-B3: (a) comparison between experimental and numerical capacity curves ( $P-\varepsilon_c$ ,  $P-\alpha$ ) and (b) GFRP mesh stress state just before failure

Figure 4.49 – Schematization of the Hordijk softening law adopted for masonry (TNO Building and Construction Research, 2002)

Figure 4.50 – Comparison between experimental and numerical capacity curves ( $P-\varepsilon_c$ ,  $P-\alpha$ ): (a) DR-B5 and (b) DC-B2

Figure 4.51 – Main in-plan geometrical characteristics of the (a) regular and (b) non-regular buildings

Figure 4.52 – Main geometrical characteristics of (a) external and (b) internal masonry walls, with indication of the Equivalent Frame schematization adopted for the numerical simulations

Figure 4.53 – Shear and bending behavior for the plastic hinges in (a) masonry piers and (b) spandrels (suffix “U” refers to unreinforced masonry)

Figure 4.54 – Shear and bending behavior for the plastic hinges in (a) masonry piers and (b) spandrels (suffix “R” refers to unreinforced masonry)

Figure 4.55 – Schematization of the procedure for the evaluation of the maximum ground acceleration  $a_{g,max}$

Figure 4.56 – Capacity curves of the solid brick unreinforced and reinforced masonry buildings in the X (a) and Y (b) direction - modal pattern “S”

Figure 4.57 – Capacity curves of the rubble stone unreinforced and reinforced masonry buildings in the X (a) and Y (b) direction - modal pattern “S”.

Figure 4.58 – Seismic performances of (a) solid brick and (b) rubble stone masonry structures, in terms of  $a_{g,max}$ , and comparison with a the seismic demand  $a_{g,req}$

Figure 5.1 – Details of the masonry surface in (a) solid brick, (b) rubble stone and (c) cobblestones samples

Figure 5.2 - Units arrangement in out-of-plane bending samples made of (a) solid brick, (b) rubble stone and (c) cobblestones masonry

Figure 5.3 - Positioning of the connections in reinforced masonry samples.

Figure 5.4 – Global views of the experimental apparatus for out-of-plane bending tests: (a) front and (b) back side

Figure 5.5 – Details of the apparatus for out-of-plane bending tests: (a) loading area, (b) upper and (c) lower steel contrasts (d) base support and (e) adjustable feet

Figure 5.6 - Experimental apparatus for out-of-plane bending tests: (a) lateral view and (b) vertical section in the transversal direction

Figure 5.7 – Position of the displacement transducers (a) on the front and (b) on the back side of the samples

Figure 5.8 - Unreinforced solid brick masonry specimen (FS-B6-U) at the end of the experimental test: (a) frontal and (b) back side global views and detail of the crack opening (c) on the masonry tensed face and (d) on the masonry thickness and compressed face

Figure 5.9 - Unreinforced rubble stone masonry specimen (FR-B6-U) at the end of the experimental test: (a) frontal and (b) back side global views and detail of the crack opening (c) on the masonry tensed face and (d) on the masonry thickness and compressed face

Figure 5.10 - Unreinforced cobblestones masonry specimen (FC-B3-U) at the end of the experimental test: (a) frontal and (b) lateral global views and detail of the crack opening (c) on the masonry tensed face and (d) on the masonry thickness and compressed face

Figure 5.11 – Load  $P$  - deflection  $\delta$  curve of unreinforced masonry specimens

Figure 5.12 - Evolution of the crack pattern of the tensed mortar coating in sample FR-B6-R at the increasing of the wall deflection: (a)  $\delta = 0.5$  mm, (b)  $\delta = 4$  mm and (c)  $\delta = 20$  mm

Figure 5.13 - Reinforced masonry samples at the end of the tests: details of the (a) vertical wire rupture in FR-B6-R and of the main crack opening (b) on the masonry thickness in FC-B2-R and (c) on the masonry back side in FS-B6-R

Figure 5.14 – Load  $P$  vs. deflection  $\delta$  curve of reinforced masonry specimens

Figure 5.15 - Crack pattern of reinforced specimens at the end of the tests, with indication of cracks occurrence sequence: (a) FS-B6-R, (b) FR-B6-R and (c) FC-B2-R

Figure 5.16 - Simplified scheme assumed for the experimental four-point bending tests

Figure 5.17 - Comparisons between unreinforced and reinforced masonry specimens in terms of (a) resisting bending moment and (b) out-of-plane ultimate deflection

Figure 5.18 - Combined effect of axial force ( $N$ ) and bending action ( $M$ ) in specimens subjected to four-point bending ( $A$  is the cross section,  $W$  the resistance modulus)

Figure 5.19 – Masonry cross section for the calculation of (a) first cracking and (b) maximum bending moment in reinforced panels

Figure 5.20 – Schematization of the numerical models adopted for the simulation of four-point bending tests: (a) bidimensional and (b) tridimensional models

Figure 5.21 - Stress – strain behaviour of the GFRM layer, of the GFRP textile and of the mortar of the coating and indication of the main parameters considered in the tension stiffening model.

Figure 5.22 – Numerical results concerning unreinforced masonry: principal (a) tensile and (b) compressive stresses just before cracking and (c) plasticity status after cracking

Figure 5.23 - Experimental (dotted lines) and numerical (solid lines) load  $P$  - deflection  $\delta$  curves of (a) unreinforced and (b) reinforced masonry specimens subjected to out-of-plane bending

Figure 5.24 – Numerical results concerning reinforced masonry: principal (a) tensile and (b) compressive stresses in masonry and mortar just before the first cracking, (c) tensile stresses in GFRP mesh just before rupture and (d) mortar and masonry plasticity status after collapse

Figure 5.25 – Comparisons between experimental  $P$ - $\delta$  curves (dotted lines) and numerical behavior (solid lines) derived from the tridimensional models: (a) unreinforced and (b) reinforced masonry

Figure 5.26 – Parametric study on solid brick reinforced masonry specimens: (a) influence of masonry stiffness  $E_m$  and (b) thickness  $t_m$

Figure 5.27 – Parametric study on rubble stone reinforced masonry specimens: (a) influence of GFRP mesh resistance  $T_w$  and (b) stiffness  $E_w$

Figure 5.28 – Parametric study on cobblestones reinforced masonry specimens: (a) influence of the mortar tensile strength, (b) of the tension stiffening effect and (c) of the mortar thickness  $t_c$

Figure 5.29 – Wall configurations analyzed: (a) frontal views and (b) static scheme assumed in the numerical simulation of the out-of-plane bending behavior

Figure 5.30 – Load deflection curves of Case 1: (a) solid brick and (b) rubble stone masonry

Figure 5.31 – Load deflection curves of Case 2: (a) solid brick and (b) rubble stone masonry

Figure 5.32 – Load deflection curves of Case 3: (a) solid brick and (b) rubble stone masonry

Figure 5.33 – Comparisons between unreinforced and reinforced masonry walls performances in terms of out-of-plane resistances: (a) solid brick and (b) rubble stone masonry

Figure 5.34 – Numerical study on masonry barrel vaults: (a) considered reinforcement technique and (b) cross section geometry of the analyzed cases

Figure 5.35 – Load patterns considered in the numerical simulations: vertical load (Case V1) and horizontal load (Case V2), acting perpendicular to vault axis, proportional to its self-weight

Figure 5.36 – Force-displacement numerical curves of unreinforced vaults subjected to vertical loads (Case V1)

Figure 5.37 – Case V1: (a) principal tensile stresses distribution and deformed shape just before the reaching of the first cracking and (b) typical failure mechanism

Figure 5.38 – Force-displacement numerical curves of reinforced vaults subjected to vertical loads (Case V1)

Figure 5.39 – Force-displacement numerical curves of unreinforced vaults subjected to horizontal loads (Case V2)

Figure 5.40 – Case V2: (a) principal tensile stresses distribution and deformed shape of unreinforced masonry vaults just before the reaching of the first cracking and (b) typical failure mechanism

Figure 5.41 – Force-displacement numerical curves of reinforced vaults subjected to horizontal loads (Case V2)

Figure 5.42 – Typical failure mechanism of reinforced vaults subjected to “Case V2” load pattern: (a) up to cracking at the extrados, (b) due to bending resistance of right haunch section provided by the GFRP mesh

Figure 5.43 – Comparisons between the load carrying capacity of unreinforced reinforced vaults for (a) Case V1 and (b) Case V2

Figure 5.44 – Simplified load patterns usually considered in quasi-static experimental tests on masonry vaults: (a) vertical load at crown - Case V3 - and (b) at 1/4 of the span - Case V4

Figure 5.45 – Numerical results of in terms of vertical force-displacement curves for (a) Case V3 and (b) Case V4



## 9 TABLE INDEX

Table 3.1 – Tensile characterization test on single GFRP wires: dry fiber cross section  $A_{fib}$ , equivalent cross section  $A_{tot}$ , tensile resistance  $T_w$  and axial stiffness  $EA_{tot}$  (the coefficients of variation, c.o.v., are also reported for  $T_w$  and  $EA_{tot}$ )

Table 3.2 – Characterization tests on GFRP angle brackets: Vertical peak load  $V_{max}$ , number of longitudinal wires  $n_w$ , equivalent axial force acting on the single longitudinal wire  $P_{max}$  and ratios between  $P_{max}/T_w$  (being  $T_w$  the single wire tensile resistance)

Table 3.3 - Pull-out tests on GFRM layers: maximum pull-out load  $T_{max}$ , wire-mortar slip corresponding to maximum load  $\Delta(T_{max})$  and failure mode

Table 3.4 – Lap-splice tests on GFRM layers: maximum force  $T_{max}$ , average wire-mortar slip corresponding to maximum load  $\Delta(T_{max})$  and failure mode

Table 3.5 – Results of the tensile tests carried out on reinforced mortar coating layers: first cracking and peak loads ( $T_{cr}$ ,  $T_{max}$ ), stresses evaluated in respect to the cross section of dry fibers ( $\sigma_{cr}$ ,  $\sigma_{max}$ ), base length of the displacements transducers ( $l_d$ ), displacements monitored by the transducers T1 and T2 in correspondence of first cracking and peak loads ( $\delta T_1(T_{cr})$ ,  $\delta T_1(T_{max})$ ,  $\delta T_2(T_{cr})$ ,  $\delta T_2(T_{max})$ ), average strains in correspondence of  $T_{cr}$  and  $T_{max}$ , ( $\varepsilon_{cr}$ ,  $\varepsilon_{max}$ ), number total cracks ( $n_{tot,cr}$ ) and of cracks detected by the transducers ( $n_{tot,mis}$ ) and average crack distance ( $\Delta_{cr,m}$ )

Table 3.6 – Main characteristics and results of the samples subjected to bond test in terms of peak load  $P_u$ , displacements  $\delta T_1$ ,  $\delta T_2$  and  $\delta T_3$  monitored by transducers T1, T2 and T3 in correspondence of the peak load and type of collapse.

Table 4.1 - Characteristics of the hydraulic lime mortars used for the masonry ( $f_{c,b}$  is the compressive strength,  $f_{t,b}$  the tensile strength, the coefficients of variation, c.o.v., are also reported)

Table 4.2 - Mechanical characteristics of masonry samples subjected to compression tests: compressive strength  $f_{c,m}$  and Young modulus  $E_m$ .

Table 4.3 – Main characteristics of the mortars used for the coating ( $f_{t,c}$  and  $f_{c,c}$  are the tensile and the compressive strengths,  $E_c$  is the Young modulus, the coefficients of variation, c.o.v., are also reported)

Table 4.4 - Main characteristics of the solid brick masonry samples, 250 mm thick (S) tested to diagonal compression

Table 4.5 - Main characteristics of the solid brick masonry samples, 380 mm thick (S2) tested to diagonal compression

Table 4.6 - Main characteristics of the infill solid brick masonry samples (I) tested to diagonal compression

Table 4.7 - Main characteristics of the rubble stone masonry samples (R, R2 and R3) tested to diagonal compression

Table 4.8 - Main characteristics of the cobblestones masonry samples (C) tested to diagonal compression

Table 4.9 - Main results concerning solid brick masonry samples, 250 mm thick (S): maximum diagonal load ( $P_m$ ), average compressive strain in correspondence of  $P_m$  ( $\varepsilon_{cp}$ ), shear modulus ( $G$ ), ratios between  $P_m$  ( $P_{m(R)} / P_{m(U)}$ ) and between  $G$  ( $G_{(R)} / G_{(U)}$ ) of the reinforced and the unreinforced specimens, shear strains associated to a resistance value after the peak of 80% and 60% of  $P_m$  ( $\gamma_{0.8}$  and  $\gamma_{0.6}$ ) and ratios  $\mu_{0.8} = \gamma_{0.8}/\gamma_y$  and  $\mu_{0.6} = \gamma_{0.6}/\gamma_y$ , being  $\gamma_y$  the shear strain associated to the conventional yield strength

Table 4.10 - Main results concerning solid brick masonry samples, 380 mm thick (S2): maximum diagonal load ( $P_m$ ), average compressive strain in correspondence of  $P_m$  ( $\varepsilon_{cp}$ ), shear modulus ( $G$ ), ratios between  $P_m$  ( $P_{m(R)} / P_{m(U)}$ ) and between  $G$  ( $G_{(R)} / G_{(U)}$ ) of the reinforced and the unreinforced specimens, shear strains associated to a resistance value after the peak of 80% and 60% of  $P_m$  ( $\gamma_{0.8}$  and  $\gamma_{0.6}$ ) and ratios  $\mu_{0.8} = \gamma_{0.8}/\gamma_y$  and  $\mu_{0.6} = \gamma_{0.6}/\gamma_y$ , being  $\gamma_y$  the shear strain associated to the conventional yield strength

Table 4.11 - Main results concerning infill solid brick masonry samples (I): maximum diagonal load ( $P_m$ ), average compressive strain in correspondence of  $P_m$  ( $\varepsilon_{cp}$ ), shear modulus ( $G$ ), ratios between  $P_m$  ( $P_{m(R)} / P_{m(U)}$ ) and between  $G$  ( $G_{(R)} / G_{(U)}$ ) of the reinforced and the unreinforced specimens, shear strains associated to a resistance value after the peak of 80% and 60% of  $P_m$  ( $\gamma_{0.8}$  and  $\gamma_{0.6}$ ) and ratios  $\mu_{0.8} = \gamma_{0.8}/\gamma_y$  and  $\mu_{0.6} = \gamma_{0.6}/\gamma_y$ , being  $\gamma_y$  the shear strain associated to the conventional yield strength

Table 4.12 - Main results concerning rubble stone masonry samples (R, R2 and R3): maximum diagonal load ( $P_m$ ), average compressive strain in correspondence of  $P_m$  ( $\varepsilon_{cp}$ ), shear modulus ( $G$ ), ratios between  $P_m$  ( $P_{m(R)} / P_{m(U)}$ ) and between  $G$  ( $G_{(R)} / G_{(U)}$ ) of the reinforced and the unreinforced specimens, shear strains associated to a resistance value after the peak of 80% and 60% of  $P_m$  ( $\gamma_{0.8}$  and  $\gamma_{0.6}$ ) and ratios  $\mu_{0.8} = \gamma_{0.8}/\gamma_y$  and  $\mu_{0.6} = \gamma_{0.6}/\gamma_y$ , being  $\gamma_y$  the shear strain associated to the conventional yield strength

Table 4.13 - Main results concerning cobblestones masonry samples (C): maximum diagonal load ( $P_m$ ), average compressive strain in correspondence of  $P_m$  ( $\varepsilon_{cp}$ ), shear modulus ( $G$ ), ratios between  $P_m$  ( $P_{m(R)} / P_{m(U)}$ ) and between  $G$  ( $G_{(R)} / G_{(U)}$ ) of the reinforced and the unreinforced specimens, shear strains associated to a resistance value after the peak of 80% and 60% of  $P_m$  ( $\gamma_{0.8}$  and  $\gamma_{0.6}$ ) and ratios  $\mu_{0.8} = \gamma_{0.8}/\gamma_y$  and  $\mu_{0.6} = \gamma_{0.6}/\gamma_y$ , being  $\gamma_y$  the shear strain associated to the conventional yield strength

Table 4.14 – Evaluation on the equivalent principal tensile tests  $f_t$  from the peak load  $P_m$  obtained from diagonal compression tests for solid brick masonry samples, 250 mm thick (S) and calculation of the masonry shear strength  $\tau_0$

Table 4.15 – Evaluation on the equivalent principal tensile tests  $f_t$  from the peak load  $P_m$  obtained from diagonal compression tests for solid brick masonry samples, 380 mm thick (S2) and calculation of the masonry shear strength  $\tau_0$

Table 4.16 – Evaluation on the equivalent principal tensile tests  $f_t$  from the peak load  $P_m$  obtained from diagonal compression tests for infill solid brick masonry samples (I) and calculation of the masonry shear strength  $\tau_0$

Table 4.17 – Evaluation on the equivalent principal tensile tests  $f_t$  from the peak load  $P_m$  obtained from diagonal compression tests for rubble stone masonry samples (R, R2 and R3) and calculation of the masonry shear strength  $\tau_0$

Table 4.18 – Evaluation on the equivalent principal tensile tests  $f_t$  from the peak load  $P_m$  obtained from diagonal compression tests for cobblestones masonry samples (C) and calculation of the masonry shear strength  $\tau_0$

Table 4.19 – Analytical evaluation of the shear modulus concerning reinforced solid brick masonry samples, 250 mm thick (S) tested to diagonal compression: experimental shear modulus of reinforced ( $G_{(R),exp}$ ) and unreinforced ( $G_{(U)}$ ) samples, mortar shear modulus ( $G_c$ ), calculated shear modulus of reinforced samples ( $G_{(R),calc}$ ) and error percentage between  $G_{(R),calc}$  and  $G_{(R),exp}$  ( $\Delta_{err}$ )

Table 4.20 – Analytical evaluation of the shear modulus concerning reinforced solid brick masonry samples, 380 mm thick (S2) tested to diagonal compression: experimental shear modulus of reinforced ( $G_{(R),exp}$ ) and unreinforced ( $G_{(U)}$ ) samples, mortar shear modulus ( $G_c$ ), calculated shear modulus of reinforced samples ( $G_{(R),calc}$ ) and error percentage between  $G_{(R),calc}$  and  $G_{(R),exp}$  ( $\Delta_{err}$ )

Table 4.21 – Analytical evaluation of the shear modulus concerning reinforced infill solid brick masonry samples (I) tested to diagonal compression: experimental shear modulus of reinforced ( $G_{(R),exp}$ ) and unreinforced ( $G_{(U)}$ ) samples, mortar shear modulus ( $G_c$ ), calculated shear modulus of reinforced samples ( $G_{(R),calc}$ ) and error percentage between  $G_{(R),calc}$  and  $G_{(R),exp}$  ( $\Delta_{err}$ )

Table 4.22 – Analytical evaluation of the shear modulus concerning reinforced rubble stone masonry samples (R, R2 and R3) tested to diagonal compression: experimental shear modulus of reinforced ( $G_{(R),exp}$ ) and unreinforced ( $G_{(U)}$ ) samples, mortar shear modulus ( $G_c$ ), calculated shear modulus of reinforced samples ( $G_{(R),calc}$ ) and error percentage between  $G_{(R),calc}$  and  $G_{(R),exp}$  ( $\Delta_{err}$ )

Table 4.23 – Analytical evaluation of the shear modulus concerning reinforced cobblestones masonry samples (C) tested to diagonal compression experimental shear modulus of reinforced ( $G_{(R),exp}$ ) and unreinforced ( $G_{(U)}$ ) samples, mortar shear modulus ( $G_c$ ), calculated shear modulus of reinforced samples ( $G_{(R),calc}$ ) and error percentage between  $G_{(R),calc}$  and  $G_{(R),exp}$  ( $\Delta_{err}$ )

Table 4.24 – Analytical evaluation concerning solid brick masonry samples, 250 mm thick (S) tested to diagonal compression: experimental resistance of reinforced ( $P_{m(R),exp}$ ) and unreinforced samples ( $P_{m(U),exp}$ ), calculated diagonal compression resistance of the mortar coating ( $P_c$ ), preliminary analytical prediction of reinforced samples resistance ( $P_{m(U)} + P_c$ ) with error percentage ( $\Delta_{err(1)}$ ), coefficients  $\beta$  and  $\beta^*$  and calculated resistance of reinforced samples ( $P_{m(R),calc}$ ) with error percentage ( $\Delta_{err(2)}$ )

Table 4.25 - Analytical evaluation concerning solid brick masonry samples, 380 mm thick (S2) tested to diagonal compression: experimental resistance of reinforced ( $P_{m(R),exp}$ ) and unreinforced samples ( $P_{m(U),exp}$ ), calculated diagonal compression resistance of the mortar coating ( $P_c$ ), preliminary analytical prediction of reinforced samples resistance ( $P_{m(U)} + P_c$ ) with error percentage ( $\Delta_{err(1)}$ ), coefficients  $\beta$  and  $\beta^*$  and calculated resistance of reinforced samples ( $P_{m(R),calc}$ ) with error percentage ( $\Delta_{err(2)}$ )

Table 4.26 - Analytical evaluation concerning infill solid brick masonry samples (I) tested to diagonal compression: experimental resistance of reinforced ( $P_{m(R),exp}$ ) and unreinforced samples ( $P_{m(U),exp}$ ), calculated diagonal compression resistance of the mortar coating ( $P_c$ ), preliminary analytical prediction of reinforced samples resistance ( $P_{m(U)} + P_c$ ) with error percentage ( $\Delta_{err(1)}$ ), coefficients  $\beta$  and  $\beta^*$  and calculated resistance of reinforced samples ( $P_{m(R),calc}$ ) with error percentage ( $\Delta_{err(2)}$ )

Table 4.27 - Analytical evaluation concerning rubble stone masonry samples (R, R2 and R3) tested to diagonal compression: experimental resistance of reinforced ( $P_{m(R),exp}$ ) and unreinforced samples ( $P_{m(U),exp}$ ), calculated diagonal compression resistance of the mortar coating ( $P_c$ ), preliminary analytical prediction of reinforced samples resistance ( $P_{m(U)} + P_c$ ) with error percentage ( $\Delta_{err(1)}$ ), coefficients  $\beta$  and  $\beta^*$  and calculated resistance of reinforced samples ( $P_{m(R),calc}$ ) with error percentage ( $\Delta_{err(2)}$ )

Table 4.28 - Analytical evaluation concerning cobblestones masonry samples (C) tested to diagonal compression: experimental resistance of reinforced ( $P_{m(R),exp}$ ) and unreinforced samples ( $P_{m(U),exp}$ ), calculated diagonal compression resistance of the mortar coating ( $P_c$ ), preliminary analytical prediction of reinforced samples resistance ( $P_{m(U)} + P_c$ ) with error percentage ( $\Delta_{err(1)}$ ), coefficients  $\beta$  and  $\beta^*$  and calculated resistance of reinforced samples ( $P_{m(R),calc}$ ) with error percentage ( $\Delta_{err(2)}$ )

Table 4.29 – Main characteristics assumed for DS-B3 in the preliminary numerical simulations of diagonal compression tests ( $G_m$  and  $\nu$  are the shear and Poisson modulus,  $f_{t,m}$  and  $f_{c,m}$  the tensile and compressive strengths of unreinforced masonry,  $G_{fth}$  the fracture energy)

Table 4.30 – Main characteristics of the mortar considered in the numerical simulation

Table 4.31 – Comparisons between analytical (suffix “calc”) and numerical (suffix “num”) results in terms of first cracking load  $P_c$  of unreinforced mortar layers

Table 4.32 – Main numerical results concerning solid brick masonry samples with unreinforced mortar layers applied at both faces: peak load  $P_{m,num}$  and principal tensile stress at the center of the panel in masonry  $\sigma_{_m}$  and in mortar layer  $\sigma_{_c}$  at peak

Table 4.33 – Constitutive relationships adopted for the tensile behaviour of the mortar of the coating (C4)

Table 4.34 – Main characteristics assumed for DR-B5 and DC-B2 samples in the preliminary numerical simulations of diagonal compression tests ( $G_m$  and  $\nu$  are the shear and Poisson modulus,  $f_{t,m}$  and  $f_{c,m}$  the tensile and compressive strengths of unreinforced masonry,  $G/h$  the fracture energy)

Table 4.35 – Mechanical characteristics of the masonry resisting elements: Young and shear modulus ( $E_m$ ,  $G_m$ ), specific weight ( $\gamma_m$ ), compressive resistance in the vertical ( $f_{c,m}$ ) and horizontal ( $f_{hc,m}$ ) directions and shear resistance ( $\tau$ ).

Table 4.36 – Shear and bending resistances of piers and spandrels (being  $t$  the masonry thickness,  $b_s$  and  $b_p$  the spandrel and pier width,  $l_p$  the pier height,  $p$  the axial compressive stress,  $f_{c,m}$  and  $f_{hc,m}$  the masonry compressive resistances in the vertical and horizontal direction,  $H_p$  the tie beam tensile resistance at floor level, which has not to be greater than  $0.4 \cdot f_{hc,m} \cdot b_s \cdot t$ ).

Table 4.37 – Seismic performances of the analyzed buildings: peak load ( $F^*_{max}$ ), target displacement ( $d^*_i$ ), effective stiffness ( $K^*_{eff}$ ) and effective period ( $T^*_{eff}$ ) of the equivalent SDOF systems, resisting ground accelerations ( $a_{g,max}$ ) and ratio between  $a_{g,max}$  of reinforced (R) and unreinforced (U) structures

Table 5.1 - Main characteristics of the out-of-plane bending samples

Table 5.2 - Main test results for out-of-plane bending tests in terms of horizontal load  $P$ , out-of-plane deflection  $\delta$  and bending moment  $M$  associated to first cracking (suffix “cr”) and collapse (suffix “u”) and ratios between the maximum bending resistance of reinforced and unreinforced samples  $M_{u(R)}/M_{u(U)}$

Table 5.3 - Evaluation of the flexural tensile strength of unreinforced masonry  $f_{t(U)}$ : bending resistance of unreinforced sample  $M_{cr(U)}$ , half wall weight  $N_U$ , masonry cross section  $A_U$ , masonry resistance modulus  $W_U$ , mortar tensile strength  $f_{t,b}$  and ratio  $f_{t(U)}/f_{t,b}$

Table 5.4 - Evaluation of the residual load after the occurrence of cracking,  $M_{r(U),calc}$ : half wall weight  $N_U$ , masonry compressive strength  $f_{c,m}$ , masonry cross section  $A_U$ , experimental residual load  $M_{r(U),exp}$  and error percentage between calculated,  $M_{r(U),calc}$ , and experimental  $M_{r(U),exp}$  values

Table 5.5 - Comparison between experimental (suffix “exp.”) and analytical (suffix “calc.”) results in reinforced panels in terms of first cracking moments  $M_{cr(R)}$  ( $N_R$  weight of half reinforced wall,  $\alpha_c$  modular ratio,  $A_{id(R)}$  and  $W_{id(R)}$  cross section and the resistance modulus of the uncracked section, idealized to masonry,  $f_{t,c}$  mortar flexural tensile strength)

Table 5.6 - Comparison between experimental (suffix “exp.”) and analytical (suffix “calc.”) results in reinforced panels in terms of maximum bending moments  $M_{u(R)}$  ( $N_R$  weight of half reinforced wall)

Table 5.7 - Masonry shear and GFRM delamination checks for the three reinforced masonry samples: masonry shear strength,  $f_{v,Rd}$ , masonry shear resistance,  $V_{Rd}$ , maximum shear acting when  $M_{u(R)calc,inc}$  is attained,  $V_{Ed}(M_U)$ , calculated values of first cracking and maximum bending resistance,  $M_{cr(R)calc}$  and  $M_{u(R)calc,inc}$ , minimum distance from the wall end of the cross section where  $M_{cr(R)calc}$  is attained,  $l(M_{cr})$ , and minimum bond length,  $l_{b,min}$

Table 5.8 - Constitutive relationships adopted for the tensile behaviour of the masonry

Table 5.9 - Constitutive relationships adopted for the tensile behaviour of the mortar of the coating, for the different coating thicknesses considered

Table 5.10 – Masonry mechanical parameters: Young modulus ( $E_m$ ), compression ( $f_{c,m}$ ) and tensile ( $f_{t,m}$ ) strengths

Table 5.11 – Numerical results: out-of-plane resistances of unreinforced ( $f_{max(U)}$ ) and reinforced ( $f_{max(R)}$ ) masonry, ratios ( $f_{max(R)}/f_{max(U)}$ ), and ratios between the maximum deflection of reinforced walls and the main wall height ( $\delta_{(R)}/h$ )

Table 5.12 – Numerical results concerning unreinforced vaults - Case V1: position of the lateral cracked sections ( $\theta_e$ ), vertical loads ( $F_v$ ) and crown section vertical displacements ( $\delta_v$ ) associated to the crack formation at extrados (suffix e) and intrados (suffix i), residual load (suffix r), self-weight ( $W$ ) and ratio  $\alpha_v$ .

Table 5.13 – Numerical results concerning reinforced vaults - Case V1: vertical loads ( $F_v$ ) and crown section displacements ( $\delta_v$ ) associated to the crack formation at intrados (suffix i) and extrados (suffix e) and to the GFRP wire rupture (suffix w), position of the cross section in which the wires rupture occurred ( $\theta_w$ ), self-weights ( $W$ ) and ratios  $\alpha_v$ .

Table 5.14 – Numerical results concerning unreinforced vaults - Case V2: inclination of the cracking planes ( $\theta$ ), loads ( $F_h$ ) and crown section displacements ( $\delta_h$ ) associated to the crack formation at extrados (suffix e) and intrados (suffix i), self-weights ( $W$ ) and ratios  $\alpha_h$

Table 5.15 – Numerical results concerning reinforced vaults - Case V2: inclination of the cracking planes ( $\theta$ ), loads ( $F_h$ ) and crown section displacements ( $\delta_h$ ) associated to the crack formation at intrados (suffixes  $i1$  and  $i2$ ) at extrados (suffix e) and to the GFRP wire rupture (suffix w), self-weights ( $W$ ) and ratios  $\alpha_h$

Table 5.16 – Numerical results of unreinforced and reinforced vaults: comparisons between Case V1 and Case V3 in terms of position of the haunch cracked section ( $\theta_{v,e}$ ), maximum over-loads ( $Q_{max}$ ) and the ratio between maximum over-loads in case V1 and V3 ( $Q_{max,V1} / Q_{max,V3}$ ).

Table 5.17 – Numerical results of unreinforced and reinforced vaults: comparisons between Case V2 and V4 in terms of position of the haunch cracked section ( $\theta$ ), maximum over-loads in the horizontal ( $H_{max}$ ) and in the vertical ( $Q_{max}$ ) direction and ratio between the reinforced and unreinforced masonry resistances.

## 10 ACKNOWLEDGMENTS

The financial support of Fibre Net S.r.l. (Pavia di Udine – UD, Italy) in the development and execution of the experimental tests, as well as in the results collection, data analysis and numerical models development is gratefully acknowledged.

I wish also to thank the financial support of the Department of Civil Protection (Reluis 2014-2016).

The use of software Midas FEA and Midas GEN has been granted by CSP Fea – Engineering Solutions (Este – PD, Italy).

Deep thanks goes to my supervisor, prof. eng. Natalino Gattesco, for being a patient, demanding and reliable guide in my doctoral course and teaching me curiosity and devotion to work.

Special consideration goes to the useful help and the encouragement provided by dr. eng. Franco Trevisan and eng. Andrea Cernigoi, technicians of the Laboratory of Testing Materials of the University of Trieste, during the execution of experimental tests.

I am very thankful also to the willingness of the members of the Department of Engineering and Architecture of the University of Trieste, and, in particular, to the valuable suggestions provided by dr. eng. Giovanni Rinaldin and dr. eng. Chiara Bedon.

I would also like to thank very much Andrea and Cecilia Zampa, Allen Dudine, Enrico Zanello, Carlos Passerino, Massimo Melotto and the whole staff of Fibre Net S.r.l. for the time, trust, help and friendly welcome they gave me in these years.

An heartfelt thanks to Marco, for his great, great patience and love, to my parents, my relatives and my friends all.